

**ULTRAVIOLET AND INFRARED SPECTROSCOPY OF SYNTHETIC
PEPTIDES AND NATURAL PRODUCTS IN THE GAS PHASE**

by

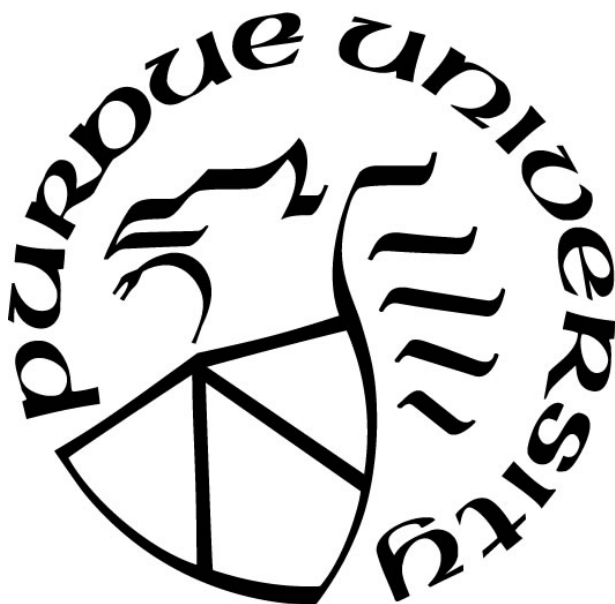
Karl N. Blodgett

A Dissertation

Submitted to the Faculty of Purdue University

In Partial Fulfillment of the Requirements for the degree of

Doctor of Philosophy



Department of Chemistry

West Lafayette, Indiana

May 2020

**THE PURDUE UNIVERSITY GRADUATE SCHOOL
STATEMENT OF COMMITTEE APPROVAL**

Dr. Timothy S. Zwier, Chair

Department of Chemistry

Dr. Garth J. Simpson

Department of Chemistry

Dr. Mary J. Wirth

Department of Chemistry

Dr. Scott A. McLuckey

Department of Chemistry

Approved by:

Dr. Christine A. Hrycyna

For Mom and Dad

ACKNOWLEDGMENTS

I want to first thank my family for providing a never-ending stream of support and encouragement throughout my academic career. Mom, thank you for being there to talk with me, regardless of the topic, when I needed someone to talk to. Your understanding, words of wisdom and encouragement, and perspective have been invaluable to me throughout my life. Dad, if any one person is responsible for setting me on the road to a Ph.D. in physical chemistry, it's you. Our early conversations about time travel, Flatland, aliens, infinity, and the empirical difference between table salt, sugar, and artificial sweeteners nurtured my ability to think deeply and critically, question, and wonder. These traits are some aspects of myself that I am most proud of. Words alone cannot express my gratitude to both of you. Thank you for being my guiding lights.

Tim, your abundant enthusiasm for science has been a source of inspiration throughout my time at Purdue. Thank you for welcoming me into your lab, and for your faith in my ability to grow as an independent scientist. When all is said and done, I can't imagine a better environment for me to learn, do research, and explore difficult ideas and concepts than in your laboratory. Thank you for always making the time to sit down with me to discuss the science and for your patience and encouragement. I consider myself lucky to have done my Ph.D. with a world-renowned spectroscopist.

To Batman, my faithful canine companion: thank you for your steadfast, loving companionship. Your acceptance and optimism are virtues us humans could learn a thing or two from.

To my fellow Zwier group alumni: it's been a wild ride. I've enjoyed getting to know all of you, and wish you all the best in your future. Thank you, Drs. Joseph Gord and Patrick Walsh, for showing me the ropes during my early days in the lab. A big thank you to Josh Fischer and John Lawler for being as interested as I am in long, deep, meandering, confusing, and, sometimes, enlightening conversations. Thanks for always being willing to listen. Khadija, I've enjoyed our discussions, especially those about baking that resulted in our exchange of baked goods. To my major collaborators, Dr. Soo Hyuk Choi, Dr. Edwin Sibert III, and Dr. Xiao Zhu: thank you all for your patience, encouragement, and dedication to the science. I've enjoyed working with and getting to know each of you. To all of my coauthors: thank you for your effort and time. To all of my teachers throughout my life: thank you for what you do. I've come to view the role of teacher

as one of the most noble pursuits one can undertake. Special thanks to Professor Schowe at Ivy Tech for formally introducing me to the wonderful world of chemistry. Through your hours-long marathon exams I first gained confidence in my ability to solve chemical problems. To the entire staff of the chemistry department at Purdue: thank you for all that you do, and for your willingness to answer questions and lend a helping hand. To the dozens of people that I've forgotten to mention: thank you for helping me along my way.

Jacquee, I'm certain that these words cannot capture the totality of how I think and feel about you. Thank you for your faith in me, especially in times when I lacked faith in myself. It means everything to me. I'm grateful to have spent these last eight years with you. The road that you and I are walking has taken some interesting turns, and when I consider where we were when we started our journey together and where we are today, my heart fills with joy and gratitude. You've been an unwavering source of encouragement, love, inspiration, and comfort during our time at Purdue. As you know, there are few things in this life that I am convinced are true. But just as Fry sees Leela in an otherwise uncertain future, I see you and I together, moving forward through the haziness and mystery of life, each with the encouragement, support, and faith of the other. I love you.

TABLE OF CONTENTS

LIST OF TABLES	11
LIST OF FIGURES	14
ABSTRACT	25
CHAPTER 1. INTRODUCTION	26
1.1 Motivation: Hydrogen Bonding in the Complexity Gap	26
1.2 Organization	28
1.2.1 Investigative Approach	29
1.2.2 Synthetic Foldamers and Asparagine-Containing Peptides	29
1.2.3 Hydrogen Atom Dislocation in Methyl Anthranilate	31
1.3 References	32
CHAPTER 2. METHODS	37
2.1 Supersonic Expansions and Molecular Beams	37
2.2 Chamber Design	38
2.2.1 Time of Flight Mass Spectrometer Chamber	39
2.2.2 Laser-Induced Fluorescence Chamber	41
2.3 Sample Handling	42
2.3.1 Thermal Heating	42
2.3.2 Nonresonant Laser Desorption	42
2.3.3 Water Cluster Formation	44
2.4 Radiation Sources	44
2.5 Spectroscopic Methods	46
2.5.1 Single-Resonance Methods	46
2.6 Double-Resonance Methods	49
2.6.1 Single-Conformation UV Spectroscopy	49
2.6.2 Single-Conformation IR Spectroscopy	50
2.7 Computational Methods	52
2.7.1 Conformational Sampling	52
2.7.2 Disconnectivity Graphs	53
2.8 References	54

CHAPTER 3. CONFORMER- AND DIASTEREOMER-SPECIFIC SPECTROSCOPY OF A MIXED α/β FOLDAMER PAIR	56
3.1 Introduction.....	56
3.2 Methods.....	58
3.2.1 Experimental Methods	58
3.2.2 Computational Methods.....	59
3.2.3 Nomenclature.....	61
3.3 Results and Analysis	61
3.3.1 (<i>SRSS</i>) Ac-Ala- β_{AHC} -Ala-NHBn.....	61
3.3.2 (<i>SSRS</i>) Ac-Ala- β_{AHC} -Ala-NHBn.....	67
3.4 Discussion	72
3.4.1 Conformational Preferences of <i>RS</i> and <i>SR</i> and Crystal Structures	72
3.4.2 Disconnectivity Graphs, Diastereomer Pairs, and Energetics.....	76
3.5 Conclusion	86
3.6 References.....	87
CHAPTER 4. COEXISTENCE OF LEFT- AND RIGHT-HANDED 12/10 MIXED HELICES IN CYCLICALLY CONSTRAINED β -PEPTIDES AND DIRECTED FORMATION OF SINGLE-HANDED HELICES UPON SITE-SPECIFIC METHYLATION	91
4.1 Introduction.....	91
4.2 Methods.....	94
4.2.1 Experimental Methods	94
4.2.2 Computational Methods.....	95
4.2.3 Nomenclature.....	96
4.3 Results and Analysis	97
4.3.1 Dimer, R-Dimer, and RR-Dimer.....	97
R2PI and IR-UV HB Spectroscopy	97
RIDIR Spectroscopy	97
4.3.2 L-Dimer and LL-Dimer	103
R2PI and IR-UV HB Spectroscopy	103
RIDIR Spectroscopy	104
4.3.3 Trimer.....	106

R2PI and IR-UV HB Spectroscopy	106
RIDIR Spectroscopy	108
Conformer B	110
4.3.4 Tetramer	111
R2PI and IR-UV HB Spectroscopy	111
RIDIR Spectroscopy	112
4.4 Discussion	116
4.4.1 Dipeptides	116
Steric Control of Helical Handedness in the Dipeptides	116
Effects of the C-Terminal NHBn Cap in the Dipeptides	119
4.4.2 Ac-(ACHC) _n -NHBn, n=2-4	121
Potential Energy Landscapes for Ac-(ACHC) _n -NHBn, n=2-4	121
Effects of the C-Terminal NHBn Cap for Ac-(ACHC) _n -NHBn, n=2-4	122
4.4.3 The ACHC Residue is a Robust Left- and Right-Handed 12/10 Mixed-Helix Former..	
.....	122
Conservation of Secondary Structure Between Phases	122
Free Energy Considerations and Structural Implications	123
4.5 Conclusion	127
4.6 References	128
CHAPTER 5. CONFORMATION-SPECIFIC SPECTROSCOPY OF ASPARAGINE-CONTAINING PEPTIDES: INFLUENCE OF SINGLE AND ADJACENT ASN RESIDUES ON INHERENT CONFORMATIONAL PREFERENCES	132
5.1 Introduction	132
5.2 Methods	134
5.2.1 Experimental Methods	134
5.2.2 Computational Methods	136
5.2.3 Nomenclature	136
5.3 Results and Analysis	137
5.3.1 Ac-Asn-NHBn	137
5.3.2 Ac-Ala-Asn-NHBn	146
5.3.3 Ac-Asn-Asn-NHBn	150

5.4	Discussion	155
5.4.1	Inverse γ -Turns	157
5.4.2	Extended Structures.....	164
5.4.3	Type I β -Turns.....	165
5.5	Conclusion	176
5.6	References	178
CHAPTER 6. VIBRONIC SPECTROSCOPY OF METHYL ANTHRANILATE AND ITS WATER COMPLEX: HYDROGEN ATOM DISLOCATION IN THE EXCITED STATE		183
6.1	Introduction	183
6.2	Experimental and Computational Methods.....	185
6.2.1	Experimental Methods	185
6.2.2	Computational Methods.....	186
6.3	Results and Analysis	187
6.3.1	Methyl Anthranilate Monomer	187
	Computational Predictions.....	187
	UV Excitation Spectroscopy.....	190
	DFL of the 0^0_0 Band and In-Plane Fundamentals.....	198
	DFL of the Out-Of-Plane Combination Bands and Fermi Resonance Pairs	204
6.3.2	Methyl Anthranilate-Water Complex	210
	Computational Predictions.....	210
	UV Excitation Spectroscopy.....	213
	Origin DFL Spectrum	217
6.4	Discussion	219
6.4.1	Structural Changes Associated with Hydrogen Atom Dislocation.....	219
6.4.2	Photophysical Properties of MA and Implications as a Sunscreen Precursor	226
6.5	Conclusion	241
6.6	References	242
CHAPTER 7. THE MISSING NH STRETCH FUNDAMENTAL IN S_1 METHYL ANTHRANILATE: IR-UV DOUBLE RESONANCE EXPERIMENTS AND LOCAL MODE THEORY		245
7.1	Introduction.....	245

7.2	Experimental Methods	247
7.3	Computational Methods	248
7.3.1	Description of the Local Mode Hamiltonians	248
7.3.2	Theoretical Modeling of the NH Stretch Fundamentals	250
	NH Stretch Vibrationally Adiabatic Surface Determination	250
	Description of the Reduced-Dimension Stretch-Bend Hamiltonian	253
7.4	Results	254
7.4.1	Methyl Anthranilate Monomer	254
7.4.2	Methyl Anthranilate-H ₂ O Complex	260
7.5	Discussion	266
7.6	Conclusion	272
7.7	References	273
	PUBLICATIONS	276

LIST OF TABLES

Table 3.1 Structural parameters and vibrational frequencies for the assigned structures of the RS and SR diastereomer pair calculated at the DFT M05-2X/6-31+G(d) level of theory, compared with experiment.	68
Table 3.2. Average backbone dihedral angles of α - and β -amino acids in the $\alpha\beta\alpha$ SR/RS 11/9 mixed helix. The RS B parameters have been inverted for more direct comparison with analogous helices	75
Table 3.3. Relative energies, free energy corrections, and free energies for structures under 15 kJ/mol of the global energy minimum of SR calculated at the DFT M052X-6-31+G(d) level of theory.	84
Table 4.1. Hydrogen bond distances (in Å) for all assigned structures studied in this work. Parameters calculated at the B3LYP-D3BJ/6-31+G(d) level of theory.	106
Table 4.2. Relative energies and backbone dihedral angles for all assigned structures. ^a	117
Table 4.3. Relative energies and free energies (at 300 K) for structures under 20 kJ/mol of the global energy minimum for the Dimer calculated at the DFT B3LYP-D3BJ/6-31+G(d) level..	124
Table 4.4. Relative energies and free energies (at 300 K) for structures under 20 kJ/mol of the global energy minimum for the L-Dimer calculated at the DFT B3LYP-D3BJ/6-31+G(d) level	124
Table 4.5. Relative energies and free energies (at 300 K) for structures under 20 kJ/mol of the global energy minimum for the R-Dimer calculated at the DFT B3LYP-D3BJ/6-31+G(d) level	125
Table 4.6. Relative energies and free energies (at 300 K) for structures under 20 kJ/mol of the global energy minimum for the LL-Dimer calculated at the DFT B3LYP-D3BJ/6-31+G(d) level	125
Table 4.7. Relative energies and free energies (at 300 K) for structures under 20 kJ/mol of the global energy minimum for the RR-Dimer calculated at the DFT B3LYP-D3BJ/6-31+G(d) level	125
Table 4.8. Relative energies and free energies (at 300 K) for structures under 20 kJ/mol of the global energy minimum for the Tetramer calculated at the DFT B3LYP-D3BJ/6-31+G(d) level	126
Table 4.9. Relative energies and free energies (at 300 K) for structures under 20 kJ/mol of the global energy minimum for the Trimer calculated at the DFT B3LYP-D3BJ/6-31+G(d) level.	126
Table 5.1. Hydrogen bonding cycles, calculated distances, and experimental vibrational frequencies for those interactions found in the Asn-containing peptides studied in this work, compared with the analogous Gln-containing peptides studied previously.	142

Table 5.2. Calculated dihedral angles (in degrees) of the Asn(N)-containing peptides studied in this work and the analogous Gln(Q)-containing peptides. Also listed are either the canonical dihedral angles or average values of those extracted from the protein data bank	160
Table 5.3. Relative potential energies and conformational families of the 30 kJ/mol lowest energy structures of Ac-Asn-NHBn upon exchange of NHBn cap for NHMe cap and geometry optimization at the DFT B3LYP-D3BJ/6-31+G(d) level of theory. Note that for the two observed conformers both the energy ordering and conformational family remain the same upon NHMe substitution.	162
Table 5.4. Relative potential energies, free energy corrections (at room temperature), and free energies for all calculated structures under 30 kJ/mol of the global energy minimum of Ac-Asn-NHBn, calculated at the DFT B3LYP-D3BJ/6-31+G(d) level of theory. Note that experimentally assigned conformers A and B are the lowest calculated potential and free energy structures	163
Table 5.5. Relative potential energies and conformational families of the 30 kJ/mol lowest energy structures of Ac-Ala-Asn-NHBn upon exchange of NHBn cap for NHMe cap and geometry optimization at the DFT B3LYP-D3BJ/6-31+G(d) level of theory. Note that the experimentally observed conformer remains the global energy minimum. Also, the type I β -turn structure is conserved even without the π interaction with the NHBn cap	169
Table 5.6. Relative potential energies and conformational families of the 30 kJ/mol lowest energy structures of Ac-Asn-Asn-NHBn upon exchange of NHBn cap for NHMe cap and geometry optimization at the DFT B3LYP-D3BJ/6-31+G(d) level of theory. Note that the experimentally observed conformer moves from the lowest to the second lowest energy structure upon NHMe cap substitution. The conformer that moved to the global minimum position is also a type I β -turn which differentiates itself from the experimentally observed structure by having a sidechain-sidechain hydrogen bond	171
Table 5.7. Relative potential energies, free energy corrections (at room temperature), and free energies for all calculated structures under 30 kJ/mol of the global energy minimum of Ac-Ala-Asn-NHBn, calculated at the DFT B3LYP-D3BJ/6-31+G(d) level of theory. Note that the experimentally assigned type I β -turn conformer remains the global minimum in both potential and free energy ranking	172
Table 5.8. Relative potential energies, free energy corrections (at room temperature), and free energies for all calculated structures under 30 kJ/mol of the global energy minimum of Ac-Asn-Asn-NHBn, calculated at the DFT B3LYP-D3BJ/6-31+G(d) level of theory. Note that the experimentally assigned type I β -turn conformer remains the global minimum in both potential and free energy ranking	173
Table 5.9. Ramachandran angle comparison of type I β -turns with sequence X(AN)X.....	175
Table 5.10. Ramachandran angle comparison of type I β -turns with sequence X(NN)X.....	176
Table 6.1. Experimental and Calculated S_0 and S_1 Frequencies of MA, Best Fit Normal Coordinate Displacement Values, and Excited to Ground State Normal Mode Projections	196
Table 6.2. Relative zero-point corrected potential energies, BSSE and zero-point corrected potential energies, adiabatic and vertical excitation energies of the water complex conformers	

calculated to lie within 10 kJ/mol of the global minimum. Calculations performed at the DFT B3LYP-D3BJ/def2TZVP level of theory.	211
Table 6.3. Experimental and Calculated S_0 and S_1 Frequencies of MA-H ₂ O	215
Table 6.4. Structural Parameters of MA and MA-H ₂ O ^a	221
Table 6.5. Electronic States in Aniline, Methyl Benzoate, Methyl Anthranilate, and Methyl Anthranilate-H ₂ O ^a	228
Table 7.1. Select experimental and theoretical frequencies of methyl anthranilate	254
Table 7.2. Select experimental and theoretical frequencies in methyl anthranilate-H ₂ O	260

LIST OF FIGURES

Figure 2.1. Illustration of a skimmed supersonic expansion	38
Figure 2.2. Schematic of the time-of-flight mass spectrometer (TOFMS) chamber.....	40
Figure 2.3. Schematic of the laser-induced fluorescence (LIF) chamber.....	41
Figure 2.4. Laser desorption scheme used to introduce non-volatile samples into the gas phase.	43
Figure 2.5. Spectroscopic schemes used in this work for recording (a) one-color and (b) two-color resonant two-photon ionization spectroscopy, (c) dispersed fluorescence spectroscopy, (d) IR-UV holeburning spectroscopy, (e) UV-UV holeburning spectroscopy, and (f) UV-depletion spectroscopy. Solid lines indicate a fixed frequency laser and dashed lines indicate a scanning laser.	48
Figure 2.6. Experimental schematic of (a) ground-state and (b) excited-state RIDIRS. (c) Pulse timings of lasers used in excited state RIDIRS.	52
Figure 3.1. The (a) <i>RS</i> and (b) <i>SR</i> diastereomers studied in this work. Examples (c) of <i>C_n</i> hydrogen bond designations as well as the color scheme used to designate hydrogen bond direction. Hydrogen bonds shown in blue go from the N- to the C-terminus whereas those in red are formed from the C- to the N-terminus. Definition of key dihedral angles (d) of relevance to the conformations observed. The two possible ACHC ring configurations (e); equatorial C=O/axial NH (top) or equatorial NH/axial C=O (bottom).....	57
Figure 3.2. R2PI (black trace) and IR-UV hole burning spectra (red, blue, and green traces) taken in the <i>S</i> ₀ – <i>S</i> ₁ region of <i>RS</i> . The UV transitions used to collect RIDIR spectra are marked with an asterisk.	62
Figure 3.3. <i>RS</i> RIDIR spectra in the a) amide I and (b) NH fundamental stretch regions of conformer A (red), conformer B (blue), and conformer C (green). Scaled, harmonic vibrational frequencies calculated at the M05-2X/6-31+G(d) level of theory are shown as black stick spectra for each conformer underneath the experimental trace and are labelled to indicate the hydrogen bonded cycle associated with each vibrational frequency. Scale factors of .96 and .94 were used in the amide I and NH stretch regions, respectively. Asterisks mark the peaks which were used to collect IR-UV HB spectra.	64
Figure 3.4. Assigned structures of <i>RS</i> (a) conformer A, (b) conformer B, (c) conformer C. Hydrogen bonds are indicated with dotted lines, labelled with O...H length, and color coated to indicate direction. Structural families, relative energies (kJ/mol), and dipole moments (<i>D</i>) are listed. Backbone hydrogens are omitted for clarity.	65
Figure 3.5. R2PI (black trace) and IR-UV hole burning spectra (blue and red trace) taken in the <i>S</i> ₀ – <i>S</i> ₁ region of <i>SR</i> . The UV transitions used to collect RIDIR spectra are marked with an asterisk.	69
Figure 3.6. <i>SR</i> RIDIR spectra in the (a) amide I and (b) NH fundamental stretch regions of conformer A (blue), and conformer B (red). Scaled, harmonic vibrational frequencies calculated	

at the M05-2X/6-31+G(d) level of theory are shown as black stick spectra for each conformer underneath the experimental trace and are labelled to indicate the hydrogen bonded cycle associated with each vibrational frequency. Scale factors of .96 and .94 were used in the amide I and NH stretch regions, respectively. Asterisks mark the peaks which were used to collect IR-UV HB spectra.70

Figure 3.7. Assigned structures of *SR* (a) conformer A and (b) conformer B. Hydrogen bonds are indicated with dotted lines, labelled with O...H length, and color coded to indicate direction. Structural families, relative energies (kJ/mol), and dipole moments (D) are listed. CH hydrogens are omitted for clarity.71

Figure 3.8. (a) Overlap of the back bone of the assigned *RS B* structure and its analogous crystal structure. (b) Overlap of the backbone of the assigned *RS B* and *SR B* helical structures. Unique stereocenters at the Ala residues circled in (b) (left), highlighting the difference in methyl group position between *SR B* and *RS B*. Formation of an incipient form of an 11/9 mixed helix is preferred in each case.74

Figure 3.9. Disconnectivity Graphs for (a) *SR* and (b) *RS* diastereomers created using the CHARMM22 force field in conjunction with parameterized potentials for cyclic β -amino acids. The assigned conformers in each case are labelled in the graphs. Highlighted portions of the graph represent different conformational families: green represents conformers that possess an eq. NH/axial C=O ACHC sub-unit, purple represents eq. C=O/axial NH, and red represents twist boat structures, which are local minima along the isomerization pathway from one chair conformation to the other.78

Figure 3.10. Energy level diagram of the lowest 30 kJ/mol disconnectivity graph structures after DFT optimization (M05-2X/6-31+G(d)) of the lowest 30 kJ/mol minima from the graph with zero-point energy correction. The relative energy defines 0.0 kJ/mol as the global minimum energy structure of the *RS* diastereomer, which was calculated to have the lowest absolute zero-point corrected energy. Structures are plotted vs. relative energy (kJ/mol) as a function of ACHC configuration and number of hydrogen bonds. Observed conformers are labelled, red lines indicate a structure with a bifurcated hydrogen bonding cycle. Cross diastereomer structural analogues are labelled with a prime (') and marked on the diagram with a blue "X". *SR A'* was not found in the disconnectivity graph search but was made by hand and submitted to DFT for optimization. Note that the global minimum for *SR* is 12 kJ/mol above that for *RS*.80

Figure 3.11. Shown above are the (a) – (c) *RS* and (b),(d) *SR* diastereomer pairs. Conservation of ACHC configuration is achieved in each pair except for *SR A/SR A'*.81

Figure 3.12. Alanine Ramachandran plot showing zero-point corrected potential energy as a function of ϕ/ψ dihedral angle pairs for Ac-Ala₃-NH₂ in the gas phase. Energies were calculated at the DFT B3LYP/D95(d,p) level of theory, and the figure was taken from Tsai et al. (Reprinted with permission from *J. Phys. Chem. B*, **2009**, *113* (1), 309-318. Copyright 2009 American Chemical Society.) Labelled circles represent the ϕ/ψ angles of the observed *RS* (red) and *SR* (blue) conformers. Color-coded energies are in kcal/mol.82

Figure 3.13. Isomerization pathway from *RS A* to *RS B* extracted from the disconnectivity diagram as calculated by the CHARMM22 force field.85

Figure 4.1. (a) *RS* and (b) *SR cis*-2-aminocyclohexanecarboxylic acid (ACHC) monomers used as the foldamer building blocks of the molecules studied in this work. Stereo- and site-specific methylation along the cyclohexane backbone of each species drives the local conformation of the ACHC residue into a chair conformation in which the methyl group is in the energetically favored equatorial position. These steric constraints serve to orient the peptide backbone into either a left- or right-handed conformation. Note that each non-methylated ACHC enantiomer may adopt either chair conformation.....92

Figure 4.2. (a) The Ac-(ACHC)₅-NHMe molecule in the right-handed 12/10 mixed-helical conformation with intramolecular hydrogen bonds labelled and color-coded as red (N → C terminal) or blue (C → N terminal). Structure taken from Shin *et al.* (ref. 6) (b) Chemical structures of the seven molecules studied in this work. Each residue is labelled, including the C-terminal NHBn cap (residue 5), and the N-terminal Acyl cap (residue A), such that the shared C-terminal motif composed of residues 3,4 and 5 may be referred to in a coherent manner across all molecular species.....93

Figure 4.3. (a) R2PI and IR-UV HB spectra in the S₀-S₁ region of the dimer. Franck-Condon progressions marked with *a* and *b* correspond to low-frequency modes of 54 and 27 cm⁻¹, respectively. Red daggers mark peaks belonging to a conformation with minor population in the expansion while peaks marked with an asterisk were used to collect holeburn spectra. (b) and (c): RIDIR spectra of the dimer in the hydride stretch and amide I/II regions, respectively. Stick spectra below each experimental trace represent the scaled, harmonic normal mode frequencies of the assigned conformation. These vibrational transitions, calculated at the B3LYP-D3BJ/6-31+G(d) level of theory, are labeled with the main carrier(s) of the vibration.98

Figure 4.4. Assigned structures and relative zero-point-corrected potential energies of (a) the dimer, R-dimer, and RR-dimer, and (b) the L-dimer and LL-dimer. In each case, the doubly methylated dipeptide is used to illustrate the steric control by which the methyl residues dictate local ACHC conformation. 2D hydrogen-bonding schematics are presented for each molecule, along with a down-axis view from N→C terminus, highlighting the preferred screw-sense of each dipeptide.100

Figure 4.5. Energy level diagrams for (a) the set of methylated dipeptides and (b) the series Ac-(ACHC)_n-NHBn with n=2,3,4. Each conformational minima has its relative zero-point-corrected energy (B3LYP-D3BJ/6-31+G(d)) plotted as a horizontal bar and color-coded to represent left-handed (red), right-handed (blue), or general turned (green) structures. Experimentally assigned conformers are represented with a heavy horizontal bar. The “pure” right- and left-handed helices as well as the cap-disrupted helical structures are labelled and connected via dotted lines to their corresponding structures across the molecules.....102

Figure 4.6. (a) R2PI and IR-UV HB spectra in the S₀-S₁ region of the LL-dimer. Franck-Condon progressions marked with *a* and *b* correspond to low-frequency modes of 32 and 27 cm⁻¹, respectively. (b) and (c) display the RIDIR spectra of the LL-dimer in the hydride stretch and amide I/II regions, respectively. Stick spectra below each experimental trace represent the scaled, harmonic normal mode frequencies of the assigned conformation. These vibrational transitions, calculated at the B3LYP-D3BJ/6-31+G(d) level of theory, are labeled with the main carrier(s) of the vibration. Transitions marked with an asterisk were those used to collect holeburn spectra.104

Figure 4.7. (a) R2PI (black) and conformer A IR-UV HB (red) spectra in the S_0 - S_1 origin region of the trimer. Blue daggers mark peaks belonging to a minor conformation (conf B) in the molecular beam (see text for details). A Franck-Condon progression in the major conformation (conf A) marked with x corresponds to a low frequency mode of 14 cm^{-1} , while a , b , and c correspond to low frequency modes in conf B of 188 , 151 , and 27 cm^{-1} , respectively. (b) and (c): RIDIR spectra of conformer A in the hydride stretch and amide I/II regions, respectively. Stick spectra below each experimental trace depict the scaled, harmonic vibrational frequencies of the assigned conformation. These vibrational transitions, calculated at the B3LYP-D3BJ/6-31+G(d) level of theory, are labeled with the main carrier(s) of the vibration. Transitions marked with an asterisk were those used to collect hole-burn spectra..... 107

Figure 4.8. Assigned structure and relative zero-point-corrected potential energies of (a) conformer A and (b) conformer B of the trimer; 3D structure and 2D hydrogen-bonding schematics are presented for each molecule, along with a down-axis view from $N \rightarrow C$ terminus, highlighting the preferred screw-sense of each conformer. 109

Figure 4.9. Calculated IR spectrum (black sticks) of Trimer conf B compared with the experimental IR spectrum of Trimer conf A. The peak marked with an asterisk at 3322 cm^{-1} was used to record the IR-UV HB spectrum of conf A, which likely accounts for the contamination from conf B..... 111

Figure 4.10. (a) R2PI (black) and IR-UV HB spectra in the S_0 - S_1 region of conformer B (blue trace) and conformer A (red trace) of the tetramer. The Franck-Condon progressions marked with a and b correspond to low-frequency modes of 187 and 54 cm^{-1} , respectively, in conformer B. The transition marked with a red dagger in the IR-UV HB spectrum of conformer B represents contamination from conformer A due to overlapping IR frequencies. (b) and (c): RIDIR spectra of conformer B (blue) and A (red) in the amide I/II and hydride stretch regions, respectively. Stick spectra below each experimental trace depict the scaled, harmonic normal mode frequencies of the assigned conformation. These vibrational transitions, calculated at the B3LYP-D3BJ/6-31+G(d) level of theory, are labeled with the main carrier(s) of the vibration. Transitions marked with an asterisk were those used to collect hole-burn spectra..... 113

Figure 4.11. Assigned structure and relative zero-point-corrected energies of (a) conformer B and (b) conformer A of the tetramer; 3D structure and 2D hydrogen-bonding schematics are presented for each molecule, along with a down-axis view from $N \rightarrow C$ terminus, highlighting the preferred screw-sense of each conformer. 115

Figure 4.12. Energy level diagrams for (a) the set of methylated dipeptides and (b) the series $\text{Ac}-(\text{ACHC})_n\text{-NHBn}$ with $n=2,3,4$, upon replacing the C-terminal NHBn cap with NHMe . Each conformational minima has its relative zero-point-corrected energy (B3LYP-D3BJ/6-31+G(d)) plotted as a horizontal bar and color-coded to represent left-handed (red), right-handed (blue), or general turned (green) structures. Experimentally assigned conformers are represented with a heavy horizontal bar. The “pure” right- and left-handed helices as well as the cap-disrupted helical structures are labelled and connected via dotted lines to their corresponding structures across the molecules..... 120

Figure 5.1. Chemical structures of the molecules studied in this work along with the definition of important dihedral angles used herein. Note that hydrogen bonds designated in blue indicate

backbone-sidechain hydrogen bonding while those designated in red indicate backbone-backbone hydrogen bonding	134
Figure 5.2. R2PI and IR-UV holeburning spectra of Ac-Asn-NHBn. Peaks marked with an asterisk ($37,629\text{ cm}^{-1}$, Conf. A; $37,569\text{ cm}^{-1}$, Conf. B) indicate transitions used to collect RIDIR spectra. Vibronic progressions are labeled with tie lines.....	138
Figure 5.3. RIDIR spectra of the two conformers of Ac-Asn-NHBn, conformer A (red trace) and conformer B (blue trace), in the hydride stretch (b) and Amide I/II (a) regions. The stick spectra presented below each experimental trace represent the scaled, harmonic normal mode frequencies of each assigned conformer calculated at the B3LYP-D3BJ/6-31+G(d) level of theory and are labelled with the main carrier(s) of the vibration. Transitions marked with an asterisk are those used to collect IR-UV holeburning spectra. See text for further discussion	139
Figure 5.4. Assigned structure of (a) conformer A and (b) conformer B of Ac-Asn-NHBn. 3D structure and 2D hydrogen bonding schematic are presented for each conformer, as well as the hydrogen bonding designation and relative zero-point corrected potential energies.	141
Figure 5.5. Structures of (a) conformer A and (b) conformer A ^{Rot} . 3D structure and 2D hydrogen bonding schematic are presented for each structure, as well as the hydrogen bonding designation, relative zero-point corrected potential energies, and the value of the CNCC dihedral angle, which serves to differentiate the two conformers from one another.	145
Figure 5.6. Relaxed potential energy scan about the CNCC dihedral angle which differentiates conformer A and A ^{Rot} . The two rotameric minima are labelled, indicating where upon the potential energy surface they lie.....	146
Figure 5.7. R2PI (black) and IR-UV holeburning (red) spectra of Ac-Ala-Asn-NHBn. The peak marked with an asterisk ($37,643\text{ cm}^{-1}$) indicates the transition used to collect RIDIR spectra. Vibronic progressions are labeled with tie lines.....	147
Figure 5.8. RIDIR spectra of the assigned conformer of Ac-Ala-Asn-NHBn in the (a) hydride stretch and (b) Amide I/II regions. Black stick spectra represent the scaled, harmonic, normal mode frequencies of the assigned structure calculated the B3LYP-D3BJ/6-31+G(d) level of theory. Labels indicate the main carrier(s) of the vibration.....	148
Figure 5.9. Assigned structure of (a) Ac-Ala-Asn-NHBn and (b) Ac-Asn-Asn-NHBn. 3D structure and 2D hydrogen bonding schematic are presented for each conformer, as well as the hydrogen bonding designation and relative zero-point corrected potential energies (among each molecule).	149
Figure 5.10. R2PI (black) and IR-UV holeburning (red) spectra of Ac-Asn-Asn-NHBn. The peak marked with an asterisk ($37,662\text{ cm}^{-1}$) indicates the transition used to collect RIDIR spectra. Vibronic progressions are labeled with tie lines.....	151
Figure 5.11. RIDIR spectra of the single observed conformer of Ac-Asn-Asn-NHBn in the hydride stretch (top) and Amide I/II (bottom) regions. Black stick spectra display the scaled, harmonic, normal mode frequencies of the assigned structure calculated the B3LYP-D3BJ/6-31+G(d) level of theory. Labels indicate the main carrier(s) of the vibration.	152

Figure 5.12. Two views of the peptide backbone overlap (with hydrogens removed) of Ac-Ala-Asn-NHBn and Ac-Asn-Asn-NHBn	153
Figure 5.13. Experimental hydride stretch RIDIR spectra for the type I β -turn conformers of (a) Ac-Ala-Asn-NHBn and (b) Ac-Asn-Asn-NHBn. The shared spectral signatures of the two conformers are highlighted.....	154
Figure 5.14. Energy level diagrams for the three asparagine-containing molecules studied herein. Each conformer has its relative zero-point corrected energy (B3LYP-D3BJ/6-31+G(d)) plotted as a function of backbone hydrogen bonding pattern with the following stylized nomenclature: backbone-backbone//sidechain-backbone// sidechain-sidechain . Asx-Turns are structures where a <i>C10</i> hydrogen bond is formed between the carboxamide C=O of an Asn on residue <i>i</i> and the backbone NH of residue <i>i</i> +2. Each conformer energy level is also color-coded to further indicate the type(s) of hydrogen bond(s) in which the amide sidechain(s) is (are) involved. Experimentally observed conformers are labelled with their letter designation. ‘Bridge’ designates structures where both the hydrogen bond donor and acceptor on the same carboxamide side chain are involved in hydrogen bonds to the backbone, or backbone and cap (Cap Bridge). Double Sidechain-Backbone designates structures in Ac-Asn-Asn-NHBn where each amide sidechain is involved in a single hydrogen bond to the backbone. Sidechain-Sidechain designates structures in Ac-Asn-Asn-NHBn where the two carboxamide sidechains are hydrogen bonding with each other	156
Figure 5.15. Hydride stretch IR spectra and experimentally assigned structures of analogous Ac-Asn-NHBn and Ac-Gln-NHBn conformers. Asn hydrogen bonds and spectra are designated in blue while those of Gln are designated in black. Transitions are labelled with the main carrier of the vibration with analogous hydrogen bonds in Asn and Gln analogs connected with dashed lines and color coded in the following way: the same hydrogen bonded cycles connected with brown lines and analogous ($C_n - (C_n + 1)$) cycles with faded blue to black lines	158
Figure 5.16. Hydride stretch IR spectra and experimentally assigned structures of analogous Ac-Ala-Asn-NHBn and Ac-Ala-Gln-NHBn (top) and Ac-Asn-Asn-NHBn and Ac-Gln-Gln-NHBn (bottom) conformers. Asn hydrogen bonds and spectra are designated in blue while those of Gln are designated in black. Transitions are labelled with the main carrier of the vibration with analogous hydrogen bonds going from Asn to Gln connected with dashed lines and color coded in the following way: the same hydrogen bonded cycles connected with brown lines and analogous ($C_n - (C_n + 1)$) cycles with faded blue to black lines	166
Figure 5.17. Two views of the peptide backbone overlap (with hydrogens removed) of Ac-Ala-Asn-NHBn and Ac-Ala-Gln-NHBn	168
Figure 5.18. Two views of the peptide backbone overlap (with hydrogens removed) of Ac-Asn-Asn-NHBn and Ac-Gln-Gln-NHBn	168
Figure 5.19. Comparison of the assigned type I β -turn structure of Ac-Asn-Asn-NHBn with the second lowest energy calculated structure which engages in sidechain-sidechain hydrogen bonding. Structures and energies are displayed for both NHBn and NHMe caps. Note that the energy ordering flips upon cap substitution	170
Figure 6.1. Chemical structures of methyl anthranilate (MA) and methyl anthranilate-water complex (MA-H ₂ O).....	184

Figure 6.2. The two low-energy rotamers of MA. Zero-point corrected energies calculated at the DFT B3LYP-D3BJ/def2TZVP level of theory	188
Figure 6.3. Optimized ground and S ₁ excited state geometries of MA with (a) bond distances and (b) bond angles labelled. Bond lengths are in angstroms (Å) and angles are in degrees. The difference between select ground and excited state parameters are shown in red parentheses. Values were calculated at the DFT B3LYP-D3BJ/def2TZVP level of theory.....	188
Figure 6.4. Relaxed potential energy scans about the improper CNHH dihedral defining the NH ₂ inversion in MA, in the S ₀ (bottom) and S ₁ (top) electronic states	189
Figure 6.5. (a) LIF excitation, (b) UV-UV hole-burning, and (c) UV depletion spectra of MA from 28,825 - 30,000 cm ⁻¹	191
Figure 6.6. Fluorescence decay traces of (a) MA and (b) MA-H ₂ O. Lifetimes were obtained by fitting each trace to a single exponential decay and extracting the time constant, τ (lifetime). The lifetime is measured to be 27 ns for MA and 23 ns for MA-H ₂ O.	192
Figure 6.7. 2C-R2PI spectra of MA (a) and MA-H ₂ O (b).....	193
Figure 6.8. Assigned S ₀ - S ₁ LIF excitation spectrum of MA. Progressions in the in-plane modes ν ₃₆ (179 cm ⁻¹), ν ₃₄ (366 cm ⁻¹), and ν ₃₃ (421 cm ⁻¹) are displayed via red, pink, and blue dotted tie-lines, respectively, while in-plane combination bands built off 36 ¹ ₀ , 34 ¹ ₀ , and 31 ¹ ₀ are shown with solid tie lines. The identity of mode X is listed above each respective tie line. The inset provides a close-up view of the two pairs of peaks identified as Fermi-resonance pairs.	194
Figure 6.9. Rotational band contour (RBC) scan of the electronic origin transition (top trace), taken at a UV laser resolution of 0.15 cm ⁻¹ . The bottom trace is the computed fit using the calculated transition dipole moment (<i>a:b:c</i> = 77:23:0) components and rotational constants from calculated ground and excited states. This fit was computed using the JB95 spectral fitting program (ref. 26).	195
Figure 6.10. Dispersed fluorescence spectrum of the S ₀ - S ₁ origin transition of MA. Progressions in the in-plane modes ν ₃₆ (179 cm ⁻¹), ν ₃₄ (361 cm ⁻¹), and ν ₃₃ (412 cm ⁻¹) are displayed via red, green, and blue dotted tie-lines, respectively, while in-plane combination bands built off 36 ¹ ₀ , 33 ¹ ₀ , and 18 ¹ ₀ are shown with solid tie lines. The identity of mode X is listed above each respective tie line	197
Figure 6.11. DFL spectra of the Franck-Condon active, in-plane fundamentals in MA: (a) 36 ¹ ₀ , (b) 35 ¹ ₀ , (c) 34 ¹ ₀ , (d) 33 ¹ ₀ , (e) 32 ¹ ₀ , (f) 31 ¹ ₀ , (g) 30 ¹ ₀ , and (h) 29 ¹ ₀ . Ground state progressions in analogous modes are labelled in blue text, and transitions which serve as false origins are marked with a red (0 ⁰ ₀).....	199
Figure 6.12. Ground state in-plane normal modes ν ₃₆ –ν ₂₉ of MA. Normal modes were calculated at the DFT B3LYP-D3BJ/def2TZVP level of theory.....	201
Figure 6.13. DFL spectra taken at increasing energies from the origin transition in MA.....	203
Figure 6.14. DFL spectra of transitions involving out-of-plane modes in MA: (a) 53 ² ₀ , (b) 51 ¹ ₀ 54 ¹ ₀ , (c) 51 ¹ ₀ 53 ¹ ₀ , (d) 50 ¹ ₀ 52 ¹ ₀ , and (e) 50 ¹ ₀ 51 ¹ ₀ . Transitions which serve as false origins are marked with a red (0 ⁰ ₀).....	205

Figure 6.15. Ground state out-of-plane normal modes ν_{54} – ν_{50} of MA, along with the reduced Duschinsky matrix of these modes. The matrix row elements give the expansion coefficients of the indicated S_1 normal coordinate in terms of the S_0 coordinates. The normal modes and Duschinsky matrix were calculated at the DFT B3LYP-D3BJ/def2TZVP level of theory.	206
Figure 6.16. DFL of Fermi resonance modes (a) $50^1_052^1_0$ and (b) 35^1_0 , and (c) $50^1_051^1_0$ and (d) 34^1_0 of MA. Ground state transitions to Fermi-mixed components are labelled in blue text, and transitions which serve as false origins are marked with a red (0^0_0).	207
Figure 6.17. The portion of the LIF spectrum containing the two pairs of Fermi-mixed vibronic levels, marked with asterisks.	209
Figure 6.18. All MA-H ₂ O conformers, with their BSSE/ZPE-corrected energies, calculated to lie within 10 kJ/mol of the global minimum	210
Figure 6.19. Optimized ground and S_1 excited state geometries of MA-H ₂ O with (a) bond distances and (b) bond angles labelled, and (c) a side view showing the change in water position upon electronic excitation. Bond lengths are in angstroms (Å) and angles are in degrees. The difference between select ground and excited state parameters are shown in red parentheses. Values were calculated at the DFT B3LYP-D3BJ/def2TZVP level of theory.	212
Figure 6.20. Assigned S_0 - S_1 LIF excitation spectrum of MA-H ₂ O. Progressions in the in-plane modes ν_{56} (189 cm^{-1}), and ν_{49} (427 cm^{-1}) are displayed via green and blue dotted tie-lines, respectively, while in-plane combination bands built off 49^1_0 are shown with solid tie lines. The identity of mode X is listed above each respective tie line.	214
Figure 6.21. Reduced Duschinsky rotation matrix, and vector displacement representation of the Franck-Condon active normal modes of MA-H ₂ O. Values in parentheses are those corresponding values in the MA monomer. Calculations performed at the DFT B3LYP-D3BJ/def2TZVP level of theory.	216
Figure 6.22. Dispersed fluorescence spectrum of the S_0 - S_1 origin transition of MA-H ₂ O. Progressions in the in-plane modes ν_{56} (187 cm^{-1}) and ν_{49} (418 cm^{-1}) are displayed via green and blue dotted tie-lines, respectively, while in-plane combination bands built off 49^0_1 and 23^0_1 are shown with solid tie lines. The identity of mode X is listed above each respective tie line.	218
Figure 6.23. Franck-Condon factor fits of the members of the mode 33 progression. The best fit displacement for this mode is 1.27.	224
Figure 6.24. Franck-Condon factor fits of the members of the mode 36 progression. The best fit displacement for this mode is 0.97.	225
Figure 6.25. The (a) molecular orbitals, transition coefficients, oscillator strength, (b) bond distance, and (c) bond angle parameters associated with the S_0 - S_1 transition of aniline. Calculations performed at the DFT B3LYP-D3BJ/def2TZVP level of theory.	227
Figure 6.26. The (a) bond distance, and (b) bond angle parameters associated with the S_0 - S_2 transition of methyl benzoate. Calculations performed at the DFT B3LYP-D3BJ/def2TZVP level of theory.	228

Figure 6.27. Molecular orbitals involved in the $S_0 - S_2$ electronic transition of methyl benzoate, along with the coefficients, calculated vertical excitation wavelength, and oscillator strength. Calculations performed at the DFT B3LYP-D3BJ/def2TZVP level of theory.	229
Figure 6.28. Molecular orbitals involved in the $S_0 - T_3$ electronic transition of methyl benzoate, along with the coefficients, calculated vertical excitation wavelength, and oscillator strength. Calculations performed at the DFT B3LYP-D3BJ/def2TZVP level of theory.	230
Figure 6.29. Molecular orbitals involved in the $S_0 - S_1$ electronic transition of MA, along with the coefficients, calculated vertical excitation wavelength, and oscillator strength. Calculations performed at the DFT B3LYP-D3BJ/def2TZVP level of theory.	232
Figure 6.30. Molecular orbitals involved in the $S_0 - T_4$ electronic transition of MA, along with the coefficients, calculated vertical excitation wavelength, and oscillator strength. Calculations performed at the DFT B3LYP-D3BJ/def2TZVP level of theory.	233
Figure 6.31. Molecular orbitals involved in the $S_0 - S_2$ electronic transition of MA, along with the coefficients, calculated vertical excitation wavelength, and oscillator strength. Calculations performed at the DFT B3LYP-D3BJ/def2TZVP level of theory.	234
Figure 6.32. Molecular orbitals involved in the $S_0 - S_3$ electronic transition of MA, along with the coefficients, calculated vertical excitation wavelength, and oscillator strength. Calculations performed at the DFT B3LYP-D3BJ/def2TZVP level of theory.	235
Figure 6.33. Molecular orbitals involved in the $S_0 - S_1$ electronic transition of MA-H ₂ O, along with the coefficients, calculated vertical excitation wavelength, and oscillator strength. Calculations performed at the DFT B3LYP-D3BJ/def2TZVP level of theory.	236
Figure 6.34. Molecular orbitals involved in the $S_0 - T_4$ electronic transition of MA-H ₂ O, along with the coefficients, calculated vertical excitation wavelength, and oscillator strength. Calculations performed at the DFT B3LYP-D3BJ/def2TZVP level of theory.	237
Figure 6.35. Molecular orbitals involved in the $S_0 - S_2$ electronic transition of MA-H ₂ O, along with the coefficients, calculated vertical excitation wavelength, and oscillator strength. Calculations performed at the DFT B3LYP-D3BJ/def2TZVP level of theory.	238
Figure 6.36. Molecular orbitals involved in the $S_0 - S_3$ electronic transition of MA-H ₂ O, along with the coefficients, calculated vertical excitation wavelength, and oscillator strength. Calculations performed at the DFT B3LYP-D3BJ/def2TZVP level of theory.	239
Figure 6.37. Transition dipole moment vectors for the lowest energy “bright” $S_0 - S_n$ electronic transition of (a) aniline ($S_0 - S_1$), (b) methyl benzoate ($S_0 - S_2$), and (c) methyl anthranilate ($S_0 - S_1$).	240
Figure 7.1. S_1 excited state optimized geometries of (a) methyl anthranilate and (b) its water complex. Bond distances are labelled in black text and angles in blue text. Changes in these parameters from their ground state values are shown in parentheses. Adapted from <i>Phys. Chem. Chem. Phys.</i> , 2019, 21, 21355 by permission of the PCCP Owner Societies.	246
Figure 7.2. The $\Psi_1(R)$ wavefunction of Eq. (6) plotted as a function of NH stretch bond length R (in angstroms). Remaining coordinates are chosen to minimize the energy corresponding to this	

state. The points correspond to the centers of the DVR sinc functions used in the minimization. The solid red line is the force along the HNC angle in $\text{cm}^{-1}/\text{rad}$ as a function of R252

Figure 7.3. (a) Ground and (b) S_1 excited state FDIR spectra from 2400 - 3700 cm^{-1} of methyl anthranilate. The spectra are divided into four regions: NH stretch, aromatic CH stretch (shaded in grey), CH_3 stretch (shaded in red), and low frequency. The experimental spectrum (black trace) is compared with the predictions of local mode modeling (unmarked stick spectra) in both electronic states. In both states the red stick spectra corresponding to the CH_3 Fermi-mixed transitions have been multiplied by a scale factor for a more ready comparison with experiment. The blue stick in (b) with a single asterisk at 2991 cm^{-1} is the calculated harmonic dislocated NH stretch while the blue stick marked with a double asterisk at 2761 cm^{-1} is the calculated standard anharmonic dislocated NH stretch transition. See text for further discussion.255

Figure 7.4. (a) Ground and (b) S_1 excited state RIDIR spectra from 1400 - 1800 cm^{-1} of methyl anthranilate. The calculated scaled harmonic normal mode frequencies (black stick spectra) are compared with experiment. See text for further discussion.257

Figure 7.5. The change in electrostatic potential mapped onto the surface of increasing electron density in going from S_0 - S_1 in methyl anthranilate. Calculated at the TD-DFT B3LYP-D3BJ/def2TZVP level of theory.259

Figure 7.6. (a) Ground and (b) S_1 excited state FDIR spectra from 2800 - 3800 cm^{-1} of methyl anthranilate- H_2O . The spectra are divided into three regions: NH stretch, aromatic CH stretch (shaded in grey), and CH_3 stretch (shaded in red). The experimental spectrum (black trace) is compared with the predictions of local mode modeling (unmarked stick spectra) in both electronic states. The transitions marked with daggers in (b) are small contributions from the S_0 MA- H_2O spectrum, which appear as a result of the slight overlap of the UV and IR lasers necessitated by a short excited state lifetime (23 ns) and less than ideal fluorescence signal. In both states the red stick spectra corresponding to the CH_3 Fermi-mixed transitions have been multiplied by a scale factor for a more ready comparison with experiment. The blue stick in (b) with a single asterisk at 3072 cm^{-1} is the calculated harmonic dislocated NH stretch transition. See text for further discussion.261

Figure 7.7. (a) Ground and (b) S_1 excited state RIDIR spectra from 1400 - 1800 cm^{-1} of methyl anthranilate- H_2O . The calculated scaled harmonic normal mode frequencies (black stick spectra) are compared with experiment. See text for further discussion.263

Figure 7.8. The change in electrostatic potential mapped onto the surface of increasing electron density in going from S_0 - S_1 in methyl anthranilate- H_2O . Calculated at the TD-DFT B3LYP-D3BJ/def2TZVP level of theory.265

Figure 7.9. (a) and (b) show the two lowest energy NH stretch eigenfunctions and corresponding potentials in S_1 plotted as a function of bond length. The zero of energy is the true calculated potential minimum of the excited state. Remaining coordinates values were chosen to minimize $E(v=0)$ in (a) and $E(v=1)$ in (b). In (a) there is 99 cm^{-1} of energy at the bottom of the well; in (b) there is 1202 cm^{-1} of energy. In (a) $E(v=0)$ is 1618 cm^{-1} and $E(v=1)$ is 4542 cm^{-1} . In (b) $E(v=0)$ is 2296 cm^{-1} and $E(v=1)$ is 3900 cm^{-1} . The energy difference between 4542 and 3900 cm^{-1} will get deposited into the remaining degrees of freedom. Results are for excited states using TD/B3LYP/6-311++(d,p) level of theory with dispersion. (c) and (d) show analogous results for

the S_0 electronic state. In both plots all coordinates but the NH stretch internal coordinate are held fixed. The NH stretch coordinate is varied to obtain the potential (red) and the associated wave functions. In (c) the remaining internal coordinates are held at the equilibrium geometry, and in (d) the remaining internal coordinates are held at values that minimize the energy of the state with one quantum of excitation in the NH stretch.268

Figure 7.10. (a) and (b) show the two lowest energy NH stretch eigenfunctions and corresponding potentials in S_1 plotted as a function of bond length. The zero of energy is the true calculated potential minimum of the excited state. Remaining coordinates values were chosen to minimize $E(v=0)$ in (a) and $E(v=1)$ in (b). In (a) there is 99 cm^{-1} of energy at the bottom of the well; in (b) there is 1202 cm^{-1} of energy. In (a) $E(v=0)$ is 1618 cm^{-1} and $E(v=1)$ is 4542 cm^{-1} . In (b) $E(v=0)$ is 2296 cm^{-1} and $E(v=1)$ is 3900 cm^{-1} . The energy difference between 4542 and 3900 cm^{-1} will get deposited into the remaining degrees of freedom. Results are for excited states using TD/B3LYP/6-311++(d,p) level of theory with dispersion. (c) and (d) displays analogous results for the S_1 state of the ND stretch. The difference between vertical and minimum energies for the $\nu_{\text{ND}} = 1$ state is $\Delta E_s = 151 \text{ cm}^{-1}$ compared to the analogous 642 cm^{-1} value found for the NH stretch.269

Figure 7.11. Equipotential curves plotted every 1000 cm^{-1} as a function of NH stretch and HNC bend coordinates. The remaining coordinates are constrained to the geometry that minimizes the $\nu_{\text{NH}} = 0$ state following the adiabatic procedure described in the text. (a) displays the anharmonic calculated potential energy surface and (b) - (e) show the four corresponding lowest energy eigenfunctions along with their associated eigenvalues. Intensities (km/mol) are given for select transitions using a linear dipole (I_L) and full dipole (I_F), the latter of which is evaluated at the DVR grid of points. (f) and (g) - (j) show analogous plots obtained with a quadratic potential from a Taylor series for the two degrees of freedom at the $\nu_{\text{NH}} = 0$ geometry. See text for further discussion.271

ABSTRACT

The hydrogen bond is one of nature's ubiquitous molecular interactions. Its role ranges from that of a static provider of structural integrity in proteins to that of a dynamic coordinate, along which excited state deactivation in sunscreen molecules is achieved. The work in this dissertation employs a supersonic expansion to collisionally cool peptide oligomers and a sunscreen chromophore to the zero-point vibrational level of their low lying conformational minima. These species are interrogated using high-resolution, conformer-specific ultraviolet and infrared laser spectroscopic techniques with the aim of elucidating their intrinsic conformational preferences, hydrogen bonding networks, and excited state deactivation mechanisms.

Synthetic foldamers are oligomers composed of non-natural building blocks, such as β - and γ -amino acids. Incorporation of such residues into a peptide backbone results in secondary and tertiary structures that are distinct from those found in nature. Herein, the folding propensity of a series of mixed α/β and pure β -peptides is presented. In each case, both the left- and right-handed emergence of mixed-helical secondary structures, the 11/9- and the 12/10-helix, are observed. Next, the intrinsic conformational preferences of a series of increasingly complex asparagine-containing peptides are characterized. Asparagine, with its flexible carboxamide sidechain, is omnipresent within the prion forming domain of the misfolded proteins associated with several neurodegenerative diseases. Asparagine's propensity for β -turn structures is discussed and compared with that of analogous peptide sequences found in nature.

Methyl anthranilate is a natural product that contains an identical electronic chromophore to the sunscreen agent, meradimate. The excited state deactivation mechanism of methyl anthranilate and its water complex is determined with extensive ultraviolet spectroscopic characterization, and is discussed within the broader context of its role as a sunscreen agent. Vibronic analysis coupled with computational results indicate extensive heavy-atom rearrangement leading to hydrogen atom dislocation, rather than full transfer, on the S_1 surface. This phenomenon is further characterized with infrared spectroscopy and theoretical modeling, in which the NH stretch is adiabatically separated from other internal coordinates. Extensive dilution of the dislocated NH stretch oscillator strength over many transitions and $\sim 1,300\text{ cm}^{-1}$ is predicted. These results may have implications for similar molecules, such as salicylic acid and its derivatives.

CHAPTER 1. INTRODUCTION

1.1 Motivation: Hydrogen Bonding in the Complexity Gap

The axiom that molecular structure dictates function has an impact on both the study and rational design of biologically active species that cannot be overstated. Using only 21 amino acids, the human body synthesizes the thousands of proteins necessary for carrying out life's processes, and among the interactions which stabilize a precisely folded protein structure, the hydrogen bond plays an unparalleled role. Indeed, without hydrogen bonding life as we know it would not exist. In addition to its static role in providing structural integrity, the hydrogen bond may be dynamic, as is the case in molecular species which undergo excited-state intramolecular proton transfer, where the nature of the hydrogen bond varies with the changing electronic structure of the molecule.

Classic experimental techniques used for the determination of secondary and tertiary structure of proteins and large molecules in solution and crystalline form include proton nuclear magnetic resonance (NMR) spectroscopy, X-ray crystallography, cryogenic electron microscopy (cryoEM), and, more recently, electron paramagnetic resonance (EPR) spectroscopy. These methods are powerful means for determining the three-dimensional configuration of entire proteins, and have recently been leveraged towards elucidating the structure of the repeating β -sheet unit which makes up the amyloid fibrils associated with diseases such as Alzheimer's.¹⁻⁸ Modern spectroscopic techniques aimed at understanding molecular structure and dynamics of large molecules in solution include two-dimensional infrared (IR) and electronic spectroscopy, both of which have been made possible by the advent of ultrafast lasers.⁹ While these techniques are powerful at determining the fate of vibrational and electronic excitations in complex systems, their corresponding spectra are generally difficult to interpret due to spectral broadening effects brought on by temperature, solvent interactions, and a manifold of states being populated.

On the other extreme, spectroscopic data from small chemical species composed of one to approximately ten atoms may be thoroughly analyzed and understood with high-resolution spectroscopy and quantum chemical calculations. The relatively simple potential energy surface of these molecules, along with their respective reaction coordinates, are generally well-characterized and amenable to high-level quantum modelling. Recording the spectra of such

species under isolated and jet-cooled conditions in the gas-phase overcomes the spectral congestion and broadening issues inherent to condensed-phased measurements.

In between small systems with a handful ($3N-6$, where N =number of atoms) of degrees of freedom and large systems ($N>1000$) characterized by complex potential energy hypersurfaces, there exists a substantial complexity gap in the both the understanding of intrinsic molecular properties and the theoretical models used for their description.¹⁰ The spectroscopic and theoretical study of species in this size regime is concerned with characterizing and understanding structural preferences,¹¹⁻²² stepwise solvation effects,²³⁻²⁸ isomerization dynamics,^{10, 29-34} vibronic coupling,^{24, 35-38} Fermi resonance effects,³⁹⁻⁴² amide/amide coupling,^{43, 44} and excited-state deactivation mechanisms.⁴⁵⁻⁵⁰

Of particular relevance to the work presented in this thesis are the first molecular beam studies of the amino acid tryptophan by Levy and coworkers.⁵¹⁻⁵³ These experiments, along with advances in tunable, high-power IR radiation sources, paved the way for experimentalists to test the intrinsic conformational preferences of increasingly large and complex biologically relevant molecules under isolated, jet-cooled conditions. The resulting spectra were free from the inhomogeneous broadening with which condensed phase measurements are replete, providing unparalleled detail on molecules of a size regime not hitherto experimentally feasible. Additionally, the use of mass spectrometry as a detection mechanism has allowed researchers to decompose a spectrum into its mass-specific components. This is especially useful for the study of water-bound species, ions, and molecular clusters.

In collaboration with the synthetic chemistry community, researchers eventually began to move beyond the amino acids provided by mother nature to study what effects the incorporation of non-natural amino acids, including β - and γ -residues, have on peptide backbone flexibility and intrinsic folding propensity.^{54,55} The properties of these non-natural oligomers, known as synthetic foldamers, have been a longstanding interest in the Zwier group.^{11, 12, 14, 56-65}

As researchers wade further and further into the complexity-gap, the ever-increasing size of the molecules under investigation require exponentially more computational time and resources for energetic and normal mode frequency calculations to compare with experiment. This makes the intelligent and intentional choosing of conformational minima, among potentially thousands, on which to run high-level calculations increasingly important. To this end, substantial efforts by the computational chemistry community, in particular Prof. David Wales at Cambridge University,

have resulted in the ability to calculate the potential energy surface of arbitrarily sized molecules using molecular mechanics force field potentials and searching algorithms.^{66, 67} Presented visually as a disconnectivity graph where the x-axis is a reduced-dimension isomerization coordinate, the isomerization pathways connecting all minima, along with their calculated energetic barriers, can be easily traced. This can be extremely helpful in understanding how isomerization barriers drive the conformational landscape of a given molecule. The calculated isomerization barriers can aid researchers in deciding which conformational families are worth devoting further computational resources to. Additionally, conformational minima and transition state structures and energies may be used to calculate rate constants using Rice-Ramsperger-Kassel-Marcus calculations, which may be of particular use in laser-induced population transfer experiments.^{10, 29-34}

This work represents another step into the complexity gap. The data presented in this dissertation is focused on the spectroscopic investigation of molecules that lie within the complexity gap, with a special focus on the role that the hydrogen bond plays in dictating molecular structure and stability in select natural and synthetic peptide sequences, as well as a naturally occurring UV filter. Ranging from N=20-102, the size of the molecules studied herein push the state-of-the-art quantum mechanical calculations to their limit. By coupling supersonic expansion sources, capable of collisionally-cooling molecules to their respective zero-point vibrational energy levels, with conformer-specific IR and ultraviolet (UV) single- and double-resonance spectroscopic techniques, the intrinsic properties of such species may be unveiled.^{10, 68}

1.2 Organization

The research presented in this dissertation falls into one of two categories. The first is concerned with the spectroscopic characterization of both natural and non-natural amino acid sequences isolated in the gas-phase, free from perturbative intermolecular interactions. Particular emphasis is placed on the effect that the sidechain and peptide backbone have on driving secondary structure. The second is concerned with extensive spectroscopic characterization of methyl anthranilate, a naturally occurring sunscreen precursor, and its water complex, via electronic and infrared spectroscopy. The ground and excited state geometries are experimentally and computationally characterized, with emphasis placed on the intramolecular H-bond and its surprising change in strength and character upon electronic excitation.

1.2.1 Investigative Approach

Chapter 2 describes the equipment and techniques used for the investigation of molecules cooled to their vibrational zero-point levels in the gas-phase. The production of molecular beams via collisional cooling in a supersonic expansion is described in some detail, followed by a description of the two vacuum chambers used to record the data presented in this work. The challenging task of coaxing non-volatile species into the gas-phase via non-resonant laser desorption is discussed, followed by a description of the various radiation sources and spectroscopic techniques used herein. The end of chapter 2 focuses on the computational aspect of the studies, with special attention paid to the force field searching procedure implemented in the study of large molecules, as well as the disconnectivity graphs which can be used to generate their potential energy surface at a molecular mechanics level.

1.2.2 Synthetic Foldamers and Asparagine-Containing Peptides

Established collaborations between the Zwier group and the synthetic chemistry groups of Professors Gellman and Choi have focused on elucidating and understanding the conformational preferences of non-natural amino acid-containing sequences in the gas-phase.^{11, 12, 14, 56-65} Much of this work is motivated by the fact that protein secondary structure is dictated by the conformational flexibility and interactions of individual amino acids along the peptide backbone. The secondary structures accessible to natural proteins are constrained by virtue of their being composed entirely of enantiomerically pure L- α -amino acid residues. Incorporation of various β - and γ -amino acid residues in the peptide chain confers novel flexibility (or rigidity) and sidechain interactions not accessible to those found in nature.

Single-conformation spectroscopic data under jet-cooled conditions of such peptide oligomers provide exquisite detail regarding their folding propensities as a function of monomeric building block. Such studies of molecules of increasing size, placing them rightfully in the complexity gap, are made possible through incorporation of non-resonant laser desorption sources.^{12, 18, 69, 70} The effort to characterize the fundamental properties of novel peptide sequences is continued in this work. Chapter 3 of this thesis presents a study of the folding propensities of a capped, cyclically constrained, mixed α/β diastereomer tripeptide pair: (*SSRS*) Ac-Ala- β_{ACHC} -Ala-NHBn and (*SRSS*) Ac-Ala- β_{ACHC} -Ala-NHBn. These molecules each contain a cyclohexane

residue, along which their stereochemistries differ. Steric constraints dictate that any stable ACHC structure adopt one of two chair conformations: equatorial C=O/axial NH, or *vice versa*. The *SRSS* diastereomer forms an 11/9 mixed-helical conformation in crystalline form, in which C11 and C9 hydrogen bonds alternate directions along the helical axis.⁷¹ In describing hydrogen bonds, the C_n notation is used, in which n represents the number of atoms involved in a hydrogen bonded ring. Experimentally assigned conformers, as well as their calculated energies and structural features, are presented and discussed. Additionally, disconnectivity graphs of each diastereomer are presented and the complex impact of the stereochemistry along the β_{ACHC} residue discussed.

Chapter 4 presents single-conformer data on a series of peptides comprised entirely of the β_{ACHC} residue. In the condensed phase these oligomers adopt both right- and left-handed 12/10 mixed helices, the screw sense of which is interconvertible via the concerted ring flip of all cyclohexane moieties.^{72, 73} The inherent folding propensities of the neutral series, Ac-(β_{ACHC}) $_n$ -NHBn, $n=2-4$, using conformation-specific infrared and ultraviolet spectroscopy is presented. Additionally, the ability of site- and stereo-specific methylation along the cyclohexane backbone at the dipeptide ($n=2$) level to sterically lock in one cyclohexane chair conformation as a means of driving helical formation of one screw sense is investigated. The gas-phase data is compared with that of the condensed phase, and the intriguing results of calculated free and potential energy is discussed.

Chapter 5 investigates the effect that the natural α -amino acid asparagine, with its flexible carboxamide side chain ($-\text{CH}_2\text{-C(=O)-NH}_2$), has on local peptide backbone conformation. This work builds upon that of Walsh and coworkers, where the effect of glutamine on peptide conformation was probed.^{12, 65} Glutamine differs from asparagine only in that it has one additional methylene group in its sidechain. Both of these polar amino acids are abundant in the so-called prion-forming domains of misfolded proteins associated with Prion diseases such as Creutzfeldt-Jakob disease, fatal familial disease, and Gerstmann-Straussler-Scheinker syndrome.^{74, 75} Much work across many domains of science has been directed towards elucidating the role of asparagine and glutamine in these diseases. In this chapter, the role that asparagine plays in local protein conformation is determined through spectroscopic characterization of a series of increasingly complex, capped peptides: Ac-Asn-NHBn, Ac-Ala-Asn-NHBn, and Ac-Asn-Asn-NHBn. The results are discussed, compared and contrasted with those of analogous glutamine-containing peptides.

1.2.3 Hydrogen Atom Dislocation in Methyl Anthranilate

Methyl anthranilate (MA) is a natural product found in citrus honey, neroli and bergamot oils, and used by the food industry as a grape-flavoring agent. Of particular relevance to this thesis, MA is the precursor to menthyl anthranilate (MenA), an FDA approved sunscreen agent, both of which contain an intramolecular 6-membered $\text{HNH}\cdots\text{O}=\text{C}$ hydrogen bond between ortho ring substituents. Stavros and coworkers have recently demonstrated that MA and MenA share nearly identical photophysical properties in the condensed phase, rendering insights from a spectroscopic study of MA particularly relevant to that of MenA.⁷⁶

Efficient sunscreen molecules need some mechanism by which their UV-absorbing capacities may be recycled. Physically, this requires the absorbing species to return to its ground electronic state via internal conversion (IC), for example. In some sunscreen molecules, IC is facilitated on the excited state surface by H-atom transfer, in which a hydrogen atom is transferred from the donor to the acceptor nucleus. Chapter 6 investigates the UV-absorbing properties and excited state fate of MA with extensive spectroscopic characterization including laser-induced fluorescence, dispersed fluorescence, and UV-depletion spectroscopies. The excited-state deactivation mechanism is determined, and the vibrational structure of the ground and first excited singlet states comprehensively assigned. Rather than a full H-atom transfer, MA is found to undergo a H-atom dislocation, characterized by a reorientation, constriction, and significant strengthening of the intramolecular hydrogen bond. Corroborating computational evidence is presented and discussed. Additionally, the structural and spectroscopic effect of a single water molecule binding to MA is presented.

Chapter 7 further investigates the nature of the H-atom dislocation with infrared spectroscopy in both the S_0 and S_1 electronic states by continuing a longstanding collaboration between the Zwier (experimental) and Sibert (theoretical) research groups. In the excited electronic state, the coupled stretching vibrations of the NH_2 group uncouple from one another, giving rise to a ‘free’ and a ‘dislocated’ NH stretch mode, the latter of which exhibits bizarre qualities in the spectrum. Experimental IR spectra in the hydride stretch region is assigned with the aid of a local mode Hamiltonian, leading to the accurate designation of nearly every band from 2400 - 3800 cm^{-1} in both electronic states. The excited state ‘dislocated’ NH stretch transition is modeled by Sibert with an adiabatic separation of nuclear coordinates, resulting in a refined description of hydrogen atom dislocation, as well as its elusive effect on the corresponding spectroscopy.

1.3 References

1. T. L. Benzinger, D. M. Gregory, T. S. Burkoth, H. Miller-Auer, D. G. Lynn, R. E. Botto and S. C. Meredith, *Proc. Natl. Acad. Sci. U. S. A.*, 1998, **95**, 13407-13412.
2. A. K. Paravastu, R. D. Leapman, W.-M. Yau and R. Tycko, *Proc. Natl. Acad. Sci. U. S. A.*, 2008, **105**, 18349-18354.
3. A. T. Petkova, W.-M. Yau and R. Tycko, *Biochem. (Mosc.)*, 2006, **45**, 498-512.
4. F. Shewmaker, R. B. Wickner and R. Tycko, *Proc. Natl. Acad. Sci. U. S. A.*, 2006, **103**, 19754-19759.
5. A. Gorkovskiy, K. R. Thurber, R. Tycko and R. B. Wickner, *Proc. Natl. Acad. Sci. U. S. A.*, 2014, **111**, E4615-E4622.
6. D. S. Kryndushkin, R. B. Wickner and R. Tycko, *J. Mol. Biol.*, 2011, **409**, 263-277.
7. S. Ngo, L. Gu and Z. Guo, *J. Biol. Chem.*, 2011, **286**, 29691-29699.
8. U. Baxa, R. B. Wickner, A. C. Steven, D. E. Anderson, L. N. Marekov, W.-M. Yau and R. Tycko, *Biochem. (Mosc.)*, 2007, **46**, 13149-13162.
9. P. Hamm and M. Zanni, *Concepts and methods of 2D infrared spectroscopy*, Cambridge University Press, 2011.
10. T. S. Zwier, *J. Phys. Chem. A*, 2006, **110**, 4133-4150.
11. P. S. Walsh, R. Kusaka, E. G. Buchanan, W. H. James, B. F. Fisher, S. H. Gellman and T. S. Zwier, *J. Phys. Chem. A*, 2013, **117**, 12350-12362.
12. P. S. Walsh, K. N. Blodgett, C. McBurney, S. H. Gellman and T. S. Zwier, *Angew. Chem. Int. Ed.*, 2016, **55**, 14618-14622.
13. V. A. Shubert, E. E. Baquero, J. R. Clarkson, W. H. James III, J. A. Turk, A. A. Hare, K. Worrel, M. A. Lipton, D. P. Schofield and K. D. Jordan, *J. Chem. Phys.*, 2007, **127**, 234315.
14. R. Kusaka, D. Zhang, P. S. Walsh, J. R. Gord, B. F. Fisher, S. H. Gellman and T. S. Zwier, *J. Phys. Chem. A*, 2013, **117**, 10847-10862.
15. N. M. Kidwell, N. J. Reilly, B. Nebgen, D. N. Mehta-Hurt, R. D. Hoehn, D. L. Kokkin, M. C. McCarthy, L. V. Slipchenko and T. S. Zwier, *J. Phys. Chem. A*, 2013, **117**, 13465-13480.
16. F. Jiang, W. Han and Y.-D. Wu, *PCCP*, 2013, **15**, 3413-3428.
17. D. M. Hewett, S. Bocklitz, D. P. Tabor, E. L. Sibert III, M. A. Suhm and T. S. Zwier, *Chemical Science*, 2017, **8**, 5305-5318.

18. J. R. Gord, D. M. Hewett, A. O. Hernandez-Castillo, K. N. Blodgett, M. C. Rotondaro, A. Varuolo, M. A. Kubasik and T. S. Zwier, *PCCP*, 2016, **18**, 25512-25527.
19. E. Gloaguen and M. Mons, in *Gas-Phase IR Spectroscopy and Structure of Biological Molecules*, eds. A. M. Rijs and J. Oomens, Springer International Publishing, Cham, 2015, DOI: 10.1007/128_2014_580, pp. 225-270.
20. W. Chin, F. Piuzzi, I. Dimicoli and M. Mons, *PCCP*, 2006, **8**, 1033-1048.
21. W. Chin, M. Mons, J.-P. Dognon, F. Piuzzi, B. Tardivel and I. Dimicoli, *PCCP*, 2004, **6**, 2700-2709.
22. V. Brenner, F. Piuzzi, I. Dimicoli, B. Tardivel and M. Mons, *J. Phys. Chem. A*, 2007, **111**, 7347-7354.
23. T. S. Zwier, *Annu. Rev. Phys. Chem.*, 1996, **47**, 205-241.
24. P. S. Walsh, E. G. Buchanan, J. R. Gord and T. S. Zwier, *J. Chem. Phys.*, 2015, **142**, 154304.
25. D. Zhang, K. N. Blodgett, X. Zhu and T. S. Zwier, *J. Phys. Chem. A*, 2017, **121**, 986-997.
26. P. S. Walsh, E. G. Buchanan, J. R. Gord and T. S. Zwier, *J. Chem. Phys.*, 2015, **142**, 154303.
27. D. P. Tabor, R. Kusaka, P. S. Walsh, T. S. Zwier and E. L. Sibert, *J. Phys. Chem. A*, 2015, **119**, 9917-9930.
28. D. P. Tabor, R. Kusaka, P. S. Walsh, E. L. Sibert III and T. S. Zwier, *J. Phys. Chem. L.*, 2015, **6**, 1989-1995.
29. W. L. Ryan and D. H. Levy, *J. Am. Chem. Soc.*, 2001, **123**, 961-966.
30. J. J. Newby, C. W. Müller, C.-P. Liu and T. S. Zwier, *J. Am. Chem. Soc.*, 2010, **132**, 1611-1620.
31. C. P. Harrilal, A. F. DeBlase, J. L. Fischer, J. T. Lawler, S. A. McLuckey and T. S. Zwier, *J. Phys. Chem. A*, 2018, **122**, 2096-2107.
32. B. C. Dian, A. Longarte and T. S. Zwier, *Science*, 2002, **296**, 2369-2373.
33. B. C. Dian, A. Longarte, P. R. Winter and T. S. Zwier, *J. Chem. Phys.*, 2004, **120**, 133-147.
34. B. C. Dian, J. R. Clarkson and T. S. Zwier, *Science*, 2004, **303**, 1169-1173.
35. N. R. Pillsbury, N. M. Kidwell, B. Nebgen, L. V. Slipchenko, K. O. Douglass, J. R. Cable, D. F. Plusquellic and T. S. Zwier, *J. Chem. Phys.*, 2014, **141**, 064316.
36. P. Ottiger and S. Leutwyler, *J. Chem. Phys.*, 2012, **137**, 204303.
37. P. Ottiger, H. Köppel and S. Leutwyler, *Chemical Science*, 2015, **6**, 6059-6068.

38. E. G. Buchanan, P. S. Walsh, D. F. Plusquellic and T. S. Zwier, *J. Chem. Phys.*, 2013, **138**, 204313.
39. E. L. Sibert III, N. M. Kidwell and T. S. Zwier, *J. Phys. Chem. B*, 2014, **118**, 8236-8245.
40. E. L. Sibert, D. P. Tabor, N. M. Kidwell, J. C. Dean and T. S. Zwier, *J. Phys. Chem. A*, 2014, **118**, 11272-11281.
41. N. M. Kidwell, D. N. Mehta-Hurt, J. A. Korn, E. L. Sibert III and T. S. Zwier, *J. Chem. Phys.*, 2014, **140**, 214302.
42. E. G. Buchanan, J. C. Dean, T. S. Zwier and E. L. Sibert III, *J. Chem. Phys.*, 2013, **138**, 064308.
43. S. Ham, S. Cha, J.-H. Choi and M. Cho, *J. Chem. Phys.*, 2003, **119**, 1451-1461.
44. E. G. Buchanan, W. H. James, S. H. Choi, L. Guo, S. H. Gellman, C. W. Müller and T. S. Zwier, *J. Chem. Phys.*, 2012, **137**, 094301.
45. K. Yamazaki, Y. Miyazaki, Y. Harabuchi, T. Taketsugu, S. Maeda, Y. Inokuchi, S.-n. Kinoshita, M. Sumida, Y. Onitsuka and H. Kohguchi, *J. Phys. Chem. L.*, 2016, **7**, 4001-4007.
46. J. Zhao, S. Ji, Y. Chen, H. Guo and P. Yang, *PCCP*, 2012, **14**, 8803-8817.
47. D. Tuna, A. L. Sobolewski and W. Domcke, *J. Phys. Chem. B*, 2014, **118**, 976-985.
48. P. S. Sherin, J. Grilj, Y. P. Tsentalovich and E. Vauthey, *J. Phys. Chem. B*, 2009, **113**, 4953-4962.
49. T. Raeker and B. Hartke, *J. Phys. Chem. A*, 2017, **121**, 5967-5977.
50. L. A. Baker, M. D. Horbury, S. E. Greenough, P. M. Coulter, T. N. Karsili, G. M. Roberts, A. J. Orr-Ewing, M. N. Ashfold and V. G. Stavros, *J. Phys. Chem. L.*, 2015, **6**, 1363-1368.
51. T. R. Rizzo, Y. D. Park and D. H. Levy, *J. Chem. Phys.*, 1986, **85**, 6945-6951.
52. T. R. Rizzo, Y. D. Park, L. A. Peteanu and D. H. Levy, *J. Chem. Phys.*, 1986, **84**, 2534-2541.
53. L. A. Philips, S. Webb, S. J. Martinez, G. Fleming and D. H. Levy, *J. Am. Chem. Soc.*, 1988, **110**, 1352-1355.
54. D. Seebach and J. Gardiner, *Acc. Chem. Res.*, 2008, **41**, 1366-1375.
55. S. H. Gellman, *Acc. Chem. Res.*, 1998, **31**, 173-180.
56. E. E. Baquero, W. H. James, S. H. Choi, S. H. Gellman and T. S. Zwier, *J. Am. Chem. Soc.*, 2008, **130**, 4784-4794.

57. E. E. Baquero, W. H. James, S. H. Choi, S. H. Gellman and T. S. Zwier, *J. Am. Chem. Soc.*, 2008, **130**, 4795-4807.
58. W. H. James, E. E. Baquero, V. A. Shubert, S. H. Choi, S. H. Gellman and T. S. Zwier, *J. Am. Chem. Soc.*, 2009, **131**, 6574-6590.
59. W. H. James, E. E. Baquero, S. H. Choi, S. H. Gellman and T. S. Zwier, *J. Phys. Chem. A*, 2010, **114**, 1581-1591.
60. E. G. Buchanan, W. H. James Iii, A. Gutberlet, J. C. Dean, L. Guo, S. H. Gellman and T. S. Zwier, *Faraday Discuss.*, 2011, **150**, 209-226.
61. W. H. James, E. G. Buchanan, L. Guo, S. H. Gellman and T. S. Zwier, *J. Phys. Chem. A*, 2011, **115**, 11960-11970.
62. W. H. James, E. G. Buchanan, C. W. Müller, J. C. Dean, D. Kosenkov, L. V. Slipchenko, L. Guo, A. G. Reidenbach, S. H. Gellman and T. S. Zwier, *J. Phys. Chem. A*, 2011, **115**, 13783-13798.
63. E. G. Buchanan, W. H. J. III, S. H. Choi, L. Guo, S. H. Gellman, C. W. Müller and T. S. Zwier, *J. Chem. Phys.*, 2012, **137**, 094301.
64. J. R. Gord, P. S. Walsh, B. F. Fisher, S. H. Gellman and T. S. Zwier, *J. Phys. Chem. B*, 2014, **118**, 8246-8256.
65. P. S. Walsh, J. C. Dean, C. McBurney, H. Kang, S. H. Gellman and T. S. Zwier, *PCCP*, 2016, **18**, 11306-11322.
66. D. A. Evans and D. J. Wales, *J. Chem. Phys.*, 2003, **118**, 3891-3897.
67. D. J. Wales, M. A. Miller and T. R. Walsh, *Nature*, 1998, **394**, 758-760.
68. T. S. Zwier, *J. Phys. Chem. A*, 2001, **105**, 8827-8839.
69. J. C. Dean, E. G. Buchanan and T. S. Zwier, *J. Am. Chem. Soc.*, 2012, **134**, 17186-17201.
70. J. R. Gord, Purdue University, 2016.
71. M. Lee, J. Shim, P. Kang, I. A. Guzei and S. H. Choi, *Angew. Chem. Int. Ed.*, 2013, **52**, 12564-12567.
72. S. Shin, M. Lee, I. A. Guzei, Y. K. Kang and S. H. Choi, *J. Am. Chem. Soc.*, 2016.
73. G. Jang, S. Shin, I. A. Guzei, S. Jung, M.-G. Choi and S. H. Choi, *Bull. Korean Chem. Soc.*, 2018, **39**, 265-268.
74. M. D. Geschwind, *Continuum (Minneapolis, Minn.)*, 2015, **21**, 1612-1638.

75. S. B. Prusiner, R. A. Barry, M. P. McKinley, C. G. Bellinger, R. K. Meyer, S. J. DeArmond and D. T. Kingsbury, in *Viruses, Immunity, and Mental Disorders*, Springer, 1987, pp. 23-32.
76. N. d. N. Rodrigues, N. C. Cole-Filipiak, K. N. Blodgett, C. Abeysekera, T. S. Zwiier and V. G. Stavros, *Nature Communications*, 2018, **9**, 5188.

CHAPTER 2. METHODS

A combination of theoretical and experimental methods is used for the work presented in this thesis. Many of these techniques have been described in greater detail elsewhere.¹⁻⁴ This section gives an overview of the hardware and experimental/computational techniques used to record and interpret conformation specific infrared and ultraviolet spectra in the gas phase. Project dependent details are given at the beginning of each chapter.

2.1 Supersonic Expansions and Molecular Beams

All experiments described in this thesis utilize a supersonic expansion to collisionally cool and collapse the Boltzmann distributed population of the sample molecule to its energetically low-lying conformational isomers (conformers) in the gas phase, represented as minima on the molecule's complex potential energy surface (PES). The narrow velocity distribution within the moving frame of the expansion provides the added benefit of an isolated environment which enables the recording of high-resolution spectral data that is free from inhomogeneous broadening effects with which the condensed phase is replete.⁵

In the simplest case, a small fraction of the target molecules are seeded into He or Ne backing gas (stagnation pressures, p_0 , of 20-40 psi) which is held in a reservoir just behind the nozzle (diameter, $D = 500$ -1,000 μm) of a pulsed solenoid valve. A free jet is created by pulsing a small amount of the gas-mixture through the pinhole nozzle into the vacuum chamber. The expansion is deemed supersonic when the average flow velocity of the gas exceeds the local speed of sound, which occurs when the pressure ratio of the stagnation reservoir and the vacuum chamber exceeds 2.1.⁶

Upon pulsed expansion into the vacuum chamber, the random atomic motion of the high-pressure backing gas is converted into directional flow, resulting in many collisions of the sample molecule with the noble backing gas. The number of two-body and three-body collisions are proportional to p_0D and p_0^2D , respectively.⁶ These collisions result in the transfer of internal energy, stored in vibrationally and rotationally excited quantum states, from the sample molecule into kinetic energy of the backing gas. These collisions fall off nearly quadratically as a function of distance from the expansion source, the finite number of which results in a competition between

kinetic and thermodynamic cooling.⁷ Once cold and isolated, the gas-phase molecules are probed with lasers. In experiments utilizing time-of-flight mass spectrometric measurements, the free jet is passed through a 3 mm skimmer, which samples the coldest part of the expansion, thereby forming a molecular beam. A schematic of the supersonic expansion process is shown in Figure 2.1.

Once in the collision free regime, the molecules have been cooled to translational, rotational, and vibrational temperatures of ~ 1 K, ~ 2 -5 K, and ~ 10 -15 K, respectively.⁷ This is usually sufficient to rattle the molecule down into its zero-point vibrational level (ZPVL), which greatly reduces spectral congestion by eliminating hot and sequence bands. The resulting vibronic spectra contain transitions with full width at half maximum (FWHM) of 1-2 cm^{-1} , an ideal resolution for detailed analysis.

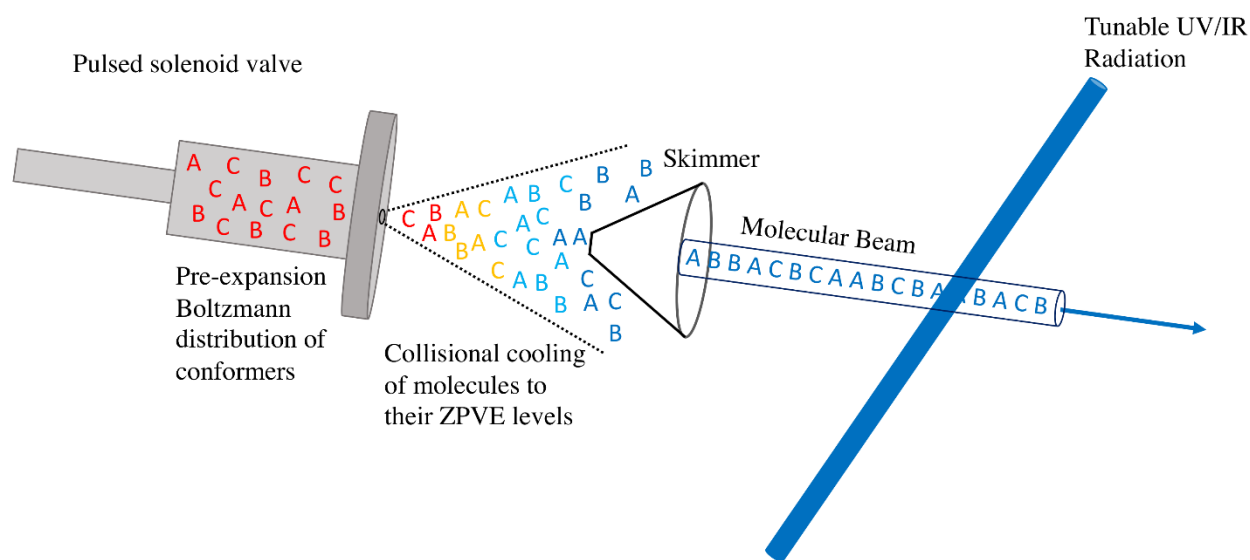


Figure 2.1. Illustration of a skimmed supersonic expansion

2.2 Chamber Design

The data presented herein were collected with one of two experimental chambers. In this section we describe each chamber briefly, along with a description of the experimental procedure. Since the hardware has been described in detail elsewhere, only the most relevant details are discussed.

2.2.1 Time of Flight Mass Spectrometer Chamber

The majority of the data presented herein were collected using a differentially pumped Wiley-McLaren time of flight mass spectrometer (TOFMS)^{8, 9} with a 25 mm chevron-geometry dual microchannel plate (MCP) detector. A schematic of this chamber is shown in Figure 2.2. The mass-selective capability of this chamber makes it ideal for taking data on clusters and complexes.

The source region of this chamber reaches an operating pressure of 10^{-5} mbar (10^{-7} mbar with no gas pulsing) and is pumped by an 880 l/s turbomolecular pump (TMU 1001, Pfeiffer Vacuum). The detector region is maintained at 10^{-9} mbar with a 220 l/s turbomolecular pump (TMU 261, Pfeiffer Vacuum). Each turbo vacuum is backed by a Welch mechanical pump.

In a typical experiment, the sample molecule is co-expanded with an inert noble backing gas (He, Ne, or Ar) into the source region of the chamber. The supersonic expansion collisionally cools the molecule to its zero-point vibrational level, where a 3 mm skimmer then samples the coldest part of the free jet, thereby forming a molecular beam. The molecular beam enters the extraction region of the TOF mass spectrometer, in between a repeller and draw-off-grid that are held at voltages of +4270 and +3950 V, respectively, wherein the lasers interact with the sample. When the molecule is ionized, it is extracted vertically into a 1 m long flight tube, where the ions are directed onto the MCP detector using a pair of steering plates.

The signal from the detector is amplified 25X by a DC-300 MHz pre-amplifier (Stanford Research Systems, SR455) and sent to a 300 MHz digital oscilloscope (Tektronix 3032B) and a gated integrator (Stanford Research Systems, SR250). Conformation-specific IR and UV data are acquired with the gated-integrator in active baseline subtraction mode whose output is sent to a data acquisition card (National Instruments) and read by a computer. Laser timings, scanning, and data acquisition are controlled with in-house LabVIEW code.

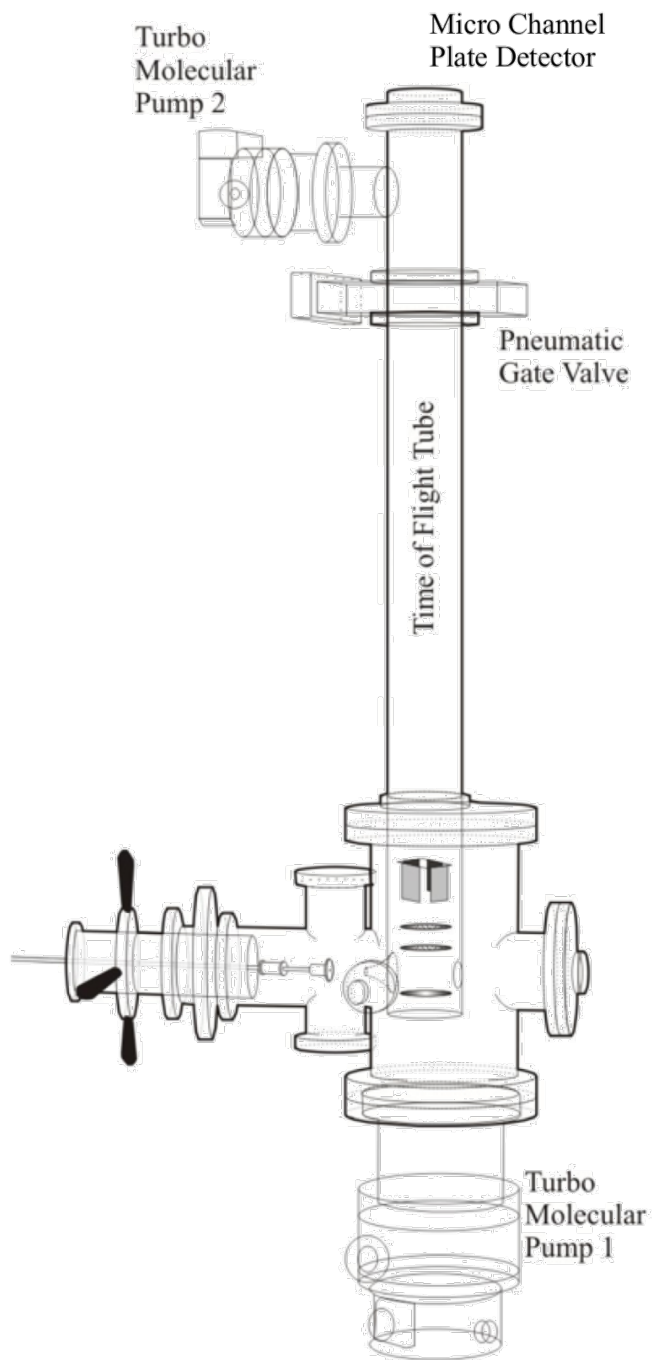


Figure 2.2. Schematic of the time-of-flight mass spectrometer (TOFMS) chamber

2.2.2 Laser-Induced Fluorescence Chamber

A second chamber, capable of detecting resonant fluorescence, was used to record some of the data presented herein.¹ A schematic of this chamber is shown in Figure 2.3. Rather than detecting ions as the action event, this chamber is designed to detect resonant fluorescence of laser-excited molecules. As is the case in the TOFMS instrument, molecules are introduced into the vacuum chamber via a supersonic expansion. This free jet travels, unskimmed, into the focal point of two spherical mirrors where the lasers interact with the cold molecular species.

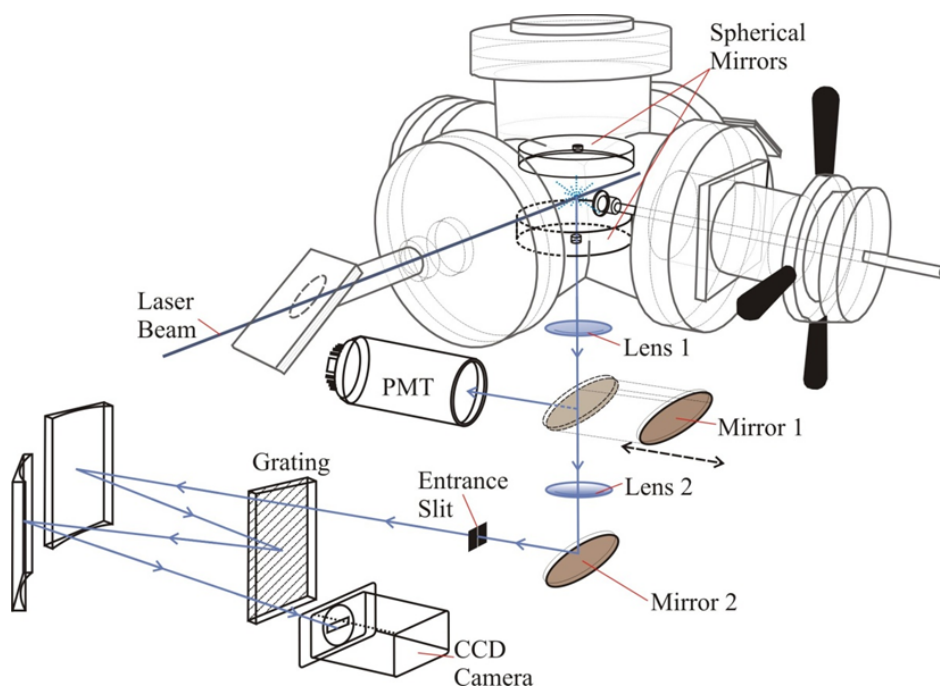


Figure 2.3. Schematic of the laser-induced fluorescence (LIF) chamber

Once electronically excited, the molecules relax back down to their electronic ground state, giving off a fluorescent photon in the process. When collecting conformer-specific IR or UV data these photons are focused by the spherical mirrors onto a UV-sensitive photomultiplier tube. Alternatively, the fluorescence may be dispersed off of a 0.75 m monochromator and a 2400 groove/mm grating (HORIBA Jobin Yvon) and imaged onto an intensified charge-coupled device (iCCD, Andor). Resolving the resonant fluorescence into its component parts yields information regarding the vibrational structure of the ground electronic state.

2.3 Sample Handling

2.3.1 Thermal Heating

The simplest method of introducing the molecule of interest into the gas-phase is by gently heating the sample until sufficient vapor pressure is reached such that it mixes with the noble backing gas and is carried into the supersonic expansion. In this scenario, the sample is wrapped in either glass wool or cotton and placed in a glass holder, which is then placed into a stainless-steel sample cell (Swagelok). The sample cell is situated directly behind the pulsed valve nozzle (Parker Series 9, 500 or 800 μm pinhole), which introduces bursts of gas into the vacuum chamber at 20 Hz. The sample cell, pulsed valve apparatus, and gas-line are wrapped with a resistively heated rope (OMEGALUX), the temperature of which is controlled with a Variac and monitored with a K-type thermocouple.

20° below the experimentally determined melting point is typically where one begins to look for signal, with small increases to temperature as needed. General solenoid valves may be used up to a temperature of about 120° C, while temperatures up to 250° C require the use of “high temp” solenoid valves which have been modified in-house by replacing the solenoid wire with high temperature insulated wiring to withstand hotter conditions. When the molecule is thermally stable, this method is the ideal way of coaxing the sample into the gas.

2.3.2 Nonresonant Laser Desorption

Most peptide samples decompose at high temperatures before sufficient vapor pressure is reached. In this case, the molecules are introduced into the gas via laser desorption, a schematic of which is shown in Figure 2.4. This procedure has been described in detail elsewhere.^{2, 10, 11} Briefly, the solid sample is first crushed into a fine powder with a razor blade. The powdered sample is then rubbed onto the surface of a small, sanded smooth, fine extruded graphite rod (purchased from graphitestore.com), measuring approximately 5 mm wide, 2 mm thick, 50 mm long. The rod is placed onto a flat aluminum boat which is then attached to the end of a stainless-steel rod. The sample tip of the rod is pushed into a load-lock port situated perpendicular to the pulsed valve expansion axis. The load-lock assembly is mounted on a translation stage which allows for precise positioning of the graphite rod with respect to the pulsed valve.

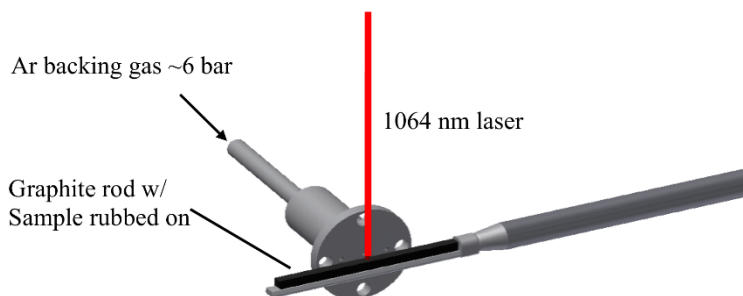


Figure 2.4. Laser desorption scheme used to introduce non-volatile samples into the gas phase.

The unfocused output of a 1064 nm laser (20 Hz, Continuum MiniLight, 6 ns, ~ 5 mJ/pulse) is directed through a CaF_2 window to strike the rod in a normal orientation. The interaction of the laser with the graphite rod results in a plume of gaseous sample in front of the pulsed valve, which the supersonically expanding backing gas captures and collisionally cools. A linear actuator is used to push the rod into the chamber at a controllable velocity (generally ~ 1 mm/min), ensuring steady-state sampling of the graphite surface.

Argon is used as the backing gas when performing laser desorption experiments. Its large mass relative to He and Ne means that it may extract more internal energy from a hot molecule per collision. This is ideal in laser desorption for a couple of reasons. First, the molecules studied are relatively large and capable of storing more internal energy than smaller molecules. The amount of energy imparted into a molecule undergoing laser desorption is not well understood, with some studies suggesting that temperatures may reach as high as 700 K.^{12, 13} This non-negligible thermal contribution to the internal energy of the laser-desorbed molecules has the potential to modify the conformer population distribution early in the expansion, since at temperatures in the hundreds of Kelvin it is free energy rather than potential energy that drives the conformational population distribution.

In addition, since laser desorption puts the sample into the gas phase after the supersonic expansion has already begun, it misses out on the highest density of two-body cooling collisions. Ideally, the number of collisions in the supersonic expansion is sufficient to thermodynamically cool the molecules to the vibrational zero-point levels of the most stable conformations with respect to potential energy. Under conditions of kinetic cooling of a free energy distribution, however, it is possible to experimentally observe conformers with unusually high potential

energy.^{10, 14} These considerations make Argon the ideal backing gas for laser desorption experiments.

Larger pulsed valve nozzles (800 or 1,000 μm) have the effect of extending the length from the expansion source during which cooling collisions take place, at a cost of slightly decreasing the net number of collisions. As such, either 800 or 1,000 μm nozzles are used in conjunction with laser desorption. Additionally, higher backing gas pressures are used to increase the number of two-body collisions, as per their scaling with p_0D .

2.3.3 Water Cluster Formation

The influence of water molecules on molecular properties such as geometry and vibrational structure is spectroscopically measurable. In order to make such measurements it is necessary to add a well-defined number of water molecules onto the solute molecule, forming solute-(H_2O)_n molecular clusters. To accomplish this, the TOFMS instrument is equipped at the front end with a gas manifold which allows a partial pressure of water (or some other liquid sample) to be seeded into the carrier gas *en route* to the sample cell. The manifold splits the main gas line into three lines running in parallel. The central line provides direct access to the sample cell while the two additional lines provide access to chambers containing cotton soaked with the species of interest. Each line is equipped with its own flow meter as well as an inlet needle valve to precisely control the flow over the solvent. Monitoring the magnitude of mass-resolved signal as a function of flow allows one to dial in the proper conditions for the experiment.

2.4 Radiation Sources

High power, tunable ultraviolet (UV) radiation is produced by pumping a dye laser (Radiant Dyes Narrowscan or Lambda Physik Scanmate) with either the second (532 nm, ~ 120 mJ/pulse) or third (355 nm, ~ 80 mJ/pulse) harmonic of a pulsed nanosecond Q-switched Nd:YAG laser (20 Hz, Continuum Surelite II). The oscillator stage of each dye laser is equipped with a motor-driven grating, which serves to select the wavelength of spontaneously emitted light from the oscillator stage, which in turn stimulates emission from the pumped pre-amplifier and amplifier cells. The radiation output is frequency doubled in an angle-tuned BBO-I, BBO-III, or KDP crystal and the residual fundamental light is separated from the frequency doubled light with a Pellin

Broca prism. The UV output has a resolution of $\sim 0.15 \text{ cm}^{-1}$ and powers ranging from 0.1 - 1.0 mJ/pulse. Neutral density filters are routinely placed before the frequency-doubling crystal to keep absorption spectra in the linear regime.

High power, tunable infrared (IR) radiation is produced by pumping an optical parametric converter (OPC, LaserVision) with the fundamental (1064 nm, 9397 cm^{-1}) of an injection seeded Nd:YAG laser (Continuum Surelite EX, 10 Hz, $\sim 640 \text{ mJ/pulse}$). The OPC consists of two stages: an optical parametric oscillator (OPO) and an optical parametric amplifier (OPA), both of which utilize nonlinear mixing to generate the desired IR photon frequency.

The incoming 9397 cm^{-1} light passes through a beam splitter which directs 33% into the OPO stage and 67% into the OPA stage. The light directed to the OPO is frequency doubled in a KTP crystal to 532 nm ($18,794 \text{ cm}^{-1}$). This green light enters the OPO cavity which contains a pair of phase matched KTP crystals in the center with a grating/tuning mirror arrangement on the back end. The KTP crystals are angle tuned such that the $18,794 \text{ cm}^{-1}$ photon is split into two photons by a process called optical parametric generation.¹⁵ Conservation of energy dictates that the sum of the two photon's energies are equal to $18,794 \text{ cm}^{-1}$.

Traditionally, the higher frequency photon is called the signal while the lower frequency photon is called the idler. The grating/tuning mirror arrangement serves to increase spectral resolution as well as to close the back end of the cavity. The frequencies of the signal and idler photons are a function of the KTP crystal angles, which in conjunction with the grating position, are calibrated to allow a broad region of the IR spectrum to be scanned. The signal and idler beams possess opposite polarization which allows for the signal photon to be filtered by a "stack-of-plates" silicon polarizer.

The idler photon from the OPO is injected into the OPA stage, where it is difference frequency mixed in a series of four KTA crystals with the remaining 67% of the $18,794 \text{ cm}^{-1}$ pump beam. This mixing results in new signal and idler photon frequencies. At the OPC output, the signal from the OPA stage is removed by a "stack-of-plates" silicon polarizer and the idler is used for spectroscopy measurements in the hydride stretch region ($2800 - 3700 \text{ cm}^{-1}$). Typical energies for the idler output are 12 - 15 mJ/pulse.

The idler output from the OPC can reach as low in frequency as $2,000 \text{ cm}^{-1}$. There are circumstances, however, where spectroscopic measurements using lower frequency IR radiation is desirable, for example in the carbonyl stretch (amide I) and NH bend (amide II) regions.

Radiation from $\sim 1,000 - 1,800 \text{ cm}^{-1}$ is generated by difference frequency mixing the OPA idler and signal photons in a AgGaSe₂ crystal. To do this, the OPC output light is propagated ~ 6 feet before entering the angle tuned crystal. This is done to generate a more uniform beam intensity profile, since the crystal is quite sensitive to high power “hot spots”. One generally images the light at the input and output the AgGaSe₂ crystal with highly developed Kodak Linograph paper to both steer the radiation fully through the crystal and judge whether the power is acceptable. In the proper pump power regime ($\leq 70 \text{ mJ}$) the beam will create a faint burn on the paper. Once light is aligned through the crystal, output power is measured, while angle-tuning the crystal, with a sensitive IR power meter. Powers in this frequency range measure from 400 - 1,000 $\mu\text{J}/\text{pulse}$.

2.5 Spectroscopic Methods

A variety of laser-based methods are used in this work to record spectroscopic measurements on target molecules. These methods can be broken down into two general categories; single- and double-resonance methods. Techniques belonging to each group are presented in the following two sections.

2.5.1 Single-Resonance Methods

The first step in any experiment reported herein is to record the total electronic absorption spectrum of the collisionally cooled molecules. Two complementary techniques may be used to record this data: resonant two-photon ionization (R2PI)¹⁶ or laser-induced fluorescence (LIF). In LIF, the output of a dye laser is frequency scanned across the absorption region of interest. When the laser frequency is resonant with a vibronic transition of a populated conformer a single photon is absorbed, promoting the molecule from the S₀ electronic state to the absorbing S_n electronic state. The excited molecule relaxes back down to the vibrational manifold of the S₀ state by emitting a photon (fluorescence) whose frequency is determined by the energy difference of the two states. The time-profile of the fluorescence is monitored from the output of the PMT detector as a function of laser frequency. This results in a non-conformer-specific vibronic spectrum with contributions from all isomers present in the expansion. It is important to note that for LIF measurements to be taken on a molecule, that molecule must have a non-zero fluorescence quantum yield. When wavelength-dependent non-radiative processes occur in the excited

electronic state, the LIF absorption spectrum does not represent the true absorption properties of the molecule, but rather the product of the absorption cross section times the fluorescence quantum yield. The shortcoming of this technique can be overcome and is discussed in section 2.6.1.

The intensities of the vibronic transitions in the LIF excitation spectrum are largely determined by Franck-Condon factors between the electronic ground ($v=0$) and excited state vibrational levels. These relative intensities and frequency differences yield valuable information regarding the change in molecular geometry between the ground and excited electronic states. Complementary vibronic data originating from the excited electronic state can be recorded with dispersed fluorescence (DFL) spectroscopy (Figure 2.5). In this scheme, a single vibronic transition is pumped while the emitted fluorescence is dispersed by a grating and imaged onto a gated, intensified charge-coupled device (iCCD) detector. DFL reveals the projection of the pumped vibronic state onto the vibrational levels in the ground electronic state. In the simplest case, the geometry change indicated by the relative intensities in the LIF and DFL spectra can be modelled by simple one-dimensional normal mode displacements. Most molecules, however, undergo Duschinsky mode mixing in addition to displacement, making the multidimensional vibronic analysis less intuitive and more complex.¹⁷

Most of the work in this thesis uses R2PI spectroscopy within the TOFMS instrument described in section 2.2.1 to record electronic spectra. R2PI comes in two variants: one-color R2PI (1C-R2PI) and two-color R2PI (2C-R2PI), shown schematically in Figure 2.5. As its name implies, R2PI requires two single-photon-absorbing events; one photon to electronically excite and a second photon to promote to the ionization continuum. In 1C-R2PI, both photons come from the same laser pulse, where the ionization potential (IP) of the molecule is such that two times the absorption frequency is sufficient for ionization. The scanning laser orthogonally overlaps the molecular beam in the extraction region of the TOFMS. When the laser is resonant with a vibronic transition of a populated conformer in the molecular beam, a photon is absorbed, immediately after which a second ionizing photon in the same ns light pulse is absorbed. This ion is accelerated up the flight tube and strikes the MCP detector. An absorption spectrum is generated by plotting the ion signal as a function of laser excitation wavelength.

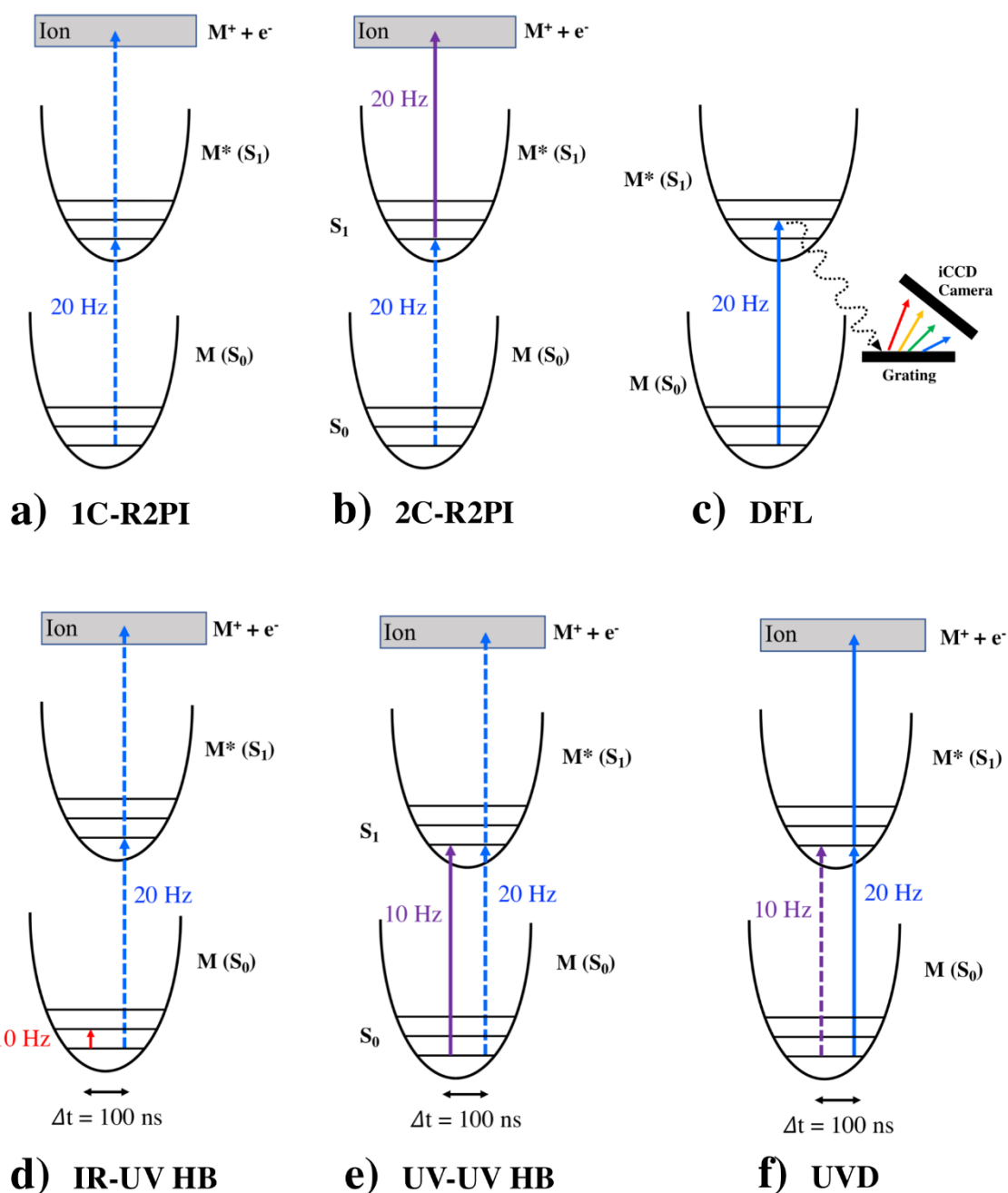


Figure 2.5. Spectroscopic schemes used in this work for recording (a) one-color and (b) two-color resonant two-photon ionization spectroscopy, (c) dispersed fluorescence spectroscopy, (d) IR-UV holeburning spectroscopy, (e) UV-UV holeburning spectroscopy, and (f) UV-depletion spectroscopy. Solid lines indicate a fixed frequency laser and dashed lines indicate a scanning laser.

2C-R2PI is necessary when the IP of a molecule exceeds twice the excitation frequency of the scanning laser. In this scheme, a second higher energy, fixed frequency, ionizing laser is spatially and temporally overlapped and counter-propagated with the excitation laser. The ionizing laser photon energies are kept high ($\sim 0.3 - 1.0$ mJ/pulse), while the absorbing laser energies are decreased ($< \sim 0.2$ mJ/pulse), resulting, ideally, in a background free, unsaturated absorption spectrum. As in 1C-R2PI, the excitation laser is scanned over the region of interest. When resonant with some vibronic transition, a photon is absorbed. The second, ionizing laser, then promotes the electronically excited molecule to the ionization continuum. This method may be useful when recording the UV spectra of molecular clusters, which have a tendency to fragment into each other's mass channel upon photoionization. Tuning near-threshold with the ionizing photon energies can reduce such fragmentation. 2C-R2PI is used when recording infrared spectra of electronically excited molecules. This is discussed in detail in section 2.6.2.

2.6 Double-Resonance Methods

Two groups of double-resonance methods are used in this work: those that record conformer-specific UV spectra, and those that record conformer-specific IR spectra. The following sections will describe these techniques in turn.

2.6.1 Single-Conformation UV Spectroscopy

Double-resonance laser techniques are used to decompose the non-conformer-specific LIF and R2PI UV spectra into their component parts. The result is a set of conformer-specific UV spectra, which when coadded together duplicate the total R2PI of LIF vibronic spectrum. These techniques serve to reveal the number of conformers in the cold expansion and to identify clean vibronic transitions with which to record conformer-specific IR spectra (section 2.6.2). Three methods are used towards this end: IR-UV holeburning, UV-UV holeburning, and UV-depletion spectroscopy (Figure 2.5). All of these techniques use two lasers: a 10 Hz holeburn laser and a 20 Hz probe laser. In IR-UV holeburning, a 10 Hz IR holeburn laser has its frequency fixed on some vibrational transition belonging to one of the conformers in the expansion. Counter propagating, spatially overlapping, and firing ~ 100 ns after the IR laser, a 20 Hz probe UV laser scans over the absorption region of interest. When the UV laser is resonant with a vibronic transition of the same

conformer that the IR laser is resonant with, there is a depletion of ion signal resulting from the reduction of zero-point populated conformers. The 20 Hz signal is sent through a gated integrator in active baseline subtraction (ABS) mode, which outputs the difference in signal with and without the holeburn laser firing. The resulting data trace is a conformer-specific UV spectrum of the conformer that the IR laser is exciting.

UV-UV holeburning is similar to IR-UV holeburning, the difference being that both the probe and holeburn lasers are in the UV. In this scheme, a 10 Hz UV holeburn laser has its wavelength fixed on some vibronic transition of one of the conformers in the molecular beam. Approximately 100 ns later, a 20 Hz UV probe laser scans the absorption region. The 20 Hz signal is sent to a gated integrator in ABS mode, where the output is a conformer-specific UV spectrum. A twist on the UV-UV double resonance technique is to scan the 10 Hz holeburn laser and fix the 20 Hz probe laser. This UV-depletion (UVD) technique is so named because what is being measured is the shot to shot depletion of constant signal generated by pumping a single vibronic transition, which is being modulated by the 10 Hz scanning holeburn laser. UVD consequently suffers from poorer signal to noise due to the constant subtraction of large signals. The great advantage to this technique is that it allows for a true absorption spectrum to be measured since the signal is simply a function of ground state depletion and not excited state ionization or fluorescence. This is important for molecules that access some non-radiative process in excited electronic states.

2.6.2 Single-Conformation IR Spectroscopy

Conformer-specific infrared spectra are at the heart of most experiments in this thesis. Ground state IR spectra are recorded using resonant ion-dip infrared spectroscopy^{18, 19} (RIDIRS, Figure 2.6). This technique is nearly identical to IR-UV holeburning, except that in this case the 10 Hz IR holeburn laser is scanned while the 20 Hz UV probe laser is fixed on some conformer-specific vibronic transition. The timing between the laser pulses is such that the IR laser interacts with the gaseous sample ~ 100 ns before the UV laser. When the IR laser scans across an electronic ground state vibrational transition of the same conformer that the UV laser is exciting, a decrease in zero-point populated conformers results in a subsequent dip in ion (or fluorescence) signal. The dip in ion (fluorescence) signal is processed by a gated integrator in ABS mode and plotted as a function of IR frequency, resulting in a conformer-specific IR spectrum.

Single-conformer IR spectra of electronically excited molecules may also be recorded using excited state RIDIRS (S_1 RIDIRS). For a molecule to have its excited state IR spectrum recorded, it must first produce clean 2C-R2PI signal, where electronic excitation is caused by λ_1 and excited state ionization is achieved by a second laser pulse, λ_2 . Maximum 2C-R2PI signal generally occurs with temporally coincidental laser pulses. Recording of excited state infrared spectra, however, requires that the scanning IR laser pulse, λ_{IR} , interacts with the gaseous sample in between the two UV lasers (Figure 2.6c). In this scheme, λ_1 electronically excites the conformer of interest (generally to the zero-point level of the excited S_1 electronic state), λ_{IR} vibrationally excites out of this prepared state, and λ_2 ionizes out of the electronically excited state. Similar to ground state RIDIRS, the signal from the ion packet produced by λ_2 is processed through a gated integrator in ABS mode. Modulation of this signal only occurs when λ_{IR} has moved some population out of the electronically excited zero-point level ($v=0$), which redistributes into a manifold of states that are less likely to be ionized by λ_2 . Plotting the signal depletion as a function of λ_{IR} generates an excited state infrared spectrum.

Ideally, all three laser pulses used in this experiment are temporally isolated from one another. This ensures that modulation of the ion signal is not caused by ground state IR absorption. Since the temporal profiles of the lasers used in this work are ~ 6 ns wide, all molecules studied using this technique must have excited state lifetimes of at least 16 ns. Additionally, excited state IR data may be recorded using fluorescence detection. In this case, only two laser pulses are required, λ_1 and λ_{IR} . λ_{IR} is timed such that its pulse width is immediately after and isolated from λ_1 . Fluorescence from the excited state is modulated by the same phenomenon that reduces excited state ionization. For this experiment to work, the fluorescence lifetime of the molecule must be at least ~ 12 ns.

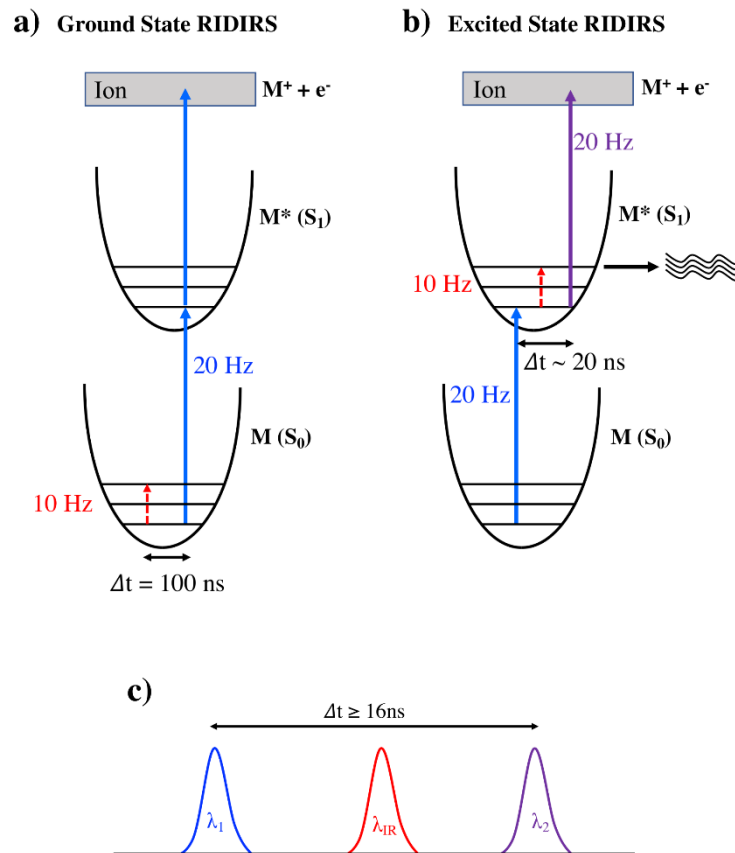


Figure 2.6. Experimental schematic of (a) ground-state and (b) excited-state RIDIRS. (c) Pulse timings of lasers used in excited state RIDIRS.

2.7 Computational Methods

The computational results from density functional theory (DFT) and force field methods are used in this work to aid in and enrich the understanding of experimental data. Disconnectivity graphs are employed in chapter 3 to better understanding the complex potential energy surface of a mixed α/β diastereomer tripeptide pair. In the following two sections we outline the general procedure for both of these methods.

2.7.1 Conformational Sampling

Many experiments in this work depend on vibrational frequency calculations to make conformational assignments of experimentally observed structures. The large size of the molecules studied herein results in each molecule possessing a large number of internal degrees of freedom.

This conformational flexibility leads to complex multi-dimensional potential energy surfaces. The results of DFT calculations are ultimately compared with experimental data, but there are simply not enough computational resources or time to sample the entire potential energy surface with high level quantum chemical calculations. To address this problem, force field searches are employed as screening tools for low energy candidate conformers.

The candidate structures for DFT optimization and frequency calculations are calculated within the MacroModel²⁰ program. Generally, a hand-built structure is used as input for conformational searching using a torsional-sampling Monte Carlo Multiple Minima search algorithm in conjunction with both the OPLS3²¹ and Amber*²² force fields. Exhaustive searches are performed with both force fields until further iterations yield no new structures within 50 kJ/mol of the global energy minima. This is accomplished by applying a redundant conformer elimination filter on the existing and newly generated pools of calculated minima after each successive force field search. The pool of structures from each successful force-field search are then filtered in a similar manner to remove redundant structures. All unique structures among both force field searches are used as starting structures for DFT geometry optimization and harmonic frequency calculation.

Both the Gaussian09²³ and Gaussian16²⁴ computational packages are used in this work. The Becke 3LYP and M052x²⁵ hybrid functionals in conjunction with the 6-31+G(d) Pople basis set are used for DFT calculations. Project-specific computational details are given at the beginning of each chapter, along with scale factors for the calculated harmonic normal mode frequencies.

2.7.2 Disconnectivity Graphs

The advantage of disconnectivity graphs over the classical force field sampling method described above is the ability to project and visualize the complex 3N-6 dimensional potential energy surface along a reduced isomerization coordinate.²⁶ The resulting surface is a two-dimensional interconnected “tree” structure, where each conformational minimum is represented by a vertical minimum and the transition state structure between any two minima is represented as a nodal point. These surfaces are useful for understanding how isomerization barriers drive the conformational landscape and can help with understanding the presence, or lack thereof, of experimentally observed conformers. The rate-limiting energy barrier between any two minima may be used as a first approximation when calculating isomerization rates with Rice-Ramsperger-

Kassel-Marcus calculations. Additionally, the minima and transition state structures may be optimized and verified using the Synchronous Transition-Guided Quasi-Newton method (QST3) in conjunction with DFT in order to obtain higher level energetics.

A theoretical description of constructing disconnectivity graphs have been given in detail elsewhere.²⁷ Briefly, local minima were calculated using a basin-hopping algorithm within a Monte Carlo simulation.²⁸ This process was carried out using the GMIN 2.0 program of Wales et al.²⁹ Transition states are calculated by calculating the Hessian of each individual minima and walking uphill in both directions along the smallest eigenvalues using a hybrid BFGS/eigenvector-following transition-state search. These stationary points were converged to a root-mean-squared gradient of $< 10^{-6}$ kcal mol⁻¹ Å⁻¹. Then, a DNEB/L-BFGS method, also developed by Wales et al., was used to determine which minima are connected to the calculated transition state.^{30, 31} Newly generated minima were added to the database of minima, and the process was iterated several times to generate a fleshed out potential energy surface.

Both the CHARM22 and AMBER force fields may be used to generate disconnectivity graphs. This author recommends the thesis of Zachary Davis as well as the WalesWiki webpage for detailed instructions on carrying out this procedure.

2.8 References

1. E. G. Buchanan, Purdue University, 2014.
2. J. C. Dean, Purdue University, 2014.
3. J. R. Gord, Purdue University, 2016.
4. P. S. Walsh, Purdue University, 2016.
5. D. H. Levy, *Annu. Rev. Phys. Chem.*, 1980, **31**, 197-225.
6. M. D. Morse, *Experimental methods in the physical sciences*, 1996, **29**, 21-47.
7. D. M. Lubman, C. T. Rettner and R. N. Zare, *The Journal of Physical Chemistry*, 1982, **86**, 1129-1135.
8. W. Wiley and I. H. McLaren, *Rev. Sci. Instrum.*, 1955, **26**, 1150-1157.
9. D. M. Lubman and R. M. Jordan, *Rev. Sci. Instrum.*, 1985, **56**, 373-376.
10. J. C. Dean, E. G. Buchanan and T. S. Zwier, *J. Am. Chem. Soc.*, 2012, **134**, 17186-17201.

11. G. Meijer, M. De Vries, H. Hunziker and H. Wendt, *Appl. Phys. B*, 1990, **51**, 395-403.
12. C. R. Maechling, S. J. Clemett, F. Engelke and R. N. Zare, *J. Chem. Phys.*, 1996, **104**, 8768-8776.
13. M. Handschuh, S. Nettesheim and R. Zenobi, *J. Chem. Phys.*, 1997, **107**, 2603-2610.
14. K. N. Blodgett, X. Zhu, P. S. Walsh, D. Sun, J. Lee, S. H. Choi and T. S. Zwier, *J. Phys. Chem. A*, 2018, DOI: 10.1021/acs.jpca.8b01273.
15. W. Bosenberg and D. R. Guyer, *JOSA B*, 1993, **10**, 1716-1722.
16. D. M. Lubman, *Mass Spectrom. Rev.*, 1988, **7**, 559-592.
17. F. Duschinsky, *Acta Physicochim. URSS*, 1937, **7**, 551-566.
18. R. H. Page, Y. Shen and Y.-T. Lee, *J. Chem. Phys.*, 1988, **88**, 4621-4636.
19. T. S. Zwier, *Annu. Rev. Phys. Chem.*, 1996, **47**, 205-241.
20. F. Mohamadi, N. G. Richards, W. C. Guida, R. Liskamp, M. Lipton, C. Caufield, G. Chang, T. Hendrickson and W. C. Still, *J. Comput. Chem.*, 1990, **11**, 440-467.
21. E. Harder, W. Damm, J. Maple, C. Wu, M. Reboul, J. Y. Xiang, L. Wang, D. Lupyan, M. K. Dahlgren and J. L. Knight, *J. Chem. Theor. Comp.*, 2015, **12**, 281-296.
22. P. K. Weiner and P. A. Kollman, *J. Comput. Chem.*, 1981, **2**, 287-303.
23. M. J. Frisch, G. W. Trucks, H. B. Schlegel, G. E. Scuseria, M. A. Robb, J. R. Cheeseman, G. Scalmani, V. Barone, B. Mennucci and G. e. Petersson, 2014.
24. M. Frisch, G. Trucks, H. Schlegel, G. Scuseria, M. Robb, J. Cheeseman, G. Scalmani, V. Barone, G. Petersson and H. Nakatsuji, *Revision A*, 2016, **3**.
25. Y. Zhao and D. G. Truhlar, *J. Chem. Theor. Comp.*, 2007, **3**, 289-300.
26. D. Wales, *Energy landscapes: Applications to clusters, biomolecules and glasses*, Cambridge University Press, 2003.
27. V. A. Shubert, E. E. Baquero, J. R. Clarkson, W. H. James III, J. A. Turk, A. A. Hare, K. Worrel, M. A. Lipton, D. P. Schofield and K. D. Jordan, *J. Chem. Phys.*, 2007, **127**, 234315.
28. D. J. Wales and J. P. Doye, *J. Phys. Chem. A*, 1997, **101**, 5111-5116.
29. D. J. Wales, *University of Cambridge*.
30. S. A. Trygubenko and D. J. Wales, *J. Chem. Phys.*, 2004, **120**, 2082-2094.
31. D. C. Liu and J. Nocedal, *Mathematical Programming*, 1989, **45**, 503-528.

CHAPTER 3. CONFORMER- AND DIASTEREOMER-SPECIFIC SPECTROSCOPY OF A MIXED α/β FOLDAMER PAIR

Adapted with permission from *J. Phys. Chem. A*, 2018, 122, 14, 3697-3710. Copyright 2018 American Chemical Society.

3.1 Introduction

Synthetic foldamers are oligomers that are composed of any mixture of natural and/or non-natural monomeric building blocks, usually designed to mimic the natural machinery of nature, or expand upon it.¹⁻³ These compounds have been designed to have applications as potent antimicrobial agents, cholesteryl ester uptake inhibitors, and possess resistance to natural protein degradation mechanisms.⁴⁻⁷ Among α -peptides, helices are the most common secondary structure, and among helices the α -helix (3.6₁₃-helix) and the 3₁₀-helix are the most prominent.⁸⁻¹⁰ Studies on homogeneous backbone peptides using purely β -amino acid building blocks, which extend the backbone chain length by one carbon, revealed new helical structures not available to α -peptides, including the 12/10-, 14-, 8-, and 10-helices, where the numbers indicate the number of atoms in each hydrogen bonded cycle that comprises the helix.¹¹⁻¹⁴

Building off of the Zwieter group's longstanding interest in the study of the inherent conformational preferences of synthetic foldamers^{8, 14-22}, we consider here a diastereomeric mixed α/β pair, (*SRSS*) Ac-Ala- β _{ACHC}-Ala-NHBn (referred to as *RS*) and (*SSRS*) Ac-Ala- β _{ACHC}-Ala-NHBn (*SR*), molecules which differ from one another by their exchange of chirality along the ACHC (*cis*-2-aminocyclo-hexanecarboxylic acid) residue. These structures are presented in Figures 3a) and 3b), respectively. The ACHC residue has two stable minimum structures, a chair conformation in which the NH is in the equatorial (eq.) position and the C=O is in the axial position, and vice versa (Figure 3e).

Lee *et al.* showed that a structure analogous to the *RS* diastereomer, differing only in the capping units (N-terminal *tert*-butyloxycarbonyl and C-terminal methyl ester caps) is known in crystalline form to prefer 11/9 mixed helical folding, which arises from (*i, i+3*) and (*i, i-1*) C=O \cdots H-N hydrogen bonding.²³ A similarly analogous structure to the *SR* diastereomer crystallizes with no intramolecular hydrogen bonding while room temperature IR data reveal complementary hydrogen bonding propensities for each diastereomer in solution.²⁴

In contrast to naturally formed helices, such as the α - and 3_{10} -helix, mixed helices are stabilized by a hydrogen bonded architecture which alternates hydrogen bond direction along the helical axis, thus mitigating the macro-dipole moment inherent to the above-mentioned helices.²⁵ The spectroscopic investigation of these diastereomers in the gas phase, free from perturbative solvent or nearest neighbor intermolecular interactions, provides fundamental insight to the folding propensities and conformational preferences of these isolated, non-natural oligomers.

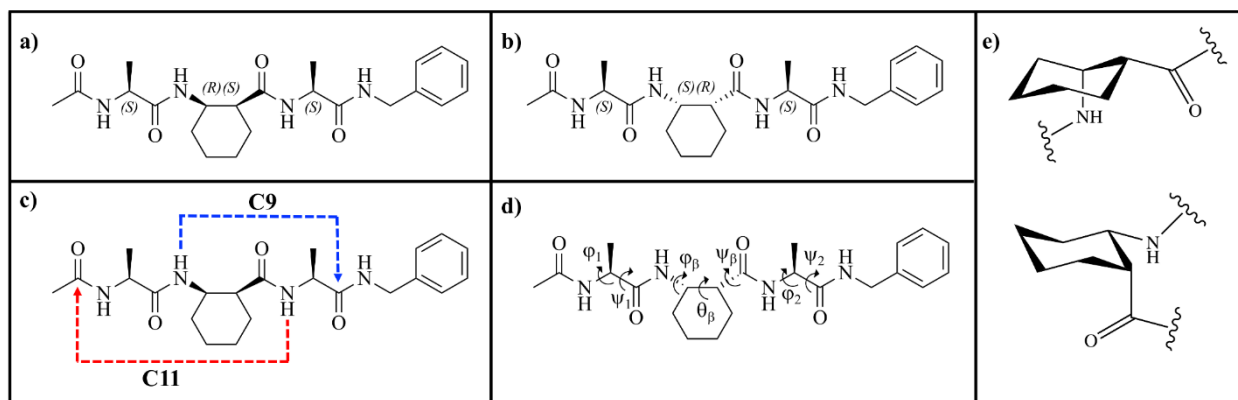


Figure 3.1. The (a) *RS* and (b) *SR* diastereomers studied in this work. Examples (c) of C_n hydrogen bond designations as well as the color scheme used to designate hydrogen bond direction. Hydrogen bonds shown in blue go from the N- to the C-terminus whereas those in red are formed from the C- to the N-terminus. Definition of key dihedral angles (d) of relevance to the conformations observed. The two possible ACHC ring configurations (e); equatorial C=O/axial NH (top) or equatorial NH/axial C=O (bottom).

The local chair conformation of ACHC in which the NH assumes the equatorial position is an essential component of 11/9 helical formation. While this helix has been observed in both solution and in crystalline form, it has yet to be identified as a stable, low-energy minimum in the gas phase. The existence of this helix in the gas phase would provide further evidence that the 11/9 helical motif is a particularly stable secondary structure accessible to mixed α/β synthetic foldamers. A second, related goal is to compare and contrast the preferred structures of the *RS* and *SR* diastereomers to gain further insight to the differences observed in non-polar solvent.

The cooling and isolation afforded by the supersonic expansion provides an environment in which high-resolution single conformer UV and IR spectra can be obtained. DFT calculations will be used to compare with the recorded IR spectra, leading to the assignment of five unique structures across the diastereomeric pair. As we shall see, structures due to several conformational

families are observed, including incipient mixed helices, bifurcated (bif) hydrogen bonded cycles and β -turn analogues. Our work provides a first spectroscopic characterization of these hydrogen-bonded structures. Finally, disconnectivity graphs are calculated for the two diastereomers as an aid to explain why the observed conformational isomers are present, and to help in understanding in a more comprehensive way the complex potential energy surface of these capped tripeptides.

3.2 Methods

3.2.1 Experimental Methods

Samples were synthesized by the Choi research group at Yonsei University. Vaporization of the sample was achieved by laser desorption.^{15, 26-28} The solid-state sample was crushed into a fine powder and rubbed onto the surface of a graphite rod which was coupled into a vacuum chamber via a load lock assembly. The sample was desorbed from the surface of the graphite rod by the fundamental of a Nd:YAG laser operating at 20 Hz (Continuum Minilite II, 5mJ/pulse, 2mm beam diameter). A linear actuator (NSC 200, Newport) pushed the rod forward to ensure uniform sampling. The graphite rod was kept just under the nozzle of a pulsed valve (Parker, Series 9) operating at 20 Hz and measuring 500 μm in diameter. Laser desorbed molecules were subsequently entrained in the supersonic expansion of Argon gas at approximately 5.5 bar backing pressure and collisionally cooled to the zero-point vibrational energies of the most stable conformers.^{29, 30} A molecular beam was formed by passing the free expansion through a 3 mm conical skimmer approximately 2 cm downstream from the pulse valve, which then entered the extraction region of a Wiley McLaren time-of-flight (TOF) mass spectrometer, where we cross the molecular beam with lasers to perform various single- and double-resonance based spectroscopic techniques.

The UV spectrum in the $S_0 - S_1$ origin region was recorded using one color resonant two-photon ionization (R2PI) in which the frequency doubled output of a tunable dye laser, (Radiant Dyes NarrowScan, Coumarin 540A) pumped by the third harmonic of a Nd:YAG laser (Continuum, SureLite II), overlapped the molecular beam in the TOF extraction region. The UV spectrum was generated by monitoring the parent mass channel as a function of UV frequency. By scanning the UV frequency over a wavelength range (37400-37750 cm^{-1}) in which the NHBn cap

absorbs, vibronic spectra can be recorded that contain contributions from all conformers present in the expansion.

Conformation specific IR spectra were recorded using resonant ion-dip infrared spectroscopy (RIDIRS). In RIDIRS, the UV laser is fixed on a conformer-specific vibronic transition, thereby providing constant signal in the parent channel of the TOF mass spectrum. A Nd:YAG pumped KTP/KTA based infrared optical parametric converter (LaserVision) was used to generate light in the NH stretch region from 3200 – 3500 cm^{-1} . A AgGaSe₂ crystal was used as an additional difference frequency mixing stage to generate light in the Amide I (C=O stretch) region, from 1600 – 1800 cm^{-1} . Typical IR output energies were 12-15 mJ/pulse and 500 – 1000 μJ /pulse in the NH and amide I regions, respectively. The IR laser (10 Hz) spatially overlaps, but temporally precedes, the UV laser (20 Hz) and is scanned across the region of interest. When the IR laser is resonant with a vibrational transition belonging to the same conformer on which the UV laser is fixed, ground state population of that conformer is removed, resulting in a dip in ion signal. Active baseline subtraction is performed with a Stanford Research Systems gated integrator (SR 250) on each pair of IR-on and IR-off shots as the IR laser is scanned. The fractional depletion of ion signal is plotted as a function of IR frequency, thus generating conformer-specific IR spectra. IR-UV hole-burning (IR-UV HB) can then be used to obtain conformer-specific UV spectra. This technique uses the same ion depletion scheme as RIDIRS to collect data, but in this case the IR laser is fixed on a conformer-specific vibrational transition while the UV laser is scanned across the $S_0 - S_1$ origin region. Fractional ion depletion is plotted as a function of UV frequency, resulting in conformer-specific electronic spectra.

3.2.2 Computational Methods

To properly describe the conformational potential energy surface of this diastereomeric pair, we employed the CHARMM22 all-atom force field for α -amino acids³¹ and augmented it with a force field parameterized specifically for cyclic β -amino acids³², which was developed in the framework of the CHARMM22 force field and is therefore compatible with those used for natural amino acids. The parameters for β -amino acids have been optimized to reproduce relative energetics and location of minima as well as the curvatures of the potential energy surface, using a multi-objective evolutionary algorithm.³³

We followed an approach used in our previous work³⁴ in generating a disconnectivity graph to display the energies of local minima on the PES and the transition states connecting them. The disconnectivity graph is a powerful tool for visualizing the entire potential energy landscape, the way in which it divides into basins, and the rate-limiting barrier height separating them. The theoretical background for generating disconnectivity graphs has been described in detail elsewhere.³⁵ In brief, local minima on the PES were located using a basin-hopping algorithm³⁶ within a canonical Monte Carlo simulation carried out by the GMIN 2.0 program of Wales and co-workers.³⁷ We carried out up to 100 basin-hopping steps until the global minimum was found and the step size was adjusted in each Monte Carlo step for an acceptance ratio of 0.5. For each minimum determined by the basin-hopping algorithm, the transition states were located by calculating the Hessian from the force field and walking uphill in both directions along the smallest eigenvalues using a hybrid BFGS/eigenvector-following transition state search. All stationary points were converged to a root-mean-squared gradient of less than 10^{-6} kcal mol⁻¹ Å⁻¹. Then the minima connected to the transition states were identified using the DNEB/L-BFGS method developed by Wales and coworkers.^{38, 39} Previously unknown minima were added to the growing database of minima, transition states, and pathways, which were then used to generate the disconnectivity graph. Finally, we further systematically expanded the tree by increasing the number of connections per minimum through single-ended transition state searches and the overall connectivity of the disconnectivity graph through parallel double-ended transition state searching.

Prior to generating a disconnectivity graph, we carried out a conformational search using the AMBER* force field⁴⁰ within the MacroModel⁴¹ suite of programs and used this output to generate starting structures for DFT geometry optimization using the Gaussian09 computational package⁴². Conformational minima within 50 kJ/mol of the global minimum were optimized using the M05-2X⁴³ hybrid functional with the 6-31+G(d) basis set using tight optimization. Harmonic frequencies were scaled by the established values of 0.94 and 0.96 in the NH and amide I regions, respectively.^{8, 15, 20, 22} Best fit of the scaled, calculated harmonic frequencies and intensities with the single-conformation IR spectra, guided by the calculated predictions of their energies, led to assignments of experimental conformations.

Initially, we created the disconnectivity graph with the hope of better understanding the complex potential energy surface, as well as to test whether different structures which better fit experimental data could be produced. In this case the disconnectivity graph did not produce a

better fit structure. In the future, we intend to use disconnectivity graphs for the production of starting structures, as a means of gaining a qualitative understanding of the complex potential energy surface, and as a guide to isomerization pathways and energetics for population transfer experiments.⁴⁴⁻⁴⁶ The assigned structures presented herein were found in both the AMBER* force field search, as well as the CHARM22 disconnectivity graph.

3.2.3 Nomenclature

The hydrogen bonds present in each structure are described using the C_n notation, in which n represents the number of atoms involved in a hydrogen bonded ring. The naming scheme in this work begins from the N-terminus and ends at the C-terminus of the peptide. For example, the structure in Figure 3.1 would be designated as a C11/C9 hydrogen bonded structure. C7 hydrogen bonds are designated as either equatorial ($C7_{eq}$) or axial ($C7_{ax}$), where these designations refer to the position of the functional group in between the involved amide components, with respect to the C7 plane.⁴⁷ In the assigned structures, blue hydrogen bonded lines represent N- to C-terminus directional hydrogen bonding while red lines represent C- to N- terminus hydrogen bonding. Finally, $NH\cdots\pi$ hydrogen bond interactions are designated as such.

3.3 Results and Analysis

3.3.1 (SRSS) Ac-Ala- β_{ACHC} -Ala-NHBn

The R2PI spectrum of the *RS* diastereomer is shown in the top trace of Figure 3.2 along with a series of IR-UV hole burning spectra. Asterisks in the IR-UV HB spectra mark the UV transitions used to record conformation-specific RIDIR spectra without significant interference. The R2PI spectrum from 37380 – 37770 cm^{-1} is quite congested, and, as the IR-UV HB spectra below show, is a composite of three unique UV spectra due to three unique conformational isomers. Conformer A has its $S_0 - S_1$ origin transition at 37510 cm^{-1} with two clear transitions at +14 cm^{-1} and +131 cm^{-1} . The highly-congested region from 37520 – 37570 cm^{-1} makes identification of weaker UV transitions belonging to conformer A difficult, due mainly to the incomplete subtraction from the spectrum of conformer B.

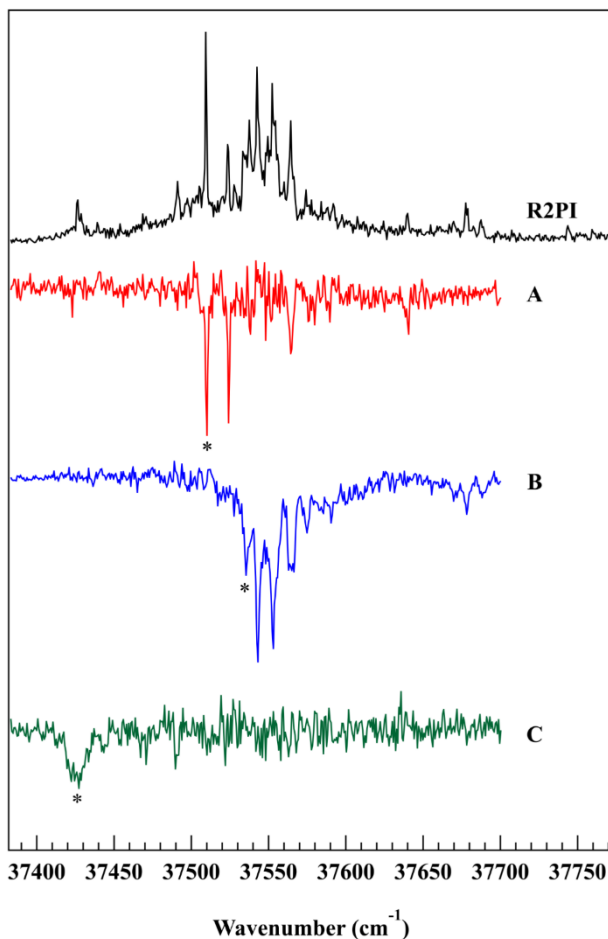


Figure 3.2. R2PI (black trace) and IR-UV hole burning spectra (red, blue, and green traces) taken in the $S_0 - S_1$ region of *RS*. The UV transitions used to collect RIDIR spectra are marked with an asterisk.

The set of transitions belonging to conformer B begins 25 cm^{-1} to the blue of the origin of conformer A at 37535 cm^{-1} and shows a long Franck-Condon progression in a low frequency vibration of $\sim 10 \text{ cm}^{-1}$. This mode corresponds to the terminal phenyl ring rocking against the remainder of the molecule, thereby coupling the localized $\pi - \pi^*$ electronic transition on the phenyl ring with the coordinate of the low frequency rocking vibrational mode. A second peak at $+143 \text{ cm}^{-1}$ from the origin is present in the UV spectrum of conformer B, indicating excitation into a second low frequency vibrational mode in the S_1 state.

The S_0 - S_1 origin of conformer C lies 84 cm^{-1} shifted down in frequency relative to that of the origin of conformer A (37246 cm^{-1}). To obtain sufficient signal to take conformation specific data for conformer C, experimental conditions were altered that led to rotational warming, and

therefore broadened UV transitions, of conformer C, as is evident by its IR-UV HB spectrum. Due to its weak UV signal coupled with the considerable noise inherent in laser desorption experiments, the assignment of any peak except the origin transition was not attempted. It does appear, however, that the peak at 37491 cm^{-1} is a vibronic transition belonging to conformer C. The large electronic frequency shift of conformer C relative to both conformers A and B suggests that the electrostatic environment of the ultraviolet chromophore in C is considerably different from that of both conformers A and B.

RIDIR spectra for conformers A (red), B (blue), and C (green) in the amide I ($1600\text{-}1800\text{ cm}^{-1}$) and NH stretch fundamental ($3200\text{-}3500\text{ cm}^{-1}$) regions are shown in Figures 3.3a and 3.3b, respectively. Here, asterisks mark the transitions unique to each conformer that were used to record the IR-UV HB spectra shown in Figure 3.2. As expected, based on the number of amide groups present in this molecule, each conformer shows four NH stretch fundamentals, and four transitions in the amide I region, which is nominally attributed to the C=O stretch. Figure 3.3 also compares the experimental spectrum with the computed best fit vibrational frequencies and IR intensities (black sticks) of each structure, calculated at the M05-2X/6-31+G(d) level of theory. The structures associated with the best fit spectra are shown in Figure 3.4. The varied appearance of both the amide I and NH stretch regions imply that the three conformers are indeed quite structurally distinct from one another.

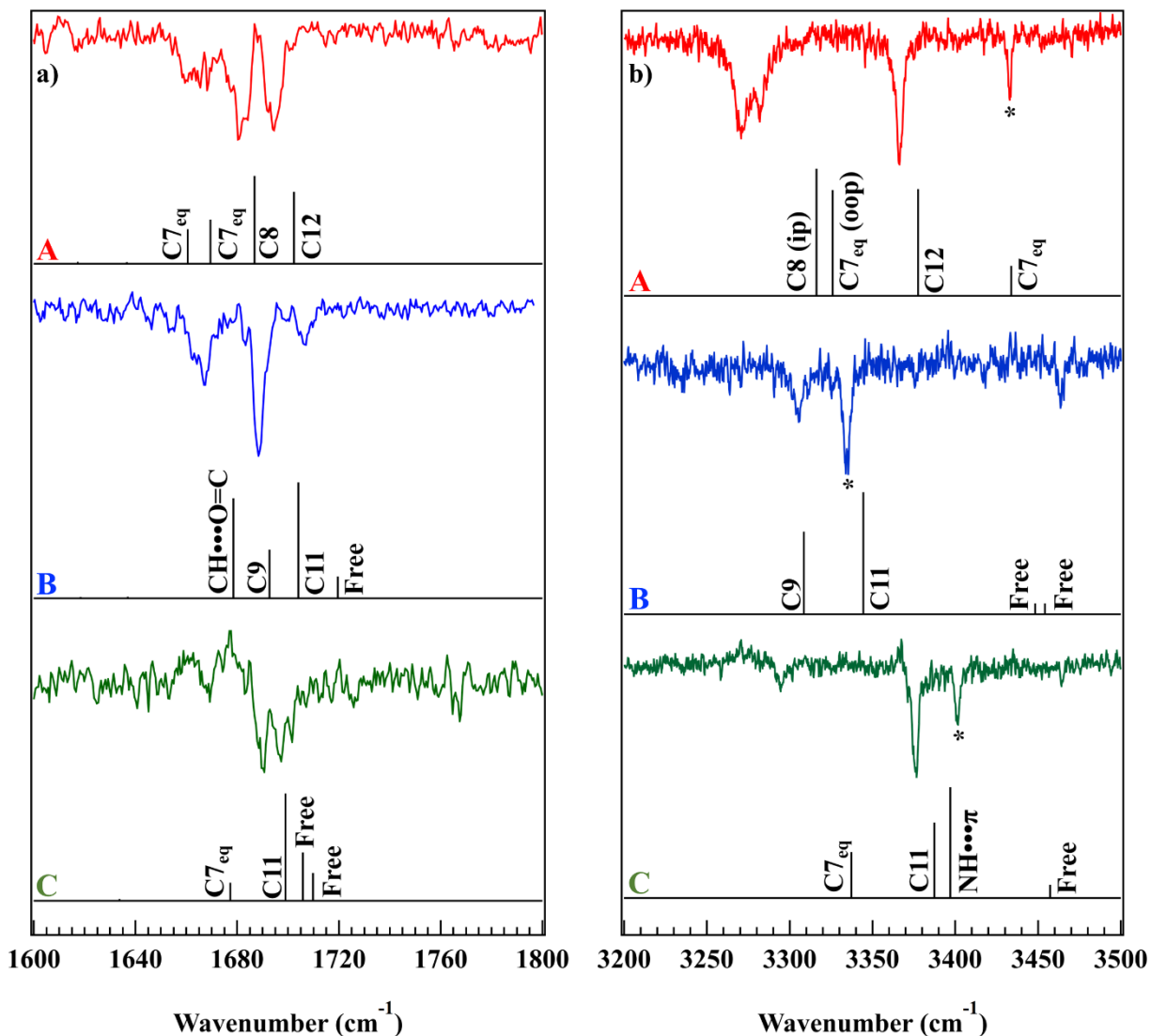


Figure 3.3. *RS* RIDIR spectra in the a) amide I and (b) NH fundamental stretch regions of conformer A (red), conformer B (blue), and conformer C (green). Scaled, harmonic vibrational frequencies calculated at the M05-2X/6-31+G(d) level of theory are shown as black stick spectra for each conformer underneath the experimental trace and are labelled to indicate the hydrogen bonded cycle associated with each vibrational frequency. Scale factors of .96 and .94 were used in the amide I and NH stretch regions, respectively. Asterisks mark the peaks which were used to collect IR-UV HB spectra.

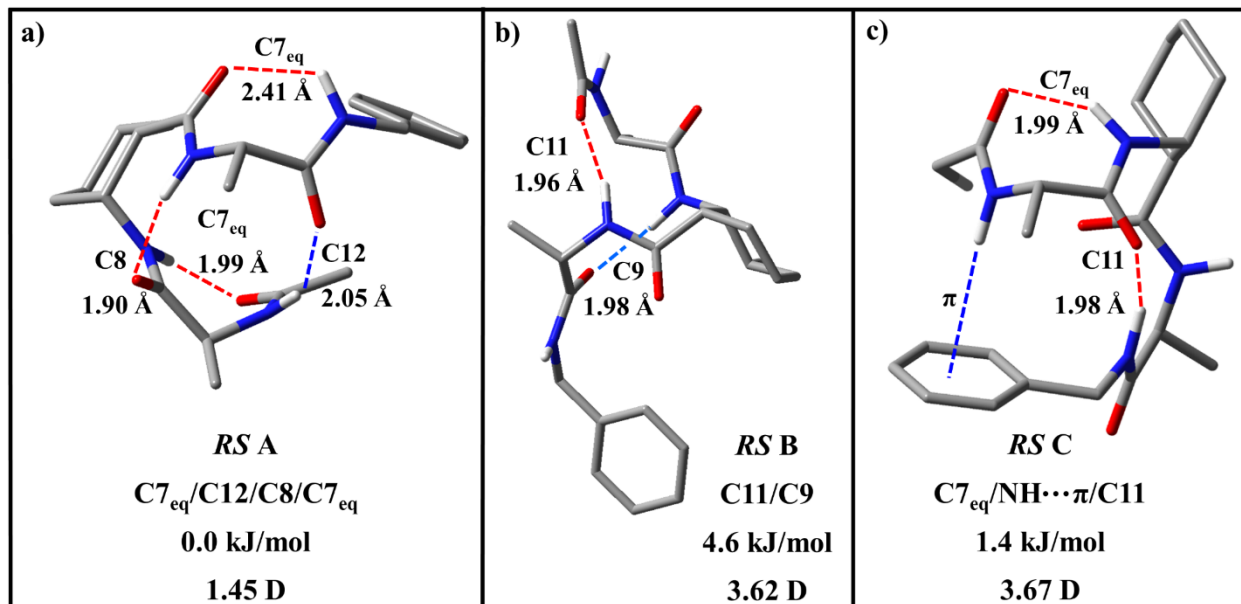


Figure 3.4. Assigned structures of RS (a) conformer A, (b) conformer B, (c) conformer C. Hydrogen bonds are indicated with dotted lines, labelled with O...H length, and color coated to indicate direction. Structural families, relative energies (kJ/mol), and dipole moments (D) are listed. Backbone hydrogens are omitted for clarity.

The size and complexity of the molecules studied herein require harmonic, normal mode analysis to generate simulated IR spectra. Oscillators involved in strongly hydrogen bonded interactions reside in more anharmonic potential wells than those less involved in hydrogen bonding. As a result, single scale factors for entire regions of the calculated vibrational spectrum do not adequately capture the low frequency shifts of strongly hydrogen bonded oscillators. In this case, experience has shown that it is the intensity and frequency pattern, rather than absolute frequency position, which serves to establish the assigned structure. Inspection of the assigned spectra in this chapter reveal the strong dependence of calculated harmonic, normal mode frequencies on hydrogen bonding architecture.

Conformer A has four well resolved peaks in the NH stretch region: a weak $C7_{eq}$ hydrogen bond at 3433 cm^{-1} , an intermediate strength C12 at 3366 cm^{-1} , and two strongly hydrogen bonded peaks at 3282 and 3271 cm^{-1} , attributed to the out of phase (oop) and in phase (ip) oscillation, respectively, of strong $C7_{eq}$ and C8 H-bonds. The uncharacteristic high frequency of the weakly hydrogen bond $C7_{eq}$ is due to the long $NH\cdots O=C$ bond distance (2.40 \AA).^{20, 48} The similarity in intensity of the in-phase and out-of-phase vibrations of the stronger $C7_{eq}$ and C8 NH stretch fundamental is due to the amide groups of the corresponding NH oscillators being nearly

perpendicular to one another, as revealed by the best fit structure, resulting in similar magnitude dipole derivatives for in-phase and out-of-phase combinations.

It is important to note that the C=O and NH groups of every amide sub-unit in this conformer is involved in a hydrogen bond, leading to the assignment of conformer A as a tightly folded $C7_{eq}/C12/C8/C7_{eq}$ structure, which was calculated to be the global minimum energy structure (0.0 kJ/mol, see Figure 3.4). The local conformation of the ACHC ring of this assigned structure is eq. CO/axial NH and it possesses a dipole moment of 1.45 D, a strikingly low value, but one which makes sense upon inspection of the assigned structure. The two amide groups on either side of the ACHC ring orient themselves across from one another, resulting in a structure reminiscent of a β -turn. The amide groups are arranged in a “box” formation, such that the individual amide dipole moments sum to a small value. The amide I spectrum of conformer A also shows excellent agreement between experiment and theory, adding confidence to this assignment.

Conformer B shows two closely spaced free NH stretch transitions as 3466 and 3464 cm^{-1} and two well resolved moderate strength hydrogen bonds at 3335 and 3306 cm^{-1} , assigned to NH groups in C11 and C9 H-bonds, respectively. The amide I spectrum reflects the C11 and C9 assignment, with the corresponding C=O vibrations appearing at 1688 and 1682 cm^{-1} , respectively. The amide I spectrum also possesses one free C=O stretch fundamental at 1707 cm^{-1} , and a transition at 1666 cm^{-1} whose frequency may be influenced by the interaction of the C=O with a CH on the aromatic ring. The structure corresponding to the best fit calculated structure is an emergent form of a right handed C11/C9 mixed helical structure, with its hydrogen bonds pointing in opposite directions along the helical axis, resulting in a dipole moment of 3.6 D. This structure has axial CO/eq. NH on the ACHC ring, as can be seen in Figure 3.4. Based on the form of the normal modes, it seems likely that the aromatic $\text{CH}\cdots\text{O}=\text{C}$ interaction is responsible for the long Franck-Condon progression in a low-frequency vibration of 10 cm^{-1} (Figure 3.2).

The NH stretch spectrum of conformer C possesses one free NH stretch at 3463 cm^{-1} , two intermediate strength hydrogen bonds at 3401 and 3377 cm^{-1} , and one strong hydrogen bond at 3295 cm^{-1} . The amide I spectrum has limited signal-to-noise and can only be used to provide confirming evidence for the assignment. The spectrum exhibits two C=O stretch transitions shifted to lower frequency ($<1700 \text{ cm}^{-1}$) as they should be if they are involved in hydrogen bonding, while the other two are not well-resolved, but contribute to the clump of transitions just above 1700 cm^{-1} where free C=O stretch groups would appear. Based upon comparison with the best fit calculated

structure conformer C is assigned as a C7/NH \cdots π /C11 structure, with two free C=O groups, one free NH group, and eq. CO/axial NH substituents on the ACHC ring. This structure has the largest dipole moment of the three *RS* structures at 3.7 D. A summary of structural parameters and vibrational/theoretical frequencies is given in Table 3.1.

3.3.2 (*SSRS*) Ac-Ala- β _{ACHC}-Ala-NHBn

The R2PI and IR-UV HB spectra of *SR* is shown in Figure 3.5. The R2PI spectrum shows a congested region centered around 37550 cm⁻¹ and two well resolved and relatively isolated peaks at ~37630 cm⁻¹. The dense cluster of peaks show up in the same region as electronic origins from conformer B of *RS*, while the most intense peak in the spectrum is shifted to higher frequency away from this region by ~80 cm⁻¹. IR-UV HB identify two major conformers present in the molecular beam, labelled A and B with HB spectra in blue and red, respectively. The peak assigned to the origin transition of conformer A is located at 37615 cm⁻¹ while that for conformer B is located at ~37530 cm⁻¹. The noisy region of the IR-UV HB spectrum on conformer A at ~37550 cm⁻¹ is due to incomplete subtraction of conformer B, which absorbs continuously over a 60 cm⁻¹ region. The small cluster of peaks at ~37455 cm⁻¹ and the sharp transition at 37632 cm⁻¹ likely belong to other minor conformers in the expansion, but due their low signal no further characterization was carried out on them.

Conformer A shows a clear Franck-Condon progression of three peaks in a ~27 cm⁻¹ mode. Vibrational assignments based on best fit structures indicate that this progression is caused by the phenyl ring rocking in a plane nearly perpendicular to the C terminal N-H \cdots π hydrogen bond axis. Conformer B shows a closely-spaced progression with spacing ~10 cm⁻¹. A low frequency mode of the assigned structure agrees well with the ~10 cm⁻¹ vibronic spacing. Both the appearance and absolute frequency of the R2PI spectra of *SR* B and *RS* B are markedly similar to one another, suggesting that both diastereomers of the ACHC residue are capable of forming the same mixed helical structure despite their L-Ala neighbors.

Table 3.1 Structural parameters and vibrational frequencies for the assigned structures of the RS and SR diastereomer pair calculated at the DFT M05-2X/6-31+G(d) level of theory, compared with experiment.

SRSS Diastereomer												
Molecule	ΔE (kJ/mol)	φ_1	ψ_1	φ_β	θ_β	ψ_β	φ_2	ψ_2	H-bonding pattern	Dipole moment (Debye)	ACHC Configuration	
Conf A:	0.00	-86	62	110	-61	-9	-71	105	$C7_{eq}/C12/C8/C7_{eq}$	1.45	eq. CO/axial NH	
Conf B:	4.62	-58	150	85	54	-93	-59	142	C11/C9	3.62	axial CO/eq. NH	
Conf C:	1.37	-78	79	95	-58	-90	-86	1	$C7_{eq}/NH \cdots \pi/C11$	3.67	eq. CO/axial NH	
		Conf A				Conf B				Conf C		
		exp.		theory		exp.		theory		exp.		theory
NH stretch (cm^{-1})		3433		3434		3466		3454		3463		3457
		3366		3378		3464		3449		3401		3397
		3282		3326		3335		3344		3377		3387
		3271		3316		3306		3309		3295		3337
Amide I (cm^{-1})		1695		1702		1707		1719		1702		1710
		1681		1687		1688		1704		1697		1706
		1668		1669		1682		1693		1691		1699
		1663		1660		1668		1679		1669		1677
SSRS Diastereomer												
Molecule	ΔE (kJ/mol)	φ_1	ψ_1	φ_β	θ_β	ψ_β	φ_2	ψ_2	H-bonding pattern	Dipole moment (Debye)	ACHC Configuration	
Conf A:	0.00	74	-57	-165	65	-99	-83	57	Bif $C7_{ax}-C11/$ $NH \cdots \pi/C7_{eq}$	2.89	eq. CO/axial NH	
Conf B:	12.52	54	-142	-84	-56	86	51	-142	C11/C9	4.04	axial CO/eq. NH	
		Conf. A				Conf. B						
		exp.		theory		exp.		theory				
NH stretch (cm^{-1})		3413		3416		3479		3478				
		3409		3400		3472		3473				
		3293		3312		3412		3385				
		3282		3300		3343		3324				
Amide I (cm^{-1})		1702		1712		1698		1704				
		1691		1697		1693		1699				
		1660		1664		1679		1688				
		1651		1652		1672		1682				

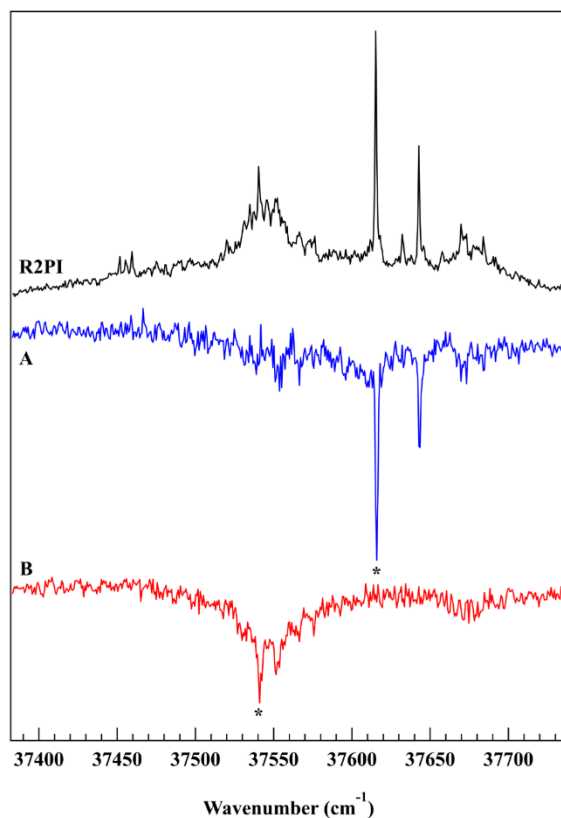


Figure 3.5. R2PI (black trace) and IR-UV hole burning spectra (blue and red trace) taken in the $S_0 - S_1$ region of *SR*. The UV transitions used to collect RIDIR spectra are marked with an asterisk.

Figures 3.6a and 3.6b presents the RIDIR spectra for conformer A (blue) and B (red) in the amide I and NH stretch fundamental region, respectively. As before, calculated, scaled harmonic frequencies of the best fit structures are shown below the experimental traces as black stick spectra. The structure assigned to conformer A is a bifurcated $C7_{ax}-C11/NH\cdots\pi/C7_{eq}$ conformer shown in Figure 3.7a. Conformer A has its highest frequency stretch at 3433 cm^{-1} , which is associated with a weak $NH\cdots\pi$ hydrogen bond interaction. The 32 cm^{-1} shift to higher frequency of this $NH\cdots\pi$ interaction relative to that of *RS* conformer C (3401 cm^{-1}), suggests that the $NH\cdots\pi$ interaction in *SR* conformer A is substantially weaker than that in *RS* conformer C. Indeed, the NH group is not well aligned with the center of the π cloud in *RS* conformer C, consistent with this notion.

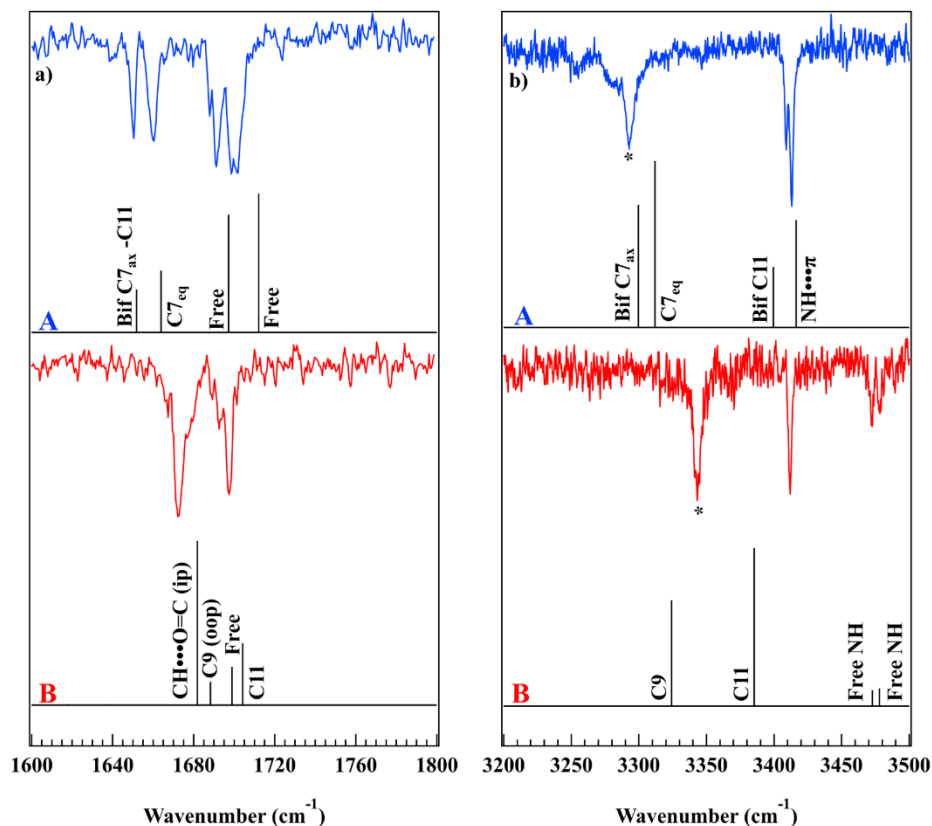


Figure 3.6. SR RIDIR spectra in the (a) amide I and (b) NH fundamental stretch regions of conformer A (blue), and conformer B (red). Scaled, harmonic vibrational frequencies calculated at the M05-2X/6-31+G(d) level of theory are shown as black stick spectra for each conformer underneath the experimental trace and are labelled to indicate the hydrogen bonded cycle associated with each vibrational frequency. Scale factors of .96 and .94 were used in the amide I and NH stretch regions, respectively. Asterisks mark the peaks which were used to collect IR-UV HB spectra.

The peaks at 3409 and 3282 cm^{-1} in conformer A's NH stretch spectrum are assigned to a bifurcated C11/C7_{ax} hydrogen bond pair, respectively, where the C=O is acting as H-bond acceptor simultaneously to both NH donors. According to the calculations, the bifurcated C7_{ax} NH stretch fundamental (3282 cm^{-1}) is shifted to lower frequency than the C7_{eq} cycle (3293 cm^{-1}) due to its shorter H-bond length ($R_{\text{NH}\cdots\text{O}=\text{C}} = 1.85 \text{ \AA}$ versus 1.93 \AA). The NH stretch transition at 3433 cm^{-1} is assigned to the bifurcated C11 NH group. Compared with the pure C11 cycles in RS conformers B and C, it is shifted in frequency by 98 and 56 cm^{-1} , respectively, indicating that the bifurcated C11 hydrogen bond distance and angle of approach is distorted away from optimum values in order to join the bifurcated cycle. Indeed, the bifurcated C11 NH \cdots O=C bond distance

(2.2 Å) and angle (143°) are shifted unfavorably away from both *RS* conformers B (2.0 Å, 165°) and C (2.0 Å, 146°).

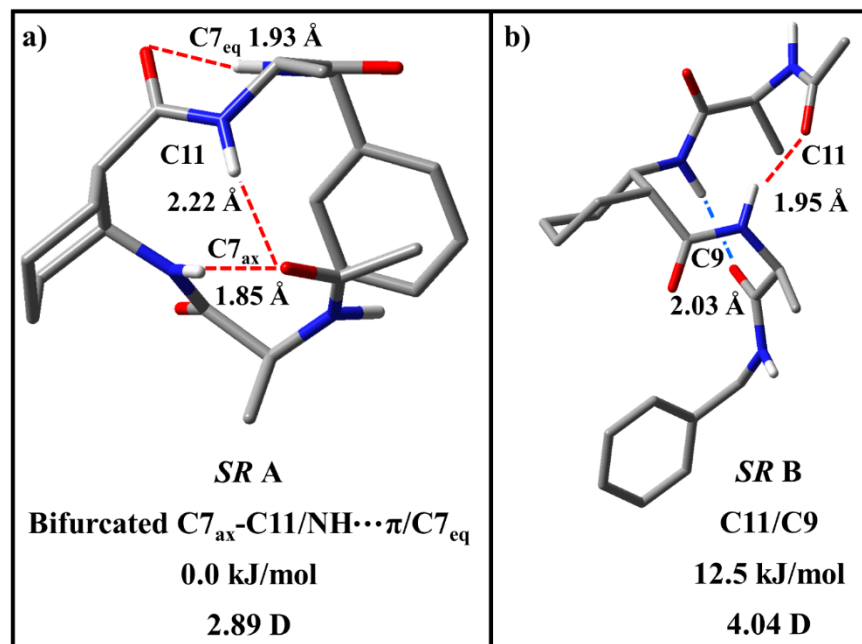


Figure 3.7. Assigned structures of *SR* (a) conformer A and (b) conformer B. Hydrogen bonds are indicated with dotted lines, labelled with O...H length, and color coded to indicate direction. Structural families, relative energies (kJ/mol), and dipole moments (D) are listed. CH hydrogens are omitted for clarity.

The amide I data on conformer A shows excellent agreement between theory and experiment, and reinforces the structural elements deduced from the NH stretch region. The two high frequency peaks correspond to the two free C=O oscillators, while the transition at 1660 and 1651 cm⁻¹ belong to the C7_{eq} and bifurcated C7_{ax}-C11 C=O groups. Based on the agreement between experiment and simulated frequency calculation, *SR* A is assigned to a Bif C7_{ax}-C11/NH...π/C7_{eq} structure with eq. C=O/axial NH AHC configuration, and dipole moment of 2.9 D. This structure was calculated to be the global minimum energy structure (0.0 kJ/mol) for this diastereomer (see Figure 3.7).

The NH and amide I spectra of *SR* B are presented as the bottom two traces of Figure 6, where they are compared with the best-fit stick spectra. The NH spectrum shows two closely spaced, well resolved free NH stretches at 3479 and 3472 cm⁻¹, one intermediate strength hydrogen bond at 3412 cm⁻¹, and one strong hydrogen bond at 3343 cm⁻¹. Based on comparison with the best

fit simulated spectrum, the intermediate strength transition is assigned to a C11, with the strong hydrogen bond assigned to a C9 hydrogen bond oriented in the opposite direction of the C11. Analysis of the best fit structure (Figure 3.7b)) reveals that conformer B is a left handed C11/C9 mixed helix former, analogous to the right handed C11/C9 mixed helix of *RS* B.

The amide I spectrum, as in the case of *RS* B, reflects the C11 and C9 assignment. The highest frequency stretch at 1698 cm^{-1} is assigned to the C11 hydrogen bonded C=O vibration. The two lowest frequency peaks, which are somewhat unresolved from one another, correspond to the in phase and out of phase vibrations of the C9 C=O and the ACHC C=O involved in a weak interaction with a C-H on the aromatic ring. As with *RS* B, it seems likely that this aromatic $\text{CH}\cdots\text{O}=\text{C}$ interaction couples molecular vibrations to the ring excitation, as revealed by the electronic spectrum (Figure 3.5). The C11/C9 helix structure of *SR* B possesses an axial C=O/eq. NH ACHC ring environment, and a dipole moment of 4.0 D. Its relative energy is calculated to be 12.5 kJ/mol above the *SR* global minimum. Further discussion of the relative energies will be undertaken in the next section.

3.4 Discussion

3.4.1 Conformational Preferences of *RS* and *SR* and Crystal Structures

In the preceding section, the experimentally observed spectra were assigned to five conformational isomers, three in the *RS* diastereomer and two in *SR*. These five structures are constituted by four unique hydrogen-bonding networks, and therefore distinct conformational families. There are, however, some interesting similarities between the different structures, most notably in that *RS* A/C and *SR* A all share the same N-terminal C7 hydrogen bond between the C=O of the acyl cap and the NH of the ACHC residue. The *RS* conformers possess a C7_{eq} H-bonded ring, while a C7_{ax} ring is taken up by the *SR* conformer. Similarly, *SR* A and *RS* A both have a C-terminal C7_{eq} hydrogen bond between the NHBn cap NH and ACHC C=O (see Figures 3.4 and 3.7). This abundance of C7 hydrogen bonded rings across alanine residues is consistent with previous theoretical and experimental explorations of alanine containing peptides.^{20, 49, 50} Finally, *RS* B, *SR* A, and *SR* B share a common C11 hydrogen bond between the C=O of the acyl cap and the NH of the C-terminal alanine residue. This C11, however, is a constituent of two very different secondary structures.

The tightly folded C7_{eq}/C12/C8/C7_{eq} structure of *RS* A marks a rare example of a gas phase foldamer in which all amide group components are involved in hydrogen bonding, forming a total of four NH \cdots O=C H-bonds in which each amide group acts simultaneously as H-bond donor and acceptor.¹⁹ Three of the four H-bonds are C \rightarrow N-terminal (red) while the C12 H-bond closes the tetramer cycle with a single N \rightarrow C-terminal H-bond (blue), as shown in Figure 3.4. Looked at from another vantage point, this structure is a β -turn analogue in that the peptide chain on either side of the ACHC residue are oriented in nearly anti-parallel fashion. While the dihedrals and inclusion of a β -amino acid fall short of canonical β -turn parameters, the ability of the ACHC residue to turn the peptide chain upon itself is evident (see Figure 3.4).

One of the principal goals of the present study is to determine whether a single cyclically constrained β -peptide sub-unit is sufficient to induce formation of a C11/C9 mixed helix in a model alternating α/β -peptide in isolated form. A motivation for our gas-phase, single-conformation studies was the demonstration by some of us that a close analogue of the *RS* diastereomer (with different N-terminal and C-terminal caps) did indeed form the first stages of an 11/9 mixed helix when crystallized.²³ While packing interactions could play a role in stabilizing the mixed helix in the crystalline solid, in the gas phase, such intermolecular interactions are notably missing; yet, an emergent form of the 11/9 mixed helix competes for the global minimum energetically at the smallest sized $\alpha\beta\alpha$ peptide, with a single C11 and single C9 H-bond holding it together.

RS B, *SR* B, and the crystal analogue of *RS* B all form a C11/C9 structure which requires the ACHC residue to adopt an eq. NH/axial C=O configuration. Since the *RS* analogous structure was the enantiomer of the molecule studied here, that structure was inverted in order to overlap and compare the backbones. As can be seen in Figure 3.8a, overlap of the C11/C9 backbone of the structure assigned to *RS* B with that of the crystal structure shows a near-perfect match. Figure 3.8b) shows the backbone overlap of the assigned structures of *RS* B and *SR* B (inverted). This overlap is also quite good, although there is more variance between these two structures than the two previously considered. Since structure inversion changes all stereocenters along a molecule, what is being considered in Figure 3.8b is RRSR v. SRSS, i.e., effectively the only difference between the two diastereomers is the chirality at the two Ala residues. This is clear upon inspection of Figure 3.8b where the Ala containing chiral centers are circled (left), highlighting the differences between these analogous structures (see discussion of Alanine ϕ and ψ angles below).

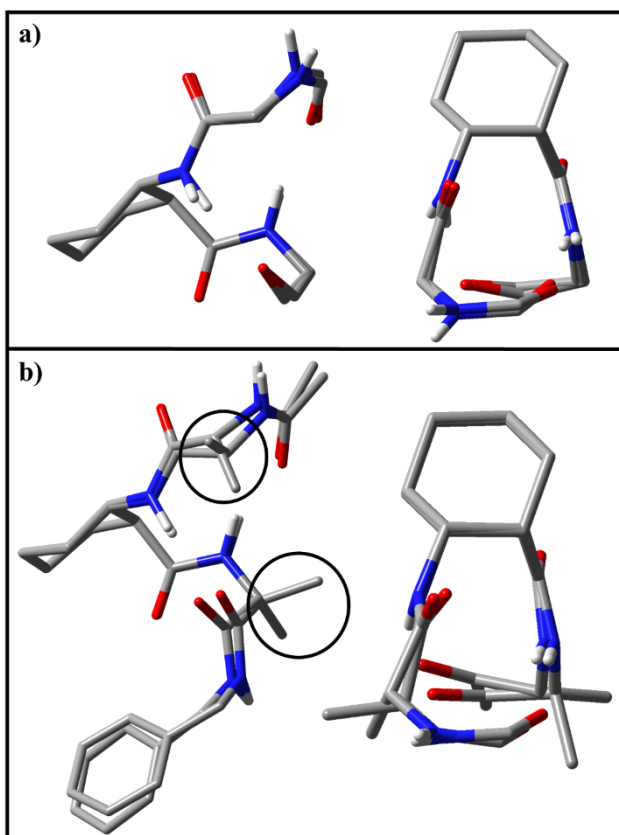


Figure 3.8. (a) Overlap of the back bone of the assigned *RS* B structure and its analogous crystal structure. (b) Overlap of the backbone of the assigned *RS* B and *SR* B helical structures. Unique stereocenters at the *Ala* residues circled in (b) (left), highlighting the difference in methyl group position between *SR* B and *RS* B. Formation of an incipient form of an 11/9 mixed helix is preferred in each case.

This cross-phase/cross-diastereomer conservation of structure suggests that the 11/9 mixed helix is a canonical helical structure, representative of alternating α/β -peptides containing cyclically constrained β -residues. Indeed, a theoretical exploration of helical structures comprised of alternating mixed α/β residue types predicted the 11/9 helix to be the most stable helix type in both solution and vacuum, even in the absence of the constraining ACHC ring.⁵¹ Table 3.2 shows a comparison of the average dihedral angles between the two 11/9 helices derived from best fit structures in this work, in crystalline form,²³ and the predictions from previous theory⁵¹. While three residues are not sufficient in length to produce a fully-formed helix, the C11/C9 conformation reported here incorporates a single C11 H-bond between the C=O of β -residue (*i*) and H-N of α -residue (*i*+3), and a single C9 H-bond between the C=O of α -residue (*i*) and H-N of β -residue (*i*-

1), appearing in the gas phase at the shortest peptide backbone possible. Gas phase tests of helical fidelity and evolution in longer oligomers are still needed

Table 3.2. Average backbone dihedral angles of α - and β -amino acids in the $\alpha\beta\alpha$ *SR/RS* 11/9 mixed helix. The *RS B* parameters have been inverted for more direct comparison with analogous

<i>11/9 Helical Backbone Dihedral Angles (degrees)</i>					
Molecule	φ_α	ψ_α	φ_β	θ_β	ψ_β
<i>RS B</i>	59	-146	-85	-54	93
<i>SR B</i>	53	-142	-84	-56	86
Crystal Structure ²³	61	-151	-87	-52	97
Theoretical Model ⁵¹	60	-150	-77	-60	100

The $C7_{eq}/NH\cdots\pi/C11$ structure assigned to *RS C* represents a “cap influenced” structure, in which the NHBn cap is directly contributing to the conformational stability by utilizing the π cloud on the aromatic ring as a hydrogen bond acceptor. Indeed, DFT calculations performed on structures with the NHBn cap replaced with an NHMe cap raise the *RS C* analogue 8.2 kJ/mol in energy above the corresponding *RS A* analogue, a decrease in relative stability of 6.8 kJ/mol. By contrast, the *RS B* NHMe analogue, which lacks this interaction, has almost the same energy as its NHBn counterpart (4.9 vs. 4.6 kJ/mol).

The *SR A* assigned structure is characterized by having a bifurcated hydrogen bonding cycle in which the ACHC NH acts as hydrogen bond donor to form the N-terminal $C7_{ax}$ ring, contributing to one half of the bifurcated cycle. The remainder of the structure is driven by the eq. C=O/axial NH ACHC conformation. The ACHC-induced turn in *SR A* orients the C-terminal Ala NH in such a way that it points towards the N-terminal C=O, thereby allowing formation of the bifurcated $C7_{ax}$ -C11 cycle. This conformer is further stabilized by an $NH\cdots\pi$ and C-terminal $C7_{eq}$ interactions. Indeed, while $C7_{ax}$ motifs are more sterically hindered than their $C7_{eq}$ counterpart, in this structure’s case the additional stabilization of the $NH\cdots\pi$ interaction necessitates $C7_{ax}$ formation. The extent to which this structure is “cap influenced” is apparent upon geometry optimization after substituting the NHBn cap for a NHMe cap. In this case, the structure changes from a Bif $C7_{ax}$ -C11/ $NH\cdots\pi/C7_{eq}$ to adopt a $C7_{ax}/C12/C7_{eq}$ conformation, in which the C11 H-bond

is broken, allowing the C-terminal Ala C=O to hydrogen bond with the N-terminal Ala NH, forming the same C12 hydrogen bond found in *RS A*

In this work two out of four of the chiral centers are changed between the two diastereomers. Three unique conformers were present in the supersonic expansion for *RS*, while two were observed for *SR*. Among these assigned structures, *RS B* and *SR B* form a diastereomer pair, in which hydrogen bonding properties remain invariant under the change of ACHC chiral centers. This is compared to previous work from our group, in which the stereochemistry of a single α -amino acid was altered between two di-peptides, which resulted in three diastereomeric pairs being observed.¹⁷ The fact that only a single diastereomer pair is identified in the present work is likely a consequence of considering a tri-peptide with more degrees of freedom in which the cyclically constraining β -amino acid has its stereochemistry altered. This increase in complexity makes it much more sterically difficult for a given hydrogen bonded structure to preserve itself in its diastereomeric form. In the next section we consider the structural and energetic differences among the diastereomer pairs for each observed conformer.

3.4.2 Disconnectivity Graphs, Diastereomer Pairs, and Energetics

One goal of this study was to understand the effect that switching the chirality along the ACHC backbone had on the conformational preferences of the observed structures. Due to the relatively large size of the molecules studied, we chose to create disconnectivity graphs for each diastereomer with the hope that the representation of similar structural forms presented as clusters of minima grouped into conformational basins could aid in understanding the complex potential energy surface of such molecules with many degrees of freedom which is otherwise difficult, or impossible, to intuit. Disconnectivity graphs are also helpful in that they present isomerization pathways from one minimum to any other, providing energies and transition state structures along each step. The major drawback of the disconnectivity graphs presented herein is that they are generated from structures calculated using a classical force field, and thus can be considered only approximately correct. Nevertheless, the minima and transition states can then be used as a starting point for pathways employing higher level electronic structure methods.

The lowest energy portions of the disconnectivity graphs for *SR* and *RS* are presented in Figure 3.9. In this representation, conformational minima are represented as vertical minima, with the vertical position corresponding to the relative energy of each structure. These minima are

connected to each other through transition states, which are represented as nodes on the graph. Transition state energies are binned by a user-determined energy window; in this case, 4.18 kJ/mol (1.00 kcal/mol). In this way, the nodal points on the disconnectivity surface represent not a single transition state, but a cluster of transition states connecting the conformational minima below them, grouped together by similar energies. This makes the presentation of the potential energy surface much simpler to view and interpret. Structures that are connected to one another through transition states that fall within the same energy window are naturally grouped into conformational basins. These basins are characterized by containing structures that are in some way similar to one another.³⁴ In this way, the disconnectivity graph collects, and visually represents, different families of conformations in a visually intuitive manner, aiding the analysis of the complex potential energy surface.

It is clear upon inspection of Figure 3.9 that both graphs have two main basins that distinguish themselves by being lowest in energy. These basins, highlighted in green and purple, contain structures where the ACHC residue is in the eq. NH/axial C=O or eq. C=O/axial NH chair conformation, respectively. A third basin type, highlighted in red, distinguishes itself by containing structures in which the cyclohexane is in one of three possible twist boat conformations, which is a local minima along the isomerization pathway from one chair conformation to the other.⁵² The observed structures, in both *RS* and *SR* are seen to adapt both types of chair conformations, and, with the exception of *SR* B, are calculated by the modified CHARMM22 force field to be near the bottom of each respective basin. This gives hope that the overall shape of the disconnectivity graph is useful as a qualitative representation of the conformational landscape.

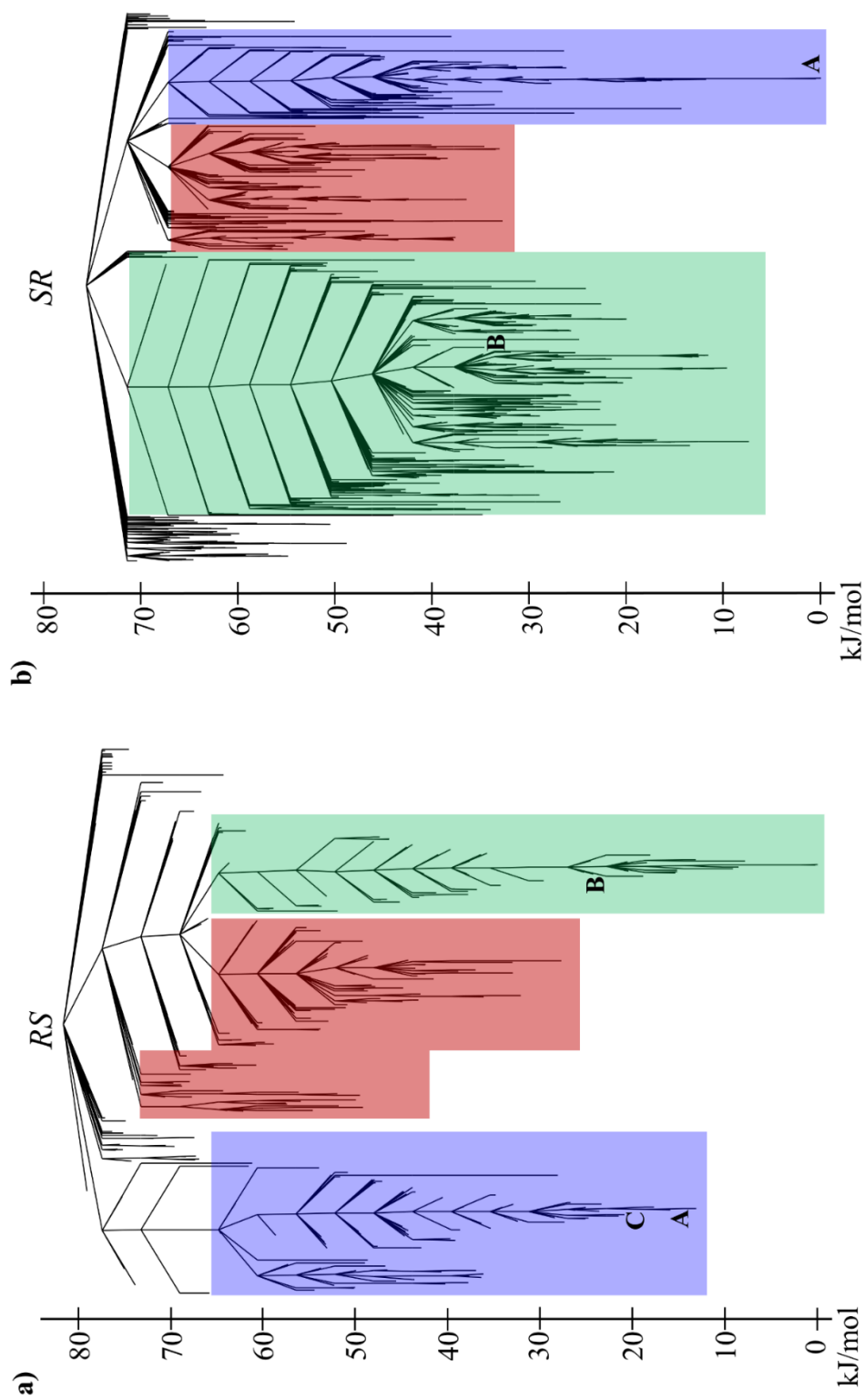


Figure 3.9. Disconnectivity Graphs for (a) SR and (b) RS diastereomers created using the CHARMM22 force field in conjunction with parameterized potentials for cyclic β -amino acids. The assigned conformers in each case are labelled in the graphs. Highlighted portions of the graph represent different conformational families: green represents conformers that possess an eq. NH/axial C=O ACHC subunit, purple represents eq. C=O/axial NH, and red represents twist boat structures, which are local minima along the isomerization pathway from one chair conformation to the other.

The low energy structures from the disconnectivity graph were further optimized at the M05-2X/6-31+G(d) level of theory. Figure 3.10 presents the M05-2X results as an energy level diagram showing the structures within 30 kJ/mol of the global minimum after DFT optimization of the force-field optimized structures from the graph (also within 30 kJ/mol of the force field global minimum). What is immediately clear is that *SR* has a much greater preference for bifurcated H-bonds (shown in red) than *RS*, with thirteen of the thirty-five structures containing bifurcated H-bonded cycles, with two NH groups H-bonded to the same C=O group. It is not surprising, then, that the global minimum for *SR* (*SR* A (0.0 kJ/mol)) contains a C7_{ax}/C11 bifurcated H-bond. Interestingly, the presence of these bifurcated double-rings produces an anti-cooperative effect resulting in at least one of the hydrogen bonds being weaker than it would be in an isolated cycle.^{20, 53-55} The abundance of anti-cooperative bifurcated double rings in *SR*, and the lack thereof in *RS*, suggests that the *RS* diastereomer is a more energetically and structurally stable species than the *SR* diastereomer. Indeed, as Figure 3.10 shows, the global minimum *RS* conformer is about 12 kJ/mol lower in energy than the *SR* global minimum. This may arise at least in part because there are more low-energy structures with three or four hydrogen bonds in *RS* compared to *SR*.

It is noteworthy that only two of the five observed conformers form a diastereomer pair. The relative energies of the diastereomer analogues of each assigned structure are displayed in Figure 3.10 with a blue “X”. A comparison of the diastereomer pair structures is shown in Figure 3.11. The C11/C9 diastereomer pair is observed experimentally, with *RS* B forming a right-handed helix and *SR* B forming a left-handed helix. The methyl groups in *RS* B are pointed away from the helical axis, and therefore minimize steric overlap more so than their counterparts in *SR* B, resulting in *SR* B ($E_{\text{rel}}(\textit{SR B})=12.5$) having a relative energy 19.9 kJ/mol higher than *RS* B ($E_{\text{rel}}(\textit{RS B}) = 4.6$ kJ/mol) when the difference in energies of the *RS* and *SR* global minima are taken into account. The ϕ and ψ backbone dihedrals of the Ala residues in each assigned conformer are plotted in the Alanine Ramachandran diagram in Figure 3.12, adapted from the work of Tsai et al.⁵⁶ At least one Ala dihedral angle pair of both *SR* conformers are found to be in a region of the Ramachandran plot that is highly unusual for Ala residues.

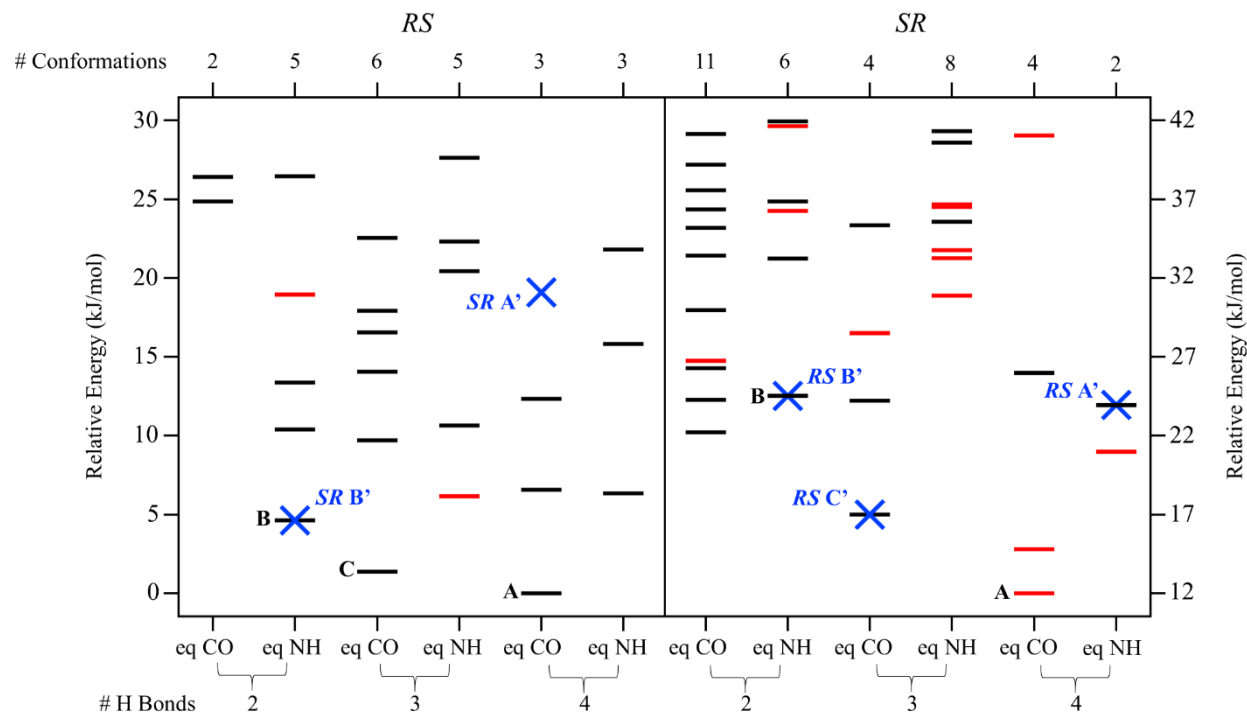


Figure 3.10. Energy level diagram of the lowest 30 kJ/mol disconnectivity graph structures after DFT optimization (M05-2X/6-31+G(d)) of the lowest 30 kJ/mol minima from the graph with zero-point energy correction. The relative energy defines 0.0 kJ/mol as the global minimum energy structure of the *RS* diastereomer, which was calculated to have the lowest absolute zero-point corrected energy. Structures are plotted vs. relative energy (kJ/mol) as a function of ACHC configuration and number of hydrogen bonds. Observed conformers are labelled, red lines indicate a structure with a bifurcated hydrogen bonding cycle. Cross diastereomer structural analogues are labelled with a prime (') and marked on the diagram with a blue "X". *SR A'* was not found in the disconnectivity graph search but was made by hand and submitted to DFT for optimization. Note that the global minimum for *SR* is 12 kJ/mol above that for *RS*.

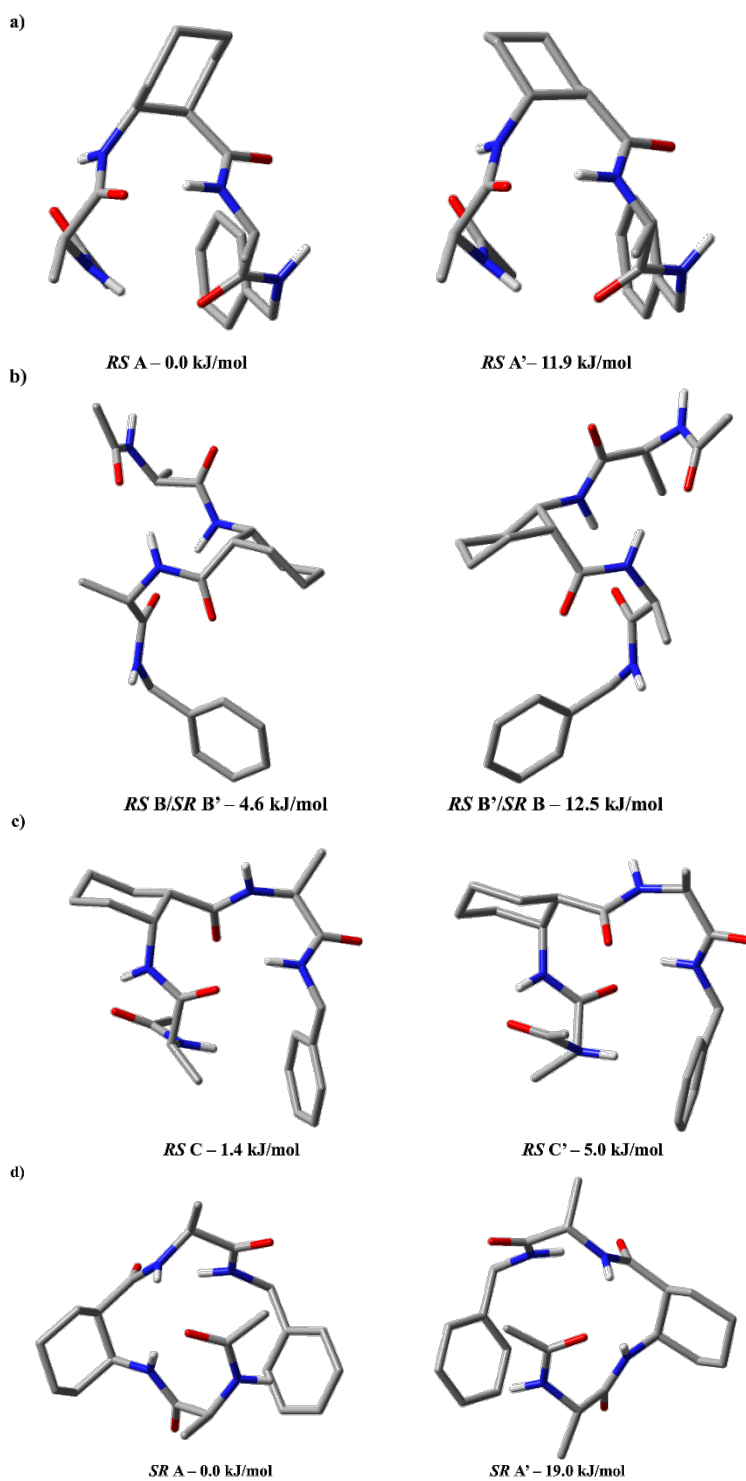


Figure 3.11. Shown above are the (a) – (c) RS and (b),(d) SR diastereomer pairs. Conservation of ACHC configuration is achieved in each pair except for SR A/SR A'.

The fact that *SR* A, the global *SR* energy minimum, possesses a non-natural dihedral pair provides a ready explanation for the 12 kJ/mol destabilization of the *SR* diastereomer relative to the *RS* global minimum. Indeed, inspection of the calculated lowest energy structures reveals that all lowest energy *SR* conformers within 10 kJ/mol contain one dihedral pair that falls outside of the allowed region of the Ramachandran diagram, while those angle pairs of the analogous *RS* structures all fall within normal Ramachandran space. The apparent requirement of *SR* to strain the backbone dihedrals along the Ala residues in order to form its lowest energy conformational minima suggests an inherent instability in the *SR* species not present in the *RS*.

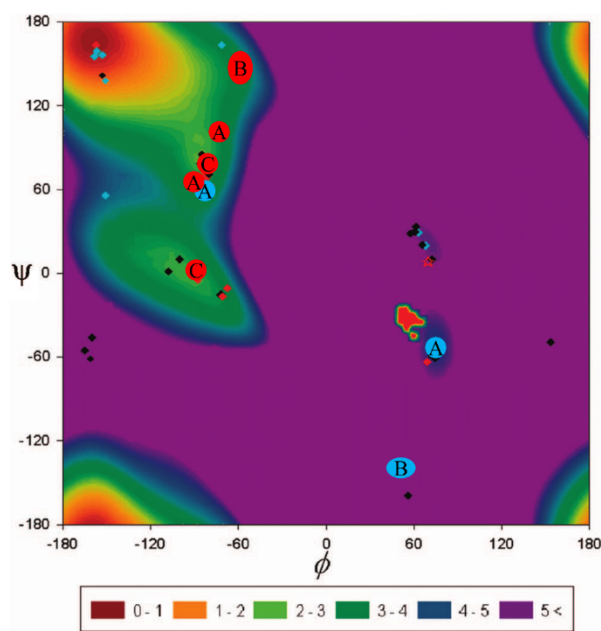


Figure 3.12. Alanine Ramachandran plot showing zero-point corrected potential energy as a function of ϕ/ψ dihedral angle pairs for Ac-Ala₃-NH₂ in the gas phase. Energies were calculated at the DFT B3LYP/D95(d,p) level of theory, and the figure was taken from Tsai et al. (Reprinted with permission from *J. Phys. Chem. B*, **2009**, *113* (1), 309-318. Copyright 2009 American Chemical Society.) Labelled circles represent the ϕ/ψ angles of the observed *RS* (red) and *SR* (blue) conformers. Color-coded energies are in kcal/mol.

The *SR* analogue of tightly-folded *RS* A (referred to as *RS* A') has its energy raised to 23.9 kJ/mol absolute energy, 11.9 kJ/mol above the *SR* global minimum. In retaining the structure's four hydrogen bonds, the ring distorts from eq. CO/axial NH in *RS* to eq. NH/axial CO in *SR*. As is seen from Figure 3.10, this ACHC conformation of *SR* is the less stable of the two, as there is

only one structure within 10 kJ/mol of the global minimum with the eq. NH/axial CO configuration. Both Ala dihedral pairs in *RS A'* fall within normal range.

RS C' is 3.6 kJ/mol higher in relative energy than its *RS* counterpart, and 15.6 kJ/mol higher in absolute energy, which can be understood by seeing that the $C7_{eq}$ is distorted to $C7_{ax}$ resulting in steric hindrance and loss of a weak $CH\cdots\pi$ interaction. Going from *RS C* to *RS C'* requires one Ala dihedral pair to distort away from its allowed value. Finally, the other member of the diastereomeric pair of the global minimum *SR A* (*SR A'*) has relative energy raised up to 19.0 kJ/mol above the *RS* global minimum, and an absolute energy difference of 7.1 kJ/mol adopting a Bif $C7_{eq}$ - $C11/NH\cdots\pi/C7_{ax}$ pattern. In this case, the change from $C7_{axial}$ to $C7_{eq}$ places the N-terminal Ala methyl group in close proximity to the benzene ring, adding to the destabilization already inherent to the change from $C7_{eq}$ to $C7_{axial}$. This change additionally requires one Ala dihedral pair to access the non-allowed dihedral space region.

While *RS A*, *B*, and *C* are the three lowest-energy conformers of *RS*, and *SR A* is the global minimum of the *SR* diastereomer, conformer *B* of *SR* is, at a relative energy of 12.5 kJ/mol, significantly less stable. In order to see the trends in free energy with temperature we calculated the free energy contribution of each low energy structure to see whether the relative energies would reorder themselves. This data is presented in Table 3.3. Some studies suggest that desorption temperatures may reach as high as 700 K.^{57, 58} However, for lack of better knowledge of the exact laser desorption temperature, we chose 300 K to calculate the free energies in order to see the temperature-dependent trends. At 300 K the relative free energy for *SR B* drops to 5.9 kJ/mol above the global minimum in free energy, and positions *SR B* as the lowest free energy structure with eq. NH/axial CO configuration. This raises the possibility of *SR B* being populated prior to cooling, which could help explain its presence in the experiment. It is also worth noting that at 12.5 kJ/mol zero-point corrected energy *SR B* is among the three lowest eq. NH/axial CO structures, within 3.5 kJ/mol of the eq. NH/axial CO minimum. Based on the isomerization rate constant argument presented in the supporting information, it is likely that *SR B* is in competition only with similar AHC configured structures, rendering the 12.5 kJ/mol into an effective 3.5 kJ/mol energy ranking, thus aiding in understanding why *SR B* is among the observed conformers. Indeed, the integrated intensity in the R2PI spectrum (Figure 3.5) suggests that this conformer has significant population.

According to the disconnectivity graph, the basins that make up the potential energy surface are clearly driven by the local conformation of the ACHC residue, with calculated isomerization barriers separating one chair form from the other of about 80 kJ/mol. In the analogous crystal structures, only one chair conformation is present (eq. NH/ax C=O in *RS* analogue and eq. C=O/ax NH in *SR* analogue) whereas both chair conformations are observed in this gas phase study. We hypothesize two possibilities, either that both conformations are present in the starting crystal structure of the samples studied in this work, which are not interconverted by the desorption process, or the desorption laser itself provides enough energy for isomerization from one chair to the other in the early stages of the expansion. Rice-Ramsperger-Kassel-Marcus (RRKM) rate constant calculations of isomerization between *RS* A and *RS* B performed at an average internal energy of 5900 cm⁻¹ (at an estimated laser desorption temperature of 300 K) reveals that the cooling rate is three orders of magnitude higher than the calculated isomerization rate. This isomerization pathway, presented in Figure 3.13, suggests that the conformers do not possess enough energy to isomerize from one chair conformation to the other during the desorption process.

Table 3.3. Relative energies, free energy corrections, and free energies for structures under 15 kJ/mol of the global energy minimum of *SR* calculated at the DFT M052X-6-31+G(d) level of

<u>Conformer</u>	<u>ACHC Configuration</u>	<u>ΔE (kJ/mol)</u>	<u>G correction (kJ/mol)</u>	<u>ΔG (kJ/mol)</u>
SR A	eq. CO/axial NH	0	0	0
min10.log:	eq. CO/axial NH	2.8	-1.1	1.7
min22.log:	eq. CO/axial NH	5.0	-5.3	-0.4
min4.log:	eq. NH/axial CO	8.9	-1.1	7.9
min458.log:	eq. CO/axial NH	10.2	-7.8	2.4
min374.log:	eq. NH/axial CO	11.9	-3.8	8.1
min215.log:	eq. CO/axial NH	12.2	-4.7	7.5
min271.log:	eq. CO/axial NH	12.3	-7.7	4.5
SR B	eq. NH/axial CO	12.5	-7.0	5.6
min778.log:	eq. CO/axial NH	14.0	-2.4	11.6
min23.log:	eq. CO/axial NH	14.3	-6.4	7.8
min580.log:	eq. CO/axial NH	14.7	-8.8	6.0

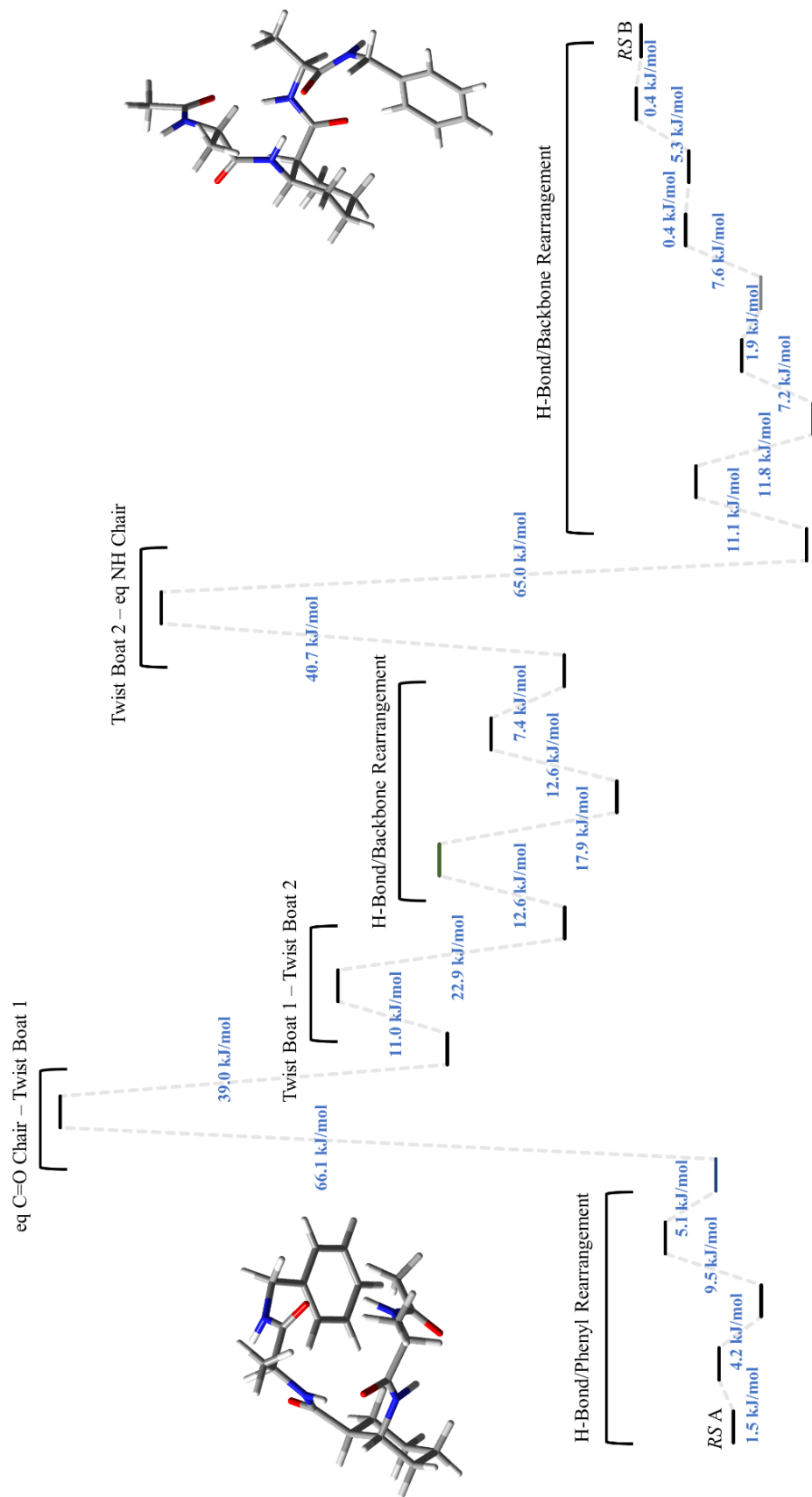


Figure 3.13. Isomerization pathway from *RS A* to *RS B* extracted from the disconnectivity diagram as calculated by the CHARMM22 force field.

The isomerization pathway presented in Figure 3.13 is characterized by six segments marked in the figure: (i) initial hydrogen bond breaking and phenyl ring rearrangement, (ii) the eq. C=O chair isomerizing into an initial twist boat (twist boat 1), (iii) dihedrals in the ACHC changing into the second twist boat (twist boat 2), (iv) hydrogen bond and backbone rearrangement, (v) twist boat 2 relaxing into eq. NH chair conformation, and (vi) further hydrogen bond and back bond rearrangement into the C11/C9 mixed helix of *RS* B. While the CHARM22 force field calculates the highest energy barrier at 66.1 kJ/mol associated with the initial chair to twist boat 1 transition, DFT QST3 transition state calculations determine the highest energy barrier to be 40.6 kJ/mol associated with the eq. NH chair to twist boat 2 transition (the high-energy transition going from *RS* B to *RS* A). To test the chair isomerization likelihood, we performed Rice-Ramsperger-Kassel-Marcus (RRKM) rate constant calculations over of the 40.6 kJ/mol barrier. At the average internal energy of the *RS* diastereomer at 300 K ($\langle E_{\text{vib}} \rangle = 71 \text{ kJ/mol} = 5900 \text{ cm}^{-1}$) the isomerization rate was calculated to be of order $k(\text{A} \rightarrow \text{B}) \approx 10^3 \text{ s}^{-1}$. This rate is much slower than the cooling rate ($\sim 10^6 \text{ s}^{-1}$), suggesting that unlike the analogous crystal structure of *RS*, the sample used in this experiment may exist in both ACHC conformations in the solid phase out of which laser desorption occurs, explaining the experimental presence of both ACHC conformations. This is a hypothesis that remains to be tested experimentally, since the crystal structures for *RS* and *SR* are not known.

3.5 Conclusion

This study has sought to determine the conformational preferences of a mixed α/β diastereomer pair of tripeptide foldamers in the gas phase. Conformation-specific IR and UV spectra recorded in a molecular beam demonstrated the presence of a total of five conformers. The comparison of these spectra with scaled harmonic vibrational frequencies and IR intensities led to a firm structural assignment for all five observed conformers. Formation of incipient C11/C9 helices is observed in each diastereomer, which, coupled with the crystal and solution phase helix in the *RS* analogue (with different caps),^{23, 24} suggests that the C11/C9 helix is a canonical helical structure. In *RS*, this structure is in energetic competition with a tightly-folded C7_{eq}/C12/C8/C7_{eq} conformer in which all amide groups are engaged in hydrogen bonding, as well as a cap influenced C7_{eq}/NH \cdots π /C11 structure.

The 11/9-mixed helix is also formed in the *SR* diastereomer. However, more generally, the conformational landscape for the *SR* diastereomer prefers formation of bifurcated hydrogen

bonded cycles, with the experimentally observed global minimum structure forming a Bif $C7_{ax}$ - $C11/NH\cdots\pi/C7_{eq}$ conformation. Analysis of the low energy structures of each diastereomer revealed that the dihedral pair of one Alanine residue in *SR* must reside in the non-allowed region of the Ramachandran diagram in forming each of the conformational minima, a requirement not found within *RS*. This backbone dihedral strain suggests that the *SR* diastereomer is inherently less stable than its *RS* counterpart, and indeed, the global minimum structure of the *SR* diastereomer is calculated to be 12 kJ/mol less stable than the *RS* global minimum. This argument is further strengthened by the fact that the *SR* diastereomer analogue forms no intramolecular hydrogen bonds in the crystal.²⁴

This diverse set of observed structures is perhaps not surprising, given the many degrees of freedom that these tripeptides possess, with two low-energy ACHC configurations and two flexible Ala residues. Indeed, as the disconnectivity graph indicates, the over-all shape of the conformational landscape is driven by the cyclically constrained ACHC residue. It would be interesting to test the gas phase 11/9 helicity of the analogous $\alpha\beta\alpha\beta\alpha$ *RS* pentamer analogue, as this would provide further evidence that this non-natural helical motif is a canonical helix available to foldamers comprised of alternating α/β residues.

It is our hope that the high-resolution, single conformation spectra presented herein may be of use to both the ab initio/DFT and classical mechanics computational communities. Refinement of both types of methods, making use of experimental data as benchmarks, would pave the way for accurate predictions of conformational minima of ever-larger molecules, coinciding with analogous experimental efforts towards the same goal. Additionally, we believe that the 2D-IR community may benefit from the spectral signatures of model foldamers in their effort to interpret increasingly complex spectra.

3.6 References

1. G. Guichard and I. Huc, *Chem. Commun.*, 2011, **47**, 5933-5941.
2. S. H. Gellman, *Acc. Chem. Res.*, 1998, **31**, 173-180.
3. K. Kirshenbaum, R. N. Zuckermann and K. A. Dill, *Curr. Opin. Struct. Biol.*, 1999, **9**, 530-535.
4. W. S. Horne and S. H. Gellman, *Acc. Chem. Res.*, 2008, **41**, 1399-1408.

5. L. M. Johnson and S. H. Gellman, in *Methods Enzymol.*, ed. A. E. Keating, Academic Press, 2013, vol. 523, pp. 407-429.
6. Y. Hamuro, J. P. Schneider and W. F. DeGrado, *J. Am. Chem. Soc.*, 1999, **121**, 12200-12201.
7. M. Werder, H. Hauser, S. Abele and D. Seebach, *Helv. Chim. Acta*, 1999, **82**, 1774-1783.
8. J. R. Gord, P. S. Walsh, B. F. Fisher, S. H. Gellman and T. S. Zwier, *J. Phys. Chem. B*, 2014, **118**, 8246-8256.
9. S. H. Choi, *Biomed. Eng. Lett.*, 2013, **3**, 226-231.
10. M. Crisma, F. Formaggio, A. Moretto and C. Toniolo, *Pept. Sci.*, 2006, **84**, 3-12.
11. R. P. Cheng, S. H. Gellman and W. F. DeGrado, *Chem. Rev.*, 2001, **101**, 3219-3232.
12. D. Seebach, D. F. Hook and A. Glättli, *Pept. Sci.*, 2006, **84**, 23-37.
13. D. Seebach and J. Gardiner, *Acc. Chem. Res.*, 2008, **41**, 1366-1375.
14. E. E. Baquero, W. H. James, S. H. Choi, S. H. Gellman and T. S. Zwier, *J. Am. Chem. Soc.*, 2008, **130**, 4784-4794.
15. J. C. Dean, E. G. Buchanan and T. S. Zwier, *J. Am. Chem. Soc.*, 2012, **134**, 17186-17201.
16. W. H. James, E. E. Baquero, S. H. Choi, S. H. Gellman and T. S. Zwier, *J. Phys. Chem. A*, 2010, **114**, 1581-1591.
17. W. H. James, E. E. Baquero, V. A. Shubert, S. H. Choi, S. H. Gellman and T. S. Zwier, *J. Am. Chem. Soc.*, 2009, **131**, 6574-6590.
18. W. H. James, E. G. Buchanan, L. Guo, S. H. Gellman and T. S. Zwier, *J. Phys. Chem. A*, 2011, **115**, 11960-11970.
19. W. H. James, E. G. Buchanan, C. W. Müller, J. C. Dean, D. Kosenkov, L. V. Slipchenko, L. Guo, A. G. Reidenbach, S. H. Gellman and T. S. Zwier, *J. Phys. Chem. A*, 2011, **115**, 13783-13798.
20. R. Kusaka, D. Zhang, P. S. Walsh, J. R. Gord, B. F. Fisher, S. H. Gellman and T. S. Zwier, *J. Phys. Chem. A*, 2013, **117**, 10847-10862.
21. P. S. Walsh, K. N. Blodgett, C. McBurney, S. H. Gellman and T. S. Zwier, *Angew. Chem. Int. Ed.*, 2016, **55**, 14618-14622.
22. P. S. Walsh, R. Kusaka, E. G. Buchanan, W. H. James, B. F. Fisher, S. H. Gellman and T. S. Zwier, *J. Phys. Chem. A*, 2013, **117**, 12350-12362.

23. M. Lee, J. Shim, P. Kang, I. A. Guzei and S. H. Choi, *Angew. Chem.*, 2013, **125**, 12796-12799.
24. G. Jang, M. Lee, J. Lee, J. Shim, P. Kang, M. G. Choi and S. H. Choi, *Bull. Korean Chem. Soc.*, 2018, **39**, 244-249.
25. C. Baldauf, R. Günther and H.-J. Hofmann, *Angew. Chem. Int. Ed.*, 2004, **43**, 1594-1597.
26. T. S. Zwier, *Annu. Rev. Phys. Chem.*, 1996, **47**, 205-241.
27. J. C. Dean, R. Kusaka, P. S. Walsh, F. Allais and T. S. Zwier, *J. Am. Chem. Soc.*, 2014, **136**, 14780-14795.
28. D. M. Lubman, *Mass Spectrom. Rev.*, 1988, **7**, 559-592.
29. D. H. Levy, *Annu. Rev. Phys. Chem.*, 1980, **31**, 197-225.
30. M. D. Morse, *Experimental methods in the physical sciences*, 1996, **29**, 21-47.
31. A. D. MacKerell Jr, D. Bashford, M. Bellott, R. L. Dunbrack Jr, J. D. Evanseck, M. J. Field, S. Fischer, J. Gao, H. Guo and S. Ha, *J. Phys. Chem. B*, 1998, **102**, 3586-3616.
32. X. Zhu, P. Koenig, S. H. Gellman, A. Yethiraj and Q. Cui, *J. Phys. Chem. B*, 2008, **112**, 5439-5448.
33. K. Deb and D. Kalyanmoy, *Multi-Objective Optimization Using Evolutionary Algorithms*, John Wiley & Sons, Inc., 2001.
34. D. Zhang, K. N. Blodgett, X. Zhu and T. S. Zwier, *J. Phys. Chem. A*, 2017, **121**, 986-997.
35. V. A. Shubert, E. E. Baquero, J. R. Clarkson, W. H. James III, J. A. Turk, A. A. Hare, K. Worrel, M. A. Lipton, D. P. Schofield and K. D. Jordan, *J. Chem. Phys.*, 2007, **127**, 234315.
36. D. J. Wales and J. P. Doye, *J. Phys. Chem. A*, 1997, **101**, 5111-5116.
37. D. J. Wales, *University of Cambridge*.
38. S. A. Trygubenko and D. J. Wales, *J. Chem. Phys.*, 2004, **120**, 2082-2094.
39. D. C. Liu and J. Nocedal, *Mathematical Programming*, 1989, **45**, 503-528.
40. P. K. Weiner and P. A. Kollman, *J. Comput. Chem.*, 1981, **2**, 287-303.
41. F. Mohamadi, N. G. Richards, W. C. Guida, R. Liskamp, M. Lipton, C. Caufield, G. Chang, T. Hendrickson and W. C. Still, *J. Comput. Chem.*, 1990, **11**, 440-467.
42. M. J. T. Frisch, G.W.; Schlegel, H.B.; Scuseria, G.E.; Robb, M.A.; Cheeseman, J.R.; Scalmani, G.; Barone, V.; Mennucci, B.; Petersson, G.A.; et al., Gaussian, Inc.: Wallingford, CT, 2010.

43. Y. Zhao and D. G. Truhlar, *J. Chem. Theor. Comp.*, 2007, **3**, 289-300.
44. B. C. Dian, J. R. Clarkson and T. S. Zwier, *Science*, 2004, **303**, 1169-1173.
45. B. C. Dian, A. Longarte, P. R. Winter and T. S. Zwier, *J. Chem. Phys.*, 2004, **120**, 133-147.
46. B. C. Dian, A. Longarte and T. S. Zwier, *Science*, 2002, **296**, 2369-2373.
47. W. Chin, F. PiuZZi, I. Dimicoli and M. Mons, *PCCP*, 2006, **8**, 1033-1048.
48. J. R. Gord, D. M. Hewett, A. O. Hernandez-Castillo, K. N. Blodgett, M. C. Rotondaro, A. Varuolo, M. A. Kubasik and T. S. Zwier, *PCCP*, 2016, **18**, 25512-25527.
49. M. Elstner, K. J. Jalkanen, M. Knapp-Mohammady, T. Frauenheim and S. Suhai, *Chem. Phys.*, 2001, **263**, 203-219.
50. R. J. Lavrich, D. F. Plusquellic, R. D. Suenram, G. T. Fraser, A. R. H. Walker and M. J. Tubergen, *J. Chem. Phys.*, 2003, **118**, 1253-1265.
51. C. Baldauf, R. Günther and H.-J. Hofmann, *Pept. Sci.*, 2006, **84**, 408-413.
52. N. Leventis, S. B. Hanna and C. Sotiriou-Leventis, *J. Chem. Educ.*, 1997, **74**, 813.
53. C. J. Tainter and J. L. Skinner, *J. Chem. Phys.*, 2012, **137**, 104304.
54. J. Yang, L. A. Christianson and S. H. Gellman, *Org. Lett.*, 1999, **1**, 11-14.
55. D. H. Williams, E. Stephens, D. P. O'Brien and M. Zhou, *Angew. Chem. Int. Ed.*, 2004, **43**, 6596-6616.
56. M. Tsai, Y. Xu and J. J. Dannenberg, *J. Phys. Chem. B*, 2009, **113**, 309-318.
57. C. R. Maechling, S. J. Clemett, F. Engelke and R. N. Zare, *J. Chem. Phys.*, 1996, **104**, 8768-8776.
58. M. Handschuh, S. Nettesheim and R. Zenobi, *J. Chem. Phys.*, 1997, **107**, 2603-2610.

CHAPTER 4. COEXISTENCE OF LEFT- AND RIGHT-HANDED 12/10 MIXED HELICES IN CYCLICALLY CONSTRAINED β -PEPTIDES AND DIRECTED FORMATION OF SINGLE-HANDED HELICES UPON SITE-SPECIFIC METHYLATION

4.1 Introduction

The secondary structures adopted by peptides result from a delicate balance of intermolecular and intramolecular interactions, including hydrogen bonding and amino acid-specific steric effects. Among natural proteins, which are composed entirely of L- α -amino acid residues, the most common secondary structure is the helix, and the most common helices are the α -helix (3.6₁₃-helix) and the 3₁₀-helix.¹⁻³ Due to their enantiomerically pure amino acid composition, natural peptides preferentially adopt either left- or right-handed helices, which are chiral with respect to one another.⁴ Peptide sequences composed of achiral residues, however, have access to both left- and right-handed helical conformations, which may rapidly interconvert with one another in solution.⁵⁻⁷ The helical screw-sense of such peptides has been shown to be controllable by environmental factors such as temperature and interaction with chiral molecules. Several research groups are devoting effort to leveraging the environment-dependent helical screw-sense of these molecules towards stimuli-responsive applications such as molecular recognition and catalysis.^{4, 8-11}

Since the first systematic studies of β -peptide helices by Gellman and Seebach, several helical structures not accessible to pure α -peptides have been identified, including the 12/10-, 10-, 8-, and 14-helices, where the number designates the number of atoms in the macrocycles enclosed by an NH \cdots O=C H-bond.¹²⁻¹⁶ Such synthetic foldamers have been shown to have diverse properties such as cholesteryl ester uptake inhibition, antimicrobial action, and the projection of carbohydrates into specific three-dimensional patterns.¹⁷⁻²¹ In the last decade, the chiral β -amino acid, *cis*-2-aminocyclohexanecarboxylic acid (ACHC), shown in Figure 4.1, has received much attention as a foldamer building block.^{1, 6, 7, 15, 22-26} The cyclically constrained nature of its 6-membered ring demands that the ACHC residue adopt one of two energetically stable chair conformations: one in which the NH group is equatorial (eq) and the carbonyl group is axial (ax), or *vice versa*.

Temperature-dependent $^1\text{H-NMR}$ data from Shin *et. al.*, and Jang *et. al.*, showed that tetramer and pentamer oligomers composed of alternating enantiomers of ACHC units result in an equilibrium of left- and right-handed 12/10-mixed helices in chloroform, with left:right ratios of 2:1 and 4:1, respectively.^{6,7} The 12/10 mixed helix, shown in Figure 4.2, is comprised of hydrogen bonds oriented in alternating directions, $\text{N} \rightarrow \text{C}$ terminal, and $\text{C} \rightarrow \text{N}$ terminal. The antiparallel alignment of hydrogen bonds along the helical axis results in a small net dipole moment relative to the macrodipoles acquired by the ubiquitous α - and 3_{10} -helices in α -peptides. Such mixed-helices are common in β -, γ -, α/β -, α/γ -peptides, but are quite rare in naturally occurring proteins.²⁷

28

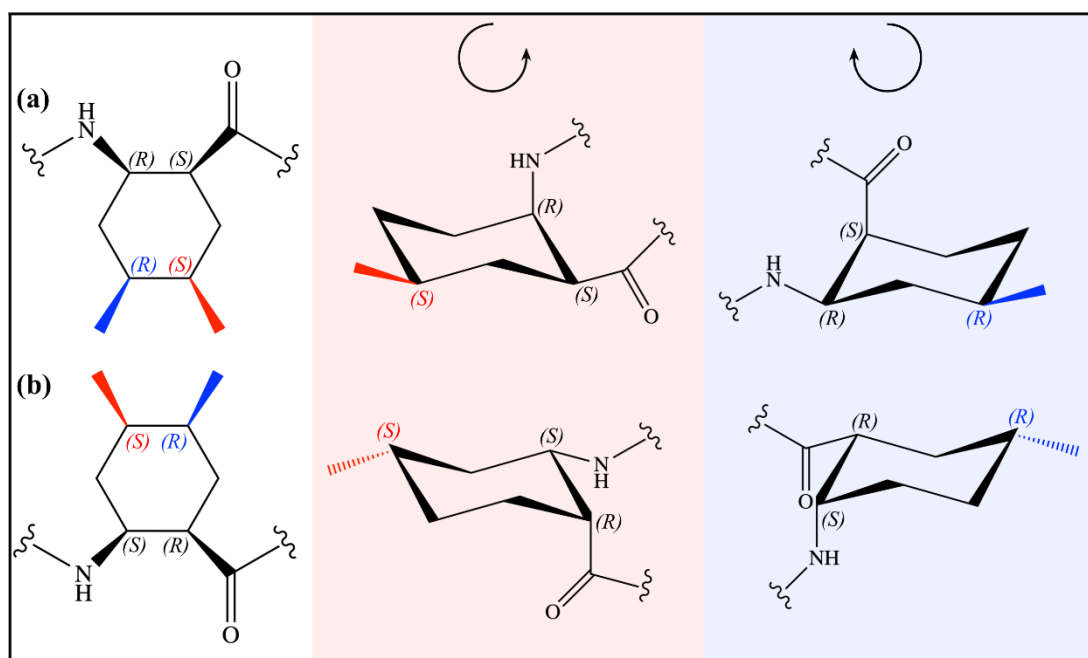


Figure 4.1. (a) *RS* and (b) *SR* *cis*-2-aminocyclohexanecarboxylic acid (ACHC) monomers used as the foldamer building blocks of the molecules studied in this work. Stereo- and site-specific methylation along the cyclohexane backbone of each species drives the local conformation of the ACHC residue into a chair conformation in which the methyl group is in the energetically favored equatorial position. These steric constraints serve to orient the peptide backbone into either a left- or right-handed conformation. Note that each non-methylated ACHC enantiomer may adopt either chair conformation.

That the ACHC oligomer demonstrates reversible helical handedness in solution despite being composed of chiral residues is a remarkable fact that may be understood by viewing each oligomer as being composed, not of alternating chiral ACHC residues, but of repeating “pseudo-symmetric” achiral dimer units, composed of two ACHC residues of opposite chirality (*RS* and *SR*). The cyclohexane ring flip of both ACHC residues in one such dimer unit results in a left-handed (right-handed) motif inverting to its right-handed (left-handed) counterpart, where each dimer may be thought of as achiral. Similarly, the cooperative cyclohexane ring flip of all ACHC moieties along a peptide backbone, where all chair conformations are inverted, results in the unwinding of the helix from one screw sense while re-forming the other screw sense, i.e., from left \rightarrow right, or right \rightarrow left-handed helices.

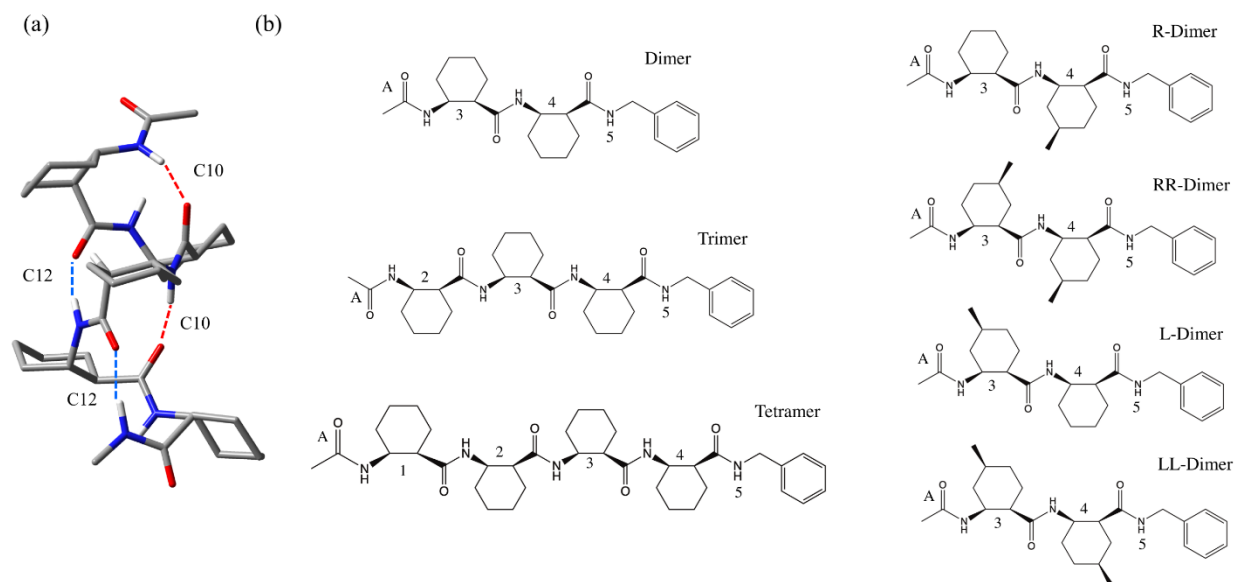


Figure 4.2. (a) The Ac-(ACHC)₅-NHMe molecule in the right-handed 12/10 mixed-helical conformation with intramolecular hydrogen bonds labelled and color-coded as red (N \rightarrow C terminal) or blue (C \rightarrow N terminal). Structure taken from Shin *et al.* (ref. 6) (b) Chemical structures of the seven molecules studied in this work. Each residue is labelled, including the C-terminal NHBn cap (residue 5), and the N-terminal Acyl cap (residue A), such that the shared C-terminal motif composed of residues 3,4 and 5 may be referred to in a coherent manner across all molecular species.

The conformations that isolated molecules adopt are free from perturbative solvent and intermolecular interactions present in solution and crystal environments. As a result, the constituent-specific intramolecular interactions and steric effects act in an unencumbered fashion

to drive conformational preferences. Laser spectroscopy of isolated, expansion-cooled molecules enables the study of these inherent conformational preferences at a spectral resolution sufficient for recording single-conformation spectra. In this chapter, we study the conformational preferences inherent to a series of neutral ACHC-containing β -peptides, Ac-(ACHC)_n-NHBn, n=2,3,4, using IR-UV double-resonance spectroscopy in conjunction with supersonic cooling in the gas phase. The structures of the three molecules that make up this fundamental series are shown in the middle of Figure 4.2.

Additionally, we investigate the effect that substitution of a methyl group at selected positions on the cyclohexane ring has on driving a particular helical screw-sense at the dipeptide level. As shown in Figure 4.1, orientation of the ACHC residue by methyl substitution in the energetically and sterically favored equatorial position predisposes the peptide backbone toward either left- or right-handed helical formation. Choi and coworkers have shown that incorporation of a specific methylated residue at every other ACHC unit in the tetramer or pentamer efficiently locks in a particular helical screw-sense in solution.^{6,7} Herein, we investigate the conformational effect that one or two such residues have on driving conformational preferences toward a particular handed helix. The structures of these substituted dipeptides are shown in the right column of Figure 4.2.

As we will see, the conformations of the seven molecules shown in Figure 4.2 fall into just two unique helical secondary structures, implying that the ACHC residue effectively organizes itself and the peptide backbone into its preferred structure at the dipeptide level, where additional residues build on and extend the existing structural motif.

4.2 Methods

4.2.1 Experimental Methods

Samples were synthesized by the Choi research group at Yonsei University. The experimental procedure for recording single-conformer spectra has been described in detail in Chapter 2, and will be outlined briefly here. The solid-state samples were brought into the gas-phase by non-resonant laser desorption from a graphite rod. Resonant two-photon ionization (R2PI) was used to record the non-conformer-specific UV excitation spectra for all molecules. The frequency-doubled 20 Hz output of a tunable dye laser (Radiant Dyes, NarrowScan), pumped by

the third harmonic of a Q-switched Nd:YAG laser (Continuum Surelite II) was scanned across the S_0 - S_1 origin region ($37,000$ - $37,800\text{ cm}^{-1}$) of the NHBn chromophore. Mass-selected ion signal at the molecular ion mass was plotted against excitation wavelength to generate the one-color R2PI spectrum.

Conformation-specific IR spectra were recorded in the hydride stretch (3200 - 3500 cm^{-1} , 12 - 15 mJ/pulse) and amide I/II (1400 - 1800 cm^{-1} , 500 - $1,000\text{ }\mu\text{J/pulse}$) regions using resonant ion-dip infrared (RIDIR) spectroscopy.²⁹ The 10 Hz output of a Q-switched Nd:YAG pumped KTP/KTA-based IR optical parametric converter (LaserVision) temporally precedes by 100 ns , and spatially overlaps with, the UV laser, which has its wavelength fixed on some vibronic transition unique to one conformer in the molecular beam. A gated integrator (Stanford Research) acting in active baseline subtraction mode captures the 20 Hz ion signal generated by the UV laser. When the IR laser is resonant with a vibrational transition of the same conformer being monitored by the UV laser, ground state population of that conformer is removed, resulting in a subsequent dip in the UV-generated ion signal. This difference signal is output from the gated integrator and plotted as a function of IR frequency. IR radiation in the amide I/II regions was generated by difference frequency mixing the signal and idler output of the optical parametric converter in a AgGaSe₂ crystal.

With R2PI and RIDIR spectra in hand, the non-conformer-specific R2PI spectrum may be decomposed into its component parts using IR-UV holeburning (HB) spectroscopy. This scheme is identical to RIDIR spectroscopy, except that now the IR wavelength is fixed on some conformer-specific vibrational transition while the UV laser is scanned across the S_0 - S_1 absorption region. Fractional ion signal depletion is plotted as a function of UV wavelength, resulting in single-conformation UV spectrum.

4.2.2 Computational Methods

The conformational landscapes of the molecules studied herein were initially explored within the MACROMODEL suite of programs using a torsional-sampling Monte Carlo Multiple Minimum algorithm in conjunction with the OPLS3 and Amber* force fields.³⁰ Exhaustive searches were performed with each force field such that additional searching yielded no new structures. Redundant conformer elimination performed on the group of structures from both

OPLS3 and Amber* force fields calculated to lie within 50 kJ/mol of their respective global minimum generated starting structures for further DFT optimization.

Density functional theory within the Gaussian16 computational package was used to perform geometry optimizations and normal mode frequency calculations on each candidate structure.³¹ The Becke 3LYP hybrid functional was used in conjunction with Grimme's dispersion correction³² (version D3), Becke-Johnson damping³³, and the 6-31+G(d) Pople basis set. An ultrafine grid and tight convergence were used to ensure reliable normal mode frequencies to be compared with experimental values. Scale factors of 0.958, 0.982, and 0.970 were used in the hydride stretch, amide I, and amide II regions to correct for anharmonicity of the calculated harmonic normal modes.

4.2.3 Nomenclature

The named molecules studied in this work are shown in Figure 4.2. The Dimer, Trimer, and Tetramer are so named because they are composed of two, three, and four ACHC residues. The four additional dimers include either L (Left) or R (Right) in front of their name. These represent the helical screw sense in which they have been engineered to turn (see Figure 4.1). As can be seen, the dimers with one methylated ACHC ring use a single letter (R or L) to specify them, while those dipeptides with both ACHC groups methylated are named RR or LL. A 'Cn' notation is used to describe hydrogen bonded cycles, where *n* represents the number of atoms involved in the ring closed by an NH...O=C H-bond. π H-bonds are labeled " π ", and NH groups not involved in H-bonding are labelled "F" for Free. Our labeling scheme describes the interaction of each amide NH group along the peptide backbone, going from the N to the C terminus. Additionally, each residue is labelled, including the C-terminal NHBn cap (labelled residue 5), and the N-terminal Acyl cap (labelled residue A), such that the C-terminal motif composed of residues 3,4 and 5, which is common among all molecules studied here, may be referred to in a coherent manner across all molecular species. In the assigned 2D and 3D structures, blue dashed lines represent C \rightarrow N-terminal, (NH \rightarrow O=C) directed hydrogen bonds, while red dashed lines represent N \rightarrow C-terminal directed hydrogen bonding. Backbone dihedral angles ϕ , θ , and ψ are defined in the conventional manner.

4.3 Results and Analysis

4.3.1 Dimer, R-Dimer, and RR-Dimer

R2PI and IR-UV HB Spectroscopy

R2PI and IR-UV HB spectra for the dimer are shown in Figure 4.3a. The IR-UV HB spectrum recorded with the IR HB laser fixed at $37,288\text{ cm}^{-1}$ shows that most of the peaks in the R2PI spectrum belong to one major conformer. The remaining peaks, marked with red daggers, likely belong to some minor conformer in the jet with a small population. Insufficient signal prohibited further investigation of this minor conformer. The major conformer has its S_0 - S_1 origin transition at $37,288\text{ cm}^{-1}$, with Franck-Condon progressions up to $v=3$ in a 54 cm^{-1} mode, and $v=1$ in a 27 cm^{-1} mode. According to the calculated vibrational frequencies of the assigned structure (see next section), these low-frequency modes correspond to the absorbing phenyl ring rocking against NH[4] and ACHC[3]. Additionally, the members of the 54 cm^{-1} mode progression have a 5 cm^{-1} transition built off them. These peaks are likely sequence bands of the same mode originating from $v=1$ in the ground state, whose corresponding S_1 frequency is 5 cm^{-1} larger. Sequence bands such as these are common among laser-desorbed species due to incomplete cooling to their zero-point vibrational level.³⁴⁻³⁶

The R- and RR-dimer have nearly identical UV and IR spectra to the dimer. Their S_0 - S_1 origin transitions are shifted down by 1 and 3 cm^{-1} , respectively, from that of the dimer. Even smaller shifts are found in their recorded IR spectra. Therefore, the UV and IR spectra of the R- and RR-dimer will not be discussed in detail. One important difference, however, is that the UV spectra of both the R- and RR-dimer are composed entirely of transitions from one conformer, whereas the dimer contains small contributions from a second minor conformer. This point will be returned to in section 4.3.2.

RIDIR Spectroscopy

Figure 3b and **3c** present the RIDIR spectra of the major conformer of the dimer in the NH and amide I/II regions, respectively. In anticipation of observing 12/10 mixed-helices, we should be on the lookout for their characteristic spectral features. The structure of the 12/10-helix in **Figure 2a** shows two free NH groups, which are in positions such that the addition of one ACHC

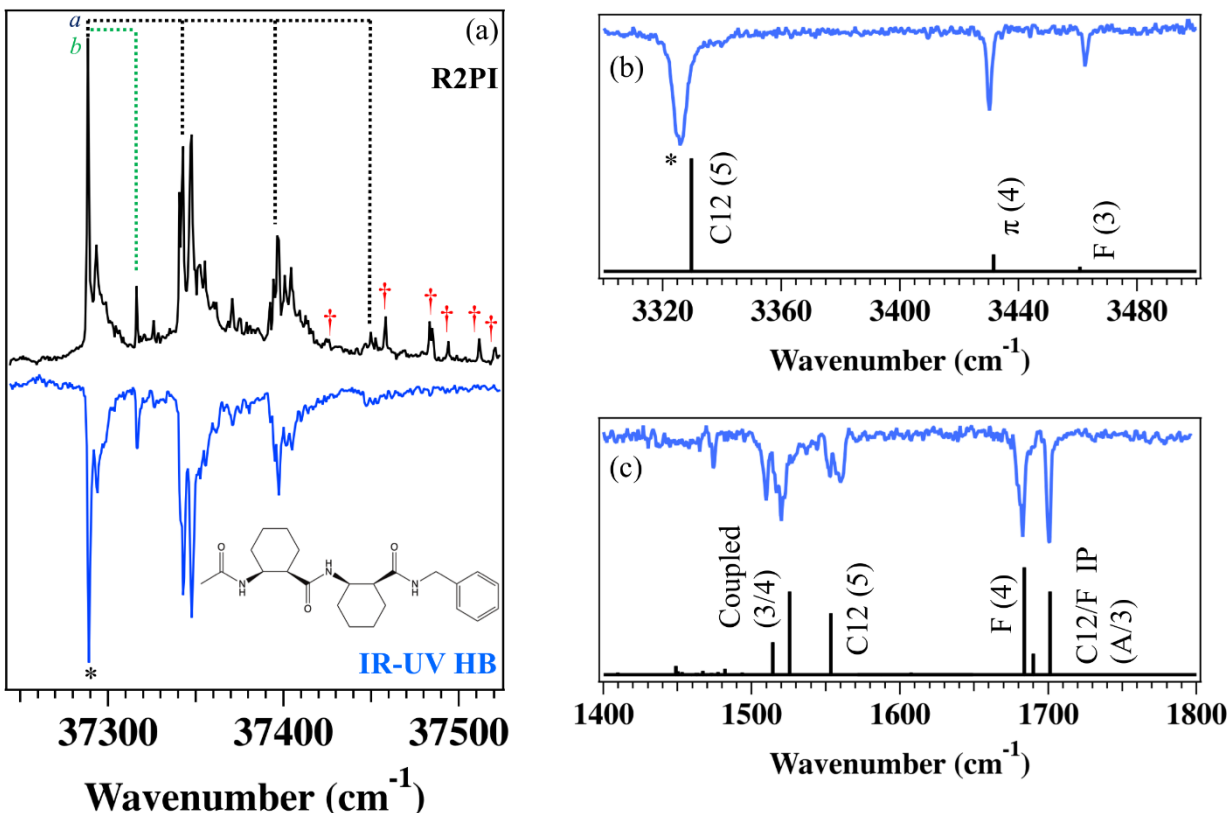


Figure 4.3. (a) R2PI and IR-UV HB spectra in the S_0 - S_1 region of the dimer. Franck-Condon progressions marked with *a* and *b* correspond to low-frequency modes of 54 and 27 cm^{-1} , respectively. Red daggers mark peaks belonging to a conformation with minor population in the expansion while peaks marked with an asterisk were used to collect holeburn spectra. (b) and (c): RIDIR spectra of the dimer in the hydride stretch and amide I/II regions, respectively. Stick spectra below each experimental trace represent the scaled, harmonic normal mode frequencies of the assigned conformation. These vibrational transitions, calculated at the B3LYP-D3BJ/6-31+G(d) level of theory, are labeled with the main carrier(s) of the vibration.

residue on the N- and C-terminus of the helix would result in new C12 and C10 H-bonds, respectively, that grow the helix in either direction. One would anticipate, then, as a signature of the 12/10-helix, two free NH stretch transitions in the IR spectrum, with the remainder of transitions resulting from NH groups involved in C10 and C12 H-bonds. The C-terminal NHBn cap with which our molecules have been modified, however, can interfere with the repeating helical pattern.

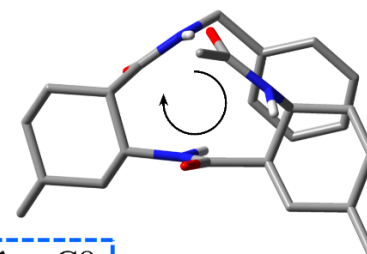
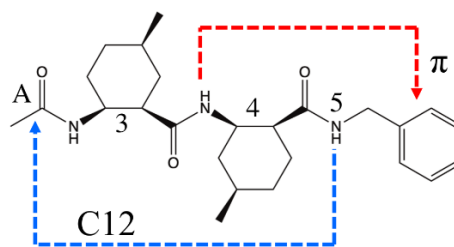
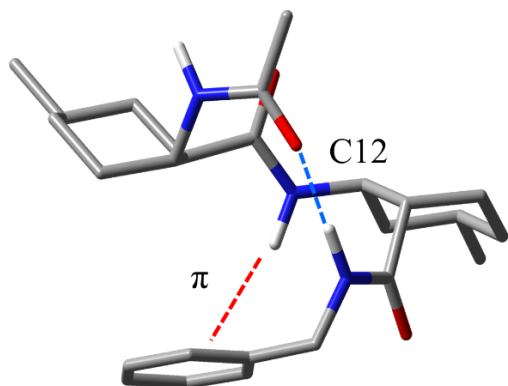
There are many previous examples of $\text{NH}\cdots\pi$ interactions in the conformational makeup of aromatic ring-containing molecules in the gas phase.^{24, 34, 35, 37, 38} Calculations suggest that the right-handed 12/10-helix will have one free NH near the N-terminus, and the $\text{NH}[4]$ involved in

dispersive interactions with the π -cloud of the phenyl ring. The left-handed 12/10-helix, on the other hand, is expected to take up a configuration in which dispersive interactions with the π -cloud are not possible, resulting in two free NH groups, one on either end of the helix. Calculations suggest, however, that this helical purity may be disrupted by forming the NH[5] \cdots O=C[3] C8 and NH[3] $\cdots\pi$ interactions rather than the NH[3] \cdots O=C[4] C10 H-bond of the ‘pure’ left-handed helix. We keep these considerations in mind as we analyze the following spectra.

As mentioned in the previous section, the spectra of the dimer are nearly identical with those of the R- and RR-dimer. In discussing one, then, we discuss them all. The dimer shows two high-frequency NH stretch transitions at 3462 and 3430 cm^{-1} , and an intense, broadened transition at 3326 cm^{-1} . The weak, highest frequency band shows up where one would expect a free NH stretch to appear, while the 3430 cm^{-1} band is consistent with formation of an NH $\cdots\pi$ bond with the aromatic ring.^{1, 24, 37} Evidence for this NH $\cdots\pi$ interaction is provided by the low-frequency Franck-Condon activity in the UV spectra of this triad of molecules. Red-shifted, broadened, intense infrared bands are generally understood to arise from NH groups involved in strong hydrogen bonding interactions. Based on the hydride stretch spectra alone one would anticipate a structure with one free, one π -interacting, and one strongly hydrogen bonded NH, which based on the considerations discussed above, we tentatively assign to an emergent form of the right-handed 12/10-helix.

The calculated spectra, shown as black sticks in Figure 4.3, capture both the relative intensity and frequency of all recorded IR transitions to a remarkable degree. The structure corresponding to the stick spectra, as well as a 2D sketch of the hydrogen bonding pattern, is shown in **Figure 4a**. This conformer was calculated to be the global minimum by DFT B3LYP-D3BJ/6-31+G(d) calculations for the R-dimer, RR-dimer and dimer. From the assigned structure we can see that NH[3] is free, NH[4] is interacting with the π -cloud of the phenyl cap, and NH[5] is in a C12 hydrogen bond with C=O[A], resulting in the inception of a right-handed 12/10-helix which is just long enough to make 1 full helical turn. The exact structure shown in **Figure 4a** is that of the RR-dimer, where one can see that the methyl groups on either ACHC ring are in the energetically favorable equatorial position, thereby sterically-locking in the right-handed helical structure.

(a) **f/ π /C12** 0.00 kJ/mol



(b) **π /C8/C8** 0.00 kJ/mol

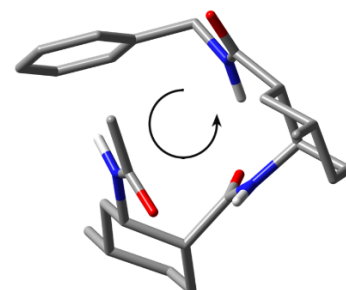
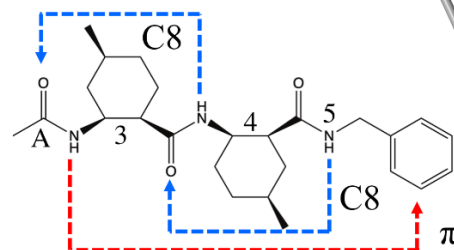
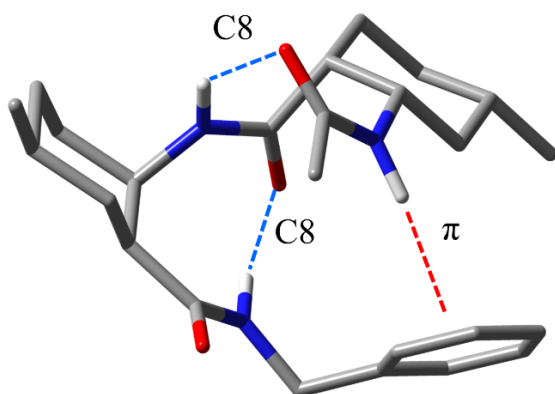


Figure 4.4. Assigned structures and relative zero-point-corrected potential energies of (a) the dimer, R-dimer, and RR-dimer, and (b) the L-dimer and LL-dimer. In each case, the doubly methylated dipeptide is used to illustrate the steric control by which the methyl residues dictate local ACHC conformation. 2D hydrogen-bonding schematics are presented for each molecule, along with a down-axis view from N \rightarrow C terminus, highlighting the preferred screw-sense of each dipeptide.

The amide I data from 1600 - 1800 cm^{-1} in Figure 4.3c report on the C=O stretch vibrations, which generally shift to lower frequency upon accepting strong H-bonds. The amide II region from 1400 - 1600 cm^{-1} is associated with the NH bend fundamentals, which generally shift up in frequency when in a strong hydrogen bonds. However, due to the high degree of local-mode coupling, the amide II region is generally more difficult to interpret without the aid of calculations. The amide I data show a symmetric band at 1701 cm^{-1} and a band with a high-frequency shoulder at 1683 cm^{-1} . According to calculations, the high-frequency band and the small shoulder belong to the in-phase and out-of-phase coupled stretches of the C=O[A] and [3] oscillators. The out-of-phase stretch has such a small intensity because the two C=O groups are oriented nearly antiparallel to one another, resulting in a small net change in dipole with respect to the coupled, out-of-phase stretch. The lowest frequency amide I band (1683 cm^{-1}) corresponds to the free C=O[4] stretch. The low frequency of this free C=O group may be understood by the fact that the NH on the same amide group is involved in the strong C12 H-bond, a scenario which is known to shift C=O stretch fundamentals to lower frequency.^{36, 39}

The amide II data shows a split, high frequency transition centered at 1557 cm^{-1} . The calculations predict that this transition is associated with the bend fundamental of NH[5], which is acting as donor in the C12 hydrogen bond. This band is likely split due to a 2:1 Fermi resonance with a mode with near half the frequency of the bend fundamental. Indeed, the calculated vibrations show several modes centered around this frequency, all of which include substantial wagging of NH[5]. It is interesting to note that in neither the R- or RR-dimer is this 1557 cm^{-1} band split. This is likely due to the change in reduced mass shifting the overtone of the lower frequency vibration out of Fermi-resonance with this band. The two lower-frequency amide II transitions shown in Figure 4.3c correspond to the coupled NH[3,4] bend fundamentals. Given the right-handed 12/10-helicity of the dimer, its IR spectra will be used as a reference to compare with other structures in what follows.

Figure 4.5a displays an energy level diagram for the dipeptides studied in this work. The horizontal lines represent the zero-point corrected energies for all structures calculated to lie within 25 kJ/mol of the global minimum. Lines are further color-coded to indicate the structural family to which each conformer belongs (Red (left-handed helix), Blue (right-handed helix), Green (turned structures)), while the bold lines indicate the experimentally observed conformers. Note that each dipeptide contains all three structural families within 25 kJ/mol. We will return to this

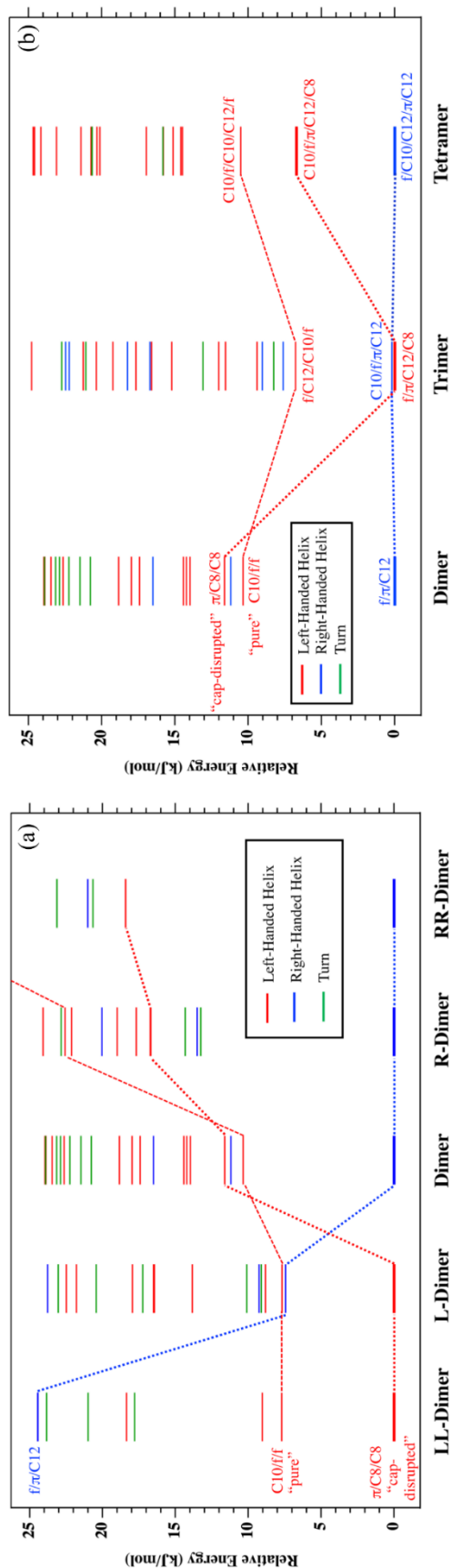


Figure 4.5. Energy level diagrams for (a) the set of methylated dipeptides and (b) the series Ac-(ACHC)_n-NHBn with n=2,3,4. Each conformational minima has its relative zero-point-corrected energy (B3LYP-D3BJ/6-31+G(d)) plotted as a horizontal bar and color-coded to represent left-handed (red), right-handed (blue), or general turned (green) structures. Experimentally assigned conformers are represented with a heavy horizontal bar. The “pure” right- and left-handed helices as well as the cap-disrupted helical structures are labelled and connected via dotted lines to their corresponding structures across the molecules.

energy level diagram in the discussion. For now, we observe the 10.4 kJ/mol energy gap between the assigned global minimum right-handed helical structure of the dimer and the next lowest energy structure, which is an incipient form of the left-handed 12/10-helix.

4.3.2 L-Dimer and LL-Dimer

R2PI and IR-UV HB Spectroscopy

The R2PI and IR-UV HB spectra of the LL-dimer are shown in Figure 4.6a. The IR-UV HB spectrum indicates that all of the peaks in the R2PI spectrum are due to one conformer, which is a point of departure from the non-methylated dimer. The sole conformer of the LL-dimer has its S_0 - S_1 origin transition at $37,423\text{ cm}^{-1}$, with Franck-Condon progressions up to $v=4$ in 27 and 32 cm^{-1} modes. The presence of combination bands involving these modes results in the increasing density of bands at higher frequencies. According to the calculated vibrational frequencies of the assigned structure (see next section), these modes correspond to the aromatic ring rocking against the NH[3] and ACHC[3] ring. The weak band red-shifted by -20 cm^{-1} from the origin is likely a hot band originating from a $v=1$ populated level in the ground state and terminating in the zero-point level in S_1 .

The L- and LL-dimer share nearly identical UV and IR spectra with one another. The UV spectrum of the L-dimer has its S_1 origin transition shifted 4 cm^{-1} higher in frequency to $37,427\text{ cm}^{-1}$, and displays the same Franck-Condon activity and intensity pattern as the LL-dimer. Given the similarity of the spectra, we do not discuss the L-dimer in detail. The $\pi\pi^*$ origin transition of the LL-dimer is shifted by about 135 cm^{-1} to higher frequency than that of the RR-dimer, suggesting that the phenyl groups are in different environments between the two structures. The minor peaks that did not burn out with the major conformer in the IR-UV HB spectrum of the non-methylated dimer appear at the same frequencies as the UV transitions of the LL-dimer. This suggests that the minor conformation of the dimer is the same as that of the LL-dimer. We will return to this point in the next section.

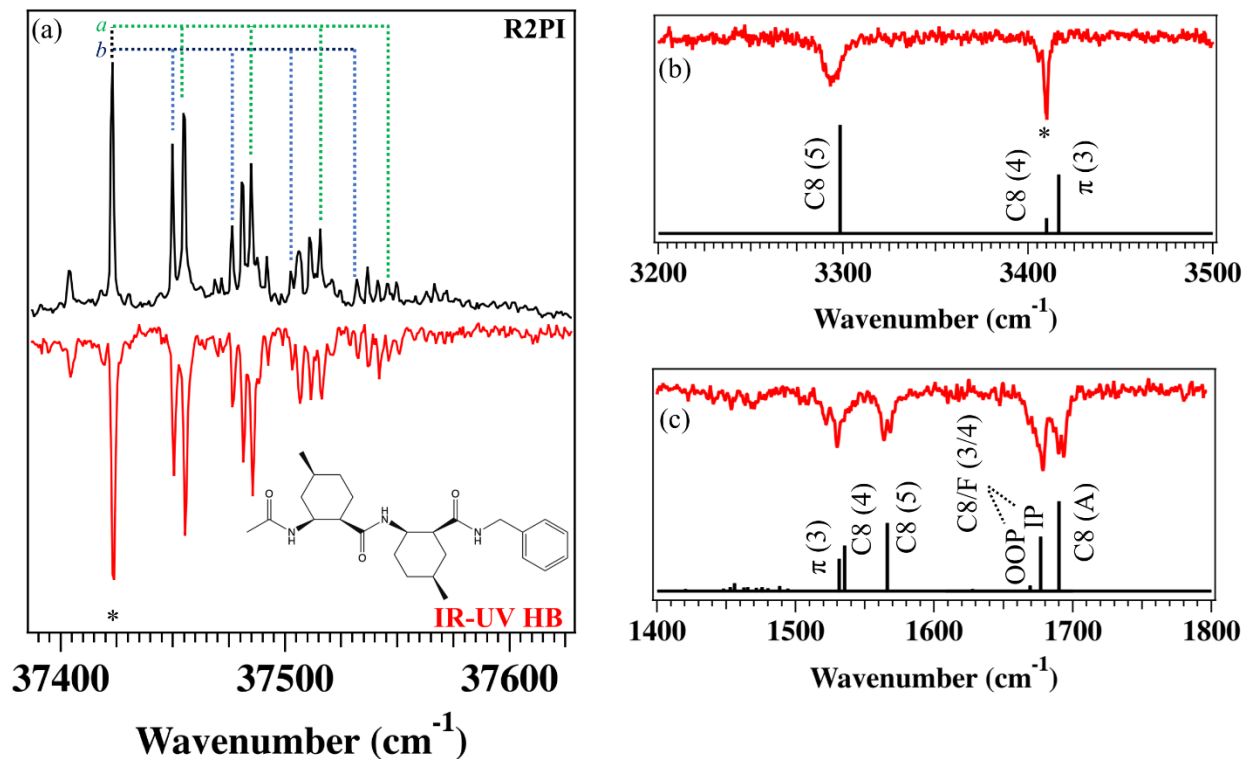


Figure 4.6. (a) R2PI and IR-UV HB spectra in the S_0 - S_1 region of the LL-dimer. Franck-Condon progressions marked with a and b correspond to low-frequency modes of 32 and 27 cm^{-1} , respectively. (b) and (c) display the RIDIR spectra of the LL-dimer in the hydride stretch and amide I/II regions, respectively. Stick spectra below each experimental trace represent the scaled, harmonic normal mode frequencies of the assigned conformation. These vibrational transitions, calculated at the B3LYP-D3BJ/6-31+G(d) level of theory, are labeled with the main carrier(s) of the vibration. Transitions marked with an asterisk were those used to collect holeburn spectra.

RIDIR Spectroscopy

Figure 4.6b and 6c presents the RIDIR spectra of the LL-dimer in the NH and amide I/II regions, respectively. Two high frequency bands of large and low intensity are present in the NH stretch spectrum at 3410 and 3405 cm^{-1} , respectively. This region may contain transitions from various types of weakly hydrogen bonded NH groups, rendering an *a priori* analysis of the spectrum difficult. The absence of transitions at higher frequencies indicates that there are no free NH groups in this conformer, and the broadened transition at 3293 cm^{-1} is associated with the presence of one strong H-bond. Thus, one would anticipate a structure in which there are two relatively weak, and one relatively strong, H-bond interactions.

The calculated IR spectra corresponding to the assigned structure, shown as black sticks below the experimental trace in Figure 4.6, replicate the experimental frequencies and intensities with high fidelity. The assigned structure corresponding to the stick spectra and a 2D sketch of the hydrogen bonding pattern are shown in Figure 4.4b. As seen in Figure 4.5a, this conformer was calculated to be the global minimum for both the L- and LL-dimer at the DFT B3LYP-D3BJ/6-31+G(d) level of theory. From the assigned structure we can see that NH[3] is interacting with the π -cloud of the phenyl cap, NH[4] and NH[5] are in C8 hydrogen bonds with C=O[A] and C=O[3], respectively, in forming a β -peptide analogue of a left-handed double γ -turn. The structure shown in Figure 4.4b is that of the LL-dimer, where one can see that the methyl groups on either ACHC ring are in the energetically favorable equatorial position, sterically locking in the local ACHC conformations.

This structure is clearly not the left-handed 12/10-helix, but it *is* the aforementioned cap-disrupted helix, where rather than a C10 H-bond, a structure is formed with C8 H-bonds at either terminus and an NH $\cdots\pi$ H-bond at the C-terminus. This structure is energetically favored for both the L- and LL-dimers (Figure 4.5a), a point we will explore further in the discussion section. It is important to keep in mind that for longer sequences of Ac-(ACHC)_n-NHBn, where n>2, the 12/10-helical hydrogen-bonding motif can co-exist with cap-disrupted C-terminal C8 and π -hydrogen bonds, which serve as a helical capping unit. This will become more relevant in the following sections.

We note that the two NH stretch transitions corresponding to the pair of C8 H-bonds are separated by over 100 cm⁻¹, and are quite different in intensity. C8 H-bonds are the β -peptide analog of C7 H-bonds in α -peptides, the transition frequency of which can span ~ 200 cm⁻¹.^{24, 35, 37, 38} The H-bond distances shown in Table 4.1 provide a firm basis for the frequency difference in the two C8 H-bond lengths. The assigned structure of the LL-dimer has an NH[5] \cdots O=C[3] H-bond distance (1.92 Å), 0.30 Å shorter than for NH[4] \cdots O=C[A] distance (1.22 Å).

The amide I data from 1600-1800 cm⁻¹ in Figure 4.6c shows a split, high frequency band at 1692 cm⁻¹ and a lower frequency band with a low frequency shoulder centered at 1679 cm⁻¹. The higher frequency transition corresponds to the C=O[A] group involved in the weaker C8 H-bond, while the two lower frequency transitions are due to in-phase and out-of-phase combinations of the C=O[3] and C=O[4] groups. The spectrum in the amide II region (1400-1600 cm⁻¹) shows a split peak at 1566 cm⁻¹, and a pair of peaks at lower frequencies of 1530 and 1522 cm⁻¹. Based

on the relative strengths of the two C8 H-bonds, we would anticipate the higher frequency transition to correspond to the NH[5] bend, the middle frequency to the NH[4] bend, and the lower frequency to the NH[3] bend. The calculations bear this out. It is interesting to note that both the L- and LL-dimer display the same split bands in the amide I and II spectra, indicating a likely common Fermi resonance.

Table 4.1. Hydrogen bond distances (in Å) for all assigned structures studied in this work. Parameters calculated at the B3LYP-D3BJ/6-31+G(d) level of theory.

Conformer/NH #	1	2	3	4	5
		<u>Right Hand 12/10 Mixed Helix</u>			
Dimer			F	~2.65 (π)	1.87 (C12)
R-Dimer			F	~2.65 (π)	1.87 (C12)
RR-Dimer			F	~2.65 (π)	1.87 (C12)
Trimer Conf B		1.89 (C10)	F	~2.56 (π)	1.85 (C12)
Tetramer Conf B	F	1.93 (C10)	1.90 (C12)	~2.56 (π)	1.84 (C12)
		<u>Cap-Disrupted Left Hand 12/10 Mixed Helix</u>			
L-Dimer			~2.54 (π)	2.22 (C8)	1.92 (C8)
LL-Dimer			~2.54 (π)	2.22 (C8)	1.92 (C8)
Trimer Conf A		F	~2.55 (π)	1.87 (C12)	1.92 (C8)
Tetramer Conf A	1.88 (C10)	F	~2.65 (π)	1.84 (C12)	1.92 (C8)

4.3.3 Trimer

R2PI and IR-UV HB Spectroscopy

The R2PI and IR-UV HB spectra of the trimer are shown in Figure 4.7a. Most of the peaks in the R2PI spectrum are accounted for in the IR-UV HB spectrum, with some exceptions: the peaks marked with blue daggers do not burn out with the same relative intensities with which they appear in the R2PI spectrum. This may be explained in one of two ways. If these peaks were due to hot or sequence band transitions, one might expect a decreased intensity pattern relative to the cold bands originating from the zero-point level in the hole burn spectrum due to shifting and broadening of the hot band IR absorption. A second possibility is that these peaks are due to another conformer in the molecular beam, which absorbs at the same IR frequency used to record the conformer-specific IR-UV HB spectra of the major conformer (the peak marked with an asterisk in the RIDIR spectra in Figure 4.7b). We will return to this point momentarily.

The major conformer (conformer A) has its S_0 - S_1 origin transition at $37,504\text{ cm}^{-1}$, with sequence bands at higher and lower frequencies due to incomplete vibrational cooling, and a Franck-Condon progression up to $v=3$ in a 14 cm^{-1} mode. Vibrational analysis of the assigned structure (see next section) indicates that this mode is due to the rocking of the phenyl cap against the ACHC[3] and NH[3] groups.

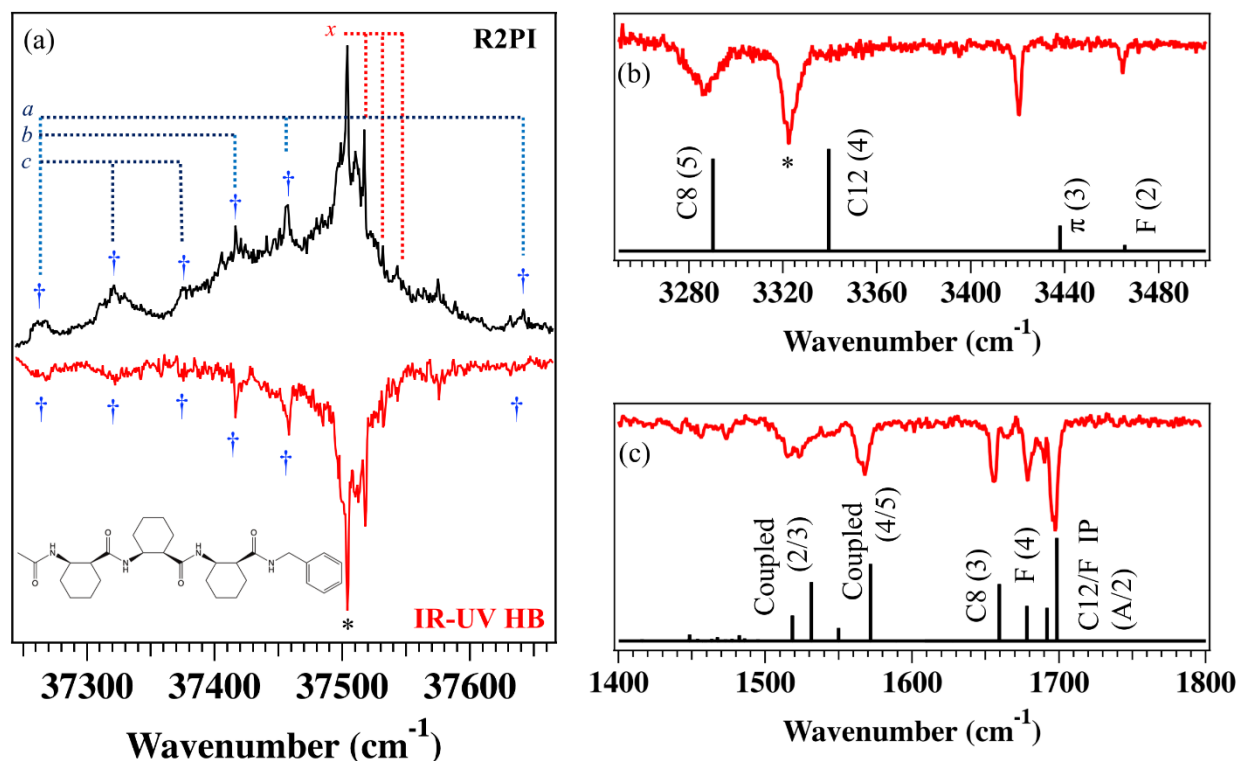


Figure 4.7. (a) R2PI (black) and conformer A IR-UV HB (red) spectra in the S_0 - S_1 origin region of the trimer. Blue daggers mark peaks belonging to a minor conformation (conf B) in the molecular beam (see text for details). A Franck-Condon progression in the major conformation (conf A) marked with x corresponds to a low frequency mode of 14 cm^{-1} , while a , b , and c correspond to low frequency modes in conf B of 188 , 151 , and 27 cm^{-1} , respectively. (b) and (c): RIDIR spectra of conformer A in the hydride stretch and amide I/II regions, respectively. Stick spectra below each experimental trace depict the scaled, harmonic vibrational frequencies of the assigned conformation. These vibrational transitions, calculated at the B3LYP-D3BJ/6-31+G(d) level of theory, are labeled with the main carrier(s) of the vibration. Transitions marked with an asterisk were those used to collect hole-burn spectra.

RIDIR Spectroscopy

Figure 4.7b and 4.7c present the RIDIR spectra of conformer A of the trimer in the NH stretch and amide I/II regions, respectively. We observe one weak, high frequency NH stretch at 3464 cm^{-1} and a more intense transition at 3420 cm^{-1} . Using similar logic as outlined above, we may tentatively assign these transitions to a free and a π -bound NH, respectively. Two broadened, lower frequency transitions appear at 3322 and 3286 cm^{-1} , in a region indicative of strong hydrogen bonds. We note the similarity between this spectrum and that of the LL-dimer, and tentatively assign the low frequency transition at 3286 cm^{-1} to a C8 hydrogen bonded NH stretch fundamental. Similarly, we see that the NH stretch spectra of the RR-dimer has a comparably intense and broadened band at 3326 cm^{-1} assigned to a C12 H-bond. We therefore tentatively assign the band at 3322 cm^{-1} to a C12 H-bond.

The calculated vibrational frequencies and IR intensities, shown as black sticks in Figure 4.7, replicate the experimental spectrum in significant detail, and corroborate our preliminary assignments. The structure corresponding to these calculated frequencies, with an $f/\pi/\text{C12}/\text{C8}$ H-bonding pattern, is shown in Figure 4.8a. We see that the C-terminal portion adopts the cap-disrupted motif of the LL-dimer with its $\text{NH}[5]\cdots\text{O}=\text{C}[3]$ C8 and $\text{NH}[3]\cdots\pi$ interactions, while the N-terminal addition of the $\text{ACHC}[2]$ unit gives rise to the $\text{NH}[4]\cdots\text{O}=\text{C}[\text{A}]$ C12 H-bond characteristic of the left-handed 12/10-helix. This structural progression implies the emergence of a preferred secondary structure. As seen in the energy level diagram in Figure 4.5b, this conformer is predicted by the calculations to be the global minimum for the trimer. This conformer forms one full turn of a left-handed 12/10-helix, not including the cap-disrupted portion, that is held together by a single C12 hydrogen bond. We henceforth refer to this secondary structure as a cap-disrupted left-handed 12/10-helix. It is worth noting that if, instead of the cap-disrupted portion, this conformer adopted a C10 H-bond between $\text{NH}[2]$ and $\text{C}=\text{O}[4]$, approximately 1.5 turns of a “pure” left-handed 12/10-helix would be formed.

The amide I and II data of conformer A also show a striking similarity with that of the LL-dimer (shown in Figure 4.6). Furthermore, the calculated spectrum for conformer A matches the experimental spectrum in significant detail. The high frequency amide I bands at 1698 and 1690 cm^{-1} correspond to the in-phase and out-of-phase stretches of the $\text{C}=\text{O}[\text{A},2]$ oscillators. The relative intensities of these bands can be understood by the fact that, in the assigned structure, these groups are nearly antiparallel with one another, rendering the net change in the dipole in the out-

of-phase stretch negligible compared with that of the in-phase combination. The two lower frequency bands at 1679 and 1655 cm^{-1} are assigned to C=O[4] and C=O[3], respectively. The relative frequencies of these bands are in keeping with our general expectation that carbonyl groups involved in stronger H-bonded interactions shift to lower frequencies. The assigned amide II transitions display the inverse pattern here, with the NH[4,5] coupled bends appearing at 1568 and 1547 cm^{-1} , and the NH[2,3] coupled bends accounting for the transitions at 1522 and 1515 cm^{-1} .

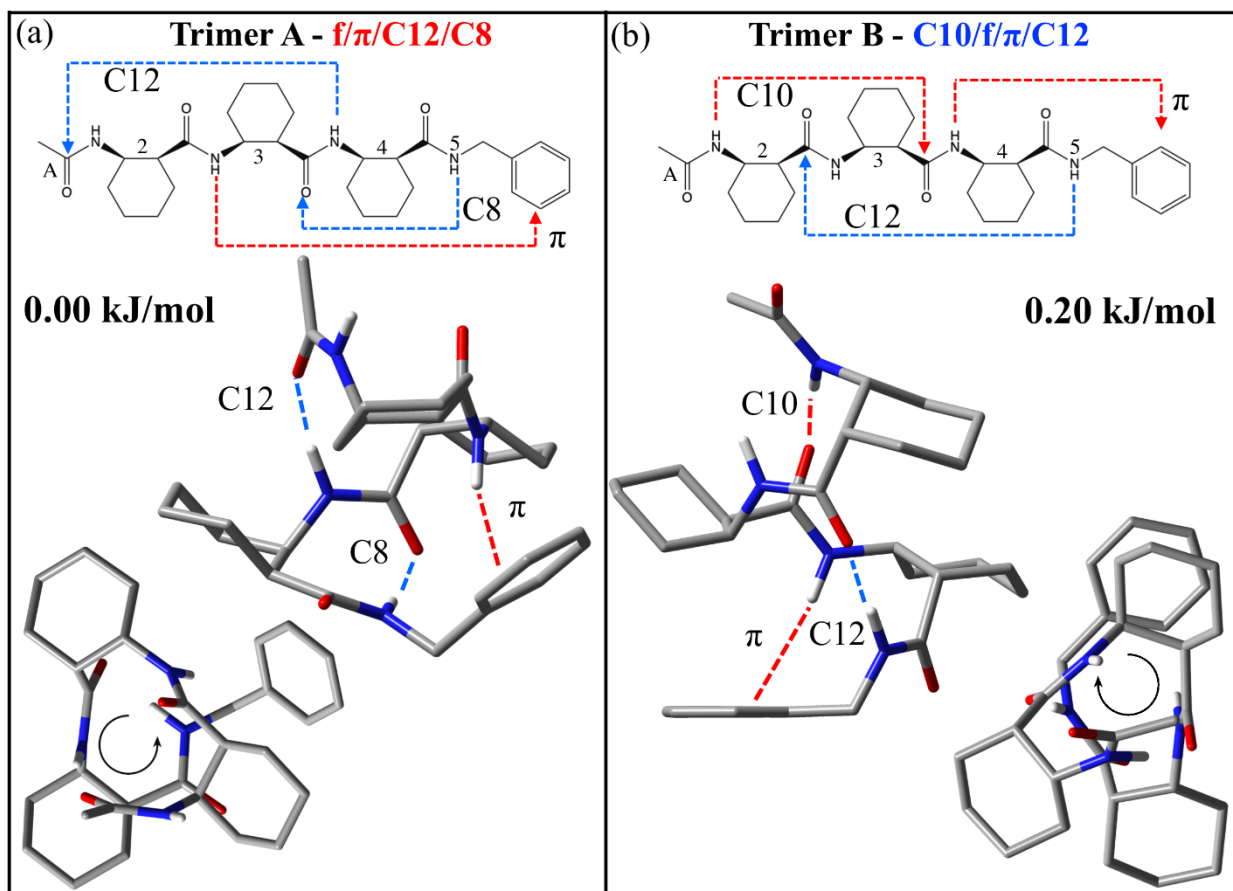


Figure 4.8. Assigned structure and relative zero-point-corrected potential energies of (a) conformer A and (b) conformer B of the trimer; 3D structure and 2D hydrogen-bonding schematics are presented for each molecule, along with a down-axis view from N \rightarrow C terminus, highlighting the preferred screw-sense of each conformer.

Conformer B

While experimental conditions were not sufficient to record IR data of this minor conformer of the trimer (conformer B), spectral and computational evidence points to its tentative structural assignment. The UV data show the S_0 - S_1 origin at $37,263\text{ cm}^{-1}$, with Franck-Condon progressions up to $v=2$, 2, and 1 in vibrations of frequency 54, 188, and 151 cm^{-1} , respectively. Vibrational analysis of the tentatively assigned structure (details given presently) shows that each of these modes involve the rocking of the phenyl group against ACHC[3] and NH[4], with the 54 cm^{-1} mode exhibiting the exact same motion as the 54 cm^{-1} mode in the RR-dimer. The UV absorption frequencies match those of the RR-dimer and conformer A of the tetramer (see next section), both of which are right-handed 12/10-helices. Additionally, the IR-UV HB frequency of 3322 cm^{-1} is where absorption of NH[5] in a C12 H-bond occurs, as seen in the IR spectra of the RR-dimer and conformer A of the tetramer. Finally, the energy level diagram in Figure 4.5b reveals a second lowest energy conformer that is only 0.2 kJ/mol above the global minimum, with a hydrogen bonding pattern of C10/f/ π /C12, making it the natural intermediate structure in the trimer that links the right-handed 12/10-helix of the RR-dimer with conformer A of the tetramer. This assignment is further substantiated by the calculated IR spectra of this structure, shown in Figure 4.9, which predicts absorption of the NH[5,2] groups in the C12 and C10 hydrogen bonds at 3316 and 3322 cm^{-1} , respectively, which very likely accounts for the IR absorption of this conformer at 3322 cm^{-1} .

Figure 4.8b presents the structure tentatively assigned to conformer B. Comparison of this structure with that of the RR-dimer reveals a striking similarity. Indeed, as was the case when comparing Tri(A) and the LL-dimer, the same structural motif present in the RR-dimer is incorporated in the common C-terminal component of Tri(B). The structure comprises approximately 1.5 turns of a fully formed right-handed 12/10-helix that is held together by single C12 and C10 H-bonds and terminates at the C-terminus with a π interaction. We see then, in going from $n=2$ to $n=3$ of Ac-(ACHC) $_n$ -NHBn, two emerging secondary structures; the cap-disrupted left-handed 12/10-helix, and the right-handed 12/10-helix.

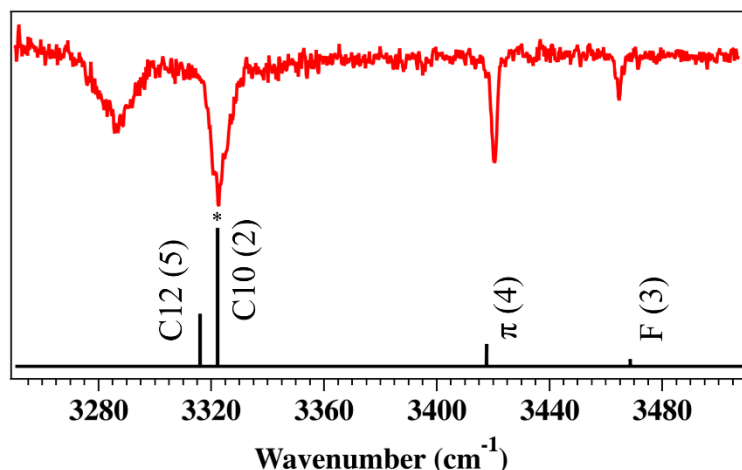


Figure 4.9. Calculated IR spectrum (black sticks) of Trimer conf B compared with the experimental IR spectrum of Trimer conf A. The peak marked with an asterisk at 3322 cm^{-1} was used to record the IR-UV HB spectrum of conf A, which likely accounts for the contamination from conf B.

4.3.4 Tetramer

R2PI and IR-UV HB Spectroscopy

The R2PI and IR-UV HB spectra of the tetramer $\text{Ac}-(\text{ACHC})_4\text{-NHBn}$ are shown in Figure 4.10a, from which we immediately notice a decrease in spectral resolution due to incomplete cooling of this large molecule following laser desorption, with molecular weight of 649 amu. The result is the presence of sequence and hot bands in the UV spectra. Nevertheless, we are able to identify two unique conformers in the molecular beam.

The IR-UV HB spectrum of conformer B shown as the blue trace, displays vibronic activity spanning 400 cm^{-1} . The peak marked with a red dagger is residual interference from conformer A, due to a small absorption from A at the IR wavelength used for hole-burning (3300 cm^{-1}). We note the similarity of this UV spectrum to that of conformer B of the trimer (Figure 4.7a), and the major conformer of the RR-dimer (Figure 4.3a). Indeed, we tentatively assign the S_0 - S_1 origin transition of conformer B to the band at 37,265 cm^{-1} , approximately the same frequency of conformer B of the trimer. While the spectrum is much less well-resolved than a fully cold counterpart, one can nevertheless still observe several peaks due to Franck-Condon (FC) activity in low-frequency modes. The IR-UV HB spectrum contains FC progressions up to $v=3$ in 54 cm^{-1} mode and $v=2$ in

a 187 cm^{-1} mode with each member of the 54 cm^{-1} progression having a smaller peak built off of it with a spacing of 18 cm^{-1} . These smaller peaks are likely due either to combination bands with an 18 cm^{-1} vibration in S_1 , or to X^1_1 sequence bands present due to incomplete vibrational cooling, where the corresponding S_1 frequency is 18 cm^{-1} larger than in S_0 . According to vibrational analysis of the assigned structure, (see next section) these FC active modes in the tetramer are close analogs of those exhibiting FC progressions in conformer B of the trimer.

The IR-UV HB spectrum of conformer A is shown as the red trace in Figure 4.10a. In striking contrast to the spectrum of conformer B, we observe a single peak with a FWHM of 15 cm^{-1} . We note the close similarity of this spectrum to that of conformer A of the trimer, which adopts a cap-disrupted left-handed 12/10-helix. Indeed, conformer A of the tetramer has its S_0 - S_1 origin transition at $37,507\text{ cm}^{-1}$, just 3 cm^{-1} higher than that of Tri(A). The width of the UV peak reflects incomplete cooling in the expansion, consistent with a molecule of this size.

RIDIR Spectroscopy

The conformer-specific RIDIR spectra of the two experimentally observed structures of the tetramer are shown in Figure 4.10b and 4.10c in the amide I/II and NH stretch regions, respectively. As with the smaller molecules in this series, the vibrational spectra of all structures calculated at the DFT B3LYP-D3BJ/6-31+G(d) level of theory were compared with experiment. We expect to see the five unique NH and C=O groups give rise to as many fundamental transitions in each of the NH stretch, amide I, and amide II regions.

The NH stretch spectrum of Tet(B) is presented as the blue trace in Figure 4.10c. We observe two high frequency transitions at 3449 and 3420 cm^{-1} , an asymmetrically broadened peak with a low frequency shoulder centered at 3325 cm^{-1} , and a symmetrically broadened low frequency peak at 3299 cm^{-1} . We note that the NH stretch spectrum of the RR-dimer exhibits a similar intensity and frequency pattern to that observed here. Additionally, recalling the close similarity of the UV spectra of the tentatively assigned right-handed 12/10 helix of Tri(B) to that of Tet(B), we tentatively assign the three highest frequency peaks to a free, a π -bonded, and a C12 hydrogen bonded NH stretch. This leaves assignment of the two remaining low frequency transitions to what must be NH groups involved in hydrogen bonds of similar strength to the C12 NH group.

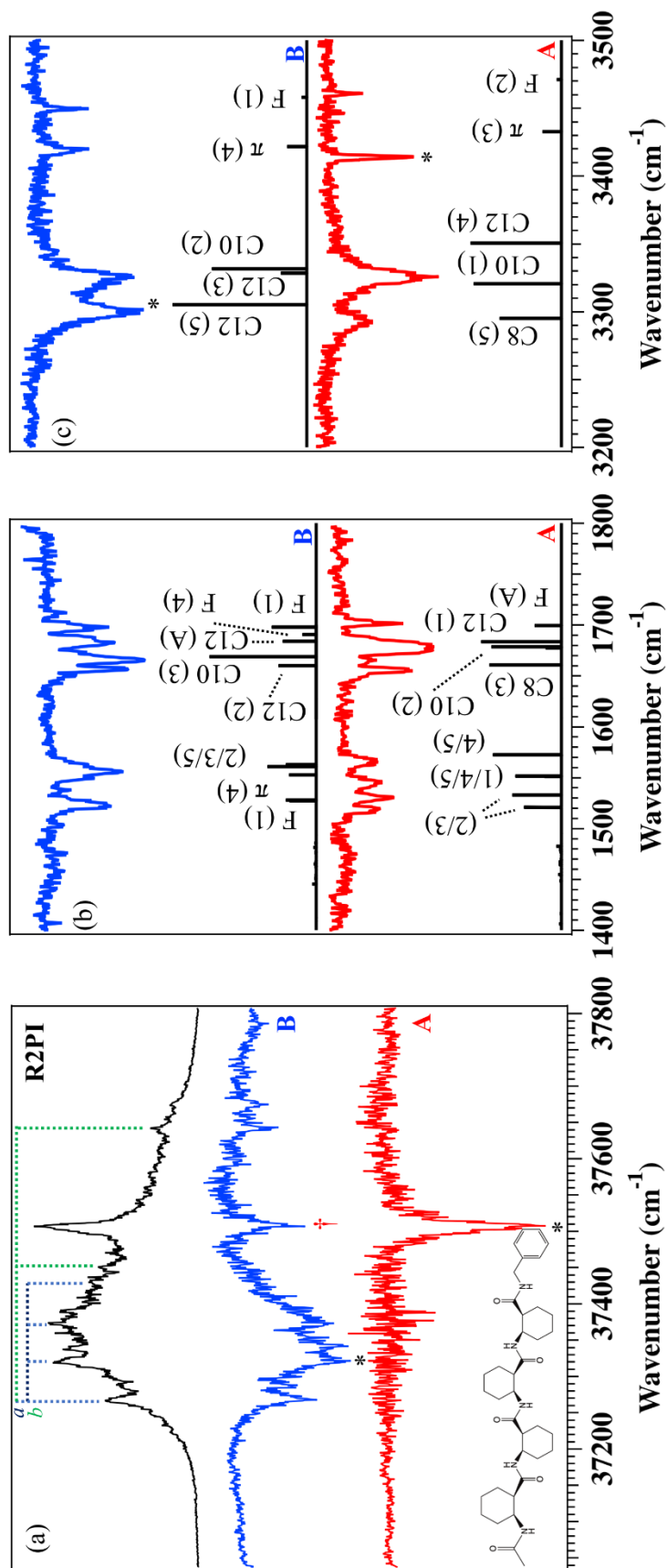


Figure 4.10. (a) R2PI (black) and IR-UV HB spectra in the S_0 - S_1 region of conformer B (blue trace) and conformer A (red trace) of the tetramer. The Franck-Condon progressions marked with *a* and *b* correspond to low-frequency modes of 187 and 54 cm^{-1} , respectively, in conformer B. The transition marked with a red dagger in the IR-UV HB spectrum of conformer B represents contamination from conformer A due to overlapping IR frequencies. (b) and (c): RIDIR spectra of conformer B (blue) and A (red) in the amide I/II and hydride stretch regions, respectively. Stick spectra below each experimental trace depict the scaled, harmonic normal mode frequencies of the assigned conformation. These vibrational transitions, calculated at the B3LYP-D3BJ/6-31+G(d) level of theory, are labeled with the main carrier(s) of the vibration. Transitions marked with an asterisk were those used to collect hole-burn spectra.

Single ACHC residue N-terminal helical growth of the right-handed 12/10-helix of Tri(B) yields one additional C12 hydrogen bonded NH. The calculated stick spectrum of this structure is shown below the experimental trace of Tet(B). We see that it is a match. The excellent agreement between experiment and theory in amide I and II, shown in the top portion of Figure 4.10b, gives us confidence that the assigned structure, shown in Figure 4.11a, is indeed a right-handed 12/10-helix, which according to our labeling scheme is f/C10/C12/ π /C12. It comprises approximately 2 turns of a fully formed right-handed 12/10-helix that is held together by two C12 hydrogen bonds (pointing N \rightarrow C-terminal) and one C10 hydrogen bond (pointing C \rightarrow N-terminal), capped at the C-terminus with a π -interaction. The dihedral angles for this structure, and all structures reported herein, are found in Table 4.2. The fact that this structure is calculated to be the global minimum among all calculated structures adds further confidence to the assignment (Figure 4.5b).

The frequency ordering of the amide I bands reflects the strengths of the hydrogen bonds of which the carbonyl groups are a part, as revealed by the relative frequencies of the assigned NH stretch transitions. The two free C=O stretch transitions occurs near 1700 cm^{-1} while the triplet of transitions at 1684 (C12[A]), 1669 cm^{-1} (C10[3]), and 1660 cm^{-1} (C12[2]) reflect an increasing strength of the H-bonds to each C=O group. The relative frequencies of the amide II bands report the same information, but with the frequency pattern inverted. The more weakly bound π and free NH bends appear at 1522 cm^{-1} , while C10 and C12 NH bends appear as a coupled set of peaks centered at 1556 cm^{-1} . In addition to the NH stretch region, the amide I and II spectra of Tet(B) and the RR-dimer are also quite similar to one another, as one might expect of molecules sharing a common secondary structure.

The NH stretch spectra of Tet(A) is shown as the red trace in Figure 4.10c. We notice the striking similarity of this spectrum to that of Tri(A), the cap-disrupted left-handed 12/10-helix. Recalling the near identical UV spectra of these conformers, we tentatively assign the two high frequency transitions at 3461 and 3414 cm^{-1} to free and π -bound NH groups, respectively, the lowest frequency transition at 3292 cm^{-1} to a C8 H-bond, and the 11 cm^{-1} FWHM peak at 3326 cm^{-1} to a C12 H-bond. There seem to be no experimental peaks left to assign. However, single ACHC residue N-terminal helical growth of the cap-disrupted left-handed 12/10-helix of Tri(A) would give rise to an additional C10 hydrogen bonded NH. We note that the integrated intensity of the assigned C12 transition in Tet(A) is nearly double that of the analogous peak in Tri(A). On

this basis, we postulate that two unique NH stretch fundamentals contribute to the peak's unusually large intensity.

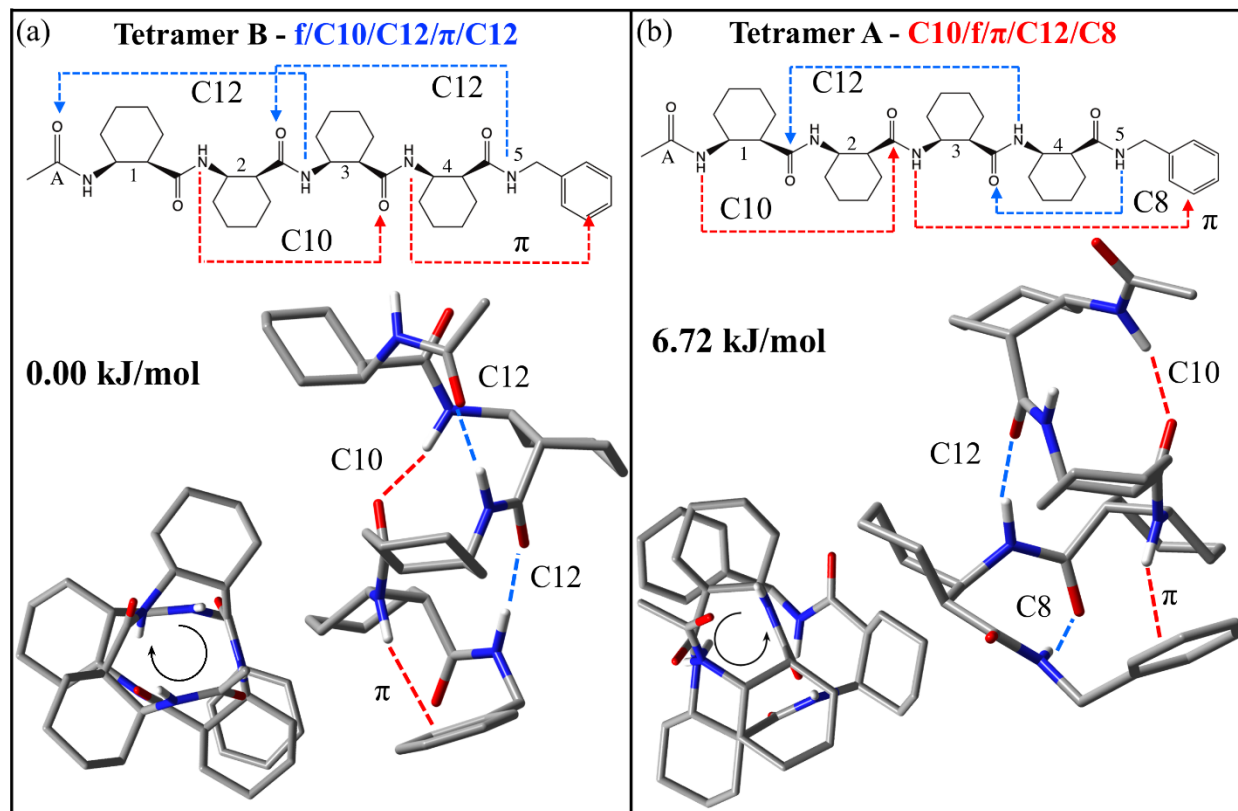


Figure 4.11. Assigned structure and relative zero-point-corrected energies of (a) conformer B and (b) conformer A of the tetramer; 3D structure and 2D hydrogen-bonding schematics are presented for each molecule, along with a down-axis view from N→C terminus, highlighting the preferred screw-sense of each conformer.

The calculated stick spectra of the cap-disrupted left-handed 12/10-helix tetramer is shown below the experimental trace of Tet(A). The match with experiment is good in the NH stretch region, and excellent in the amide I/II regions (Figure 4.10b). As was the case with Tet(B), the amide I and II data generally reflect the hydrogen bond strengths as revealed through their relative frequencies in the NH stretch spectrum.

This structure is calculated to be the second lowest energy conformer, with energy 6.72 kJ/mol above Tet(B), giving us further confidence in its assignment. The assigned structure, shown in Figure 4.11b, is the cap-disrupted left-handed 12/10-helix, labeled as C10/f/ π /C12/C8. It

comprises approximately 1.5 turns of a left-handed 12/10-helix (not including the cap-disrupted portion), which is held together by counter-propagating C12 and C10 hydrogen bonds.

4.4 Discussion

Through conformation-specific IR spectroscopy in the hydride stretch and amide I/II regions, we have determined the intrinsic conformational preferences of a series of cyclically constrained β -peptides in the gas-phase. We have shown that the gas-phase conformer population contains both left- and right-handed 12/10-mixed helical structures for Ac-(ACHC)_n-NHBn with n=2,3,4. As shown in Figure 4.5, the observed conformation is the global minimum calculated structure in each case, with the remaining assigned structures being the next lowest energy structure in all but one case. These results give us confidence that the B3LYP-D3BJ/6-31+G(d) level of theory accurately characterizes the conformational energetics of these molecules. With this in mind, we now turn to a discussion of the energy landscapes of these increasingly complex β -peptides, beginning with the dipeptides.

4.4.1 Dipeptides

Steric Control of Helical Handedness in the Dipeptides

One of the goals of this study was to determine the effect that the methylated ACHC residues would have on directing formation of a particular helical screw-sense in the isolated gas-phase molecule. Choi and coworkers have demonstrated that incorporation of an L- or R-ACHC group at every other residue in *t*-BuO-(ACHC)_n-NHMe with n=4,5, is sufficient to lock the conformation into either the left- or right-handed 12/10-helix in solution.^{6,7} We explore here what effect incorporating one or two such methylated residues has on the conformational preferences and energy landscape of the isolated, gas-phase dipeptide.

Table 4.2. Relative energies and backbone dihedral angles for all assigned structures.^a

	ACHC ₁ (SR)		ACHC ₂ (RS)		ACHC ₃ (SR)		ACHC ₄ (RS)								
ΔE (kJ/mol)	$\phi_1(^{\circ})$	$\psi_1(^{\circ})$	$\phi_2(^{\circ})$	$\psi_2(^{\circ})$	$\phi_3(^{\circ})$	$\psi_3(^{\circ})$	$\phi_4(^{\circ})$	$\psi_4(^{\circ})$	CNCC($^{\circ}$)						
Dimer f/ π /C12	0.00	-	-	-	-96	50.1	102	95	53	-102	-89				
R-Dimer f/ π /C12	0.00	-	-	-	-96	51	102	94	53	-102	-89				
RR-Dimer f/ π /C12	0.00	-	-	-	-95	50	102	94	53	-101	-89				
Trimer B C10/f/ π /C12	0.20	-	87	57	-72	51	81	114	54	-101	-90				
Tetramer B f/C10/C12/ π /C12	0.00	-116	52	83	107	57	-114	-101	51	97	99	54	54	-99	-89
Right Handed 12/10 Helix ^b	-	-96	52	95	98	54	-92	-96	52	95	98	54	-92	-	
L-Dimer π /C8/C8	0.00	-	-	-	-	-	-	-56	-47	101	110	-63	-21	-92	
LL-Dimer π /C8/C8	0.00	-	-	-	-	-	-	-56	-47	101	110	-63	-21	-92	
Trimer A f/ π /C12/C8	0.00	-	-	-	101	-57	-97	-90	-53	122	114	-62	-21	-85	
Tetramer A C10/f/ π /C12/C8	6.72	-85	-56	91	100	-60	-91	-94	-53	120	114	-61	-19	-84	
Left Handed 12/10 Helix ^b	-	-110	-58	98	103	-52	-87	-110	-58	98	103	-52	-87	-	

^aStructures calculated at the B3LYP-D3BJ/6-31+G(d) level of theory.

^bCrystal structure values taken from ref 6.

We now return to Figure 4.5a, which shows the zero-point corrected energies of all the gas-phase structures calculated to lie within 25 kJ/mol of the global minimum for each dipeptide. We have seen that all of the assigned conformations fall into one of two categories: emergent forms of either the right-handed 12/10-helix ($f/\pi/C12$) or the cap-disrupted left-handed 12/10-helix ($\pi/C8/C8$). We have labeled the lowest energy structure corresponding to these conformational families, as well as the pure left-handed 12/10-helix conformation ($C10/f/f$), for each unique molecule. Its energetic path upon ACHC methylation is traced with dotted lines.

Note, first, that the number of low-energy structures present in the dipeptides decreases as more methylated ACHC units are added, thereby increasing steric constraints. The dominant conformation of the dimer is the right-handed helix (0.0 kJ/mol) while the minor conformation is tentatively assigned to the cap-disrupted left-handed helix (11.6 kJ/mol). The 10.4 kJ/mol separation of the global minimum from the next lowest energy structure constitutes a strong energetic preference for the right-handed 12/10-helix. This preference persists with the addition of one and two methyl groups in the R-dimer and RR-dimer with energy separations of 13.2 and 18.4 kJ/mol, respectively. This large separation in the RR-dimer between the global minimum and second lowest energy structure is unprecedented in short peptides or synthetic foldamers.

N-terminal substitution of the dimer's ACHC[3] with L-ACHC (L-dimer) inverts this trend, where all population is now funneled into the cap-disrupted left-handed 12/10-helix, which is the minor conformer of the unsubstituted dimer. Additional L-ACHC substitution of ACHC[4] (LL-dimer) locks in this structure, where the energy separation between the assigned global minimum structures and the next lowest energy conformers is ~ 7.5 kJ/mol in each case. The smaller energy gap in L(L)- compared to R(R)-dipeptides, when combined with the clear preference for the right-handed helix in the dimer, point clearly to the inherent bias of the unmethylated ACHC unit to forming a right-handed helix.

Although not experimentally observed, the pure left-handed 12/10-helix ($C10/f/f$) is calculated as a low energy structure for the L(L)-dipeptides and the dimer. We return to this point momentarily. These calculated results, along with our experimentally assigned conformations, lead one to conclude that selectively methylating ACHC residue(s) is sufficient to drive population exclusively into one particular screw-sense over the other under isolated, gas-phase conditions.

Effects of the C-Terminal NHBn Cap in the Dipeptides

Zero-point corrected energy calculations were also performed on the pool of structures where the sterically intrusive C-terminal NHBn cap was replaced with an NHMe cap, to assess how the energies of the structures might change in the phenyl ring's absence. The results for the NHMe capped dipeptides are shown in Figure 4.12a. We immediately notice a sharp decrease in the number of structural minima for each dipeptide. This is due to the removal of all near-redundant phenyl rotamer structures, which all funnel into the same conformational minima upon NHMe substitution of the NHBn cap.

Focusing our attention on the right-handed helix former (blue), we see that the relative energies in going from the LL-dimer to the RR-dimer follow the same trend as its NHBn counterpart (Figure 4.5a), where it is the global energy minimum structure in the dimer, R-, and RR-dimers, but then sharply increases in energy with each L-ACHC addition. In the case of LL-Dimer, the loss of the π -interaction greatly destabilizes this structure with respect to both left-handed helices.

Upon NHMe capping, the pure left-handed 12/10-helix displaces the cap-disrupted 12/10-helix (f/C8/C8) as the global minimum structure for both the L- and LL-dimer. At the dimer level, both the pure and cap-disrupted helices are substantially more stable relative to their NHBn counterparts, with energies of 0.62 and 1.48 kJ/mol, respectively (compared with 10.36 and 11.62 kJ/mol). The preference for the pure left-handed helix in the NHMe-capped L(L)-dimers highlights the perturbative impact that π -interactions may have on preferred structure in the gas-phase. The calculations thus predict that in the absence of the C-terminal phenyl ring, the structures that we experimentally assigned to the cap-disrupted left-handed 12/10-helix would funnel their population into the 'pure' left-handed helix. Finally, the fact that the pure left- and right-handed 12/10 mixed helices are nearly isoenergetic with C-terminal NHMe capping supports the notion that the (ACHC)₂ unit may be regarded as achiral.

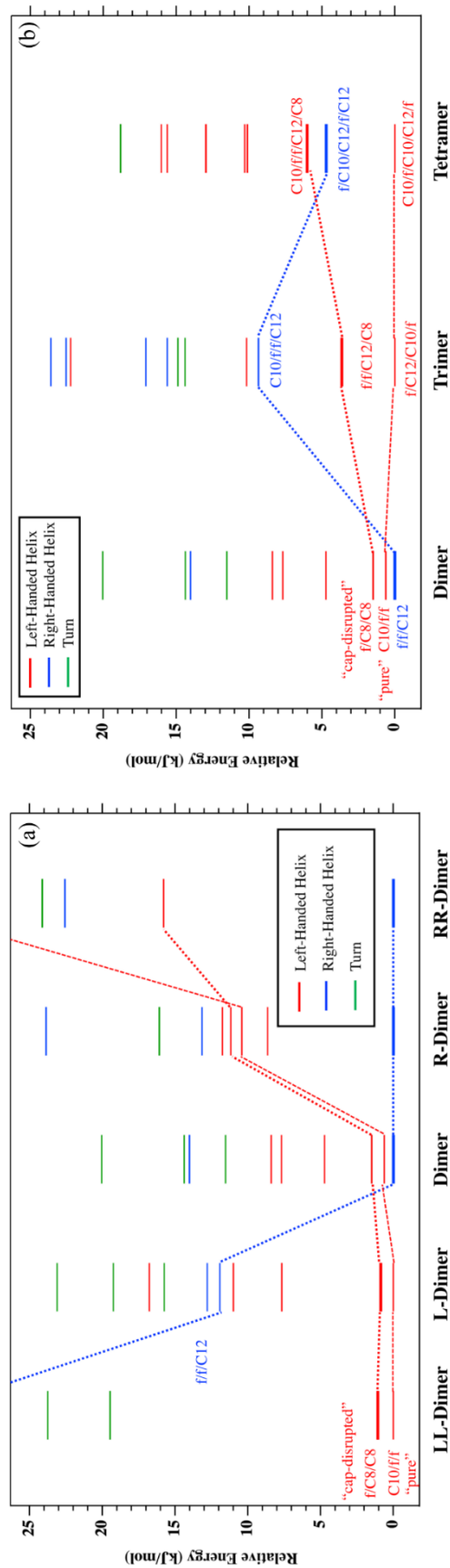


Figure 4.12. Energy level diagrams for (a) the set of methylated dipeptides and (b) the series Ac-(ACHC)_n-NHBn with n=2,3,4, upon replacing the C-terminal NHBn cap with NHMe. Each conformational minima has its relative zero-point-corrected energy (B3LYP-D3BJ/6-31+G(d)) plotted as a horizontal bar and color-coded to represent left-handed (red), right-handed (blue), or general turned (green) structures. Experimentally assigned conformers are represented with a heavy horizontal bar. The “pure” right- and left-handed helices as well as the cap-disrupted helical structures are labelled and connected via dotted lines to their corresponding structures across the molecules.

4.4.2 Ac-(ACHC)_n-NHBn, n=2-4

Potential Energy Landscapes for Ac-(ACHC)_n-NHBn, n=2-4

Another major goal of this study was to determine which screw-sense, if any, emerges in unmethylated ACHC oligomers as a function of increasing length. We have experimentally determined that for n=2-4 in Ac-(ACHC)_n-NHBn, both the right-handed 12/10-helix and the cap-disrupted left-handed 12/10-helical structures are adopted. However, the spectroscopy also points to an alternating preference with oligomer length. Using integrated vibronic transition intensities as a first-order approximation of relative abundances, the right-handed 12/10-helix is the major conformer when n=2 and 4, while the cap-disrupted left-handed 12/10-helix is the major conformer at n=3. Energetic analysis, given presently, corroborates this assessment. Possible reasons for these asymmetric distributions are given in the next section.

We refer again to Figure 4.5b, which presents the calculated zero-point corrected energies of all structures within 25 kJ/mol of the global minimum for the unmethylated dimer, trimer, and tetramer. As was the case with the dipeptides, the secondary structures of all minima fall into one of three color-coded categories: left-handed helix (red), right-handed helix (blue), and turned structures (green). The lowest energy structures corresponding to the right-handed, cap-disrupted left-handed, and pure left-handed 12/10-helices are labeled in the figure, with the energetic path accompanying the addition of each N-terminal ACHC unit traced with dotted lines.

The number of low-energy structures remains nearly constant across the dimer (20), trimer (23), and tetramer (18). This is in contrast to a previous gas-phase study from some of us of the flexible Z-Gly_n-OH series (n=1-3,5), where the number of calculated minima increased in going from n=1 to n=3 and then sharply decreased in going from n=3 to n=5.³⁶ In that series of molecules, it was the number of hydrogen bonds present in the structure which conferred stability. At n=5, fewer structures existed that maximized the number of hydrogen bonds. In our series of much more rigid molecules, the number of distinct conformational families remains nearly constant in going from n=2 to n=4, because the addition of one or two ACHC units to the N-terminus simply grows and expands upon the existing secondary structures found in the dimer manifold.

Effects of the C-Terminal NHBn Cap for Ac-(ACHC)_n-NHBn, n=2-4

Figure 4.12b presents the relative, zero-point corrected energies of the low-energy conformers of the dimer, trimer, and tetramer upon replacement of the NHBn cap with a less intrusive NHMe cap. As with the dipeptides (Figure 4.12a), there is a sharp decrease in the number of low-energy conformers available to each molecule due to the removal of conformers differing only in its phenyl rotamer.

In the dimer, the three main helical motifs are close in energy, with the right-handed helix remaining the global energy minimum. At the trimer level, the right-handed helix is destabilized by 9.37 kJ/mol relative to the pure left-handed helix, which displaced the cap-disrupted helix as the global minimum. At the tetramer level, the right-handed helix is now the second lowest energy structure at 4.71 kJ/mol above the pure left-handed helix, which has moved from third lowest energy to the global minimum. These results suggest that the cap-disrupted left-handed 12/10-helical structures that we experimentally observed in the dimer, trimer, and tetramer would likely funnel their population into the pure left-handed 12/10-helix upon capping with the more biologically relevant NHMe group, resulting in a distribution of “pure” left- and right-handed 12/10 helices. Additionally, the fact that the energy separation decreases between the pure left- and right-handed helices in Ac-(ACHC)_n-NHMe when n is even is consistent with the (ACHC)₂ dimer unit as an achiral building block.

4.4.3 The ACHC Residue is a Robust Left- and Right-Handed 12/10 Mixed-Helix Former

Conservation of Secondary Structure Between Phases

It is striking that the seven molecules studied in this work funnel their population into only two unique conformational families: the pure right-handed 12/10 mixed-helix and the cap-disrupted left-handed 12/10 mixed-helix. We have reasoned in the previous sections that in the absence of the NHBn cap it is very likely that the cap-disrupted left-handed helix population would be funneled into the pure left-handed 12/10 helix. With this in mind, in this section we compare these gas-phase structures with their analogous solution and crystal phase structures.

In solution, the left- and right-handed helices interconvert on the NMR timescale between one another via the cooperative inversion of all ACHC residues from one chair conformation to the other.

The exquisite sensitivity of the helical preference to environmental effects is apparent when one compares the structures observed in crystalline form. X-ray structures derived from crystals of the *t*-BuO/NHMe capped tetramer show it to adopt a right-handed 12/10 mixed-helix, while the X-ray structure of Ac/NHBn capped tetramer is a left-handed 12/10 mixed-helix.⁷ The change in helical handedness in the solid state crystals of such similar molecules must be attributed to crystal packing effects, where intermolecular interactions play a key role in tipping conformational preferences towards one helix or another. Finally, we note that the pentamer member of our Ac/NHBn series adopts a left-handed 12/10 helix when crystallized.⁶

Our experimental determination that both left- and right-handed helices exist in the gas-phase at the dimer, trimer, and tetramer levels occurs despite the fact that we are laser desorbing the solid, which we have just argued is of one handedness in crystalline form. Two scenarios may occur. Either laser desorption takes a single handed helical solid into the gas phase with sufficient energy that it can partially interconvert before being cooled by supersonic expansion, or the sample itself is not of a single-handed helix, since they were not prepared in crystalline form.

We test the first hypothesis based on the calculations. Laser desorption temperatures are not well characterized, with some studies suggesting that temperatures in the initial desorption plume may reach as high as 700 K.^{40, 41} In a previous study we calculated the isomerization rate of an $\alpha\beta\alpha$ -tripeptide system involving single ACHC ring isomerization from one chair conformation to the other.²⁴ At an estimated laser-desorption temperature of 300 K, we determined that the rate limiting ring-flipping step occurred three orders of magnitude slower than the collisional cooling rate in the supersonic expansion, rendering desorption-induced isomerization very unlikely. In the simplest case of the ACHC dimer, one would require two ACHC rings to flip, the rate of which is significantly slower than for the single ACHC tripeptide. Therefore, we conclude that it is far more likely that our solid-state samples contain both handed helices, which we laser desorb and subsequently detect in the gas-phase.

Free Energy Considerations and Structural Implications

We have calculated the free energies of all conformers in the present series of seven molecules calculated to lie within 50 kJ/mol of zero-point corrected relative energy. These energies are presented in Tables 4.3-9. Assuming thermal equilibrium at a laser desorption temperature of 300 K, we can use the free energy calculations to predict the initial populations prior to cooling. In all

seven molecules studied herein, the free energy trends mirror the potential energy trends quite closely. This is an interesting result, which points to the steric constraints of the ACHC ring along the peptide backbone preventing extended conformations from forming. Since these extended conformations typically possess a greater number of low-frequency modes, they grow in thermal population with temperature. The steric constraints of the ACHC residue effectively reduce the role of entropy in determining the conformational make-up. These free energy trends, in conjunction with the preservation of structure across the solution, crystal, and gas-phase, imply that poly-ACHC is a robust 12/10 mixed-helical former that is to a large degree impervious to local environment.

Table 4.3. Relative energies and free energies (at 300 K) for structures under 20 kJ/mol of the global energy minimum for the Dimer calculated at the DFT B3LYP-D3BJ/6-31+G(d) level

<u>Conformer</u>	<u>Structure Type</u>	<u>ΔE (kJ/mol)</u>	<u>ΔG (kJ/mol)</u>
Conf A	R	0	0
AMBER_bp2_cyc_90.log:	L	10.365474	10.459992
AMBER_bp2_cyc_80.log:	R	11.210885	11.2292635
AMBER_bp2_cyc_112.log:	L	11.6230885	11.6230885
AMBER_bp2_cyc_32.log:	L	13.9702855	13.972911
AMBER_bp2_cyc_37.log:	L	14.214457	14.2170825
AMBER_bp2_cyc_31.log:	L	14.4323735	14.4481265
AMBER_bp2_cyc_24.log:	R	16.5065185	16.509144
AMBER_bp2_cyc_109.log:	L	17.43332	17.43332
AMBER_bp2_cyc_85.log:	L	17.968922	17.9820495
AMBER_bp2_cyc_118.log:	L	18.840588	18.8432135

Table 4.4. Relative energies and free energies (at 300 K) for structures under 20 kJ/mol of the global energy minimum for the L-Dimer calculated at the DFT B3LYP-D3BJ/6-31+G(d) level

<u>Conformer</u>	<u>Structure Type</u>	<u>ΔE (kJ/mol)</u>	<u>ΔG (kJ/mol)</u>
Conf A	L	0	0.462088
NTerm_m__38.log:	R	7.435416	1.62781
NTerm_m__3.log:	L	7.697966	1.9507465
NTerm_m__13.log:	L	8.8243055	6.190929
NTerm_m__40.log:	T	9.1183615	0
NTerm_m__57.log:	R	9.262764	0.8375345
NTerm_m__74.log:	T	10.1055495	3.103341
NTerm_m__15.log:	L	13.8390105	15.8343905
NTerm_m__9.log:	L	16.43563	13.7917515
NTerm_m__19.log:	L	16.5117695	10.2263225
NTerm_m__24.log:	T	17.249535	12.135061
NTerm_m__34.log:	L	17.963671	15.5088285

Table 4.6. Relative energies and free energies (at 300 K) for structures under 20 kJ/mol of the global energy minimum for the LL-Dimer calculated at the DFT B3LYP-D3BJ/6-31+G(d) level

<u>Conformer</u>	<u>Structure Type</u>	<u>ΔE (kJ/mol)</u>	<u>ΔG (kJ/mol)</u>
Conf A	L	0	0
Nmm__34.log:	L	7.713719	1.1263395
Nmm__10.log:	L	9.042222	5.3901515
Nmm__92.log:	T	17.80089	12.040543
Nmm__11.log:	L	18.3496195	9.730103

Table 4.5. Relative energies and free energies (at 300 K) for structures under 20 kJ/mol of the global energy minimum for the R-Dimer calculated at the DFT B3LYP-D3BJ/6-31+G(d) level

<u>Conformer</u>	<u>Structure Type</u>	<u>ΔE (kJ/mol)</u>	<u>ΔG (kJ/mol)</u>
Conf A	R	0	0
cTrm_m__30.log:	T	13.2614005	11.016598
cTrm_m__46.log:	R	13.5186995	11.588957
cTrm_m__70.log:	T	14.3273535	14.5741505
cTrm_m__10.log:	L	16.6955545	24.480162
cTrm_m__37.log:	L	16.740188	22.868105
cTrm_m__39.log:	L	17.685368	28.0429655

Table 4.7. Relative energies and free energies (at 300 K) for structures under 20 kJ/mol of the global energy minimum for the RR-Dimer calculated at the DFT B3LYP-D3BJ/6-31+G(d) level

<u>Conformer</u>	<u>Structure Type</u>	<u>ΔE (kJ/mol)</u>	<u>ΔG (kJ/mol)</u>
Conf A	R	0	0
CTrm_mm__7.log:	L	18.420508	26.7302155
CTrm_mm__30.log:	T	20.667936	21.0486335

Table 4.9. Relative energies and free energies (at 300 K) for structures under 20 kJ/mol of the global energy minimum for the Trimer calculated at the DFT B3LYP-D3BJ/6-31+G(d) level

<u>Conformer</u>	<u>Structure Type</u>	<u>ΔE (kJ/mol)</u>	<u>ΔG (kJ/mol)</u>
Conf A	L	0	5.1118485
Conf B	R	0.199538	0
TriACHC_5.log:	L	6.768539	3.2897515
TriACHC_40.log:	R	7.6323285	9.1708715
TriACHC_42.log:	T	8.259823	9.6329595
TriACHC_27.log:	R	9.042222	12.0064115
TriACHC_93.log:	L	9.39929	12.240081
TriACHC_24.log:	L	11.5548255	11.8068735
TriACHC_19.log:	L	12.0326665	9.1183615
TriACHC_10.log:	T	13.085492	13.9230265
TriACHC_89.log:	L	15.212147	11.667722
TriACHC_18.log:	L	16.59316	15.9604145
TriACHC_13.log:	R	16.719184	16.813702
TriACHC_44.log:	L	17.6669895	19.607234
TriACHC_20.log:	R	18.2498505	15.926283
TriACHC_55.log:	L	19.2370385	23.204169

Table 4.8. Relative energies and free energies (at 300 K) for structures under 20 kJ/mol of the global energy minimum for the Tetramer calculated at the DFT B3LYP-D3BJ/6-31+G(d) level

<u>Conformer</u>	<u>Structure Type</u>	<u>ΔE (kJ/mol)</u>	<u>ΔG (kJ/mol)</u>
Conf A	R	0	0
Conf B	L	6.72128	10.3838525
Tetra_53.log:	L	10.5151275	10.55451
Tetra_3.log:	L	14.4901345	17.281041
Tetra_4.log:	L	14.603031	15.1360075
Tetra_7.log:	L	15.12288	18.835337
Tetra_20.log:	L	15.7923825	21.3531915
Am_TetR__10.log:	T	15.8133865	22.742081
Tetra_23.log:	L	16.955479	21.0223785
Tetra_40.log:	L	20.137585	21.6577495

A natural point of comparison of the conformational preferences of the present series of molecules is with the aforementioned Z-Gly_n-OH, with n=1,3,5. In so doing, we are comparing the least constrained α -peptide ((Gly)_n) with a highly-constrained ((ACHC)_n) β -peptide in the gas-phase. Interestingly, Z-Gly₅-OH adopts an ordered, 14/16 mixed-helix, somewhat analogous to the 12/10 helices studied here. At n=1 and 3 of Z-Gly_n-OH, however, the assigned structures shared little H-bonding similarity or dihedral angle patterning with the n=5 14/16 helical motif. This is in sharp contrast to the ACHC series, where even at the dipeptide level the preference for both left- and right-handed mixed helices are apparent (see Tables 4.1 and 4.2). This fact highlights the role of the ACHC residue as a pre-organized 12/10 helical former.

Furthermore, in the ACHC_n series studied here, all assigned conformers are low-energy structures, in contrast to several other peptides and foldamers studied in the gas-phase where at least one assigned structure is abnormally high in calculated relative energy.^{24, 34, 36, 42, 43} In these cases, the argument used to explain the presence of such structures is based on entropic grounds, where the temperature behind the expansion nozzle or in the laser-desorption plume renders the entropic term in free energy non-negligible. In such a circumstance, the initial conformational populations are determined not by potential energies, but by the relative free energies, where kinetic trapping and thermodynamic cooling then compete in the expansion process to produce the conformers which are then probed downstream in the molecular beam.

4.5 Conclusion

The conformational preferences of a series of cyclically constrained β -peptide foldamers were characterized in the gas-phase using single-conformation, IR-UV double resonance laser spectroscopy. At every size in the series Ac-(ACHC)_n-NHBn, n=2,3,4, two emergent secondary structures are observed: the right handed 12/10 mixed helix and the cap-disrupted left handed 12/10 mixed helix. DFT calculations predict that substitution of the intrusive C-terminal NHBn cap by a more natural NHMe cap will result in the pure left handed 12/10 mixed helix displacing the cap disrupted left handed 12/10 helix as a populated, low energy conformer.

We also investigated whether methylation at strategic sites in the cyclohexane backbone is an effective means of directing the helical sense preferred by the β -peptide. Already at the dipeptide (n=2) level, our experimental results indicate that a single methylated residue is

sufficient to shift all population into one screw sense or the other. Furthermore, computational results indicate that double methylation increases the energetic stability of the intended helical structure with respect to all other conformations.

In future studies, it would be interesting to characterize ACHC oligomers containing more than four residues, to test whether the emerging secondary structures remain the preferred conformation at even greater lengths. Such longer helices should also exhibit growing evidence of cooperative strengthening of the H-bonds within the helix.

These gas phase results indicate that even in the absence of solvent, the 12/10 mixed helix is a robust secondary structure that oligomers of the ACHC residue prefer in both the condensed phase and the vacuum. The similarity in calculated free and potential energies of this series of molecules is almost certainly due to the highly sterically constrained nature of the ACHC residue. The lack of flexibility exhibited by members of such a highly-constrained β -peptide building block could be a desirable trait when engineering foldamer based drugs which must adopt a particular secondary structure in both hydrophobic and hydrophilic environments. Additionally, the achirality of the “pseudosymmetric” (ACHC)₂ unit, which gives rise to the dynamic handed helices in certain environments, may be further constrained by ACHC methylation in situations where a single handedness is preferred over dynamic handedness.

Finally, having determined that both left- and right-handed 12/10-helices are present in these samples, IR-population transfer studies could be used to study their interconversion (or lack thereof).^{44, 45} Furthermore, laser desorption from a known, single-crystal sample would provide further insight to the role played by the molecular solid in determining the observed conformations in the gas phase.

4.6 References

1. J. R. Gord, P. S. Walsh, B. F. Fisher, S. H. Gellman and T. S. Zwier, *J. Phys. Chem. B*, 2014, **118**, 8246-8256.
2. S. H. Choi, *Biomed. Eng. Lett.*, 2013, **3**, 226-231.
3. M. Crisma, F. Formaggio, A. Moretto and C. Toniolo, *Pept. Sci.*, 2006, **84**, 3-12.
4. D. Barlow and J. Thornton, *J. Mol. Biol.*, 1988, **201**, 601-619.
5. B. A. Le Bailly and J. Clayden, *Chem. Commun.*, 2016, **52**, 4852-4863.

6. S. Shin, M. Lee, I. A. Guzei, Y. K. Kang and S. H. Choi, *J. Am. Chem. Soc.*, 2016.
7. G. Jang, S. Shin, I. A. Guzei, S. Jung, M.-G. Choi and S. H. Choi, *Bull. Korean Chem. Soc.*, 2018, **39**, 265-268.
8. M. Banno, T. Yamaguchi, K. Nagai, C. Kaiser, S. Hecht and E. Yashima, *J. Am. Chem. Soc.*, 2012, **134**, 8718-8728.
9. K. Maeda and E. Yashima, in *Supramolecular Chirality*, Springer, 2006, pp. 47-88.
10. Y. Z. Ke, Y. Nagata, T. Yamada and M. Sugimoto, *Angew. Chem. Int. Ed.*, 2015, **54**, 9333-9337.
11. S. J. Dawson, Á. Mészáros, L. Pethő, C. Colombo, M. Csékei, A. Kotschy and I. Huc, *Eur. J. Org. Chem.*, 2014, **2014**, 4265-4275.
12. D. Seebach and J. L. Matthews, *Chem. Commun.*, 1997, 2015-2022.
13. S. H. Gellman, *Acc. Chem. Res.*, 1998, **31**, 173-180.
14. R. P. Cheng, S. H. Gellman and W. F. DeGrado, *Chem. Rev.*, 2001, **101**, 3219-3232.
15. D. Seebach, D. F. Hook and A. Glättli, *Pept. Sci.*, 2006, **84**, 23-37.
16. D. Seebach and J. Gardiner, *Acc. Chem. Res.*, 2008, **41**, 1366-1375.
17. W. S. Horne and S. H. Gellman, *Acc. Chem. Res.*, 2008, **41**, 1399-1408.
18. L. M. Johnson and S. H. Gellman, in *Methods Enzymol.*, ed. A. E. Keating, Academic Press, 2013, vol. 523, pp. 407-429.
19. Y. Hamuro, J. P. Schneider and W. F. DeGrado, *J. Am. Chem. Soc.*, 1999, **121**, 12200-12201.
20. M. Werder, H. Hauser, S. Abele and D. Seebach, *Helv. Chim. Acta*, 1999, **82**, 1774-1783.
21. G. L. Simpson, A. H. Gordon, D. M. Lindsay, N. Promsawan, M. P. Crump, K. Mulholland, B. R. Hayter and T. Gallagher, *J. Am. Chem. Soc.*, 2006, **128**, 10638-10639.
22. I. M. Mándity, L. Fülöp, E. Vass, G. K. Tóth, T. A. Martinek and F. Fülöp, *Org. Lett.*, 2010, **12**, 5584-5587.
23. S. H. Choi, M. Ivancic, I. A. Guzei and S. H. Gellman, *Eur. J. Org. Chem.*, 2013, **2013**, 3464-3469.
24. K. N. Blodgett, X. Zhu, P. S. Walsh, D. Sun, J. Lee, S. H. Choi and T. S. Zwier, *J. Phys. Chem. A*, 2018, DOI: 10.1021/acs.jpca.8b01273.

25. D. H. Appella, L. A. Christianson, I. L. Karle, D. R. Powell and S. H. Gellman, *J. Am. Chem. Soc.*, 1996, **118**, 13071-13072.
26. Y.-D. Wu, W. Han, D.-P. Wang, Y. Gao and Y.-L. Zhao, *Acc. Chem. Res.*, 2008, **41**, 1418-1427.
27. C. Baldauf, R. Günther and H.-J. Hofmann, *Angew. Chem. Int. Ed.*, 2004, **43**, 1594-1597.
28. C. Baldauf, R. Günther and H.-J. Hofmann, *Pept. Sci.*, 2006, **84**, 408-413.
29. T. S. Zwier, *Annu. Rev. Phys. Chem.*, 1996, **47**, 205-241.
30. F. Mohamadi, N. G. Richards, W. C. Guida, R. Liskamp, M. Lipton, C. Caufield, G. Chang, T. Hendrickson and W. C. Still, *J. Comput. Chem.*, 1990, **11**, 440-467.
31. M. Frisch, G. Trucks, H. Schlegel, G. Scuseria, M. Robb, J. Cheeseman, G. Scalmani, V. Barone, G. Petersson and H. Nakatsuji, *Revision A*, 2016, **3**.
32. S. Grimme, *J. Comput. Chem.*, 2004, **25**, 1463-1473.
33. S. Grimme, *J. Chem. Phys.*, 2006, **124**, 034108.
34. J. R. Gord, D. M. Hewett, A. O. Hernandez-Castillo, K. N. Blodgett, M. C. Rotondaro, A. Varuolo, M. A. Kubasik and T. S. Zwier, *PCCP*, 2016, **18**, 25512-25527.
35. P. S. Walsh, J. C. Dean, C. McBurney, H. Kang, S. H. Gellman and T. S. Zwier, *PCCP*, 2016, **18**, 11306-11322.
36. J. C. Dean, E. G. Buchanan and T. S. Zwier, *J. Am. Chem. Soc.*, 2012, **134**, 17186-17201.
37. J. L. Fischer, B. R. Elvir, S.-A. DeLucia, K. N. Blodgett, M. Zeller, M. A. Kubasik and T. S. Zwier, *J. Phys. Chem. A*, 2019, DOI: 10.1021/acs.jpca.9b01698.
38. K. N. Blodgett, J. L. Fischer, J. Lee, S. H. Choi and T. S. Zwier, *J. Phys. Chem. A*, 2018, DOI: 10.1021/acs.jpca.8b08418.
39. E. G. Buchanan, W. H. James, S. H. Choi, L. Guo, S. H. Gellman, C. W. Müller and T. S. Zwier, *J. Chem. Phys.*, 2012, **137**, 094301.
40. C. R. Maechling, S. J. Clemett, F. Engelke and R. N. Zare, *J. Chem. Phys.*, 1996, **104**, 8768-8776.
41. M. Handschuh, S. Nettesheim and R. Zenobi, *J. Chem. Phys.*, 1997, **107**, 2603-2610.
42. E. Gloaguen, B. De Courcy, J.-P. Piquemal, J. Pilmé, O. Parisel, R. Pollet, H. Biswal, F. Piuze, B. Tardivel and M. Broquier, *J. Am. Chem. Soc.*, 2010, **132**, 11860-11863.
43. V. A. Shubert, E. E. Baquero, J. R. Clarkson, W. H. James III, J. A. Turk, A. A. Hare, K. Worrel, M. A. Lipton, D. P. Schofield and K. D. Jordan, *J. Chem. Phys.*, 2007, **127**, 234315.

44. B. C. Dian, A. Longarte, P. R. Winter and T. S. Zwier, *J. Chem. Phys.*, 2004, **120**, 133-147.
45. B. C. Dian, A. Longarte and T. S. Zwier, *Science*, 2002, **296**, 2369-2373.

CHAPTER 5. CONFORMATION-SPECIFIC SPECTROSCOPY OF ASPARAGINE-CONTAINING PEPTIDES: INFLUENCE OF SINGLE AND ADJACENT ASN RESIDUES ON INHERENT CONFORMATIONAL PREFERENCES

Adapted with permission from *J. Phys. Chem. A*, 2018, 122, 44, 8762-8775. Copyright 2018 American Chemical Society.

5.1 Introduction

The polar amino acids asparagine and glutamine, differing by one methylene group, are the only two naturally occurring amino acids that contain carboxamide groups in their flexible side chains. Both amino acids are heavily involved in neurodegenerative disease pathogenesis.¹⁻⁵ At the genetic level, CAG codon repeat disorders result in long tracts of glutamine residue repeats within proteins, which subsequently fold into β -sheet oligomers that aggregate to form insoluble amyloid fibrils, the hallmark of neurodegenerative disease.^{6, 7} Nine late onset neurodegenerative diseases, including Huntington's disease, are attributed to polyglutamine expansions.^{8, 9}

Prion diseases, on the other hand, are characterized by the misfolding of native proteins into self-aggregating β -sheet units which ultimately form insoluble amyloid fibrils that wreak havoc on the central nervous system.^{10, 11} The so-called prion forming domains of the proteins, which are responsible for protein misfolding, are rich in both asparagine (Asn, N) and glutamine (Gln, Q).¹²⁻¹⁴ In humans, prion diseases are caused by the misfolding of the PrP^C protein into its prion form, PrP^{Sc}.¹⁵ These diseases include Creutzfeldt-Jakob disease, fatal familial disease, and Gerstmann-Straussler-Scheinker syndrome.^{15, 16} Rather than being propagated through the genome, prion forms of misfolded proteins induce other normally folded proteins to isomerize to the prion state, thereby causing a chain reaction of protein misfolding and disease propagation.

These amyloid fibrils all appear to contain a common structural motif: the steric zipper. In this structure, at least two β -sheets are interdigitated with one another, often times sterically locking in Asparagine and Glutamine residues.^{2, 17, 18} Studies using solid state NMR spectroscopy, X-ray crystallography and EPR spectroscopy have demonstrated that many amyloids formed from prion and prion-like proteins fold into an in-register parallel β -sheet, in which steric zipper monomer units hydrogen bond with one another to form parallel β -sheets which propagate along

the fibril axis. These proteins include β -amyloid (Alzheimer's),¹⁹⁻²¹ and the yeast proteins Sup35^{22, 23} and Ure2p²⁴⁻²⁶. Many studies have sought to determine the role of Asn and Gln in the prion forming domains of proteins, as well as the difference in aggregation propensity between the residues.^{1-3, 10, 14, 27-31} In this study, we are interested in determining the role that Asn plays in local protein conformation by spectroscopically characterizing the conformational impact of the alkyl-linked carboxamide side chain in three increasingly complex peptides.

To this end, we use a bottom up approach towards understanding nature's preference for Asparagine in neurodegenerative diseases. We seek to determine the role that one or two Asn residues has on the intrinsic folding propensities of three short, capped peptides: Ac-Asn-NHBn, Ac-Ala-Asn-NHBn, and Ac-Asn-Asn-NHBn (Figure 5.1). Each peptide is capped with a benzyl group which acts as a UV chromophore. We characterize the inherent conformational preferences of each peptide in the absence of environmental perturbations, by recording spectra of the gas-phase molecules in a molecular beam using mass resolved double-resonance infrared and ultraviolet spectroscopy. Computational and experimental studies on close analogues of Ac-Asn-NHBn show extended and inverse γ -turn backbone structures to be among the lowest energy conformational isomers (conformers).^{32, 33} Previous conformational studies in our group on analogous Glutamine-containing peptides showed that Ac-Gln-NHBn had population spread out between three conformers in the molecular beam: an extended backbone structure, an inverse γ -turn backbone structure, and a turned backbone structure lacking any backbone-backbone amide hydrogen bonds.³⁴ Mons and coworkers identified three conformers of Ac-Phe-Asn-NH₂ in a molecular beam: a β -turn, a γ -turn, and an extended backbone structure.³³ The analogous Gln-containing dipeptides each funneled all population into a single conformer: the type 1 β -turn.^{34, 35}

Comparing the conformational preferences of Asn with those of the analogous Gln-containing peptides gives direct insight to the impact of the shortening of the carboxamide side chain by a single methylene group. Armed with the conformer-specific spectra and assignments, we thus address the similarities and differences of the Asn and Gln conformations.

Studies of synthetic foldamers containing β -residues are particularly relevant to the hydrogen bonding motifs accessible to the Asn side chain amide group. The elongated peptide backbones in β -peptides give access hydrogen bonding cycles not available to α -peptides.³⁶⁻³⁹ The Asn residues are capable of forming the same hydrogen bonds by virtue of them having the same number of carbon atoms (two) between backbone and sidechain amide groups as separate residues

in the peptide backbone of β -peptides. On this basis, it is fair to anticipate similar hydrogen bonding in the Asn-containing peptides to that observed in the β -peptides. As we shall see, the Asn-containing peptides presented in Figure 5.1 are capable of forming hydrogen bonds which support extended peptide backbones, inverse γ -turns, and type I β -turns.

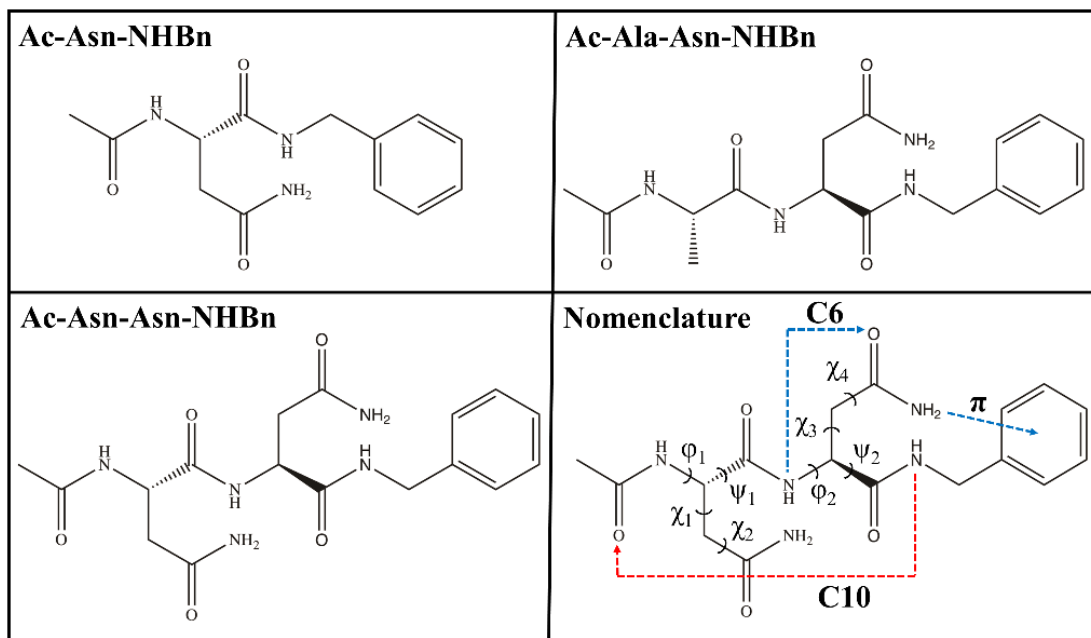


Figure 5.1. Chemical structures of the molecules studied in this work along with the definition of important dihedral angles used herein. Note that hydrogen bonds designated in blue indicate backbone-sidechain hydrogen bonding while those designated in red indicate backbone-backbone hydrogen bonding.

5.2 Methods

5.2.1 Experimental Methods

Samples were synthesized by the Choi research group at Yonsei University. The experimental procedure for studying their spectroscopy has been described in detail in Chapter 2. Briefly, sublimation of the sample was achieved by non-resonant laser desorption.^{40, 41} The crystal sample was crushed into a fine powder and rubbed onto the surface of a sanded graphite rod, which is coupled into the vacuum chamber via a load lock assembly. The fundamental of a Nd:YAG (20

Hz, Continuum minilite II, 5mJ/pulse, 2mm beam diameter) laser strikes the surface of the graphite rod, thereby desorbing neutral sample into the gas-phase. The rod is kept directly under the 1000 μm diameter orifice of a pulsed valve (Parker, series 9) which introduces short bursts of high-pressure Argon backing gas (20 Hz, ~ 5.5 bar backing pressure, 500 μs) into the vacuum chamber. The sample is entrained in the supersonic expansion and is subsequently cooled into the zero-point vibrational levels of low energy lying conformational minima. A linear actuator (NSC 200, Newport) slowly pushes the sample-containing rod into the chamber, thereby ensuring consistent sample concentration in each desorption laser pulse. The supersonic expansion passes through a conical skimmer, becoming a molecular beam, which then travels into the ion source region of a Wiley McLaren time-of-flight (TOF) mass spectrometer. The cold, neutral molecules are then characterized using a suite of laser-based methods.

The first step in characterizing each molecule is using one-color resonant two-photon ionization (R2PI), in which a UV spectrum with contributions from all conformations with measurable population is obtained. The doubled output of a Nd:YAG pumped tunable dye laser is scanned across the benzyl UV chromophore absorption region ($37,500 - 37,820 \text{ cm}^{-1}$). When the frequency is resonant with a vibronic transition of a cold conformer a photon is absorbed, immediately after which a second ionizing photon is absorbed. Monitoring the parent mass channel of the absorbing species as a function of UV frequency allows the recording of the electronic spectrum. Conformer-specific infrared spectra are recorded using resonant ion-dip infrared spectroscopy (RIDIRS). In this scheme the UV laser (20 Hz) is fixed on a vibronic transition belonging to one of the conformers in the R2PI spectrum, thereby generating a constant ion signal that is proportional to the ground state population of that conformer. The tunable output of a KTP/KTA based optical parametric converter (LaserVision, 10 Hz) spatially overlaps and temporally precedes by 200 ns the UV beam. As the IR laser is scanned across the regions of interest, resonance between the IR frequency and a ground state vibration of the conformer being probed results in the removal of a fraction of ground state population, and a subsequent dip in ion signal. A gated integrator (Stanford Research Systems, SR 250) in active baseline subtraction mode outputs the difference in integrated parent ion signal as a function of IR frequency, resulting in a conformer-specific infrared spectrum. Infrared-ultraviolet (IR-UV) holeburning is used to generate conformer-specific UV spectra. This scheme is identical to RIDIRS except that the IR laser is fixed on a conformer-specific vibrational transition while the UV laser is scanned.

5.2.2 Computational Methods

The potential energy surface of each molecule studied herein was initially explored with an exhaustive force field search using a torsional-sampling Monte Carlo Multiple Minimum conformational search within the MacroModel computational suite. Searches were performed with both the OPLS3 and Amber* force fields until successive search iterations yielded no additional structures. A redundant conformer elimination performed on the pool of structures calculated to be below 50 kJ/mol generated from both force fields yielded starting structures for higher level calculation.

Density functional theory geometry optimization and harmonic normal mode frequency calculations were carried out on each candidate structure, using the Gaussian09 computational package⁴², with Becke's B3LYP hybrid functional supplemented with the D3 version of Grimme's dispersion correction⁴³ and Becke-Johnson damping⁴⁴ (GD3BJ). This modified hybrid functional was used in conjunction with the 6-31+G(d) Pople basis set. Tight convergence and an ultrafine grid were implemented in each calculation to ensure output of the best possible normal mode frequencies to compare with experiment. Harmonic vibrational frequencies were calculated for all structures. Scale factors of 0.958, 0.981, and 0.970 were used in the hydride stretch, amide I, and amide II regions, respectively, to account for anharmonicity of the vibrations. Energy considerations, vibronic assignments, and agreement between calculated and experimental IR frequencies led to the conformational assignment of each experimentally observed conformer.

5.2.3 Nomenclature

Hydrogen bonds are designated with the C_n notation, in which n is the number of atoms involved in a hydrogen bonded cycle. We invoke the same conformational labeling scheme used in previous studies of analogous Gln-containing peptides.^{34, 35} Hydrogen bonds are listed in the following stylized order: backbone-backbone//*sidechain-backbone*//**sidechain-sidechain**. For example, the labelled conformer in Figure 5.1 is designated as a C10//C6/ π hydrogen bonded structure where a ten-membered hydrogen bond ring is formed between backbone amide groups while the N-terminal Asn carboxamide group acts as a bridge to the peptide backbone (or in this case, cap) comprised of C6 and NH \cdots π H-bonds. In addition, and unless otherwise stated,

backbone-backbone hydrogen bonds are shown as blue dashed lines in the figures, while *sidechain-backbone* hydrogen bonds are designated with red dashed lines.

In certain parts of the discussion, both ‘Asn’ and ‘N’ will be used to designate Asparagine, while both ‘Gln’ and ‘Q’ will be used to designate Glutamine. Important peptide backbone and sidechain dihedral angles are defined in Figure 5.1. Additional dihedral angles, designated as χ_{Q1} and χ_{Q2} , refer to the one additional N- and C-terminal Gln side chain dihedrals, respectively. Finally, the ‘*i*+’ notation will be used to identify groups within particular residues along the peptide backbone. The *C6* of the labelled molecule in Figure 5.1, for example, is between the amide NH and Asn C=O of residue *i*+2, while the C10 is between the amide NH of residue *i*+3 and C=O of residue *i*. Crystal structures referenced within were taken from the RCSB Protein Data Bank⁴⁵ after a secondary structure search using the Motivated Proteins web tool.⁴⁶

5.3 Results and Analysis

5.3.1 Ac-Asn-NHBn

The R2PI and IR-UV holeburning spectra for Ac-Asn-NHBn are shown in Figure 5.2. These spectra were obtained by scanning the UV laser across the S_0 - S_1 region in which the NHBn chromophore absorbs ($37,500 - 37,820 \text{ cm}^{-1}$). The R2PI spectrum displays two Franck-Condon progressions in ~ 8 and $\sim 10 \text{ cm}^{-1}$ modes, with the largest component transitions appearing at $37,627$ and $37,578 \text{ cm}^{-1}$, respectively. IR-UV holeburning spectra, shown in red and blue, reveal that these two sets of peaks are due to two unique conformers, labelled conf. A and conf. B in Figure 5.2. Normal mode analysis of the assigned conformers shows that, in each case, the Franck-Condon active vibration is the twisting of the phenyl ring, causing a modulation of the CCCN dihedral angle.

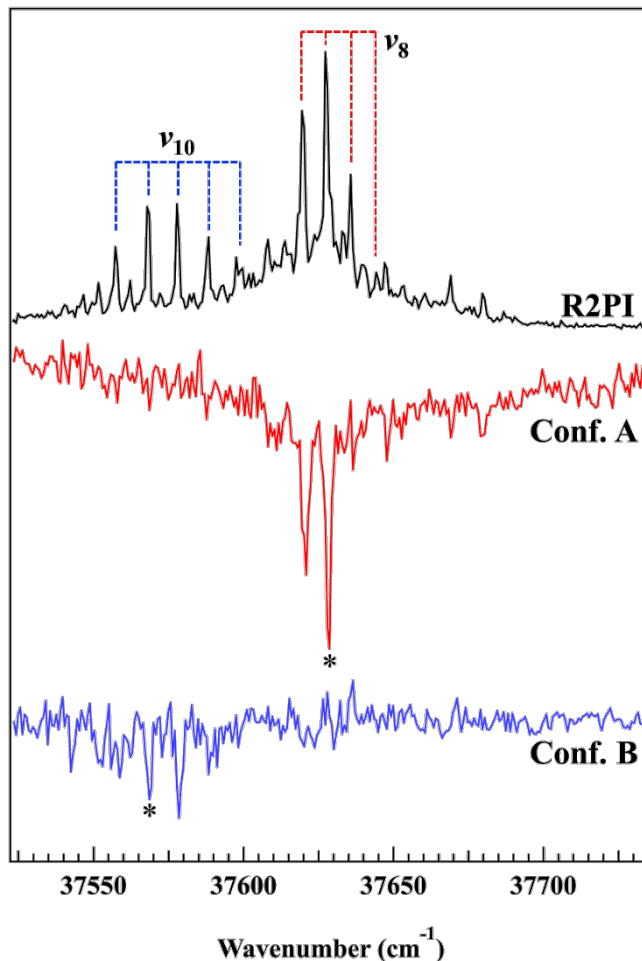


Figure 5.2. R2PI and IR-UV holeburning spectra of Ac-Asn-NHBn. Peaks marked with an asterisk ($37,629\text{ cm}^{-1}$, Conf. A; $37,569\text{ cm}^{-1}$, Conf. B) indicate transitions used to collect RIDIR spectra. Vibronic progressions are labeled with tie lines

The RIDIR spectra of conformer A and conformer B are presented in the top (red) and bottom (blue) portions of Figure 5.3, respectively. Below each experimental trace is a stick spectrum that depicts the scaled, harmonic normal mode frequencies of each best fit structure. Each transition is labelled with the main carrier(s) of the vibration as determined through inspection of the best-fit structure. The RIDIR spectra of conformers A and B are very similar to one another; however, small wavenumber shifts are present, confirming that two unique conformers are present.

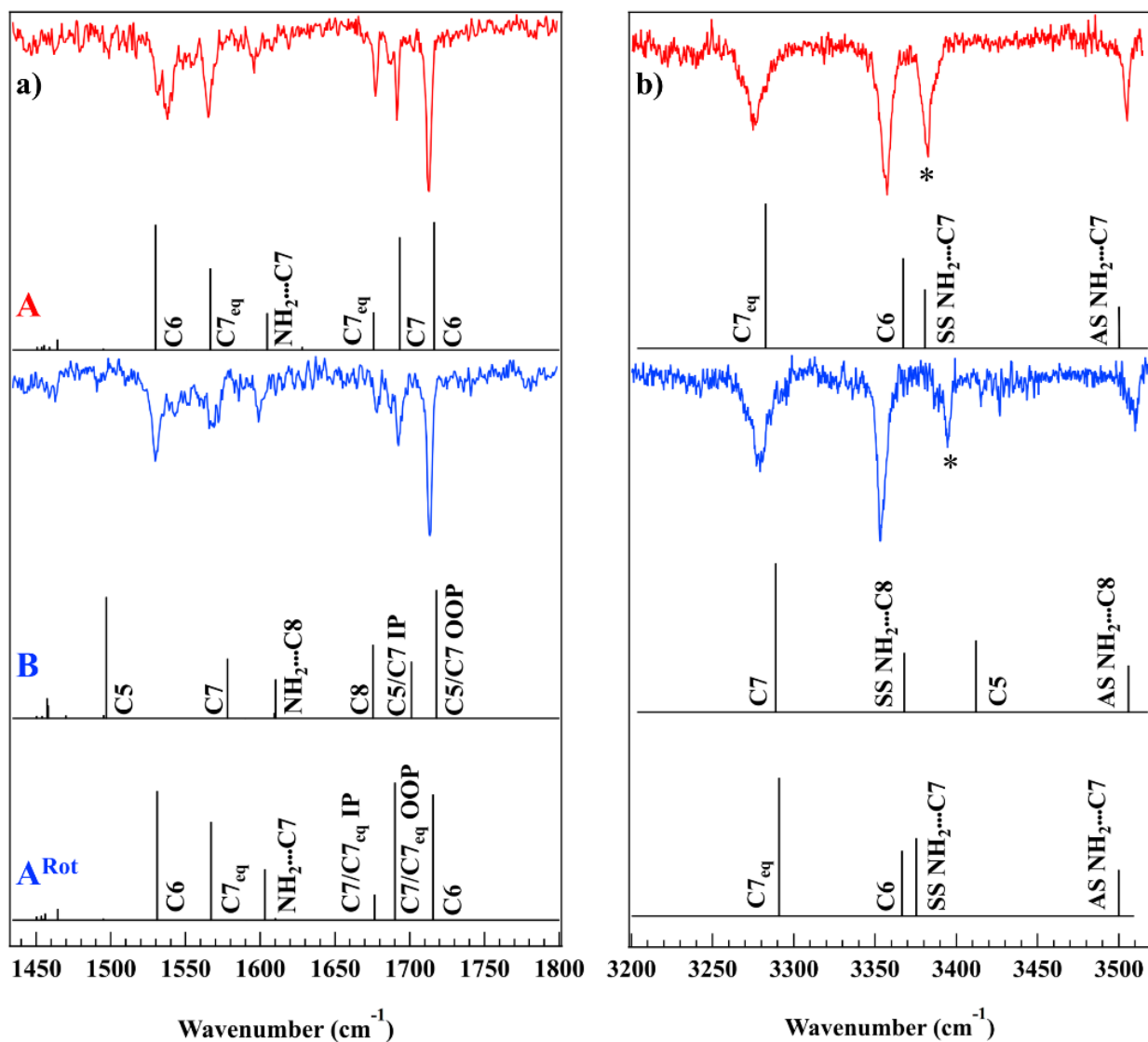


Figure 5.3. RIDIR spectra of the two conformers of Ac-Asn-NHBn, conformer A (red trace) and conformer B (blue trace), in the hydride stretch (b) and Amide I/II (a) regions. The stick spectra presented below each experimental trace represent the scaled, harmonic normal mode frequencies of each assigned conformer calculated at the B3LYP-D3BJ/6-31+G(d) level of theory and are labelled with the main carrier(s) of the vibration. Transitions marked with an asterisk are those used to collect IR-UV holeburning spectra. See text for further discussion

Given the two backbone amide NH groups and the NH₂ group on the Asn side chain, we anticipate observing four NH stretch fundamentals for each conformer, as is observed in Figure 5.3b. In the hydride stretch region both conformers have their highest frequency transition well below ~3560 cm⁻¹, the frequency at which the asymmetric (AS) stretch of a free NH₂ group appears. This indicates that both conformers have their Asn NH₂ group involved in a hydrogen bond. The highest frequency transitions of conformer A and B appear at 3505 cm⁻¹ and 3510 cm⁻¹, respectively. The RIDIR spectrum of conformer B has asymmetrically broadened peaks that are likely due to a small spectral contamination from the RIDIR spectrum of conformer A. It is likely that the UV absorption of conformer A begins in the region where conformer B absorbs. However, this is difficult to determine via the IR-UV holeburning spectra of conformer A due primarily to the low signal and shot-to-shot fluctuations inherent to laser desorption. The fact that in both conformers the two highest frequency hydride stretches occur at wavenumbers in which the other conformer has zero absorption provides evidence that although qualitatively similar, the sources of these IR spectra are indeed independent of one another.

Based on agreement between experiment and theory, and as can be seen in Figure 5.4, conformer A is assigned to a C7_{eq}/C6/C7 structure with a bridged sidechain-backbone hydrogen bonding motif and the backbone in an inverse γ -turn. This conformer was calculated to be the global energy minimum. Table 5.1 presents hydrogen bond distances and experimental vibrational frequencies for the Asn-containing peptides studied herein and analogous Gln-containing peptides.^{34, 35}

Conformer A has three additional hydride stretch fundamentals at 3383, 3357, and 3275 cm⁻¹. The transition at 3383 cm⁻¹ is assigned to the symmetric NH₂ stretch of the Asn moiety, forming a pair with the asymmetric NH₂ stretch at 3505 cm⁻¹. Analysis of the assigned structure of conformer A shows that this NH₂ group is involved in a C7 hydrogen bond with the C-terminal O=C. The vibrational splitting⁴⁷ between the coupled asymmetric and symmetric NH₂ stretches is thus 122 cm⁻¹, a relatively small value which makes sense in light of the non-optimum hydrogen bond distance (2.15 Å) and angle of approach (129.3°). As a result, throughout this work we will use asymmetric and symmetric stretch (AS and SS) designations to describe the vibrations of the NH₂ moiety, as the normal mode analysis of the NH₂ vibrations shows large contributions from each NH oscillator in the coupled vibrations, even when one NH is involved in a hydrogen bond and the other is more or less free. The band at 3357 cm⁻¹ is localized on the N-terminal NH group

which is involved in a $C6$ hydrogen bond with the O=C oxygen on the Asn side chain. The lowest frequency hydride stretch at 3275 cm^{-1} has a FWHM of $\sim 17\text{ cm}^{-1}$, which is indicative of strong coupling to background states associated with a strong hydrogen bond. This transition is assigned to the C-terminal NH oscillator involved in a $C7_{eq}$ hydrogen bond with the N-terminal O=C. This strong hydrogen bond has a calculated $\text{NH}\cdots\text{O}=\text{C}$ distance of 1.90 \AA and NHO angle of approach equal to 151° .

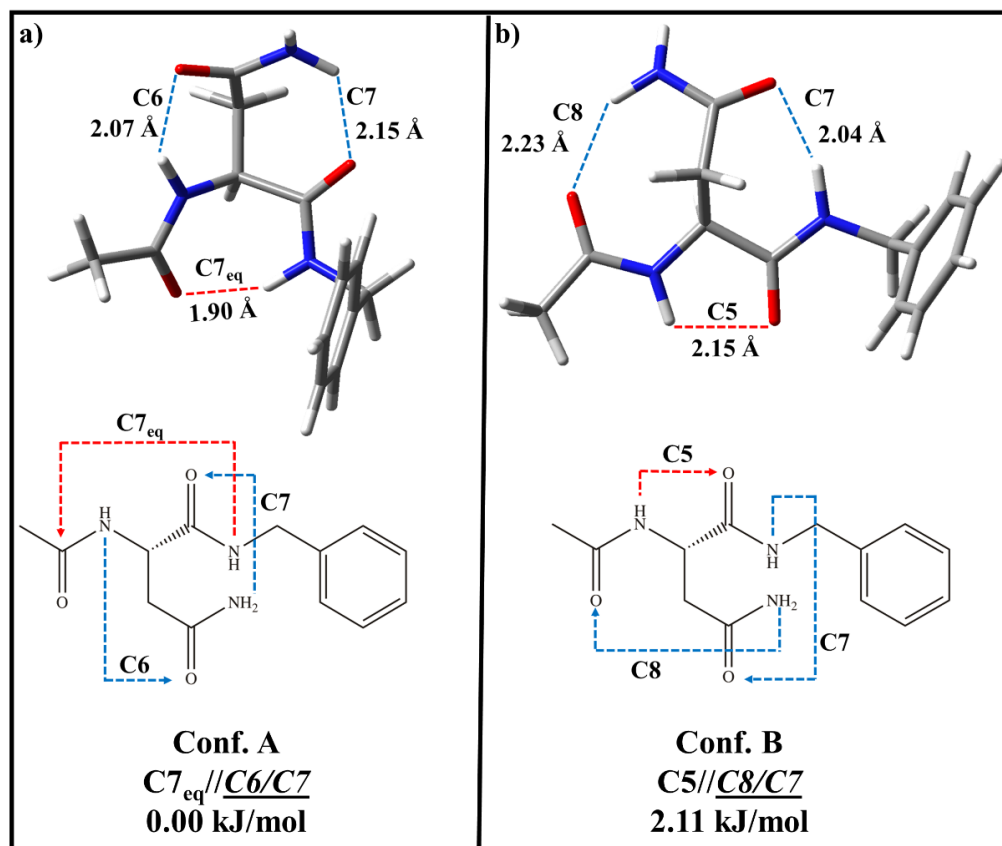


Figure 5.4. Assigned structure of (a) conformer A and (b) conformer B of Ac-Asn-NHBn. 3D structure and 2D hydrogen bonding schematic are presented for each conformer, as well as the hydrogen bonding designation and relative zero-point corrected potential energies.

Table 5.1. Hydrogen bonding cycles, calculated distances, and experimental vibrational frequencies for those interactions found in the Asn-containing peptides studied in this work, compared with the analogous Gln-containing peptides studied previously.

<u>Molecule</u>	<u>H-Bond Cycle</u>	<u>H-Bond Distance (Å)</u>	<u>Experimental Frequency (cm⁻¹)</u>
Ac-Asn-NHBn			
Conf A	C7 _{eq}	1.90	3275
(C7 _{eq} //C6/C7)	<u>C6</u>	2.07	3357
	<u>C7</u>	2.15	3383 (3505)
Conf B	C5	2.15	3394
(C5//C8/C7)	<u>C8</u>	2.23	3353 (3510)
	<u>C7</u>	2.04	3279
Conf A ^{Rot}	C7 _{eq}	1.91	3279
(C7 _{eq} //C6/C7)	<u>C6</u>	2.09	3353
	<u>C7</u>	2.13	3394 (3310)
Ac-Gln-NHBn ^a			
Conf A	C5	2.11	3402
(C5//C8)	<u>C8</u>	1.96	3310
Conf B	C7	1.97	3354
(C7/π)	π		3415 (3529)
Conf C	C7 _{eq}	1.92	3270
(C7 _{eq} //C7/C8/π)	<u>C7</u>	1.99	3343
	<u>C8</u>	2.24	3400 (3509)
Ac-Ala-Asn-NHBn			
Conf A	C10	1.99	3367
(C10//C6/π)	<u>C6</u>	2.08	3373
	π		3395 (3502)
Ac-Ala-Gln-NHBn ^a			
Conf A	C10	2.02	3357
(C10//C7/π)	<u>C7</u>	1.97	3361
	π		3408 (3520)
Ac-Asn-Asn-NHBn			
Conf A	C10	2.01	3350
(C10//C6/C6/π)	<u>C6</u>	2.16	3383
	<u>C6</u>	2.07	3359
	π		3393 (3505)
Ac-Gln-Gln-NHBn ^b			
Conf A	C10	1.99	3345
(C10//C7/C7/π)	<u>C7</u>	1.91	3324
	<u>C7</u>	1.98	3360
	π		3409 (3521)

^aFrom ref 34

^bFrom ref 35

The amide I region of conformer A (Figure 5.3) contains vibrational transitions which report on the hydrogen bonds from the perspective of the C=O hydrogen bond acceptor oscillators. Conformer A has three C=O stretch fundamentals appearing at 1713, 1691, and 1677 cm^{-1} which are assigned to the localized stretch fundamentals of the C=O oscillators involved in the C6, C7, and C7_{eq} hydrogen bonds, respectively. While the amide I (and amide II) region is less physically intuitive to analyze, C=O stretch fundamentals are generally shifted down in frequency when accepting hydrogen bonds, with further down shifts arising when the co-amide NH acts as hydrogen bond donor.^{40, 48} The C7_{eq} C=O stretch is the most down shifted in frequency, affirming the strong nature of this hydrogen bond.

The amide II region of conformer A, contributed to primarily by the NH bending motion, shows three clear transitions with increasing intensity at 1596, 1565, and 1538 cm^{-1} . The match between the experimental and calculated frequencies allows us to assign the peak at 1596 cm^{-1} to the Asn NH_2 , which acts as C7 hydrogen bond donor. The peaks at 1565 and 1538 cm^{-1} are assigned to the hydrogen bond donating groups of the C7_{eq} and C6 cycles, respectively. The integrated intensity of the C6 cycle at 1538 cm^{-1} is the largest of the amide II transitions. This intensity gain has been theoretically characterized as cooperative coupling between the dipole derivatives induced by the amide II nuclear motion and the electronic charge flux through the $\text{O}\cdots\text{H}$ interaction.^{49, 50} In the case of C5 and C6 hydrogen bonds, these two dipole derivative vectors are nearly parallel to one another, resulting in an enhancement of the transition intensity.

Conformer B has its hydride stretch fundamentals at 3510, 3394, 3353, and 3279 cm^{-1} . The highest frequency transition is readily assigned to the asymmetric NH_2 stretch, leaving the peaks at 3394 and 3353 cm^{-1} as possibilities for the symmetric stretch transition with vibrational splittings of 115 or 157 cm^{-1} , respectively. Since the asymmetric stretch is shifted down in frequency by ~ 50 cm^{-1} from where the unperturbed vibration occurs at 3562 cm^{-1} , one would anticipate the symmetric stretch to be shifted by more than 115 cm^{-1} . On that basis, the transition at 3353 cm^{-1} is tentatively assigned to the symmetric NH_2 fundamental.

Two possible assignments are presented in Figure 2 for conformer B. The assignment we deem to be most consistent with experiment is labeled as B in the figure, and is due to the conformer shown in Figure 5.4b, a $\text{C5}//\text{C8}/\text{C7}$ structure in which the Asn amide group forms C8 and C7 H-bonds with the amide groups on either side. In this assignment, the transition at 3353 cm^{-1} is ascribed to the symmetric NH_2 fundamental involved in a C8 hydrogen bond with the N-

terminal C=O group. Likewise, the transition at 3394 cm^{-1} is assigned to a C5 hydrogen bond between the Asn backbone amide group components. The shift down in frequency of the C5 hydrogen bonded NH, which can appear as high as $\sim 3440 \text{ cm}^{-1}$, may be attributed to cooperative effects from the nearest neighbor hydrogen bonded interactions (see section 4A for further discussion). The broad (15 cm^{-1} FWHM) transition at 3279 cm^{-1} is assigned to a C7 hydrogen bond between the C-terminal NH and Asn C=O. This strong hydrogen bond has a calculated NH \cdots O distance of 2.04 Å and angle of approach of 160°.

The tentative assignment of conformer B to the C5//C8/C7 structure shown in Figure 5.4b, has its energy just 2.11 kJ/mol above that of conformer A, the global minimum. The amide I spectra of conformer B show three clearly-resolved transitions at 1713, 1692, and 1678 cm^{-1} in order of decreasing intensity. The transitions at 1713 and 1692 cm^{-1} are assigned to the out-of-phase and in-phase combinations, respectively, of the carbonyl groups in the C5 and C7 cycles. The small transition at 1678 cm^{-1} is assigned to the N-terminal C=O in the C8 cycle.

The three amide II transitions appear at 1599, 1569, and 1529 cm^{-1} . The weak transition at 1599 cm^{-1} is assigned to the NH₂ group involved in the C8 cycle, while the transition at 1569 cm^{-1} is attributed to the C7 bound NH. The intense peak at 1529 cm^{-1} is assigned to the extended backbone C5 hydrogen bond. As discussed above, the large intensity of this transition is likely due to the interaction of the transition dipole caused by the NH bending motion and the electronic charge flux through the O \cdots H interaction. This interaction geometry is optimized in the C5 hydrogen bond, in which both vectors are nearly parallel to one another.

The stick diagram A^{Rot} in Figure 5.3 presents an alternative possibility for conformer B, a benzyl rotamer of the assigned conformer A inverse γ -turn structure, with structure shown in Figure 5.5. This conformer is calculated to be the second lowest energy structure, at 1.7 kJ/mol above the global minimum (conformer A). As can be seen in Figure 5.3, the simulated spectra also fits well with the experimental IR spectra of conformer B. While the currently assigned extended structure fits better with the experimental data in the hydride stretch region, the calculated spectra of A^{Rot} fits somewhat better in the Amide I and II regions.

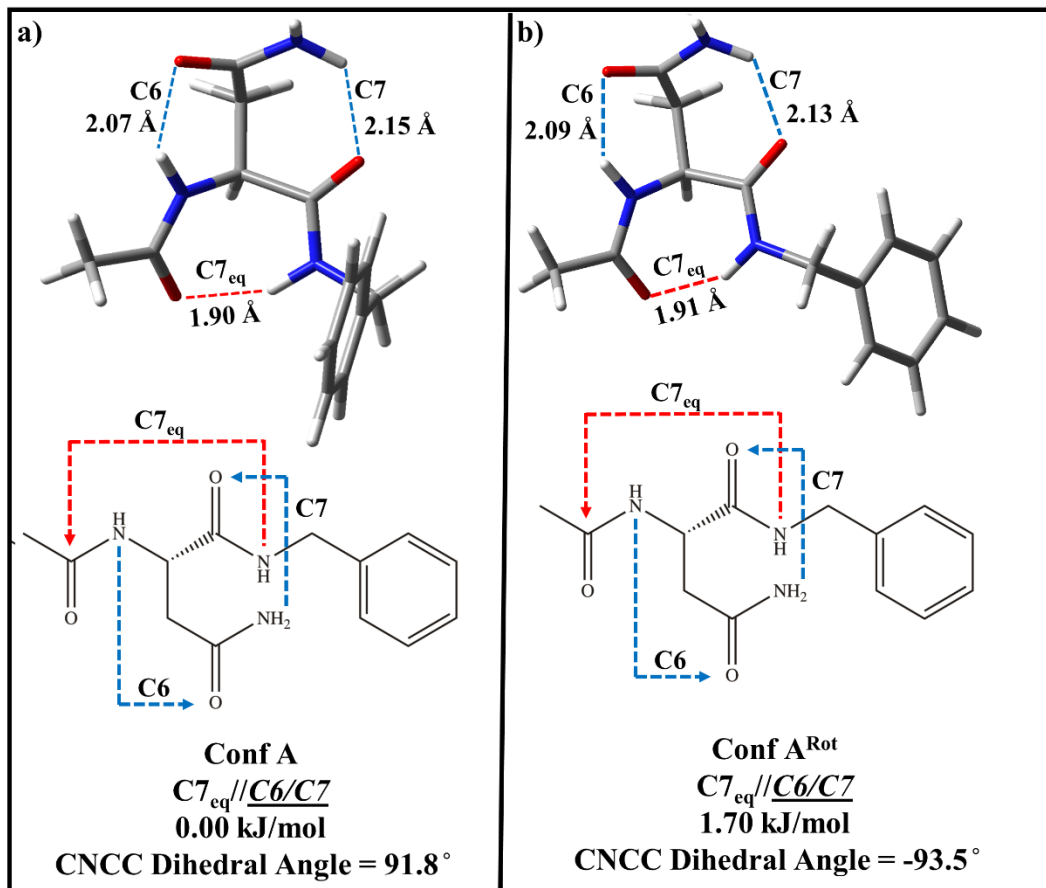


Figure 5.5. Structures of (a) conformer A and (b) conformer A^{Rot}. 3D structure and 2D hydrogen bonding schematic are presented for each structure, as well as the hydrogen bonding designation, relative zero-point corrected potential energies, and the value of the CNCC dihedral angle, which serves to differentiate the two conformers from one another.

The ambiguity of the assignment of conformer B hinges upon whether population is kinetically trapped in the laser desorption/supersonic expansion process. Figure 5.5 and 5.6 show a structural comparison of conformer A and conformer A^{Rot}, and the relaxed potential energy scan about the relevant dihedral of conformer A, respectively. Since the barrier to relaxation of A^{Rot} to A is modest (5 kJ/mol), one would anticipate cooling of population from A^{Rot} to A. However, since the energy difference between the minima is also small, we cannot definitively eliminate the possibility that the transitions of conformer B are due to A^{Rot}. In what follows, the tentative assignment of conformer B as the C5//C8/C7 extended backbone structure will be used to guide the discussion, with the understanding that this assignment is tentative

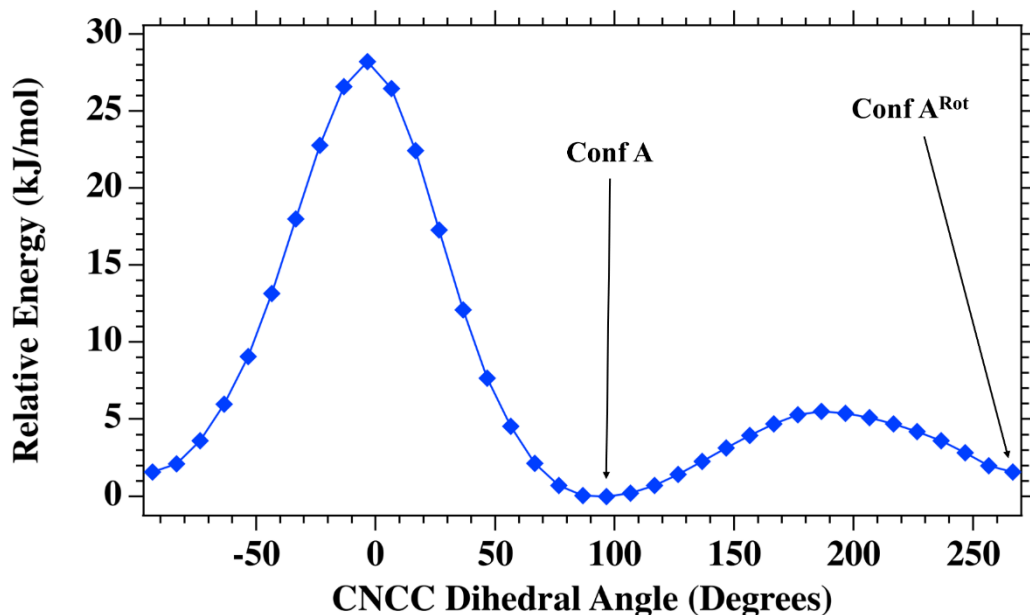


Figure 5.6. Relaxed potential energy scan about the CNCC dihedral angle which differentiates conformer A and A^{Rot}. The two rotameric minima are labelled, indicating where upon the potential energy surface they lie.

5.3.2 Ac-Ala-Asn-NHBn

The R2PI and IR-UV holeburning spectra for Ac-Ala-Asn-NHBn are presented in the top and bottom traces of Figure 5.7, respectively. The R2PI spectrum is dominated by an S₀-S₁ origin transition at 37,643 cm⁻¹. All vibronic transitions burn out in the IR-UV holeburning spectrum, demonstrating that only one conformer is present in the expansion. The spectrum has two vibronic peaks in a 61 cm⁻¹ progression. Normal mode analysis of the assigned structure shows that this Franck-Condon active vibration is contributed to by modulation of the interior amide CNCC and by the twisting of the phenyl ring, the same twisting motion responsible for the 8 and 10 cm⁻¹ progression in conformers A and B, respectively, of Ac-Asn-NHBn. Another two peaks in a 38 cm⁻¹ progression are assigned to the rocking motion of the NHBn group against the acyl cap, during which the Asn NH₂ groups distance from the aromatic ring is modulated, consistent with inducing FC intensity via the ππ* transition. Finally, a single 88 cm⁻¹ vibronic peak is due to the in-phase motion of the 38 cm⁻¹ mode

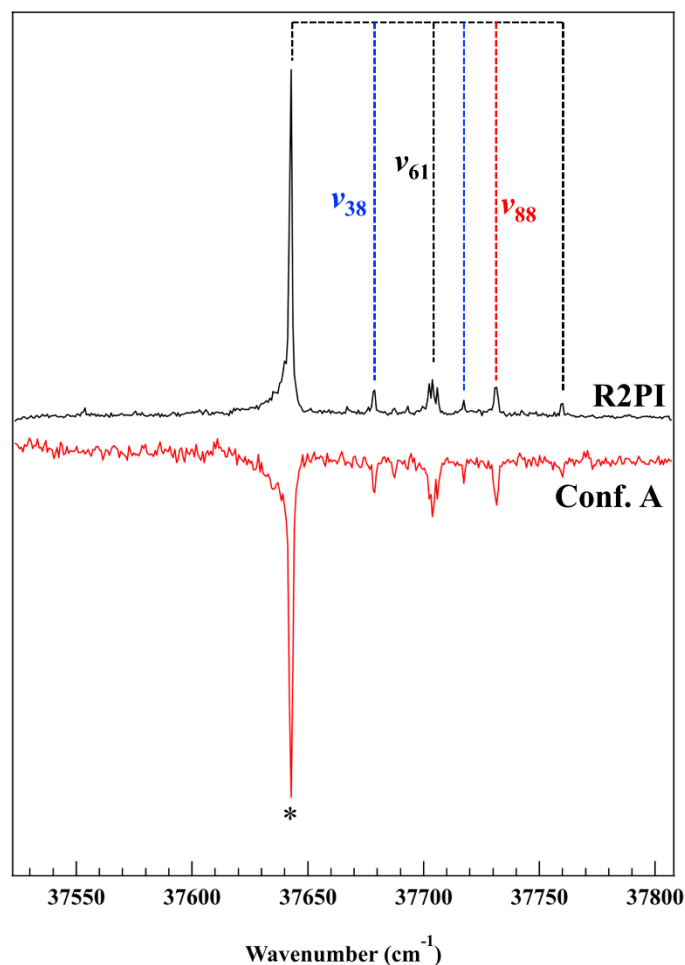


Figure 5.7. R2PI (black) and IR-UV holeburning (red) spectra of Ac-Ala-Asn-NHBn. The peak marked with an asterisk ($37,643\text{ cm}^{-1}$) indicates the transition used to collect RIDIR spectra. Vibronic progressions are labeled with tie lines

The RIDIR spectra of Ac-Ala-Asn-NHBn in the hydride stretch and amide I/II regions are presented in Figure 5.8a and 8b, respectively. The hydride stretch region shows five well-resolved peaks appearing at 3502 , 3474 , 3395 , 3373 , and 3367 cm^{-1} , as anticipated based on the structure (Figure 5.1). Given the absence of competing high frequency transitions, the band at 3502 cm^{-1} can be tentatively assigned to the asymmetric stretch of the Asn NH_2 group, which based on its shift away from the free transition frequency is in a hydrogen bond. This leads us to assign the transition at 3474 cm^{-1} to a free amide NH stretch. The three remaining transitions all fall between $3360 - 3400\text{ cm}^{-1}$, a region which has been demonstrated in previous studies to contain transitions arising from C6, C7, and C10 hydrogen bonds.^{34-38, 51, 52} Consistent with these qualitative deductions, the agreement of the experimental spectrum with the calculated spectrum presented in

Figure 5.8 leads to assignment of the sole conformer of Ac-Ala-Asn-NHBn to a C10//C6/ π structure, which was calculated to be the global energy minimum. As can be seen from the assigned structure in Figure 5.9, the NH₂ asymmetric stretch frequency is shifted down in frequency due to an NH₂ $\cdots\pi$ interaction.

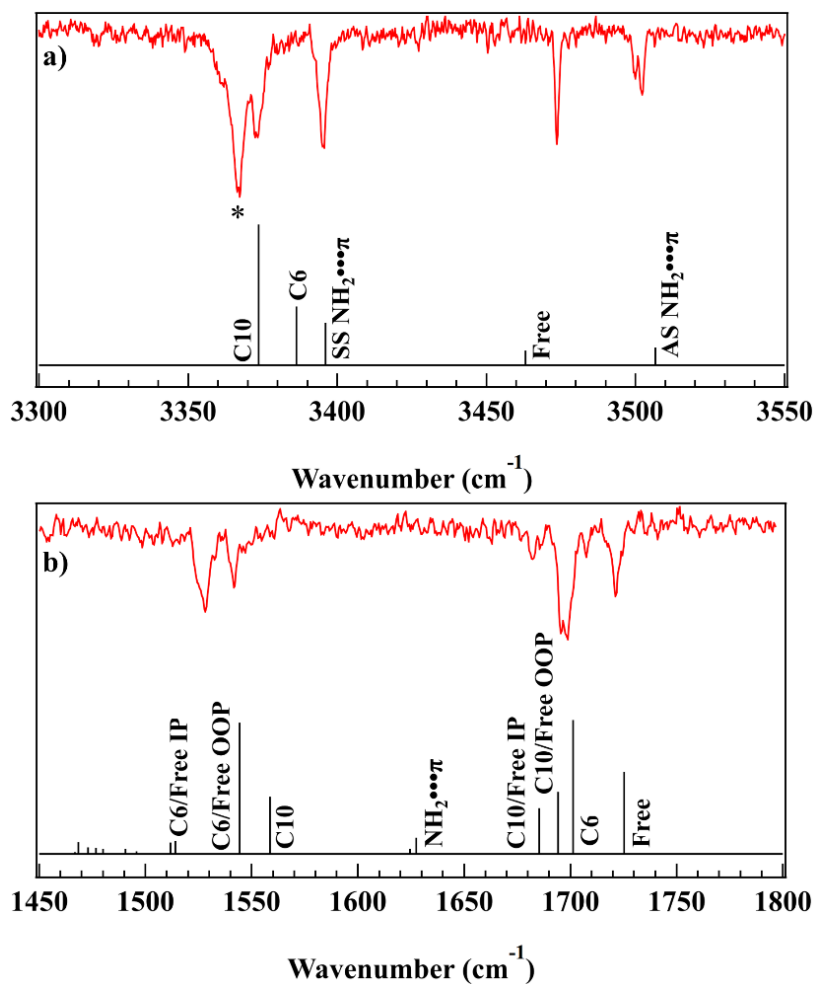


Figure 5.8. RIDIR spectra of the assigned conformer of Ac-Ala-Asn-NHBn in the (a) hydride stretch and (b) Amide I/II regions. Black stick spectra represent the scaled, harmonic, normal mode frequencies of the assigned structure calculated the B3LYP-D3BJ/6-31+G(d) level of theory. Labels indicate the main carrier(s) of the vibration.

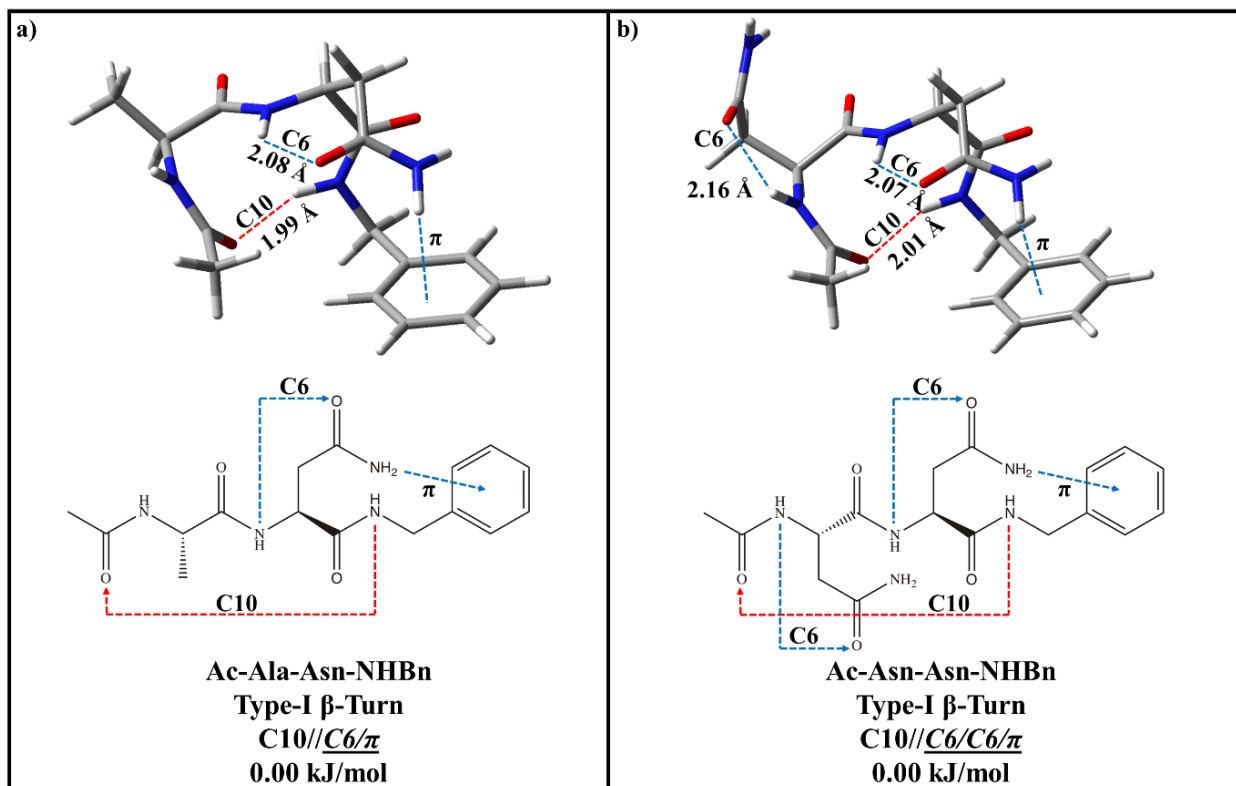


Figure 5.9. Assigned structure of (a) Ac-Ala-Asn-NHBn and (b) Ac-Asn-Asn-NHBn. 3D structure and 2D hydrogen bonding schematic are presented for each conformer, as well as the hydrogen bonding designation and relative zero-point corrected potential energies (among each molecule).

With the assigned structure in hand, the remaining hydride stretch transitions are readily assigned. The 3395 cm^{-1} transition arises from the symmetric NH_2 stretch, while the 3373 cm^{-1} is assigned to the C6 cycle comprised of the Asn amide NH and Asn side chain $\text{C}=\text{O}$. The lowest frequency transition at 3367 cm^{-1} arises from the NH group engaged in a C10 hydrogen bond between the C-terminal NH and N-terminal $\text{C}=\text{O}$. This strong hydrogen bond has an $\text{NH}\cdots\text{O}=\text{C}$ distance of 1.99 \AA and angle of approach equal to 157° . This C10 hydrogen bond between the $\text{C}=\text{O}$ of residue i and the NH of residue $i+3$ is structurally characteristic of a β -turn. Indeed, inspection of the backbone dihedral angles of residue $i+1$ and $i+2$ results in the categorization of this conformer to a type I β -turn structure. As we shall discuss, this structural motif is the same as that formed by the analogous Glutamine-containing peptide.³⁴

The amide I region consists of an isolated transition at 1721 cm^{-1} , a split peak with closely spaced maxima at 1699 and 1695 cm^{-1} , and a weak transition at 1682 cm^{-1} . The high frequency peak is assigned to the free Ala amide $\text{C}=\text{O}$ oscillator. The most intense amide I transition at 1699

cm^{-1} is assigned to the Asn side chain C=O involved in the C6 hydrogen bond. The 1695 cm^{-1} transition is assigned to the out of phase combination of the C10 and N-terminal free C=O groups, with the in-phase combination appearing at 1682 cm^{-1} . The discrepancy between calculated and experimental intensities of these modes is likely due to the out of phase transition mixing and borrowing intensity from the near-resonant C6 transition.

The amide II spectrum shows two clear transitions at 1542 and 1528 cm^{-1} , with the two weak transitions at lower frequency predicted by the best fit structure likely lost in the experimental noise. Regardless, the experimental frequency position and intensity pattern compared with that of the assigned structure give further confidence in the assignment. The experimentally observed transition at 1542 cm^{-1} is assigned to the C10 NH wagging motion, while the transition at 1528 cm^{-1} is attributed to the out of phase NH bend combination of the C6 and free N-terminal NH groups.

5.3.3 Ac-Asn-Asn-NHBn

The R2PI and IR-UV holeburning spectra for Ac-Asn-Asn-NHBn are presented as the top and bottom trace of Figure 5.10, respectively. As with Ac-Ala-Asn-NHBn, the electronic spectrum is dominated by a single transition at $37,661 \text{ cm}^{-1}$. This $S_0 - S_1$ origin transition is located only 18 cm^{-1} higher in frequency than that of the Ala-containing analogue. This fact combined with the general similarity of the R2PI spectra and their component RIDIR spectra indicate that the responsible conformers are structurally similar. All vibronic peaks burn out in the IR-UV holeburning spectra, proving that only one conformer is contributing to ultraviolet absorption in the expansion.

The vibronic band 30 cm^{-1} above the origin transition is assigned to a mode comprised of the NHBn rocking against the acyl cap, resulting in the C-terminal NH_2 group periodically modulating its distance from the aromatic ring. This is the analogous vibration to the 38 cm^{-1} Franck-Condon active mode in the R2PI spectrum of Ac-Ala-Asn-NHBn. The vibrational frequency is reduced by 8 cm^{-1} due to the increase in the reduced mass of the group vibration upon exchange of Ala for Asn (4.70 amu vs. 5.97 amu). The second most prominent vibronic peak is located 62 cm^{-1} from the origin transition. Normal mode analysis of the assigned structure reveals that the nuclear motion responsible is once again the modulation of the interior amide CNCC and

the twisting of the phenyl ring, the same Franck-Condon active vibration in the R2PI spectra of Ac-Ala-Asn-NHBn.

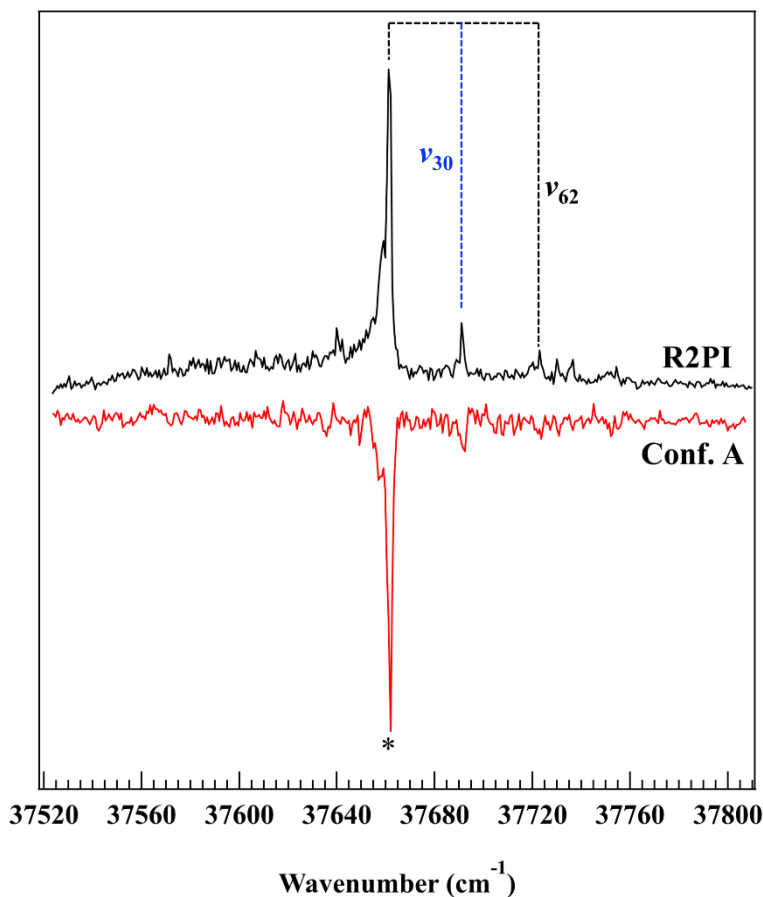


Figure 5.10. R2PI (black) and IR-UV holeburning (red) spectra of Ac-Asn-Asn-NHBn. The peak marked with an asterisk ($37,662\text{ cm}^{-1}$) indicates the transition used to collect RIDIR spectra. Vibronic progressions are labeled with tie lines.

The RIDIR spectra of Ac-Asn-Asn-NHBn in the hydride stretch and amide I/II regions are shown as the top and bottom traces of Figure 5.11, respectively. cursory comparison of the hydride stretch spectrum of Ac-Ala-Asn-NHBn with that of Ac-Asn-Asn-NHBn show qualitative similarities in frequency and intensity patterns. Of course, with the additional Asn functional group, the hydride stretch region shown in Figure 5.11 contains two additional transitions due to the coupled stretches of the N-terminal Asn NH_2 group. The two highest frequency stretches at 3543 and 3505 cm^{-1} are readily assigned to the asymmetric stretches of a free and hydrogen bound NH_2 group, respectively. The known coupling strength between the two NH bonds of the carboxamide

group allows the transition at 3430 cm^{-1} to be confidently assigned to the symmetric stretch of the free NH_2 . Given the similar frequencies of the hydrogen bound asymmetric NH_2 stretches in Ac-Ala-Asn-NHBn and Ac-Asn-Asn-NHBn, the band at 3396 cm^{-1} is tentatively assigned to the symmetric stretch of the hydrogen bound NH_2 group.

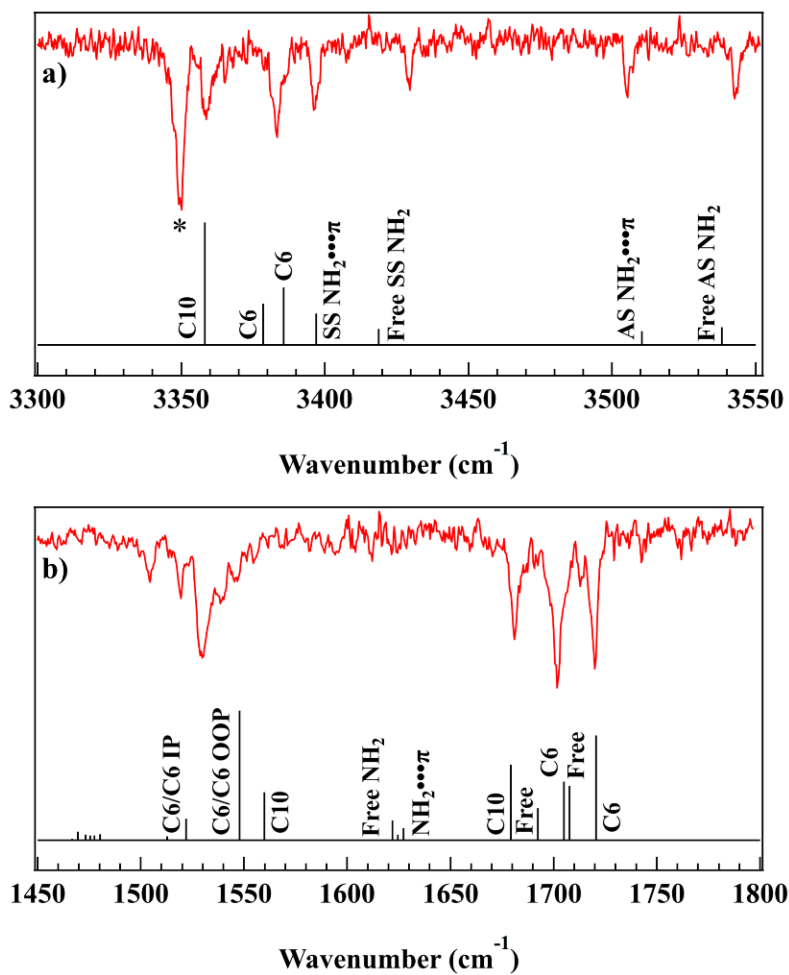


Figure 5.11. RIDIR spectra of the single observed conformer of Ac-Asn-Asn-NHBn in the hydride stretch (top) and Amide I/II (bottom) regions. Black stick spectra display the scaled, harmonic, normal mode frequencies of the assigned structure calculated the B3LYP-D3BJ/6-31+G(d) level of theory. Labels indicate the main carrier(s) of the vibration.

Comparison of the best fit calculated frequencies with experimental frequencies lead to assignment of the sole conformer of Ac-Asn-Asn-NHBn to a $C_{10}//\underline{C6}/C6/\pi$ structure, which is calculated to be the global minimum energy conformer among the pool of competing structures. Based on this assignment, the band at 3386 cm^{-1} arises from a $\underline{C6}$ hydrogen bond between the N-terminal amide NH and Asn C=O, while the transition at 3359 cm^{-1} is due to the analogous C-terminal $\underline{C6}$ hydrogen bond. This is the same hydrogen bond in Ac-Ala-Asn-NHBn that appears at 3373 cm^{-1} . The intense low frequency transition at 3350 cm^{-1} is assigned to a C10 hydrogen bond between the NHBn NH and acyl C=O. This large hydrogen bonded cycle has an $\text{NH}\cdots\text{O}=\text{C}$ distance of 2.01 \AA and angle of approach equal to 158° , properties very similar to the analogous C10 H-bond in Ac-Ala-Asn-NHBn. Indeed, the dihedral angles between residue $i+1$ and residue $i+2$ of this conformer also classify it as a type I β -turn former. Interestingly, the analogous Gln-containing dipeptide also forms a type I β -turn under isolated, jet-cooled conditions,³⁵ a point to which we will return later. As a convenient means of highlighting the similarities between Ac-Ala-Asn-NHBn and Ac-Asn-Asn-NHBn, the overlap of the assigned structures are shown in Figure 5.12 and a spectral comparison is shown in Figure 5.13.

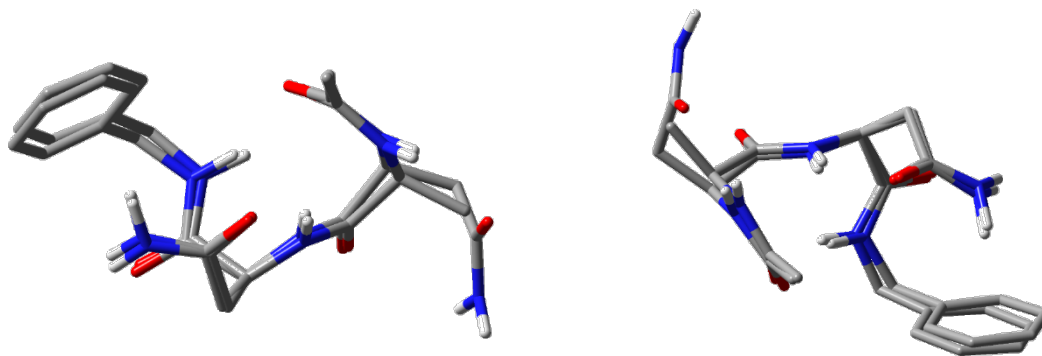


Figure 5.12. Two views of the peptide backbone overlap (with hydrogens removed) of Ac-Ala-Asn-NHBn and Ac-Asn-Asn-NHBn

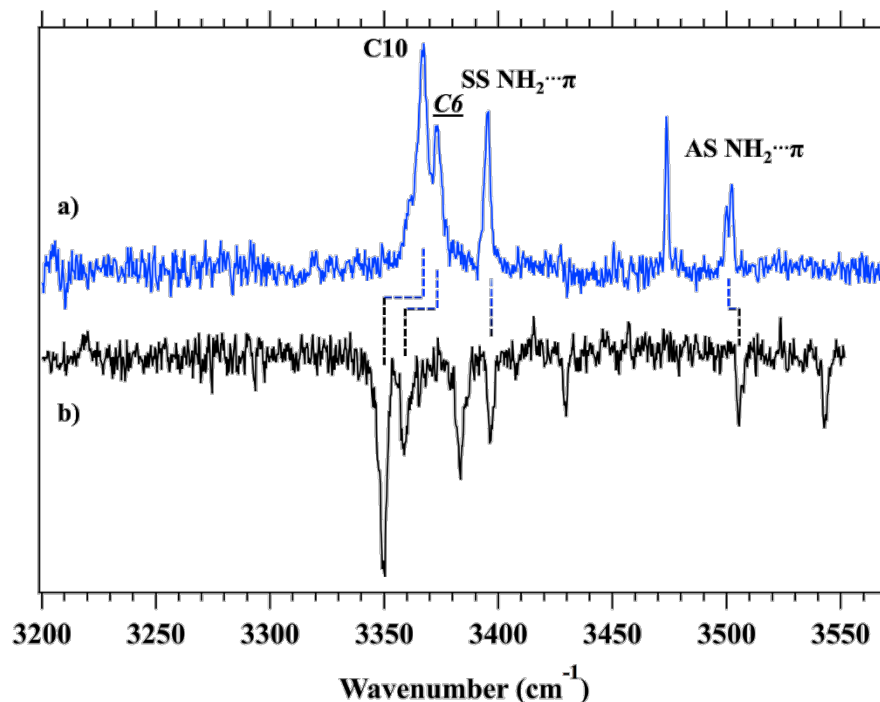


Figure 5.13. Experimental hydride stretch RIDIR spectra for the type I β -turn conformers of (a) Ac-Ala-Asn-NHBn and (b) Ac-Asn-Asn-NHBn. The shared spectral signatures of the two conformers are highlighted

The excellent fit of the spectrum calculated for the assigned conformer with experiment enables a ready analysis of the amide I and II regions of the spectrum (Figure 5.11). The highest frequency transition at 1720 cm^{-1} is assigned to the Asn C=O involved in a C6 hydrogen bond with the N-terminal amide NH. The most intense peak in the amide I region has two closely spaced maxima at 1702 and 1701 cm^{-1} . The spectral overlap of these peaks results in each transition lending intensity to, and borrowing intensity from, one another. They are assigned to the free N-terminal amide C=O and the C-terminal Asn C=O, which is involved in a C6 H-bond with its amide NH. A small maximum at 1691 cm^{-1} mostly lost in the noise, sandwiched between two much larger transitions, is tentatively assigned to the C-terminal free C=O oscillator, while the final amide I peak at 1681 is due to the N-terminal C=O involved in the cross-molecule C10 hydrogen bond.

The spectrum in the amide II region is less well resolved, and hence serves more to confirm the assignment than as a diagnostic tool. The assigned conformer has two low intensity peaks around 1625 cm^{-1} which aren't readily observed in the experimental spectrum. The transition at 1640 cm^{-1} is assigned to the bending motion of the C-terminal NH involved in the C10 hydrogen

bond. The two transitions at 1530 and 1519 cm^{-1} form the out-of-phase and in-phase combinations, respectively, of the two C6 hydrogen bonded amide NH groups, with some C10 NH bend mixed in.

5.4 Discussion

Conformer-specific infrared spectra in the hydride stretch and amide I/II regions have been used in conjunction with theoretical vibrational frequencies to assign the four conformers spanning the three Asn-containing peptides investigated in this study. In each case the assigned conformers belong to the lowest energy conformational families calculated at the B3LYP-D3BJ/6-31+G(d) level of theory. Agreement between experimental and theoretical vibrational frequencies, when combined with the fact that the structures are among the calculated energetic minima, gives confidence that the assigned structures accurately reflect the inherent conformational preferences of the cold, gas-phase molecules studied herein.

In order to understand the broader conformational landscape for these Asn-containing peptides, Figure 5.14 presents an energy diagram that displays the full set of conformers with calculated energies within 30 kJ/mol of the global minimum of the three Asn-containing peptides. In the diagrams, we have partitioned the conformers horizontally into distinct peptide backbone H-bonding patterns, and further color-coded each energy level to indicate the hydrogen bonding type for the Asn sidechain. Upon inspection of the energy diagram, it is immediately clear that the number of conformational families made available by the Asn residue increases in complexity with both the length of the peptide backbone and number of Asn residues. The three types of structures experimentally observed represent two different canonical turn types (inverse γ , type I β -turn) and an extended structure, all of which occur regularly in proteins.

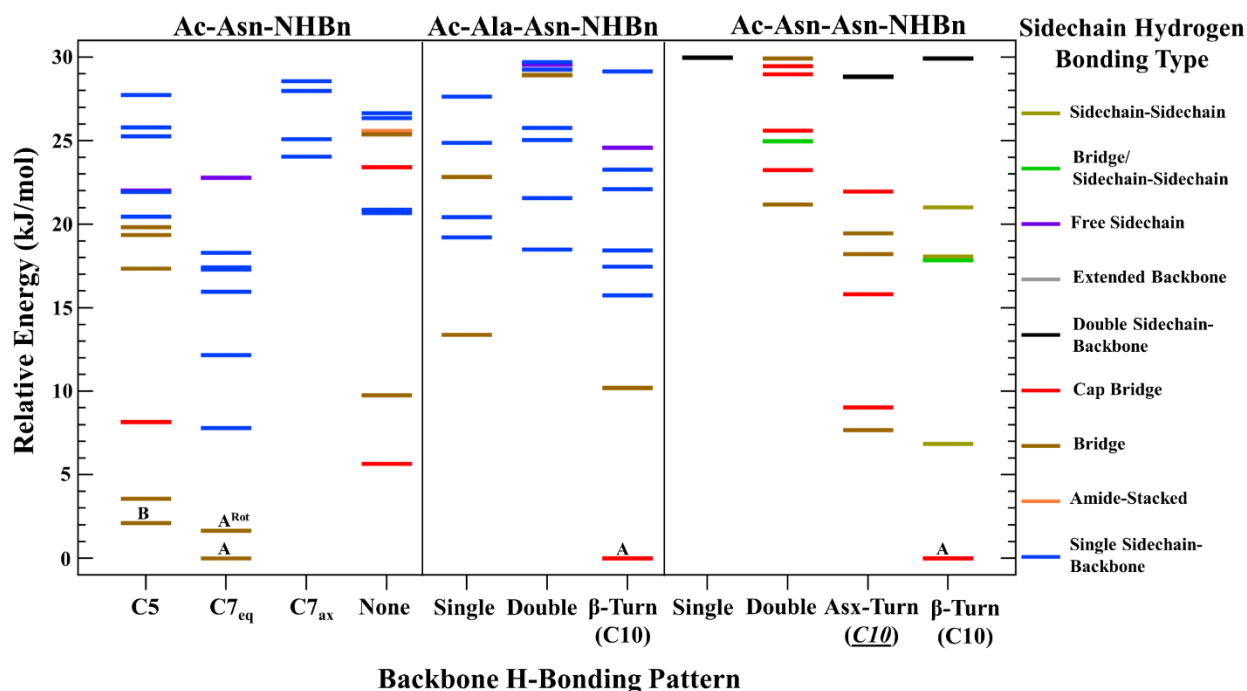


Figure 5.14. Energy level diagrams for the three asparagine-containing molecules studied herein. Each conformer has its relative zero-point corrected energy (B3LYP-D3BJ/6-31+G(d)) plotted as a function of backbone hydrogen bonding pattern with the following stylized nomenclature: backbone-backbone//sidechain-backbone//sidechain-sidechain. Asx-Turns are structures where a *C10* hydrogen bond is formed between the carboxamide C=O of an Asn on residue *i* and the backbone NH of residue *i*+2. Each conformer energy level is also color-coded to further indicate the type(s) of hydrogen bond(s) in which the amide sidechain(s) is (are) involved. Experimentally observed conformers are labelled with their letter designation. ‘Bridge’ designates structures where both the hydrogen bond donor and acceptor on the same carboxamide side chain are involved in hydrogen bonds to the backbone, or backbone and cap (Cap Bridge). Double Sidechain-Backbone designates structures in Ac-Asn-Asn-NHBn where each amide sidechain is involved in a single hydrogen bond to the backbone. Sidechain-Sidechain designates structures in Ac-Asn-Asn-NHBn where the two carboxamide sidechains are hydrogen bonding with each other

The two assigned bridged structures of Ac-Asn-NHBn energetically compete with one another and are representative of the only two conformational families under 5 kJ/mol. While both conformers have bridged sidechain-backbone interactions, the NH₂ groups engage in hydrogen bonds with C=O groups at different positions along the peptide backbone. In the extended structure the carboxamide NH₂ is interacting with the N-terminal C=O, while the analogous amido group in the inverse γ -turn structure is interacting with the C-terminal C=O. By forming these bridge

structures with the carboxamide side chain, the structure also incorporates the maximum number of hydrogen bonds for each molecule.

The two capped dipeptides funnel all population into a type I β -turn peptide backbone, with a strong energetic preference relative to all competitors. Indeed, in Ac-Ala-Asn-NHBn and Ac-Asn-Asn-NHBn, the observed type I β -turn is more stable than any other in the conformational pool by 10 and 7 kJ/mol, respectively.

With firm conformational assignments of the present Asn-containing peptides and their analogous Gln-containing peptides from previous studies by our group, we are now in a position to investigate the impact that the difference in side-chain length between Asn and Gln (which differ by a single methylene group) has on peptide structure and stability as made manifest by the experimental vibrational spectra and best fit structures. In what follows, we focus on each structure type in turn, with emphasis placed on the structural and spectral similarities and differences between analogous Asn and Gln peptides.

5.4.1 Inverse γ -Turns

Conformer A of Ac-Asn-NHBn, with its $C7_{eq} // C6/C7$ hydrogen bonding architecture, forms an inverse γ -turn at the shortest chain length possible. Conformer C of Ac-Gln-NHBn also forms an inverse γ -turn, with analogous $C7_{eq} // C7/C8/\pi$ hydrogen bonds.³⁴ Figure 5.15 compares the structures and spectra of the Asn- and Gln-stabilized γ -turns, and Table 5.2 lists the corresponding dihedral angles. In what follows, the Asn γ -turn will be referred to simply as γ N and the Gln γ -turn as γ Q. In both structures, the carboxamide side chains form hydrogen bonded bridges with the peptide backbone, resulting in $//C6/C7$ and $//C7/C8/\pi$ sidechain-backbone motifs in Asn and Gln, respectively, with very similar ϕ/ψ backbone dihedrals.

The difference of one methylene group between the carboxamide side-chains of γ N and γ Q dictates that the sidechain χ dihedrals will be different from one another. Indeed, the Gln carboxamide group bends back over the γ -turned backbone and engages in a dispersive π

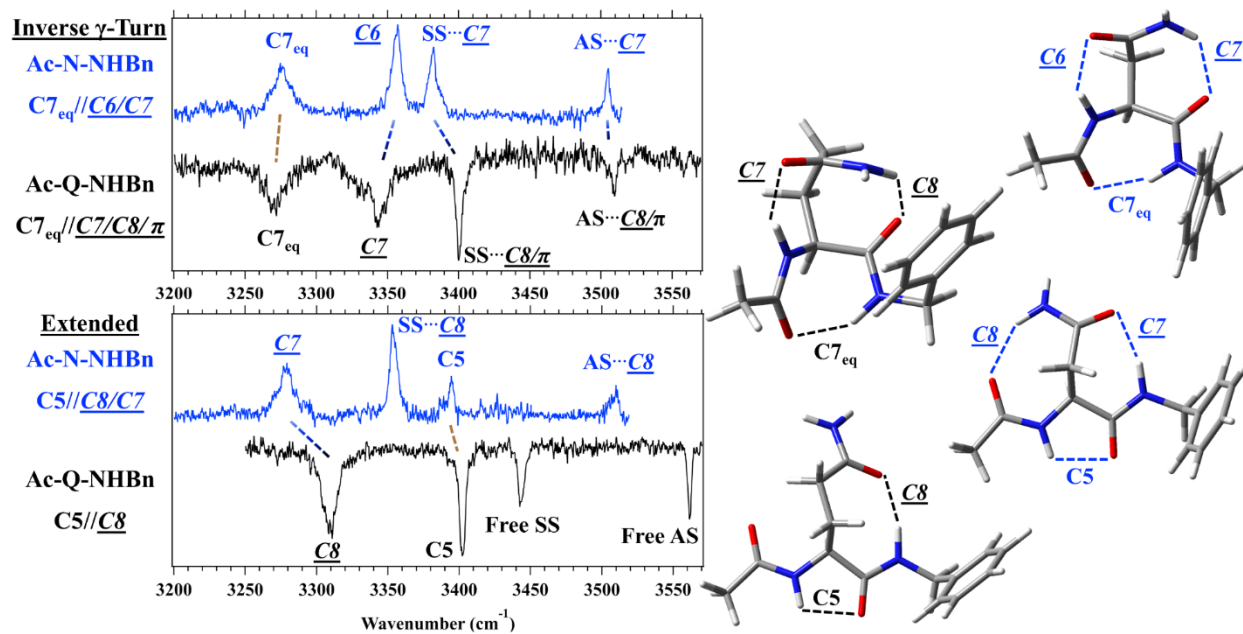


Figure 5.15. Hydride stretch IR spectra and experimentally assigned structures of analogous Ac-Asn-NHBn and Ac-Gln-NHBn conformers. Asn hydrogen bonds and spectra are designated in blue while those of Gln are designated in black. Transitions are labelled with the main carrier of the vibration with analogous hydrogen bonds in Asn and Gln analogs connected with dashed lines and color coded in the following way: the same hydrogen bonded cycles connected with brown lines and analogous $(C_n - (C_n + 1))$ cycles with faded blue to black lines

interaction with the benzyl cap, an additional interaction for which Asn lacks the required flexibility. The NH₂ AS fundamental is higher in frequency in γ Q than γ N by only 4 cm⁻¹, even though the C7 is ~ 0.1 Å shorter in γ N than the C8 in γ Q. In this case, it is the additional π interaction in γ Q which serves to shift down in frequency the AS NH₂ to within 4 cm⁻¹ of the γ N C7.

The C7_{eq} backbone H-bond is extraordinarily strong in both γ N (1.90 Å, 3275 cm⁻¹) and γ Q (1.92 Å, 3270 cm⁻¹). These two hydrogen bonds are among the strongest C7_{eq} hydrogen bonds observed, shifting down in frequency by as much as 100 cm⁻¹ from a C7_{eq} observed previously (see Table 5.1).^{53, 54} James et. al. observed, in their study of mixed α/β synthetic foldamers, that NH groups belonging to amides whose components act as both hydrogen bond donor and acceptor, have NH bond lengths longer than NH groups on amides that are not involved in such cooperative interactions.³⁸ This is explained by the notion that, during hydrogen bonding, electron density is transferred from the electron-rich C=O to the antibonding orbital of NH, with the nuance that this electron transfer appears to involve electron donors and acceptors on the *same* amide group, which cannot be directly hydrogen bonded with one another. This description offers an appealing

physical explanation for the large $C7_{eq}$ frequency shifts in γN and γQ : In both structures the bridging carboxamide group closes a triple hydrogen bonding cycle in which all three present amide groups are maximally involved in hydrogen bonding. The NH and C=O along the peptide backbones not involved in the $C7_{eq}$, which if not for the carboxamide-containing sidechains would be free, are both involved in hydrogen bonding, resulting in a large net cooperative strengthening effect. This cooperative strengthening likely contributes to the large shift down in frequency of the $C7_{eq}$ in both γN and γQ . The N-terminal bridge component in γN is a $C6$ hydrogen bond with a distance of 2.07 Å and angle of approach equal to 137°. The analogous γQ $C7$ measures 1.99 Å with an angle of approach equal to 150°. As expected, based on these metrics, the $C7$ NH stretch is shifted down in frequency to the $C6$ by 14 cm^{-1} .

Based on a search of the protein data bank, Milner-White concluded that compound inverse γ -turns, γ_n with $n=2-5$, occur regularly within β -sheet strands.⁵⁵ These γ -turn repeat segments take the form of ribbons with a slight right-handed twist, a structure the author referred to as a 2.27-helix. Given that proteinaceous β -sheets also twist in the right-handed direction, Milner-White postulated that compound inverse γ -turns could play a role in the local stabilization of β -strands en route to β -sheet formation. This proposition is especially intriguing in light of the high concentration of Asn and Gln residues in β -sheet rich amyloid fibrils, as well as the uniquely and unusually strong $C7_{eq}$ hydrogen bonds formed in both γN and γQ . Gas-phase tests of the 2.27-helicity of poly-N and poly-Q would be worthwhile in pursuit of testing Milner-White's proposition as it is applied to nature's preference for Asn and Gln in prion-forming domains.

Table 5.2. Calculated dihedral angles (in degrees) of the Asn(N)-containing peptides studied in this work and the analogous Gln(Q)-containing peptides. Also listed are either the canonical dihedral angles or average values of those extracted from the protein data bank

<u>Structure</u>	Φ_1	residue (i+1)				residue (i+2)				
		Ψ_1	χ_1	χ_2	χ_{Q1}	Φ_2	Ψ_2	χ_3	χ_4	χ_{Q2}
Inverse γ -Turn										
Ac-N-NHBn conf A	-82	63	50	103						
(C7 _{eq} //C6/C7)			(g ⁺)							
Ac-N-NHBn conf A ^{Rot}	-82	56	51	100						
(C7 _{eq} //C6/C7)			(g ⁺)							
Ac-Q-NHBn conf C	-82	56	74	-40	110					
(C7 _{eq} //C7/C8/ π) ^a			(g ⁺)	(g ⁻)						
Inverse γ -Turn Canonical	-75	65								
Value ^b										
Extended Backbone										
Ac-N-NHBn conf B	-169	-	-	91						
(C5//C8/C7)		178	137							
			(a)							
Ac-Q-NHBn conf A	-162	169	-	-64	167					
(C5//C8) ^a			103	(g ⁻)						
			(a)							
Extended Backbone	180	180								
Canonical Value										
Type I β -Turn										
Ac-A-N-NHBn	-68	-13				-80	0	62	102	
(C10//C6/ π)								(g ⁺)		
Ac-A-Q-NHBn	-70	-13				-73	-11	83	-61	151
(C10//C7/ π) ^a								(g ⁺)	(g ⁻)	
A-N Crystal Structure Avg ^c	-63	-26				-92	8			
Type I β -Turn Canonical	-60	-30				-90	0			
Value ^d										
Ac-N-N-NHBn	-76	1	61	104		-83	-3	62	105	
(C10//C6/C6/ π)			(g ⁺)					(g ⁺)		
Ac-Q-Q-NHBn	-73	-8	68	-87	-	-71	-13	84	-62	150
(C10//C7/C7/ π) ^e			(g ⁺)	(g ⁻)	165			(g ⁺)	(g ⁻)	
N-N Crystal Structure Avg ^f	-62	-25				-96	4			

^aFrom ref. ³⁴

^bFrom ref. ⁵⁵

^cFrom Table XX

^dFrom ref. ⁵⁶

^eFrom ref. ³⁵

^fFrom Table XX

To test the influence that the bulky aromatic NHBn cap has on preferred structures, geometry optimization and energy calculations were carried out on the thirty-five low energy (<30 kJ/mol) Ac-N-NHBn structures plotted in Figure 5.14, with the NHBn cap substituted with an NHMe cap (Table 5.3). Six unique structural families within 10 kJ/mol in the NHBn cap group reduce to only two unique structural families with the NHMe cap present within 15 kJ/mol of the global energy minimum: $C7_{eq} // \underline{C6/C7}$ (0.00 kJ/mol) and $C5 // \underline{C8/C7}$ (1.97 kJ/mol), the two families to which conformer A and conformer B, respectively, belong. This indicates that the two conformations observed in the case of Ac-Asn-NHBn are indeed the preferred structures, regardless of C-terminal cap.

As an additional check on the robustness of these conformational preferences to temperature changes, free energy corrections calculated at room temperature were carried out to determine whether entropic forces result in preferred structures different from those observed in the molecular beam (Table 5.4). Even when ranked in relative free energy, γN remains the energetic minimum, suggesting that this local conformation may play an important role in environments in which free energy, rather than internal energy, dictates conformation

Table 5.3. Relative potential energies and conformational families of the 30 kJ/mol lowest energy structures of Ac-Asn-NHBn upon exchange of NHBn cap for NHMe cap and geometry optimization at the DFT B3LYP-D3BJ/6-31+G(d) level of theory. Note that for the two observed conformers both the energy ordering and conformational family remain the same upon NHMe substitution.

	<u>Conformational</u> <u>Family</u>	<u>(NHBn cap)</u>	<u>Conformational</u> <u>Family</u>	<u>(NHMe cap)</u>
Conf A	C7eq//C6/C7	0.0	C7eq//C6/C7	0.0
Conf A ^{Rot}	C7eq//C6/C7	1.7	C7eq//C6/C7	0.0
Conf B	C5//C8/C7	2.1	C5//C8/C7	2.0
Phenyl ring rotamer of Conf B	C5//C8/C7	3.6	C5//C8/C7	2.0
AcAsnNHBn_36.log:	//C6/pi	5.7	C7eq//C6/C7	0.0
N_OPLS_34.log:	C7eq//C7	7.8	C7eq//C6/C7	0.0
AcAsnNHBn_1.log:	C5//C7/pi	8.2	C5//C8/C7	2.0
AcAsnNHBn_30.log:	//C6/C7	9.8	C7eq//C6/C7	0.0
AcAsnNHBn_13.log:	C7eq//C7	12.2	//C7/C7	15.5
N_OPLS_4.log:	C7eq//C6	16.0	C7eq//C6	16.9
AcAsnNHBn_46.log:	C7eq//C7	17.3	//C7/C7	15.5
AcAsnNHBn_42.log:	C5//C8/C7	17.4	C5//C8/C7	16.7
AcAsnNHBn_7.log:	C7eq//C7	17.4	//C7/C7	15.5
N_OPLS_6.log:	C7eq//C6	18.3	C7eq//C6	16.9
AcAsnNHBn_24.log:	C5//C8/C7	19.4	C5//C8/C7	16.7
AcAsnNHBn_34.log:	C5//C8/C7	19.8	C5//C8/C7	16.7
AcAsnNHBn_21.log:	C5//C8	20.5	C5//C8/C7	16.7
N_OPLS_17.log:	//C6	20.7	//C6	25.9
N_OPLS_12.log:	//C6	20.9	//C6	25.6
N_OPLS_37.log:	C5//C8	21.9	C7ax//C7	21.3
AcAsnNHBn_28.log:	C5//	22.0	C5//C7	23.9
N_OPLS_9.log:	C7eq//	22.8	C7ax	23.8
N_OPLS_28.log:	//C6/pi	23.4	C7eq//C6/C7	0.0
N_OPLS_7.log:	Bif C7ax-//-C8	24.0	C7ax	24.9
AcAsnNHBn_12.log:	C7ax//pi	25.1	C7ax	35.5
AcAsnNHBn_19.log:	C5//pi	25.3	C7eq//C6/C7	0.0
AcAsnNHBn_39.log:	//C7/pi/C8	25.4	//C8/C7	34.5
N_OPLS_43.log:	//C7	25.6	//C7	29.9
AcAsnNHBn_26.log:	C5//C7	25.8	C5//C7	23.9
N_OPLS_31.log:	//C7	26.4	//C7	30.1
AcAsnNHBn_47.log:	//C7	26.7	//C7	32.2
N_OPLS_50.log:	Bif C5-//-C7	27.7	C7eq//C6/C7	0.0
AcAsnNHBn_29.log:	C7ax//C7	28.0	C7ax//C7	28.5
AcAsnNHBn_37.log:	C7ax//C7	28.6	C7ax//C7	28.5
N_OPLS_15.log:	C7ax//C7	28.6	C7ax//C7	28.5

Table 5.4. Relative potential energies, free energy corrections (at room temperature), and free energies for all calculated structures under 30 kJ/mol of the global energy minimum of Ac-Asn-NHBn, calculated at the DFT B3LYP-D3BJ/6-31+G(d) level of theory. Note that experimentally assigned conformers A and B are the lowest calculated potential and free energy structures

<u>Ac-Asn-NHBn</u>	<u>Conformational</u>	<u>ΔE (kJ/mol)</u>	<u>G correction</u>	<u>ΔG (kJ/mol)</u>
<u>Conformer</u>	<u>Family</u>		<u>(kJ/mol)</u>	
Conf A	C7eq//C6/C7	0.0	0.0	0.0
Conf A ^{Rot}	C7eq//C6/C7	1.7	1.7	3.4
Conf B	C5//C8/C7	2.1	1.1	3.2
Phenyl ring rotamer				
of Conf B	C5//C8/C7	3.6	1.2	4.7
AcAsnNHBn_36.log:	//C6/pi	5.7	3.2	8.9
N_OPLS_34.log:	C7eq//C7	7.8	3.0	10.8
AcAsnNHBn_1.log:	C5//C7/pi	8.2	3.7	11.9
AcAsnNHBn_30.log:	//C6/C7	9.8	-2.0	7.8
AcAsnNHBn_13.log:	C7eq//C7	12.2	3.6	15.8
N_OPLS_4.log:	C7eq//C6	16.0	-2.3	13.6
AcAsnNHBn_46.log:	C7eq//C7	17.3	-4.2	13.1
AcAsnNHBn_42.log:	C5//C8/C7	17.4	0.8	18.1
AcAsnNHBn_7.log:	C7eq//C7	17.4	-2.2	15.3
N_OPLS_6.log:	C7eq//C6	18.3	-2.3	16.0
AcAsnNHBn_24.log:	C5//C8/C7	19.4	0.9	20.3
AcAsnNHBn_34.log:	C5//C8/C7	19.8	1.0	20.8
AcAsnNHBn_21.log:	C5//C8	20.5	1.7	22.2
N_OPLS_17.log:	//C6	20.7	-1.8	18.9
N_OPLS_12.log:	//C6	20.9	-1.4	19.5
N_OPLS_37.log:	C5//C8	21.9	-2.8	19.2
AcAsnNHBn_28.log:	C5//	22.0	-2.0	20.0
N_OPLS_9.log:	C7eq//	22.8	-4.1	18.7
N_OPLS_28.log:	//C6/pi	23.4	1.1	24.5
N_OPLS_7.log:	Bif C7ax-//C8	24.0	4.5	28.6
AcAsnNHBn_12.log:	C7ax//pi	25.1	2.3	27.4
AcAsnNHBn_19.log:	C5//pi	25.3	1.7	26.9
AcAsnNHBn_39.log:	//C7/pi/C8	25.4	8.5	33.9
N_OPLS_43.log:	//C7	25.6	4.8	30.4
AcAsnNHBn_26.log:	C5//C7	25.8	-3.7	22.1
N_OPLS_31.log:	//C7	26.4	-1.8	24.6
AcAsnNHBn_47.log:	//C7	26.7	-0.5	26.1
N_OPLS_50.log:	BBifC5-//C7	27.7	-2.6	25.1
AcAsnNHBn_29.log:	C7ax//C7	28.0	-2.6	25.3
AcAsnNHBn_37.log:	C7ax//C7	28.6	-1.4	27.1
N_OPLS_15.log:	C7ax//C7	28.6	-1.4	27.1

5.4.2 Extended Structures

Conformer B of Ac-Asn-NHBn has a $C5//C8/C7$ extended backbone architecture with near planar backbone ϕ/ψ dihedral angles of -169 and -178° . Conformer A of Ac-Gln-NHBn also forms an extended backbone structure, comprised of a $C5//C8$ hydrogen bonding pattern and similar ϕ/ψ backbone dihedral angles of -162 and 169° (Table 5.2). Henceforth the extended structures of Ac-Asn-NHBn and Ac-Gln-NHBn will be referred to as ϵN and ϵQ , respectively. The lower half of Figure 5.15 displays a comparison between the structures, and hydride stretch spectra, of ϵN and ϵQ . While both structures form the $C5$ nearest neighbor hydrogen bond characteristic of extended structures, the Asn-containing molecule forms a double hydrogen bonded bridge utilizing both the donor and acceptor groups on the carboxamide side chain, while the Gln-containing structure only forms one sidechain-backbone hydrogen bond between the carboxamide $C=O$ and the NHBn cap NH . In this case it appears that as a result of the more flexible Gln side chain in the extended backbone conformation *either* a sidechain-C-terminal $C8$ *or* a sidechain-N-terminal $C9$ hydrogen bond will be formed, while the less flexible Asn side chain readily accesses both types of stabilizing interactions. It may indeed seem counter-intuitive that the more flexible Gln sidechain is more limited in the formation of multiple sidechain-backbone hydrogen bonds than the less flexible Asn sidechain, but in our previous work we found that there is an energy penalty of 1.22 kJ/mol in going from the $C5//C8$ in ϵQ to a $C5//C9/C8$ structure.³⁴

As can be seen in Table 5.2, the L-chirality of the amino acids studied here results in χ_1 being similar in both extended structures (-137° in ϵN and -103° in ϵQ), with differences appearing in subsequent dihedrals. When viewed down the peptide backbone from the $N \rightarrow C$ termini, the functional groups jut out to the right side, and then fold back over towards the backbone amide groups. The $C5$ hydrogen bonds appear within 8 cm^{-1} of one another, indicating similar hydrogen bond strengths. Both the $C8$ and $C7$ H-bonds in ϵN occur with near-optimal distances and angles of approach: $2.23 \text{ \AA}/146^\circ$ and $2.04 \text{ \AA}/160^\circ$, respectively. The AS $C8$ NH_2 stretch of ϵN is 52 cm^{-1} lower in frequency than the analogous ϵQ free stretch, which appears at 3562 cm^{-1} .

The $C7$ and analogous $C8$ NH stretch transitions in ϵN and ϵQ appear at 3279 and 3310 cm^{-1} , respectively. Given that the ϵQ $C8$ is $\sim 0.1 \text{ \AA}$ shorter than its $C7$ counterpart, it is natural to wonder why it appears 31 cm^{-1} higher in frequency. We note that the ϵN and ϵQ structures differ

primarily in ϵN possessing a $//\underline{\text{C8}}/\underline{\text{C7}}$ bridged double hydrogen bonded structure while ϵQ forms only the $\underline{\text{C8}}$ hydrogen bond. This suggests that cooperative hydrogen bond strengthening could account for the discrepancy between the ϵN and ϵQ $\underline{\text{C7}}$ and $\underline{\text{C8}}$ NH stretch frequencies, respectively. Indeed, ϵN is a triply hydrogen bonded cycle, with all three hydrogen bonds experiencing cooperative effects, thereby increasing the NH bond distances, and decreasing the NH stretch absorption frequencies. Since ϵQ lacks this hydrogen bonded cycle, it would not experience the same magnitude of cooperative effects.

The peptide backbones in β -sheets adopt extended conformations which utilize the same C5 hydrogen bond found in ϵN and ϵQ . As pointed out in the Gln studies, this raises the intriguing possibility that the local extended conformation, supported by sidechain-backbone hydrogen bonds, could play a role in local β -strand formation on the way to β -sheet formation. As we have seen, however, neither Ac-Ala-Asn-NHBn nor Ac-Asn-Asn-NHBn adopt extended β -sheet structures in the gas-phase. It would be interesting to see what intramolecular interactions dominate in even longer poly-Asn and poly-Gln peptides in the gas-phase. In terms of free energy ranking, ϵN is second in energy, above γN (Table 5.4), raising the possibility that the local extended conformation could play a competitive role in a free energy environment. As mentioned above, the ϵN NHMe cap analogue is one of only two low energy structures within 15 kJ/mol of global minimum, along with γN (Table 5.3).

5.4.3 Type I β -Turns

In both Ac-Ala-Asn-NHBn and Ac-Asn-Asn-NHBn, population is funneled into one conformational isomer: the type I β -turn. Given that both Ac-Asn-NHBn conformers incorporate bridged sidechain-backbone hydrogen bonds, it is curious that neither dipeptide includes such a bridged structure. Inspection of each assigned β -turn structure, however, yields a satisfying physical explanation. In order for the $i+2$ NH to engage in a strong $\underline{\text{C6}}$ hydrogen bond with the $i+2$ carboxamide C=O while at the same time retaining the C10 hydrogen bond (that defines the β -turn), the $i+2$ Asn NH_2 group must be almost planar with the $i+2$ backbone C=O. This spatial relationship makes hydrogen bonding very unlikely.

It is important to note that both analogous Gln-containing dipeptides also exclusively form type I β -turns in the gas phase.^{34,35} In what follows, these four structures will be referred to as β_{AN} , β_{NN} , β_{AQ} , and β_{QQ} , where the subscripted letters abbreviate the amino acids in the dipeptide. We will use Figure 5.16 to guide the discussion, which presents and compares the structures and spectra of β_{AN} and β_{AQ} , and β_{NN} and β_{QQ} . As the structures in Figure 5.16 and the dihedrals listed in Table 5.2 show, these four β -turns are quite similar to one another. Structural differences made manifest in the spectra do, however, exist, and it is to these details that we now turn

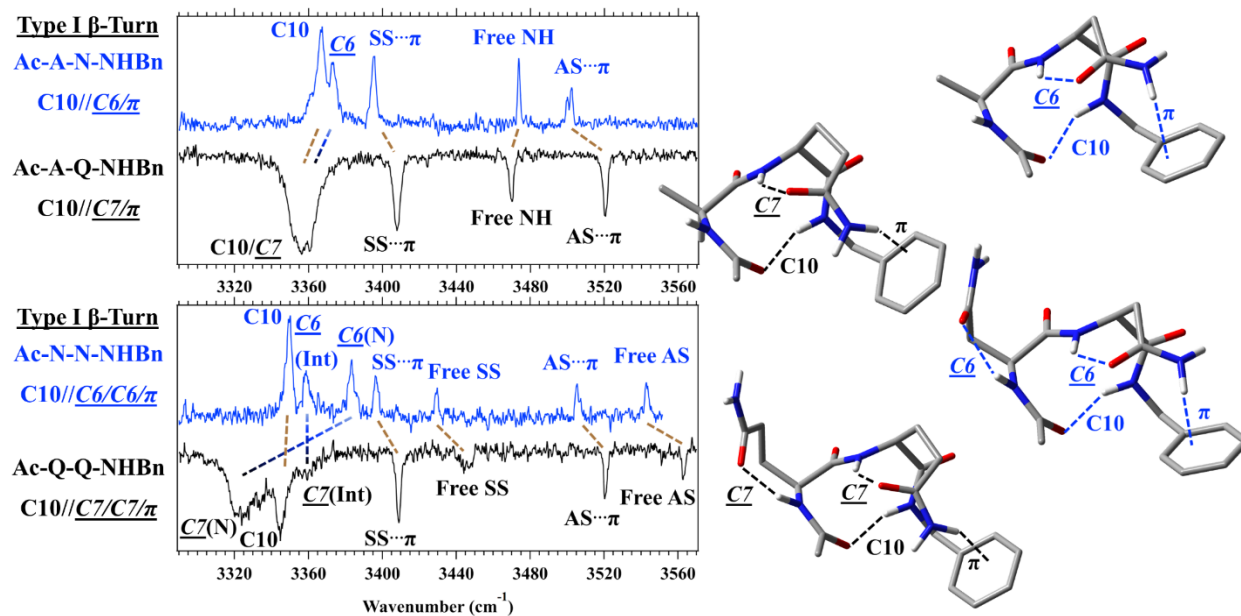


Figure 5.16. Hydride stretch IR spectra and experimentally assigned structures of analogous Ac-Ala-Asn-NHBn and Ac-Ala-Gln-NHBn (top) and Ac-Asn-Asn-NHBn and Ac-Gln-Gln-NHBn (bottom) conformers. Asn hydrogen bonds and spectra are designated in blue while those of Gln are designated in black. Transitions are labelled with the main carrier of the vibration with analogous hydrogen bonds going from Asn to Gln connected with dashed lines and color coded in the following way: the same hydrogen bonded cycles connected with brown lines and analogous ($C_n - (C_n + 1)$) cycles with faded blue to black lines

The top half of Figure 5.16 displays the structures and spectra belonging to the $C10//C6/\pi$ and $C10//C7/\pi$ hydrogen bonded conformers of β_{AN} and β_{AQ} , respectively. As one might expect, their hydride stretch spectra look very similar. The high frequency stretch assigned to the π hydrogen bound asymmetric NH_2 stretch is 18 cm^{-1} higher in frequency in β_{AQ} (3520 cm^{-1}) than in β_{AN} (3502 cm^{-1}). This is most likely a consequence of two factors: The NH_2 is more centered over

the aromatic ring in β_{AN} than in β_{AQ} , and there is a weak interaction between the NH_2 group and the C-terminal $C=O$ group. Indeed, in each pair of β -turn dipeptides the Asn and Gln residues utilize opposite NH groups for the $NH_2 \cdots \pi$ interaction. The symmetric stretch pair occurs 107 and 112 cm^{-1} down in frequency from the asymmetric stretch in β_{AN} and β_{AQ} , respectively. The C-terminal asymmetric and symmetric stretch pairs in β_{NN} and β_{QQ} all appear within 3 cm^{-1} of their Ala-containing analogue stretches mentioned above, providing spectroscopic evidence that the C-terminal environment of the NH_2 groups are very similar within each residue pair. The free NH stretches in β_{AN} and β_{AQ} occur within 4 cm^{-1} of one another. The shorter and stronger C7 NH stretch fundamental is lower in frequency (1.97 Å, 3361 cm^{-1}) than the longer and weaker C6 NH stretch (2.08 Å, 3373 cm^{-1}). The β_{AN} and β_{AQ} C10 frequencies are within 10 cm^{-1} of one another, indicating similar hydrogen bond strengths.

In going from Ac-A-N-NHBn to Ac-N-N-NHBn (and Gln analogues) the type I β -turn structure is preserved, with the N-terminal carboxamide group adding an additional C6 (C7) sidechain-backbone hydrogen bond (see Figure 5.12 for the overlap of the β_{AN} and β_{NN} backbones and Figure 5.13 for a direct comparison of their hydride stretch spectra). This conservation of structure is evident in Figure 5.16. The N-terminal free NH_2 AS and SS fundamentals appear at 3543/3430 and 3562/3444 cm^{-1} in β_{NN} and β_{QQ} , respectively. The shift to lower frequency in β_{NN} may again be attributed to a weak interaction between the N-terminal NH_2 and amide $C=O$. It is heuristically pleasing to view the four highest frequency asymmetric NH_2 transitions between β_{NN} and β_{QQ} (Figure 5.16) as equivalent NH_2 groups in different environments. In order of decreasing frequency, we classify them in the following way: Free, Free with weak interaction, π hydrogen bond, π hydrogen bond with weak interaction, with each weak interaction resulting in an additional ~ 20 cm^{-1} downshift in frequency.

The C10 hydrogen bonds in β_{NN} and β_{QQ} have NH stretch fundamentals within 5 cm^{-1} of one another, again indicating similar hydrogen bond strength. Additionally, the interior C6 in β_{NN} and C7 in β_{QQ} are of similar strength, with transitions within 1 cm^{-1} of each other in the spectra. In contrast, the N-terminal C6 and C7 are separated from one another by 60 cm^{-1} . This can be understood in the context of hydrogen bond distance: 2.16 Å in β_{NN} and a remarkably short 1.91 Å in β_{QQ} (see Figure 5.17 and Figure 5.18 for the overlap of the β_{AN} and β_{AQ} , and β_{NN} and β_{QQ} ,

respectively). The above spectroscopic and computational evidence suggests that glutamine is especially well set-up to accommodate the β -turn via strong sidechain-backbone hydrogen bond stabilization

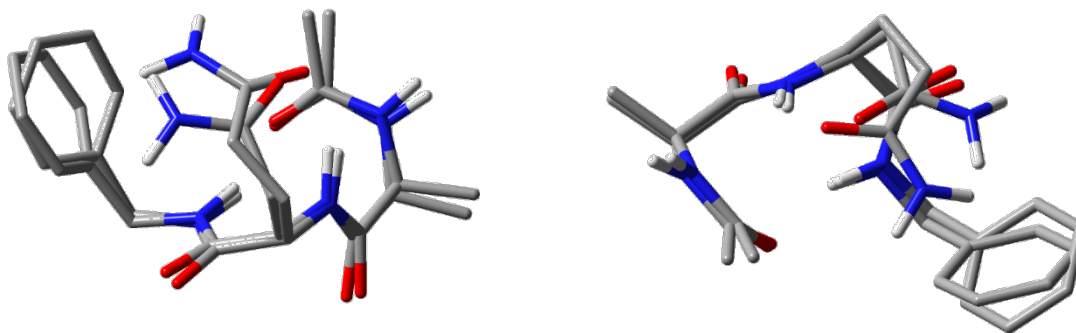


Figure 5.17. Two views of the peptide backbone overlap (with hydrogens removed) of Ac-Ala-Asn-NHBn and Ac-Ala-Gln-NHBn

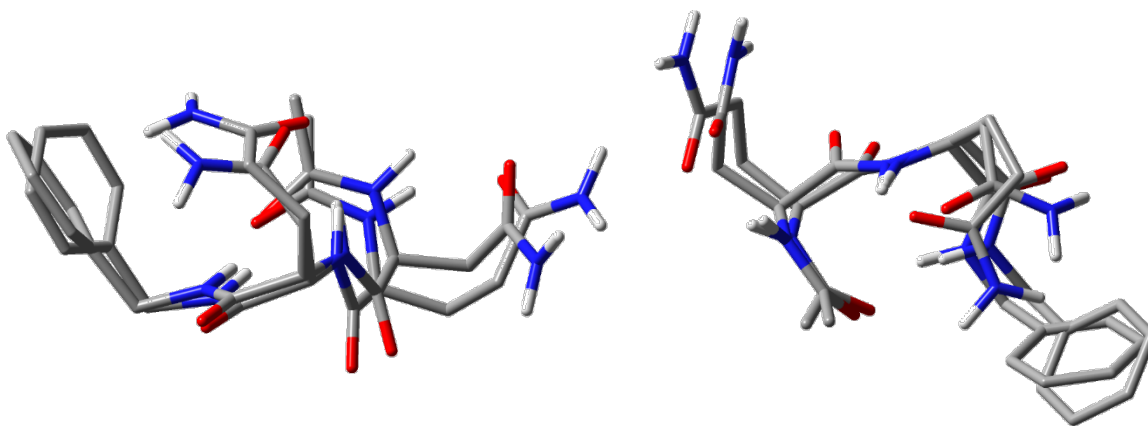


Figure 5.18. Two views of the peptide backbone overlap (with hydrogens removed) of Ac-Asn-Asn-NHBn and Ac-Gln-Gln-NHBn

Table 5.5. Relative potential energies and conformational families of the 30 kJ/mol lowest energy structures of Ac-Ala-Asn-NHBn upon exchange of NHBn cap for NHMe cap and geometry optimization at the DFT B3LYP-D3BJ/6-31+G(d)) level of theory. Note that the experimentally observed conformer remains the global energy minimum. Also, the type I β -turn structure is conserved even without the π interaction with the NHBn cap

<u>Ac-Ala-Asn-NHBn</u> <u>Conformer</u>	<u>NHBn</u> <u>Conformational</u> <u>Family</u>	<u>ΔE (kJ/mol)</u> <u>(NHBn cap)</u>	<u>NHMe</u> <u>Conformational</u> <u>Family</u>	<u>ΔE (kJ/mol)</u> <u>(NHMe cap)</u>
Conf A (type I β -turn)	C10//C6/pi	0.0	C10//C6	0.0
Ac-A-N_105.log:	C10//C6/C7	10.2	C10//C6	0.0
AN_OPLS_29.log:	C7eq//C6/C7	13.4	C7eq//C6/C7	4.6
AN_OPLS_39.log:	C10//C6	15.7	C10//C6	0.0
AN_OPLS_24.log:	C10//C6	17.5	C10//C6	0.0
AN_OPLS_31.log:	C10//C6	18.4	C10//C6/C7	10.7
AcAlaAsnNHBn_98.log:	C7eq/C7eq//C7	18.5	C7eq/C7eq//C7	9.8
AcAlaAsnNHBn_99.log:	C7eq//C7/pi	19.2	C7eq//C7	7.5
AN_OPLS_41.log:	C7eq//C7	20.4	C7eq//C7	7.5
			Bif C5-	10.7
AN_OPLS_30.log:	Bif C5-C7eq//C6	21.6	C7eq//C6/C7	
AN_OPLS_8.log:	C10//C7	22.1	C10//C7	22.3
AN_OPLS_61.log:	C7eq//C6/C7	22.8	C7eq//C6/C7	4.6
AcAlaAsnNHBn_70.log:	C10//C7	23.3	C10//C7	22.3
AN_OPLS_5.log:	C10	24.6	C10//C8	24.3
AN_OPLS_47.log:	C7eq//C7	24.9	C7eq//C7	7.5
AN_OPLS_7.log:	C7ax/pi/C7eq//C7	25.0	C7ax/C7eq//C7	24.9
AN_OPLS_19.log:	C7eq/C7eq//C7	25.8	C7eq/C7eq//C7	15.8
AcAlaAsnNHBn_62.log:	C5//C11	27.6	C5//C11/C7	13.1
	Bif C5-		Bif C5-	10.7
Ac-A-N_113.log:	C7eq//C6/C7	28.9	C7eq//C6/C7	
AN_OPLS_21.log:	C10//C8	29.1	C10//C8	22.3
AcAlaAsnNHBn_56.log:	C5/C5//C8/C7	29.2	C5/C5//C8/C7	12.4
	C7eq/pi/Bif C7ax-		C7eq/Bif C7ax-	29.0
AN_OPLS_3.log:	//-C8	29.3	//-C8	
AN_OPLS_6.log:	C7eq/C7eq	29.6	C7eq/C7eq	15.1

As with the shorter Asn-containing peptides, calculations were carried out on all structures within 30 kJ/mol of the global minimum to test the energetic influence of the NHBn cap, as well as to get an idea of the free energy landscape at room temperature. These values for Ac-Ala-Asn-NHBn and Ac-Asn-Asn-NHBn are presented in Table 5.5 and Table 5.6, respectively. In the case of β_{AN} , substitution of NHBn for NHMe results in the C10//C7// π structure remaining the global energy minimum. β_{NN} , however, is displaced as the global energy minimum by a C10//C6/C7//C11 structure (6.85 kJ/mol with NHBn cap) and takes up position as the second lowest energy structure (0.57 kJ/mol, Table 5.6, Figure 5.19). In this C10//C6/C7//C11 structure, the carboxamide NH₂ of the *i*+1 Asn residue engages in a H-bond with the carboxamide C=O of the *i*+2 Asn residue, resulting in two large hydrogen bonded cycles along the peptide backbone. In terms of free energy, both β_{AN} and β_{NN} retain their positions as the global energy minima (Table 5.7 and Table 5.8). As with the shorter peptides discussed above, this indicates that the type I β -turns studied here are entropically competitive with other structures even at room temperature

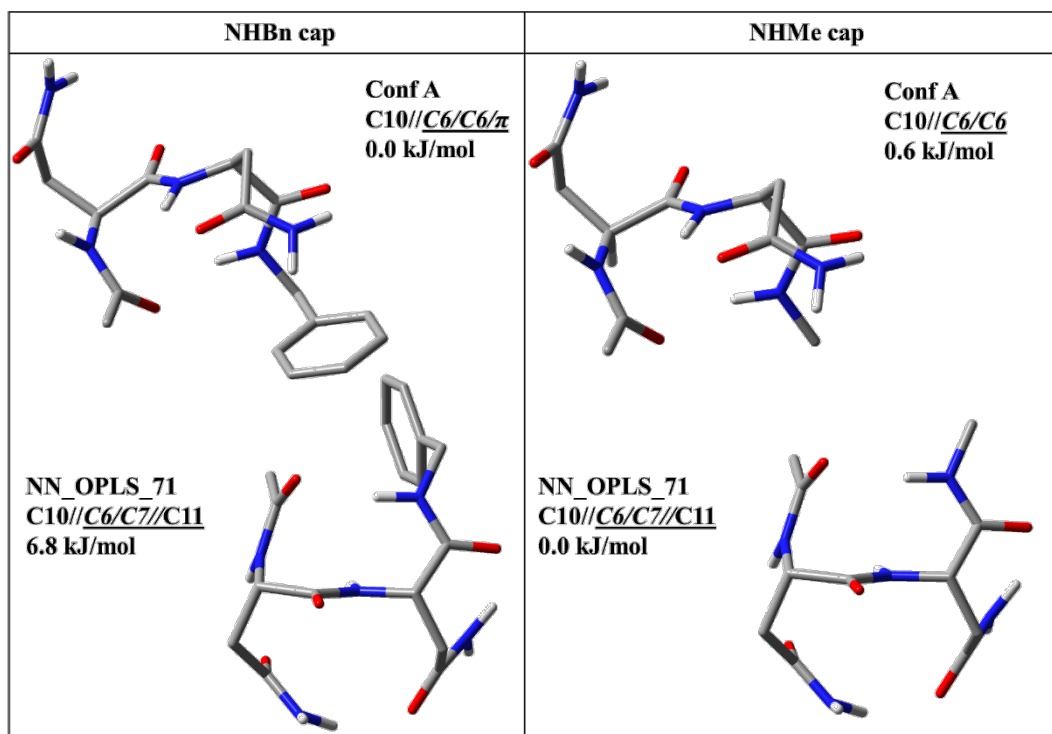


Figure 5.19. Comparison of the assigned type I β -turn structure of Ac-Asn-Asn-NHBn with the second lowest energy calculated structure which engages in sidechain-sidechain hydrogen bonding. Structures and energies are displayed for both NHBn and NHMe caps. Note that the energy ordering flips upon cap substitution

Table 5.6. Relative potential energies and conformational families of the 30 kJ/mol lowest energy structures of Ac-Asn-Asn-NHBn upon exchange of NHBn cap for NHMe cap and geometry optimization at the DFT B3LYP-D3BJ/6-31+G(d)) level of theory. Note that the experimentally observed conformer moves from the lowest to the second lowest energy structure upon NHMe cap substitution. The conformer that moved to the global minimum position is also a type I β -turn which differentiates itself from the experimentally observed structure by having a sidechain-sidechain hydrogen bond

<u>Ac-Asn-Asn-NHBn Conformer</u>	<u>NHBn Conformational Family</u>	<u>ΔE (kJ/mol) (NHBn cap)</u>	<u>NHMe Conformational Family</u>	<u>ΔE (kJ/mol) (NHMe cap)</u>
Conf A (type I β -turn)	C10//C6/C6/pi	0.0	C10//C6/C6	0.6
NN_OPLS_71.log:	C10//C6/C7//C11	6.8	C10//C6/C7//C11	0.0
Ac_NN_NHBn_AMBER_21.log:	C5//C8/C10/C6/pi	7.7	C5//C8/C10/C6	6.4
Ac_NN_NHBn_AMBER_47.log:	C5//C10/C6/pi	9.0	C5//C8/C10/C6	6.4
NN_OPLS_6.log:	C5//C10/pi/C6	15.8	C5//C8/C10/C6	6.4
Ac_NN_NHBn_AMBER_22.log:	C10//C7/pi/Bif C6-//C11	17.8	C10//C7/Bif C6-//C11	14.7
NN_OPLS_109.log:	C10//C7//C11	18.1	C10//C7//C11	14.4
NN_OPLS_83.log:	C5//C8/C10/C6	18.2	C5//C8/C10/C6/C6	3.6
NN_OPLS_55.log:	C5//C8/C10/C6	19.5	C5//C8/C10/C6	6.4
NN_OPLS_77.log:	C10//Bif C6-//C11	21.0	C10//C7/Bif C6-//C11	14.7
			Bif C5-C7eq//C8/C7/C7	16.7
Ac_NN_NHBn_AMBER_35.log:	BifC5-C7eq//C8/C7/C7	21.2		
Ac_NN_NHBn_AMBER_13.log:	C5//C10/pi/C6	22.0	C5//C8/C10/C6	6.4
NN_OPLS_3.log:	Bif C5-C7eq//C7/pi/C7	23.2	Bif C5-C7eq//C8/C7/C7	16.7
	BifC5-C7eq//pi/C7/BifC6-//C11		Bif C5-C7eq//Bif C6-//C11	16.3
Ac_NN_NHBn_AMBER_66.log:		25.0		
Ac_NN_NHBn_AMBER_44.log:	Bif C5-C7eq//C7/pi/C7	25.6	BifC5-C7eq//C8/C7/C7	18.2
Ac_NN_NHBn_AMBER_19.log:	C5//Bif C7-C10/pi/C7	28.8	C5//C8/Bif C7-C10/C7	19.2
NN_OPLS_74.log:	C5//Bif C7-C10	28.8	C5//C8/Bif C7-C10/C7	19.1
			Bif C5-C7eq//C8/BifC7-//C11	18.1
Ac_NN_NHBn_AMBER_104.log:	Bif C5-C7eq//C7/pi	29.0		
Ac_NN_NHBn_AMBER_53.log:	C7eq/Bif C7eq-//C7/pi/C7	29.5	C7eq/Bif C7eq-//C7/C7	31.2
Ac_NN_NHBn_AMBER_63.log:	C10//pi/C6	29.9	C10//C7/Bif C6-//C11	14.7
Ac_NN_NHBn_AMBER_97.log:	Bif C5-C7eq//C8/C7/C7	29.9	Bif C5-C7eq//C8/C7/C7	31.1
NN_OPLS_37.log:	C7eq//C7/C7/pi	30.0	C7eq//C7/C7	18.1

Table 5.7. Relative potential energies, free energy corrections (at room temperature), and free energies for all calculated structures under 30 kJ/mol of the global energy minimum of Ac-Ala-Asn-NHBn, calculated at the DFT B3LYP-D3BJ/6-31+G(d)) level of theory. Note that the experimentally assigned type I β -turn conformer remains the global minimum in both potential and free energy ranking

<u>Ac-Ala-Asn-NHBn</u> <u>Conformer</u>	<u>Conformational</u> <u>Family</u>	<u>ΔE (kJ/mol)</u>	<u>G correction</u> <u>(kJ/mol)</u>	<u>ΔG (kJ/mol)</u>
Conf A (type I β -Turn)	C10//C6/pi	0.0	0.0	0.0
Ac-A-N_105.log:	C10//C6/C7	10.2	-7.4	2.8
AN_OPLS_29.log:	C7eq//C6/C7	13.4	-6.4	7.0
AN_OPLS_39.log:	C10//C6	15.7	-8.5	7.3
AN_OPLS_24.log:	C10//C6	17.5	-11.0	6.5
AN_OPLS_31.log:	C10//C6	18.4	-4.3	14.2
AcAlaAsnNHBn_98.log:	C7eq/C7eq//C7	18.5	-5.6	12.8
AcAlaAsnNHBn_99.log:	C7eq//C7/pi	19.2	-3.7	15.5
AN_OPLS_41.log:	C7eq//C7	20.4	-8.4	12.0
AN_OPLS_30.log:	Bif C5-C7eq//C6	21.6	-10.7	10.8
AN_OPLS_8.log:	C10//C7	22.1	-4.6	17.5
AN_OPLS_61.log:	C7eq//C6/C7	22.8	-11.1	11.7
AcAlaAsnNHBn_70.log:	C10//C7	23.3	-5.6	17.7
AN_OPLS_5.log:	C10	24.6	-4.4	20.2
AN_OPLS_47.log:	C7eq//C7	24.9	-10.3	14.6
AN_OPLS_7.log:	C7ax/pi/C7eq//C7	25.0	-3.4	21.7
AN_OPLS_19.log:	C7eq/C7eq//C7	25.8	-8.9	16.9
AcAlaAsnNHBn_62.log:	C5//C11 Bif C5-	27.6	-9.5	18.2
Ac-A-N_113.log:	C7eq//C6/C7	28.9	-14.3	14.7
AN_OPLS_21.log:	C10//C8	29.1	-5.9	23.2
AcAlaAsnNHBn_56.log:	C5/C5//C8/C7 C7eq/pi/Bif C7ax-	29.2	-15.2	14.1
AN_OPLS_3.log:	//-C8	29.3	-2.7	26.6
AN_OPLS_6.log:	C7eq/C7eq	29.6	-8.3	21.3

Table 5.8. Relative potential energies, free energy corrections (at room temperature), and free energies for all calculated structures under 30 kJ/mol of the global energy minimum of Ac-Asn-Asn-NHBn, calculated at the DFT B3LYP-D3BJ/6-31+G(d)) level of theory. Note that the experimentally assigned type I β -turn conformer remains the global minimum in both potential and free energy ranking

<u>Ac-Asn-Asn-NHBn</u> <u>Conformer</u>	<u>Conformational Family</u>	<u>ΔE (kJ/mol)</u>	<u>G correction</u> <u>(kJ/mol)</u>	<u>ΔG (kJ/mol)</u>
Conf A (type I β -turn)	C10//C6/C6/pi	0.0	0.0	0.0
NN_OPLS_71.log:	C10//C6/C7//C11	6.8	9.7	16.5
Ac_NN_NHBn_AMBER_21.log:	C5//C8/C10/C6/pi	7.7	11.0	18.6
Ac_NN_NHBn_AMBER_47.log:	C5//C10/C6/pi	9.0	13.5	22.6
NN_OPLS_6.log:	C5//C10/pi/C6	15.8	13.0	28.8
	C10//C7/pi/Bif C6-/-			
Ac_NN_NHBn_AMBER_22.log:	C11	17.8	16.4	34.2
NN_OPLS_109.log:	C10///C7//C11	18.1	8.8	26.9
NN_OPLS_83.log:	C5//C8/C10/C6	18.2	18.7	36.9
NN_OPLS_55.log:	C5//C8/C10/C6	19.5	8.4	27.9
NN_OPLS_77.log:	C10//Bif C6-/-C11	21.0	10.1	31.1
	Bif C5-			
Ac_NN_NHBn_AMBER_35.log:	C7eq//C8/C7/C7	21.2	14.0	35.2
Ac_NN_NHBn_AMBER_13.log:	C5//C10/pi/C6	22.0	17.6	39.6
NN_OPLS_3.log:	Bif C5-C7eq//C7/pi/C7	23.2	11.7	35.0
	Bif C5-C7eq//pi/C7/Bif			
Ac_NN_NHBn_AMBER_66.log:	C6-//C11	25.0	23.1	48.0
Ac_NN_NHBn_AMBER_44.log:	Bif C5-C7eq//C7/pi/C7	25.6	25.1	50.7
Ac_NN_NHBn_AMBER_19.log:	C5//Bif C7-C10/pi/C7	28.8	17.2	46.0
NN_OPLS_74.log:	C5//Bif C7-C10	28.8	14.9	43.7
Ac_NN_NHBn_AMBER_104.log:	Bif C5-C7eq//C7/pi	29.0	18.3	47.3
	C7eq/Bif C7eq-			
Ac_NN_NHBn_AMBER_53.log:	//C7/pi/C7	29.5	22.3	51.7
Ac_NN_NHBn_AMBER_63.log:	C10//pi/C6	29.9	8.4	38.3
	Bif C5-			
Ac_NN_NHBn_AMBER_97.log:	C7eq//C8/C7/C7	29.9	11.9	41.8
NN_OPLS_37.log:	C7eq//C7/C7/pi	30.0	14.7	44.7

Upon cooling in a supersonic expansion, the entirety of the population of both β_{AN} and β_{NN} is funneled into a type I β -turn that is stabilized by the Asn side chains. The robustness of these structures to temperature and type of cap is in keeping with the prevalence of Asn-containing β -turns in biological environments.^{57, 58} To get an idea of the similarity in turn parameters between these gas-phase structures and those in naturally occurring, biologically relevant molecules, we compare the calculated backbone ϕ and ψ dihedral angles of β_{AN} and β_{NN} with those found in the Protein Data Bank comprised of the following four generic amino acid residue order: X(AN)X for β_{AN} , and X(NN)X for β_{NN} . These parameters are presented in Table 5.9 and Table 5.10, respectively. We find that, in both cases, the calculated gas-phase parameters are in good agreement with both the crystal structure average values as well as canonical literature values,⁵⁶ indicating that the gas-phase structures characterized in this work are fundamentally preserved, and preferred, in the condensed phase. Indeed, a recent study by Mons et. al. also found the type I β -turn to be among the observed conformations in gas-phase studies of Ac-Phe-Asn-NH₂. Through a Protein Data Bank search, they observed that, with Asn in the $i+2$ position of the β -turn, it is not uncommon for water molecules to bridge the $i+2$ amide NH and side chain C=O, the two groups involved in the C6 hydrogen bond. They proposed that, in hydrophilic environments, this water bridged structure could orient, and stabilize, the local protein backbone in such a way that promotes β -turn formation. This proposition is especially enticing in light of the regularity with which Asn appears in the $i+2$ position of native protein β -turns.^{57, 58}

Table 5.9. Ramachandran angle comparison of type I β -turns with sequence X(AN)X.

<u>Structure</u>	<u>Turn sequence</u>	<u>Residue #</u>	<u>Turn residues</u>	
			<u>(i+1) (phi,psi)</u> <u>(degrees)</u>	<u>(i+2) (phi,psi)</u> <u>(degrees)</u>
Ac-A-N-NHBn ^a	X(AN)X		-68.1, -13.0	-80.0, -0.5
Sulfate reductase ^b	T(AN)Q	393-396	-75.0, -6.1	-104.1, 20.4
Mutant H42Q of hipip ^c	P(AN)A	3-6	-66.7, -21.3	-103.1, 24.5
Beta-mannanase ^d	E(AN)G	13-16	-57.4, -31.6	-77.9, 1.9
Electron transport protein ^e	P(AN)L	96-99	-71.7, -20.5	-100.9, 12.6
Type II activin receptor extracellular domain ^f	N(AN)W	15-18	-63.8, -21.4	-96.0, 27.4
Phenylalanine dehydrogenase ^g	V(AN)A	286-289	-61.6, -36.7	-97.7, 12
Endoglucanase A catalytic core ^h	D(AN)N	135-138	-65.1, -13.6	-97.7, 7.9
3-Isopropylmalate dehydrogenase ⁱ	K(AN)V	195-198	-71.9, -10.5	-75.4, -13.1
Cystathionine gamma- synthase ^j	A(AN)K	382-385	-66.9, -29.6	-89.6, 22.7
Bacterial lipase ^k	G(AN)A	297-300	-57.7, -26.9	-94.6, -2.6
Deacetoxycephalosporin C synthase ^l	C(AN)G	197-200	-57.4, -35.7	-84.2, 3.9
Celcca catalytic domain ^m	F(AN)Y	156-159	-54.2, -32.8	-86.9, -4.3
DD-transpeptidase mutant ⁿ	V(AN)N	68-71	-64.3, -29.9	-106.4, 6.6
Pseudomonas aeruginosa elastase ^o	L(AN)S	236-239	-62.2, -25.5	-99.2, 11.3
Serine protease ^p	Y(AN)A	171-174	-57.3, -37.6	-87.9, 13.3
Leucine aminopeptidase ^q	P(AN)E	174-177	-58.9, -26.5	-71.1, -19.2
Deubiquitinating enzyme ^r	I(AN)N	104-107	-53.0, -38.0	-89.6, 8.4
Average of crystal structures	X(AN)X		-62.7, -26.1	-91.9, 7.9

^a This work. ^b (PDB ID: 1aop).⁵⁹ ^c (PDB ID: 1b0y).⁶⁰ ^d (PDB ID: 1bqc).⁶¹ ^e (PDB ID: 1bqk).⁶² ^f (PDB ID: 1bte).⁶³ ^g (PDB ID: 1bw9).⁶⁴ ^h (PDB ID: 1cem).⁶⁵ ⁱ (PDB ID: 1cnz).⁶⁶ ^j (PDB ID: 1cs1).⁶⁷ ^k (PDB ID: 1cvl).⁶⁸ ^l (PDB ID: 1dcs).⁶⁹ ^m (PDB ID: 1edg).⁷⁰ ⁿ (PDB ID: 1es5).⁷¹ ^o (PDB ID: 1ezm).⁷² ^p (PDB ID: 1GCI).⁷³ ^q (PDB ID: 1lam).⁷⁴ ^r (PDB ID: 1uch).⁷⁵

Table 5.10. Ramachandran angle comparison of type I β -turns with sequence X(NN)X.

<u>Structure</u>	<u>Turn sequence</u>	<u>Residue #</u>	Turn residues <u>(i+1) (phi,psi)</u> <u>(degrees)</u>	<u>(i+2) (phi,psi)</u> <u>(degrees)</u>
Ac-N-N-NHBn ^a	X(NN)X		-75.8, 0.9	-83.4, -2.7
Chromosome condensation regulator ^b	D(NN)G	148-151	-63.7, -23.8	-100.6, 0
Tetanus toxin C fragment ^c	Q(NN)Q	216-219	-55.0, -19.6	-105.7, 5.8
Human aldose reductase holoenzyme ^d	L(NN)G	6-9	-71.6, -8.4	-96.9, 8.7
Rat pancreatic lipase protein ^e	G(NN)G Z	361-364	-68.6, -16.3	-93.7, -6.8
Staphopain, cysteine proteinase ^f	L(NN)G	130-133	-59.7, -24.3	-93.0, 10.8
Galactose oxidase ^g	R(NN)W	11-14	-49.3, -66.6	-70.2, -2.8
Bacterial cellulose- binding domain ^h	T(NN)A	85-88	-69.1, -11.2	-129.6, 19.1
Human cytomegalovirus DNA polymerase subunit ⁱ	S(NN)R	205-208	-55.1, -40.8	-79.0, 10.4
Vaccinia virus DNA topoisomerase I ^j	D(NN)F	14-17	-71.7, -9.0	-95.4, -3.2
Recombinant apo- chloroperoxidase ^k	D(NN)G	520-523	-57.2, -29.1	-95.1, -0.1
Average of crystal structures	X(NN)X		-62.1, -24.9	-95.9, 4.2

^a This work. ^b (PDB ID: 1a12).⁷⁶ ^c (PDB ID: 1a8d).⁷⁷ ^d (PDB ID: 1ads).⁷⁸ ^e (PDB ID: 1bu8).⁷⁹ ^f (PDB ID: 1cv8).⁸⁰ ^g (PDB ID: 1gof).⁸¹ ^h (PDB ID: 1nbc).⁸² ⁱ (PDB ID: 1t6l).⁸³ ^j (PDB ID: 1vcc).⁸⁴ ^k (PDB ID: 1vns).⁸⁵

5.5 Conclusion

In this study, we have determined the inherent folding preferences of three Asn-containing, capped peptides: Ac-Asn-NHBn, Ac-Ala-Asn-NHBn, and Ac-Asn-Asn-NHBn. Using conformation specific infrared and ultraviolet spectroscopy, we have found that Ac-Asn-NHBn takes both an inverse γ -turn ($C7_{eq}$) and a tentatively assigned extended conformation ($C5$), while both capped dipeptides Ac-Ala-Asn-NHBn and Ac-Asn-Asn-NHBn have all of their population funneled into a type I β -turn. These two turn types and extended structure appear regularly within

the secondary structural framework of nature. In each case, a single backbone-backbone hydrogen bond is supported by at least one sidechain-backbone stabilizing interaction.

In γ N, an unusually strong $C7_{eq}$ hydrogen bond forms the inverse turn, with a doubly hydrogen bonded $//C6/C7$ bridged sidechain-backbone motif resulting in a triamide H-bonded cycle that appears to be cooperatively strengthened. The analogous Gln-containing peptide also forms the same cooperatively strengthened bridged sidechain-backbone supported inverse γ -turn. The extended backbone of ϵ N is supported by a $//C8/C7$ bridged sidechain-backbone double hydrogen bond, an auxiliary interaction not accessible to Gln as a direct result of its more flexible sidechain. The C10-containing type I β -turn structures of β_{AN} and β_{NN} are further stabilized by sidechain-backbone $C6$ H-bonds between the Asn NH_2 and the $C=O$ group on its peptide residue. These β -turns are closely similar to those found in protein crystals, where the relevant Ala and/or Asn residues occupy the $i+1$ and $i+2$ positions of the turn. They are also close in form to the analogous β_{AQ} and β_{QQ} turns, as characterized by the backbone ϕ and ψ dihedral angles. Spectroscopic and computational evidence of strong sidechain-backbone hydrogen bonding suggest that glutamine is especially well set up for β -turn accommodation.

In the case of all Asn-containing peptides studied here, energy optimizations performed with the NHMe capped analogues predicted that the lowest-energy conformations observed with the NHBn cap remain either the lowest or, in the case of β_{AN} , second lowest, energy conformation when the phenyl ring is removed. Additionally, the ranking of the conformations in free energy at room temperature confirmed that the assigned structures occupy the most stable, global free energy minimum positions as well. These results provide evidence that the assigned structures will have significant population over a wide range of conditions. Furthermore, the three structural motifs (inverse γ -turn, extended, type I β -turn) that are stabilized by Asn are all prevalent to some degree in nature.

The fundamental similarity of these Asn- and Gln-containing peptides is especially interesting in light of the requirement for specific amino acid type, rather than sequence, in prion formation, as well as the similar fibrillar properties that polyasparagine exhibits with respect to polyglutamine.^{10, 86, 87} These initial conformational tests of asparagine's local conformational preferences at the dipeptide length would benefit greatly from extension to peptides containing

longer sequences of Asn, Gln, and combinations thereof, with the goal of determining the effect that increasing peptide length has on their inherent structural preferences

5.6 References

1. Y. Zhang, V. H. Man, C. Roland and C. Sagui, *ACS Chem. Neuro.*, 2016, **7**, 576-587.
2. M. F. Perutz, B. J. Pope, D. Owen, E. E. Wanker and E. Scherzinger, *Proc. Natl. Acad. Sci. U. S. A.*, 2002, **99**, 5596-5600.
3. M. D. Michelitsch and J. S. Weissman, *Proc. Natl. Acad. Sci. U. S. A.*, 2000, **97**, 11910-11915.
4. H. Okazawa, in *Protein Misfolding, Aggregation, and Conformational Diseases: Part B: Molecular Mechanisms of Conformational Diseases*, eds. V. N. Uversky and A. L. Fink, Springer US, Boston, MA, 2007, DOI: 10.1007/978-0-387-36534-3_22, pp. 451-463.
5. G. Hoffner and P. Djian, *Mol. Neurobiol.*, 2015, **52**, 1297-1314.
6. K. J. Wolfe and D. M. Cyr, *Semin. Cell Dev. Biol.*, 2011, **22**, 476-481.
7. F. Chiti and C. M. Dobson, *Annu. Rev. Biochem.*, 2006, **75**, 333-366.
8. C. A. Ross, *Neuron*, 2002, **35**, 819-822.
9. L. Mangiarini, K. Sathasivam, M. Seller, B. Cozens, A. Harper, C. Hetherington, M. Lawton, Y. Trotter, H. Lehrach and S. W. Davies, *Cell*, 1996, **87**, 493-506.
10. T. W. Peters and M. Huang, *Prion*, 2007, **1**, 144-153.
11. F. Fornai, M. Ferrucci, M. Gesi, A. B. Di Poggio, F. Giorgi, F. Biagioni and A. Paparelli, *Brain Res. Bull.*, 2006, **69**, 95-100.
12. R. Halfmann, S. Alberti, R. Krishnan, N. Lyle, C. W. O'Donnell, O. D. King, B. Berger, R. V. Pappu and S. Lindquist, *Mol. Cell*, 2011, **43**, 72-84.
13. L. An and P. M. Harrison, *Biol. Direct*, 2016, **11**, 32.
14. T. D. Kurt, P. Aguilar-Calvo, L. Jiang, J. A. Rodriguez, N. Alderson, D. S. Eisenberg and C. J. Sigurdson, *J. Biol. Chem.*, 2017, **292**, 19076-19086.
15. M. D. Geschwind, *Continuum (Minneapolis, Minn.)*, 2015, **21**, 1612-1638.
16. S. B. Prusiner, R. A. Barry, M. P. McKinley, C. G. Bellinger, R. K. Meyer, S. J. DeArmond and D. T. Kingsbury, in *Viruses, Immunity, and Mental Disorders*, Springer, 1987, pp. 23-32.

17. M. R. Sawaya, S. Sambashivan, R. Nelson, M. I. Ivanova, S. A. Sievers, M. I. Apostol, M. J. Thompson, M. Balbirnie, J. J. Wiltzius and H. T. McFarlane, *Nature*, 2007, **447**, 453.
18. R. Nelson, M. R. Sawaya, M. Balbirnie, A. Ø. Madsen, C. Riekel, R. Grothe and D. Eisenberg, *Nature*, 2005, **435**, 773-778.
19. T. L. Benzinger, D. M. Gregory, T. S. Burkoth, H. Miller-Auer, D. G. Lynn, R. E. Botto and S. C. Meredith, *Proc. Natl. Acad. Sci. U. S. A.*, 1998, **95**, 13407-13412.
20. A. K. Paravastu, R. D. Leapman, W.-M. Yau and R. Tycko, *Proc. Natl. Acad. Sci. U. S. A.*, 2008, **105**, 18349-18354.
21. A. T. Petkova, W.-M. Yau and R. Tycko, *Biochem. (Mosc.)*, 2006, **45**, 498-512.
22. F. Shewmaker, R. B. Wickner and R. Tycko, *Proc. Natl. Acad. Sci. U. S. A.*, 2006, **103**, 19754-19759.
23. A. Gorkovskiy, K. R. Thurber, R. Tycko and R. B. Wickner, *Proc. Natl. Acad. Sci. U. S. A.*, 2014, **111**, E4615-E4622.
24. D. S. Kryndushkin, R. B. Wickner and R. Tycko, *J. Mol. Biol.*, 2011, **409**, 263-277.
25. S. Ngo, L. Gu and Z. Guo, *J. Biol. Chem.*, 2011, **286**, 29691-29699.
26. U. Baxa, R. B. Wickner, A. C. Steven, D. E. Anderson, L. N. Marekov, W.-M. Yau and R. Tycko, *Biochem. (Mosc.)*, 2007, **46**, 13149-13162.
27. A. H. DePace, A. Santoso, P. Hillner and J. S. Weissman, *Cell*, 1998, **93**, 1241-1252.
28. F. Fiumara, L. Fioriti, E. R. Kandel and W. A. Hendrickson, *Cell*, **143**, 1121-1135.
29. X. Lu and R. M. Murphy, *Biochem. (Mosc.)*, 2015, **54**, 4784-4794.
30. K. R. Paul and E. D. Ross, *Prion*, 2015, **9**, 347-354.
31. P. G. Vasudev, M. Banerjee, C. Ramakrishnan and P. Balaram, *Proteins: Structure, Function, and Bioinformatics*, 2012, **80**, 991-1002.
32. C. Alemán and J. Puiggali, *J. Phys. Chem. B*, 1997, **101**, 3441-3446.
33. S. Habka, W. Y. Sohn, V. Vaquero-Vara, M. Geleoc, B. Tardivel, V. Brenner, E. Gloaguen and M. Mons, *PCCP*, 2018, DOI: 10.1039/C7CP07605C.
34. P. S. Walsh, J. C. Dean, C. McBurney, H. Kang, S. H. Gellman and T. S. Zwier, *PCCP*, 2016, **18**, 11306-11322.
35. P. S. Walsh, K. N. Blodgett, C. McBurney, S. H. Gellman and T. S. Zwier, *Angew. Chem. Int. Ed.*, 2016, **55**, 14618-14622.

36. W. H. James, E. E. Baquero, S. H. Choi, S. H. Gellman and T. S. Zwier, *J. Phys. Chem. A*, 2010, **114**, 1581-1591.
37. E. E. Baquero, W. H. James, S. H. Choi, S. H. Gellman and T. S. Zwier, *J. Am. Chem. Soc.*, 2008, **130**, 4784-4794.
38. W. H. James, E. E. Baquero, V. A. Shubert, S. H. Choi, S. H. Gellman and T. S. Zwier, *J. Am. Chem. Soc.*, 2009, **131**, 6574-6590.
39. E. E. Baquero, W. H. James, S. H. Choi, S. H. Gellman and T. S. Zwier, *J. Am. Chem. Soc.*, 2008, **130**, 4795-4807.
40. J. C. Dean, E. G. Buchanan and T. S. Zwier, *J. Am. Chem. Soc.*, 2012, **134**, 17186-17201.
41. J. C. Dean, R. Kusaka, P. S. Walsh, F. Allais and T. S. Zwier, *J. Am. Chem. Soc.*, 2014, **136**, 14780-14795.
42. M. J. T. Frisch, G.W.; Schlegel, H.B; Scuseria, G.E.; Robb, M.A.; Cheeseman, J.R.; Scalmani, G.; Barone, V.; Mennucci, B.; Petersson, G.A.; et al., Gaussian, Inc.: Wallingford, CT, 2010.
43. S. Grimme, *J. Comput. Chem.*, 2004, **25**, 1463-1473.
44. S. Grimme, *J. Chem. Phys.*, 2006, **124**, 034108.
45. H. M. Berman, J. Westbrook, Z. Feng, G. Gilliland, T. N. Bhat, H. Weissig, I. N. Shindyalov and P. E. Bourne, *Nucleic Acids Res.*, 2000, **28**, 235-242.
46. D. P. Leader and E. J. Milner-White, *BMC Bioinformatics*, 2009, **10**, 60.
47. T. Nakanaga and F. Ito, *J. Phys. Chem. A*, 1999, **103**, 5440-5445.
48. E. G. Buchanan, W. H. James, S. H. Choi, L. Guo, S. H. Gellman, C. W. Müller and T. S. Zwier, *J. Chem. Phys.*, 2012, **137**, 094301.
49. H. Torii, *J. Phys. Chem. L.*, 2012, **3**, 112-116.
50. H. Torii and M. Kawanaka, *J. Phys. Chem. B*, 2016, **120**, 1624-1634.
51. V. Brenner, F. Piuze, I. Dimicoli, B. Tardivel and M. Mons, *J. Phys. Chem. A*, 2007, **111**, 7347-7354.
52. Y. Loquais, E. Gloaguen, S. Habka, V. Vaquero-Vara, V. Brenner, B. Tardivel and M. Mons, *J. Phys. Chem. A*, 2015, **119**, 5932-5941.
53. W. Chin, M. Mons, J.-P. Dognon, F. Piuze, B. Tardivel and I. Dimicoli, *PCCP*, 2004, **6**, 2700-2709.
54. W. Chin, F. Piuze, I. Dimicoli and M. Mons, *PCCP*, 2006, **8**, 1033-1048.

55. E. J. Milner-White, *J. Mol. Biol.*, 1990, **216**, 385-397.
56. P. N. Lewis, F. A. Momany and H. A. Scheraga, *Biochimica et Biophysica Acta (BBA) - Protein Structure*, 1973, **303**, 211-229.
57. E. G. Hutchinson and J. M. Thornton, *Protein Sci.*, 1994, **3**, 2207-2216.
58. P. Y. Chou and G. D. Fasman, *Biophys. J.*, 1979, **26**, 367-373.
59. B. R. Crane, L. M. Siegel and E. D. Getzoff, *Science*, 1995, **270**, 59.
60. E. Parisini, F. Capozzi, P. Lubini, V. Lamzin, C. Luchinat and G. M. Sheldrick, *Acta Crystallogr. Sect. D. Biol. Crystallogr.*, 1999, **55**, 1773-1784.
61. M. Hilge, S. M. Gloor, W. Rypniewski, O. Sauer, T. D. Heightman, W. Zimmermann, K. Winterhalter and K. Piontek, *Structure*, 1998, **6**, 1433-1444.
62. T. Inoue, N. Nishio, S. Suzuki, K. Kataoka, T. Kohzuma and Y. Kai, *J. Biol. Chem.*, 1999, **274**, 17845-17852.
63. J. Greenwald, W. H. Fischer, W. W. Vale and S. Choe, *Nat. Struct. Mol. Biol.*, 1999, **6**, 18-22.
64. J. L. Vanhooke, J. B. Thoden, N. M. Brunhuber, J. S. Blanchard and H. M. Holden, *Biochem. (Mosc.)*, 1999, **38**, 2326-2339.
65. P. M. Alzari, H. ne Souchon and R. Dominguez, *Structure*, 1996, **4**, 265-275.
66. G. Wallon, G. Kryger, S. T. Lovett, T. Oshima, D. Ringe and G. A. Petsko, *J. Mol. Biol.*, 1997, **266**, 1016-1031.
67. T. Clausen, R. Huber, L. Prade, M. C. Wahl and A. Messerschmidt, *The EMBO journal*, 1998, **17**, 6827-6838.
68. D. Lang, B. Hofmann, L. Haalck, H.-J. Hecht, F. Spener, R. D. Schmid and D. Schomburg, *J. Mol. Biol.*, 1996, **259**, 704-717.
69. K. Valegård, A. C. T. van Scheltinga, M. D. Lloyd, T. Hara, S. Ramaswamy, A. Perrakis, A. Thompson, H.-J. Lee, J. E. Baldwin and C. J. Schofield, *Nature*, 1998, **394**, 805-809.
70. V. Ducros, M. Czjzek, A. Belaich, C. Gaudin, H.-P. Fierobe, J.-P. Belaich, G. J. Davies and R. Haser, *Structure*, 1995, **3**, 939-949.
71. E. Fonze, Rhazi, N., Nguyen-Disteche, M., Charlier, P., *To be published* 2000.
72. M. Thayer, K. M. Flaherty and D. B. McKay, *J. Biol. Chem.*, 1991, **266**, 2864-2871.
73. P. Kuhn, M. Knapp, S. M. Soltis, G. Ganshaw, M. Thoene and R. Bott, *Biochem. (Mosc.)*, 1998, **37**, 13446-13452.

74. N. Straeter and W. N. Lipscomb, *Biochem. (Mosc.)*, 1995, **34**, 14792-14800.
75. S. C. Johnston, C. N. Larsen, W. J. Cook, K. D. Wilkinson and C. P. Hill, *The EMBO Journal*, 1997, **16**, 3787-3796.
76. L. Renault, N. Nassar, I. Vetter, J. Becker, C. Klebe, M. Roth and A. Wittinghofer, *Nature*, 1998, **392**, 97.
77. M. Knapp, Segelke, B., Rupp, B., *Am.Cryst.Assoc., Abstr.Papers (Annual Meeting)*, 1998, **25**.
78. D. Wilson, K. Bohren, K. Gabbay and F. Quioco, *Science*, 1992, **257**, 81-84.
79. A. Roussel, Y. Yang, F. Ferrato, R. Verger, C. Cambillau and M. Lowe, *J. Biol. Chem.*, 1998, **273**, 32121-32128.
80. B. Hofmann, D. Schomburg and H. Hecht, *Acta Crystallogr.*, 1993, **49**, 102.
81. N. Ito, S. E. Phillips, C. Stevens, Z. B. Ogel, M. J. McPherson, J. N. Keen, K. D. Yadav and P. F. Knowles, *Nature*, 1991, **350**, 87-90.
82. J. Tormo, R. Lamed, A. J. Chirino, E. Morag, E. A. Bayer, Y. Shoham and T. A. Steitz, *The EMBO journal*, 1996, **15**, 5739.
83. B. A. Appleton, A. Loregian, D. J. Filman, D. M. Coen and J. M. Hogle, *Mol. Cell*, 2004, **15**, 233-244.
84. A. Sharma, R. Hanai and A. Mondragón, *Structure*, 1994, **2**, 767-777.
85. S. Macedo-Ribeiro, W. Hemrika, R. Renirie, R. Wever and A. Messerschmidt, *J. Biol. Inorg. Chem.*, 1999, **4**, 209-219.
86. E. D. Ross, U. Baxa and R. B. Wickner, *Mol. Cell. Biol.*, 2004, **24**, 7206-7213.
87. E. D. Ross, H. K. Edskes, M. J. Terry and R. B. Wickner, *Proc. Natl. Acad. Sci. U. S. A.*, 2005, **102**, 12825-12830.

CHAPTER 6. VIBRONIC SPECTROSCOPY OF METHYL ANTHRANILATE AND ITS WATER COMPLEX: HYDROGEN ATOM DISLOCATION IN THE EXCITED STATE

Adapted with permission from *Phys. Chem. Chem. Phys.*, 2019, 21, 21355. Copyright 2019 the PCCP Owner Societies.

6.1 Introduction

Methyl Anthranilate (MA) is the precursor to menthyl anthranilate (MenA), an FDA approved sunscreen agent.¹ Upon UV absorption, efficient sunscreen molecules are able to non-radiatively decay back to their ground electronic state, thereby regenerating their UV-absorbing capacities. In some cases, internal conversion is thought to be facilitated on the S_1 surface by H-atom transfer.²⁻⁸ As such, much theoretical and experimental work has been directed toward understanding excited state hydrogen atom, or proton, transfer processes in this family of molecules. There are circumstances, however, in which excited state intramolecular H-atom transfer does not completely quench fluorescence, but instead leads to a Stokes-shifted fluorescence that signals its occurrence, as in the case of salicylic acid and methyl salicylate.^{3, 4, 9, 10} This shifted emission provides a ready means of assessing the efficiency of the process as a function of vibrational level in the excited state.

For a hydrogen atom transfer process to occur, a donor hydrogen must be oriented toward an acceptor atom. Upon electronic excitation the donor X-H becomes more acidic while the acceptor Y becomes more basic, and the X-H bond is broken, resulting in the transfer of the hydrogen to the acceptor atom.^{11, 12} In so doing, the excited state geometry rearranges as it moves on the potential energy surface, producing broad, red-shifted emission back to highly excited vibrational states in the ground state. This red-shifted emission is characteristic of these transient hydrogen transfer products. Alternatively, the excited state molecule may, through displacements along one or more internal coordinates, reach a conical intersection and non-radiatively decay back to the electronic ground state.^{3, 11-13}

There is a body of evidence, however, that suggests that in some cases, rather than a complete hydrogen atom transfer, it is a hydrogen atom dislocation that occurs upon electronic excitation, where the X-H bond distance is increased, but not to the point of breaking and forming

new covalent bonds.¹⁴⁻¹⁹ In many ways, this is a fascinating circumstance in which the structural change on the excited state surface heads toward chemical reaction, but in not achieving it, enables detailed structural characterization. By dispersing the emission from the excited state vibrational levels, one observes the projection of each level back into the ground state in regions where the ground state vibrations still can be used as a set of modes to characterize the excited state structural change. In a previous study of the infrared (IR) and electronic spectroscopy of anthranilic acid and its water complex in the ground (S_0) and first excited (S_1) electronic states, the body of spectroscopic evidence pointed to a hydrogen atom dislocation, rather than transfer, occurring upon electronic excitation.^{14, 15} However, no dispersed fluorescence scans were carried out, limiting the degree to which structural characterization was possible.

In the present study, we carry out just such a study on a close analog of anthranilic acid, methyl anthranilate, which replaces the carboxylic acid hydrogen with a methyl group. MA, shown in Figure 6.1, has a 6-membered hydrogen bonded ring closed by an $\text{NH}\cdots\text{O}=\text{C}$ H-bond. In this first of two chapters on MA, we report a detailed study of the vibrationally-resolved electronic spectroscopy of MA and its single-water complex, MA- H_2O , in both the ground and excited electronic states. Using a suite of laser-based techniques, coupled with density functional theory calculations, we interrogate the vibronic structure of jet-cooled MA and MA- H_2O , and extract and discuss the structural implications of the spectra.

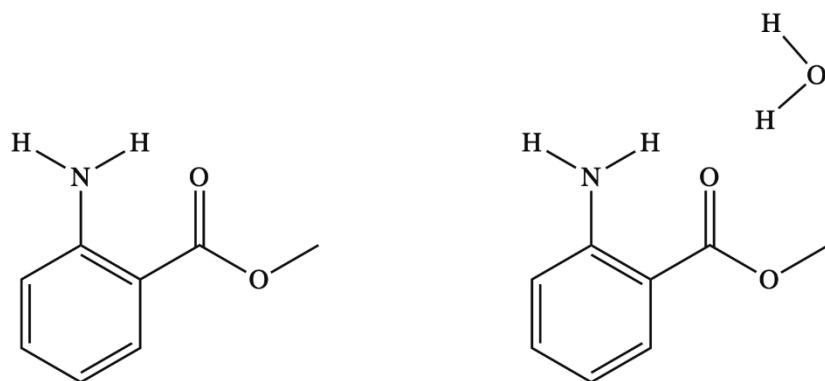


Figure 6.1. Chemical structures of methyl anthranilate (MA) and methyl anthranilate-water complex (MA- H_2O).

6.2 Experimental and Computational Methods

6.2.1 Experimental Methods

Methyl anthranilate was purchased from Sigma-Aldrich ($\geq 99\%$ purity) and used without further purification. The instrument used to collect fluorescence data has been described in detail in Chapter 2. The sample was entrained in 2.0 bar backing pressure of helium and expanded through an 800 μm orifice of a pulsed valve (Parker series 9 General valve) into a vacuum chamber pumped by a roots blower. In the ensuing supersonic expansion, collisions with the helium backing gas serve to cool MA to its ground state zero-point vibrational energy level. The MA-H₂O complex was observed in the expansion without changing experimental conditions, formed by residual H₂O present in the lines and sample. The identity of the MA monomer and water complex were verified by mass-resolved excitation spectra. The collisionally cooled molecules are interrogated by one or more lasers propagating perpendicular to the expansion, intersecting the expansion approximately 8 mm downstream from the source. Emission is collected at the focal point of two 4-inch diameter spherical mirrors, the bottom of which has a 1 cm hole through which resonant fluorescence is steered. This light is collimated through a plano-convex lens, passed through long-pass filters to reduce scattered laser light, and imaged onto a photomultiplier tube. Laser induced fluorescence (LIF) excitation spectra were collected by scanning the output of a 20 Hz frequency doubled Nd:YAG-pumped dye laser (Radiant Dyes NarrowScan) across the 28,500-30,000 cm^{-1} region associated with the S₀-S₁ transition of MA, where total collected fluorescence is plotted as a function of excitation wavelength.

Since the LIF spectrum contains contributions from all possible conformational isomers (conformers) and complexes of MA, double resonance laser techniques were employed to decompose the spectrum into its component parts. UV-UV holeburning (UV-UV HB), IR-UV holeburning (IR-UV HB), and UV depletion (UV-D) spectroscopies were used for this purpose. In UV-UV HB, a 10 Hz hole-burn laser (Lambda Physik Scanmate) has its wavelength fixed on some vibronic transition in the LIF spectrum. This hole-burn laser temporally precedes by 100 ns, a 20 Hz probe laser which is scanned through the region of interest. When the probe laser wavelength is resonant with a vibronic transition which shares the same ground state as the transition on which the hole-burn laser is fixed, a decrease in fluorescence results from the depletion of ground state zero-point populated molecules. This difference is measured by passing the 20 Hz fluorescence signal through a gated integrator operating in active baseline subtraction

mode, the output of which is equivalent to a conformer- or complex-specific UV excitation spectrum. IR-UV HB is the same as UV-UV HB, except that the 10 Hz hole-burn laser is now an IR laser (LaserVision OPO) which has its frequency fixed on a unique vibrational transition of the species of interest.

UV-D is similar to UV-UV HB, except that the 10 Hz hole-burn laser is scanned through the region of interest, while the 20 Hz probe laser is fixed on some vibronic transition, whose constant fluorescence signal is monitored. As in UV-UV HB, a conformer-specific UV spectrum is generated. The UV-D spectrum has the advantage that it enables acquisition of the true absorption spectrum, regardless of whether the tuned HB laser accesses states that fluoresce appreciably or not. In this experimental scheme, the signal is a ground state depletion, which is governed solely by the absorption properties of the molecule, rather than the modulation of excited state-dependent fluorescence. Comparison of the UV-D to the UV-UV HB spectrum gives insight into the nature and extent of non-radiative processes that may occur in the excited state. A disadvantage of the method is that the UV-D spectrum measures depletion of a constant non-zero signal, and therefore has the inherent noise associated with subtraction of two large signals.

Dispersed fluorescence (DFL) spectra were used to aid in the assignment of the transitions in the excitation spectrum by resolving the emission from individual excited state levels prepared by the laser. In this scheme, an excitation laser has its wavelength fixed on some vibronic transition of interest. The emitted fluorescence is dispersed by passing it through a $\frac{3}{4}$ -meter monochromator outfitted with a grating blazed for UV detection. The dispersed emission is then imaged at the output focal plane onto a gated-intensified CCD camera. This technique determines the ground state vibrational levels formed by emission from a single, laser-prepared excited state vibrational level.

6.2.2 Computational Methods

Conformational searches of MA and MA-H₂O were performed using a torsional-sampling Monte Carlo Multiple Minimum algorithm with the OPLS3 force field within the MacroModel computational suite. These calculated structures served as the starting structures for geometry optimization via density functional theory (DFT) calculations, using the Becke 3LYP (B3LYP) hybrid functional supplemented with the D3 version of Grimme's dispersion correction²⁰ and Becke-Johnson (BJ) damping.²¹ This functional was used in conjunction with the def2TZVP basis

set to calculate harmonic vibrational frequencies of the optimized ground state structures. Time dependent DFT (TD-DFT) calculations were then used to calculate vertical and adiabatic excitation energies as well as the geometry and harmonic vibrational frequencies of the first excited singlet state of multiple MA and MA-H₂O conformers. The Gaussian16 suite of programs was used for the DFT calculations and the visualization of normal modes.²² Molecular orbitals and optimized structures were visualized using the Gaussian16 suite and Chemcraft Software.²³

6.3 Results and Analysis

6.3.1 Methyl Anthranilate Monomer

Computational Predictions

In its ground state, MA may exist as either of two rotamers: one where the amine group hydrogen bonds with the ester oxygen, and the other in which the amine group hydrogen bonds with the carbonyl oxygen (see Figure 6.2). At the DFT B3LYP-D3BJ/def2TZVP level of theory, the second rotamer is calculated to be 13.3 kJ/mol lower in energy than the first rotamer. In the supersonic free jet environment, one would anticipate all of the population funneling to the lower energy rotamer. Key structural parameters predicted by the calculations for the C=O bound rotamer in the ground (S_0) and first excited (S_1) singlet states are shown in Figure 6.3. The S_1 geometry is predicted to be planar, while the S_0 equilibrium geometry deviates slightly from planarity along the NH₂ inversion coordinate. Relaxed potential energy scans performed along the CNHH improper dihedral angle reveal a wide symmetric double minimum potential in the S_0 electronic state with minima at $\pm 18^\circ$ and a tiny 5 cm⁻¹ inversion barrier centered at the planar geometry (see Figure 6.4). Since this barrier is well below the zero-point energy, we should anticipate a quasi-planar S_0 geometry with a vibrationally averaged planar configuration, with no inversion tunneling splitting.

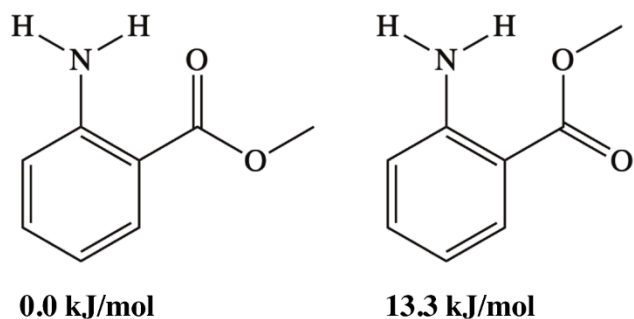


Figure 6.2. The two low-energy rotamers of MA. Zero-point corrected energies calculated at the DFT B3LYP-D3BJ/def2TZVP level of theory

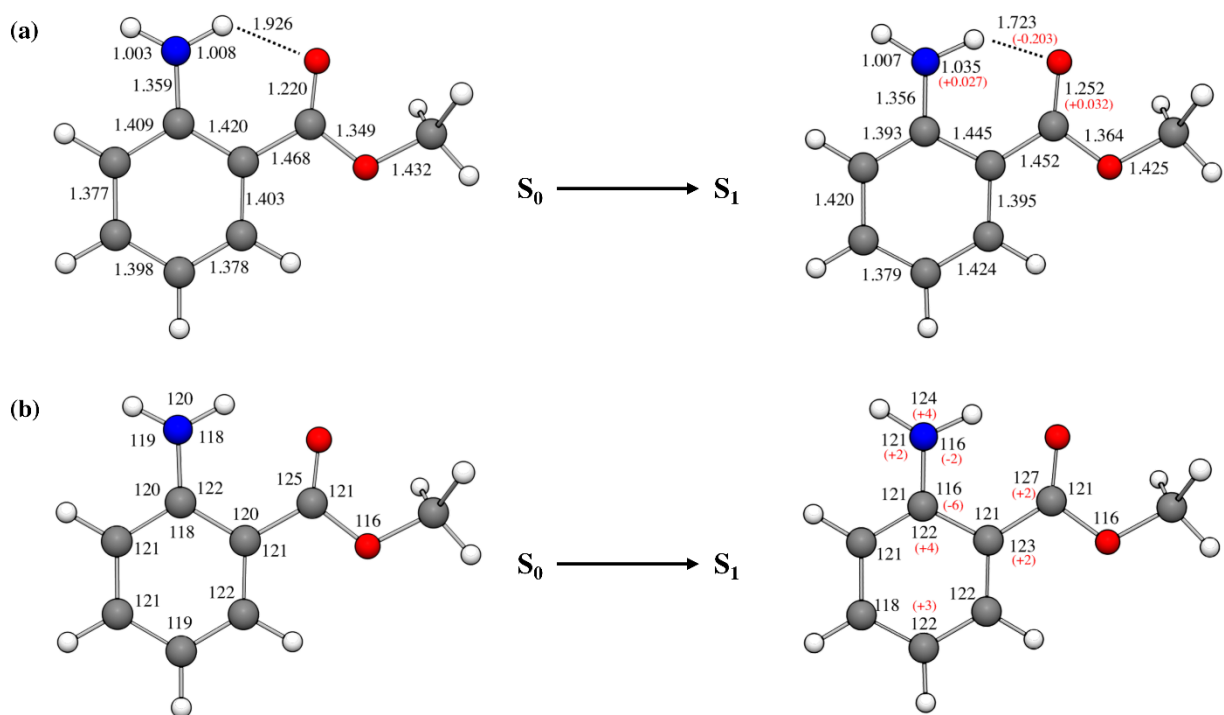


Figure 6.3. Optimized ground and S_1 excited state geometries of MA with (a) bond distances and (b) bond angles labelled. Bond lengths are in angstroms (Å) and angles are in degrees. The difference between select ground and excited state parameters are shown in red parentheses. Values were calculated at the DFT B3LYP-D3BJ/def2TZVP level of theory.

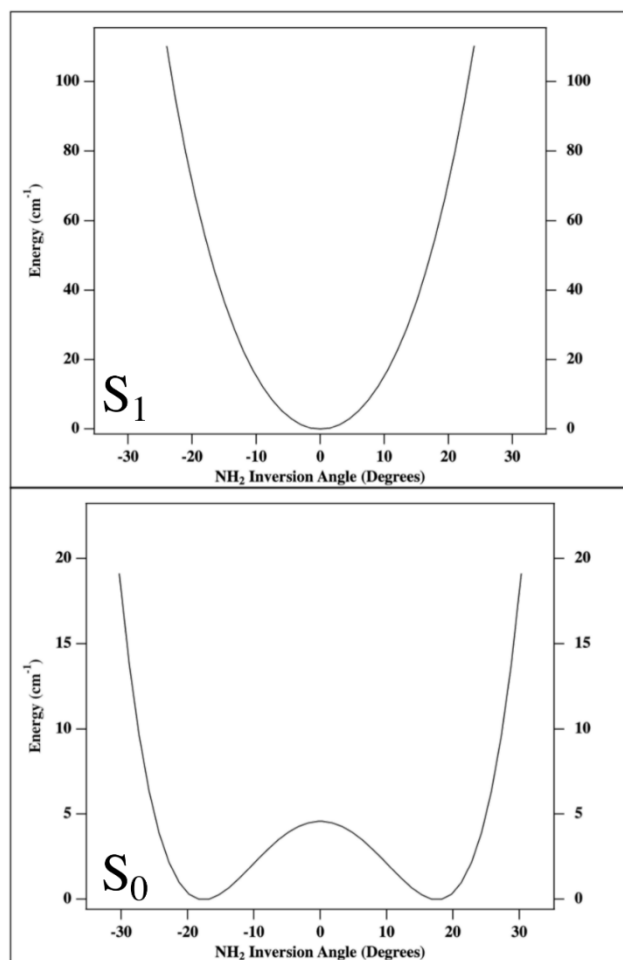


Figure 6.4. Relaxed potential energy scans about the improper CNHH dihedral defining the NH₂ inversion in MA, in the S₀ (bottom) and S₁ (top) electronic states

Since both the S₀ and S₁ geometries have one mirror plane, they both belong to the C_s point group. As such, the 54 normal modes reduce to 36 totally symmetric (a', in-plane) and 18 non-totally symmetric (a'', out-of-plane) vibrations. Symmetry also constrains the vibronic transitions: according to electric dipole selection rules within the Franck-Condon approximation, allowed transitions originating from the zero-point level include the fundamentals of all in-plane vibrations and only even combinations of out-of-plane vibrations (via overtones or combination bands, the latter of which depend on Duschinsky mode mixing for their intensity²⁴). In this chapter, we use Mulliken notation²⁵ to describe and order the normal modes of vibration.

Vertical TD-DFT B3LYP-D3BJ/def2TZVP calculations predict that the S₁ electronic state is optically accessible from S₀ via a $\pi\pi^*$ electron transition with contributions from HOMO \rightarrow

LUMO and (HOMO-1) \rightarrow (LUMO+1) transitions. This S_0 - S_1 transition has an appreciable oscillator strength ($f_{01} = 0.1036$). Furthermore, the S_1 state is well isolated from other excited states, with S_2 and S_3 1.15 and 1.30 eV above S_1 . Due to the large energy separation between S_1 and S_2/S_3 , and smaller oscillator strengths from S_0 , one would not anticipate significant manifestations of vibronic coupling in the S_0 - S_1 vibronic spectrum.

UV Excitation Spectroscopy

The LIF excitation spectrum of MA is presented in Figure 6.5a. The spectrum spans from 28,825 - 30,000 cm^{-1} (346.9-333.0 nm), with the S_0 - S_1 electronic origin transition appearing at 28,852 cm^{-1} . Fluorescence decay traces of the S_1 electronic states of MA and MA- H_2O are presented in Figure 6.6. The lifetime of the S_1 state of MA is measured to be 27 ns. Figure 6.5b shows the UV-UV HB spectra of MA, recorded with the HB laser fixed on the transition at 28,852 cm^{-1} . This spectrum shows that the majority of the peaks in the LIF excitation spectrum are due to the MA monomer. This assignment was verified via mass-resolved two-color resonant two-photon ionization (2C-R2PI) excitation spectra (see Figure 6.7). The minor peaks in the LIF spectrum that do not burn out in the UV-UV HB scan belong to the MA- H_2O complex (discussed in detail in section B). To distinguish whether the decrease in intensity in the spectra with increasing excitation energy is due to the drop-off in Franck-Condon factors or some non-radiative decay process, we collected UV-D spectra, shown in Figure 6.6c. The UV-D spectrum contains the same peaks and intensity pattern as the UV-UV HB spectra. This indicates that, in the wavelength region we have probed, there is no turn-on of a non-radiative process at play, and that the intensities in the LIF and UV-UV HB spectra presented in Figure 6.6a and 6b are determined primarily by the absorption properties of MA.

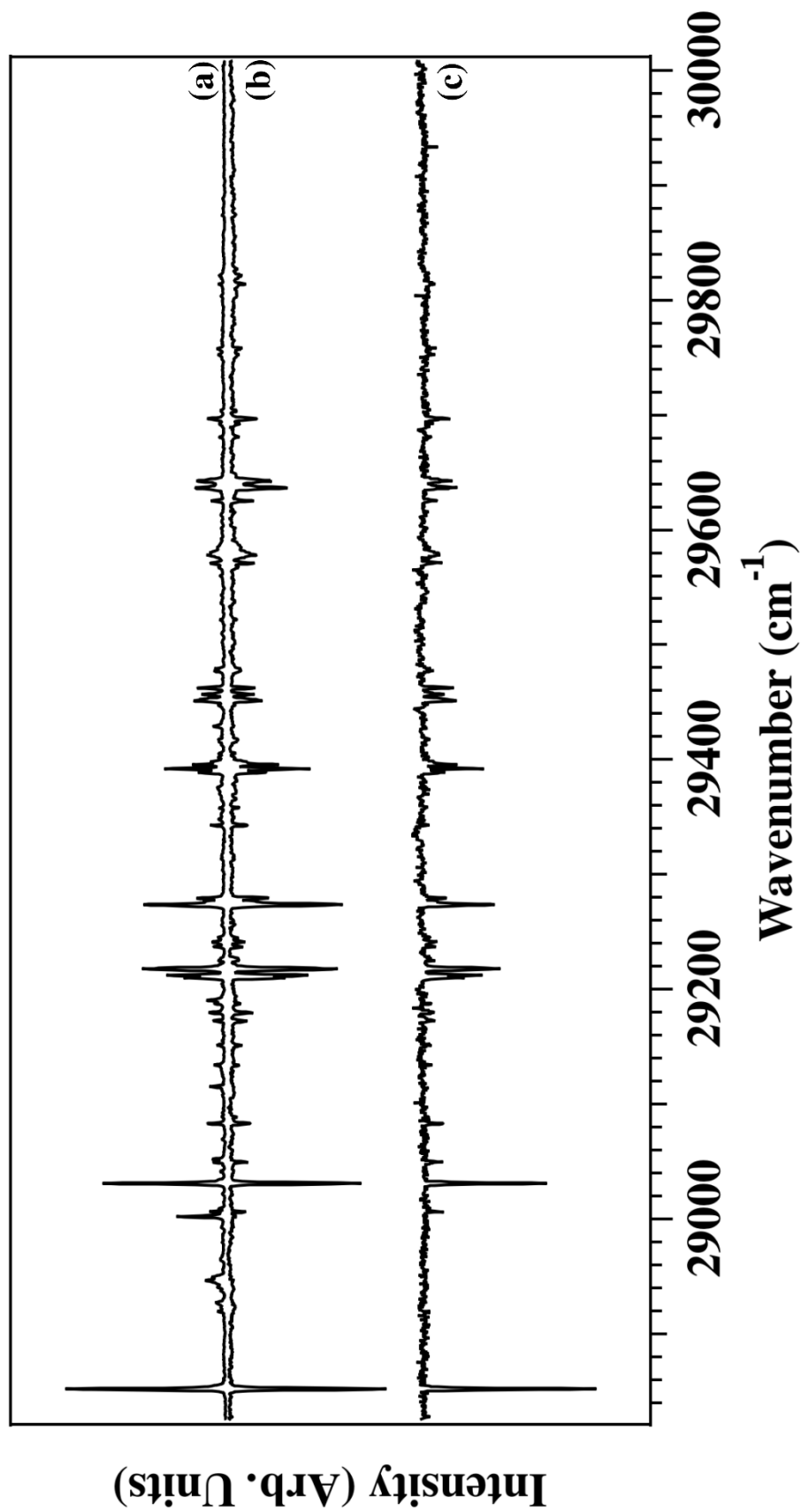


Figure 6.5. (a) LIF excitation, (b) UV-UV hole-burning, and (c) UV depletion spectra of MA from 28,825 - 30,000 cm⁻¹.

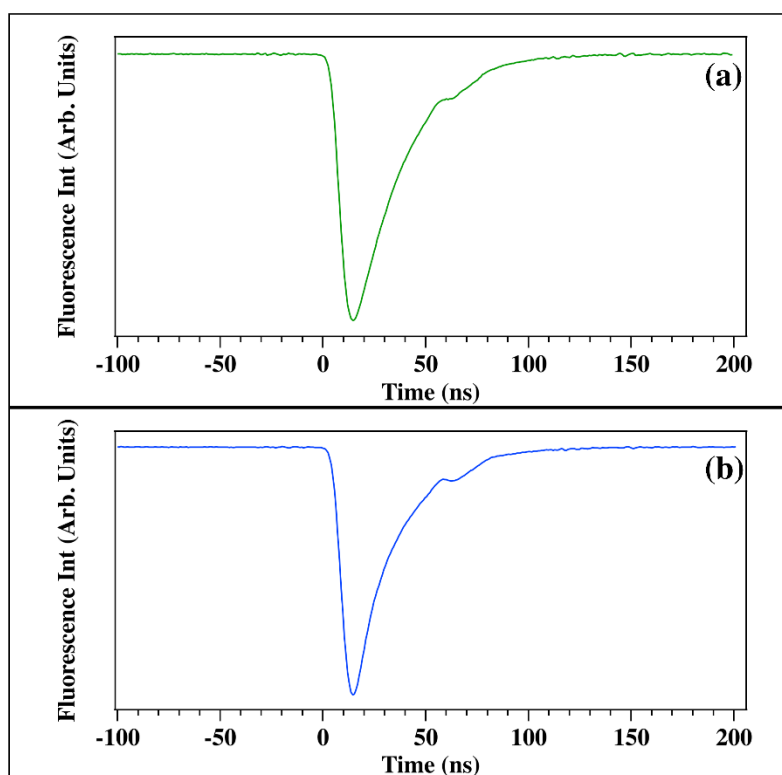


Figure 6.6. Fluorescence decay traces of (a) MA and (b) MA-H₂O. Lifetimes were obtained by fitting each trace to a single exponential decay and extracting the time constant, τ (lifetime). The lifetime is measured to be 27 ns for MA and 23 ns for MA-H₂O.

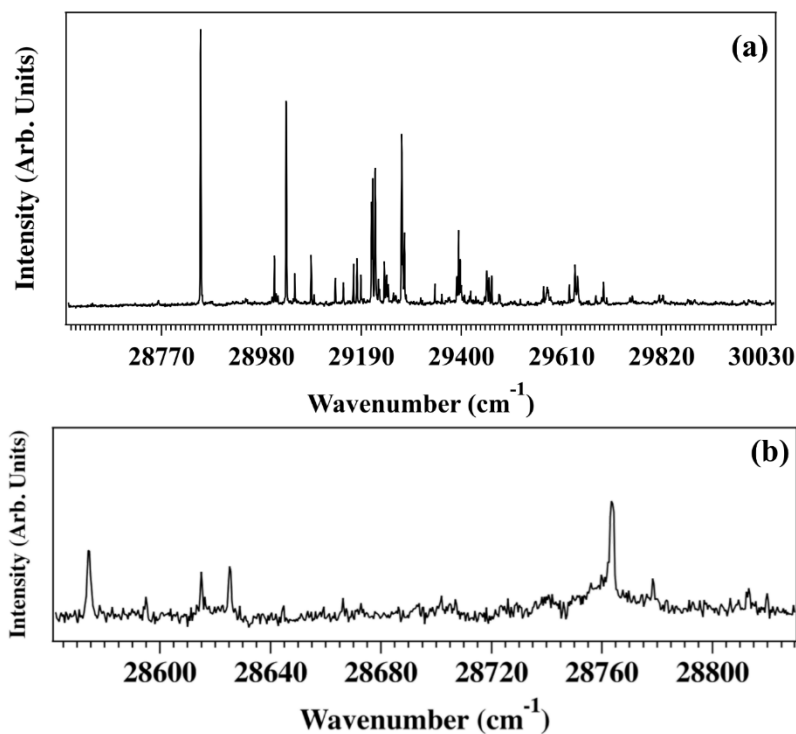


Figure 6.7. 2C-R2PI spectra of MA (a) and MA-H₂O (b).

The assigned IR-UV HB spectrum of MA is displayed in Figure 6.8. These assignments were reached based on corroborating evidence from S_0 and S_1 vibrational frequency calculations, excitation spectra, and DFL spectra, as will be discussed in detail below. A rotational band contour (RBC) scan of the electronic origin transition, taken at a laser resolution of 0.15 cm^{-1} (in the UV) is shown as the top trace in Figure 6.9. Using the spectral fitting program JB95²⁶, along with transition dipole moment ($a:b:c = 77:23:0$) components and rotational constants from the calculated ground and excited states, we obtained the simulated RBC shown as the bottom trace in Figure 6.9. The excellent match between experiment and theory bolsters the assignment of MA to the lower energy rotamer.

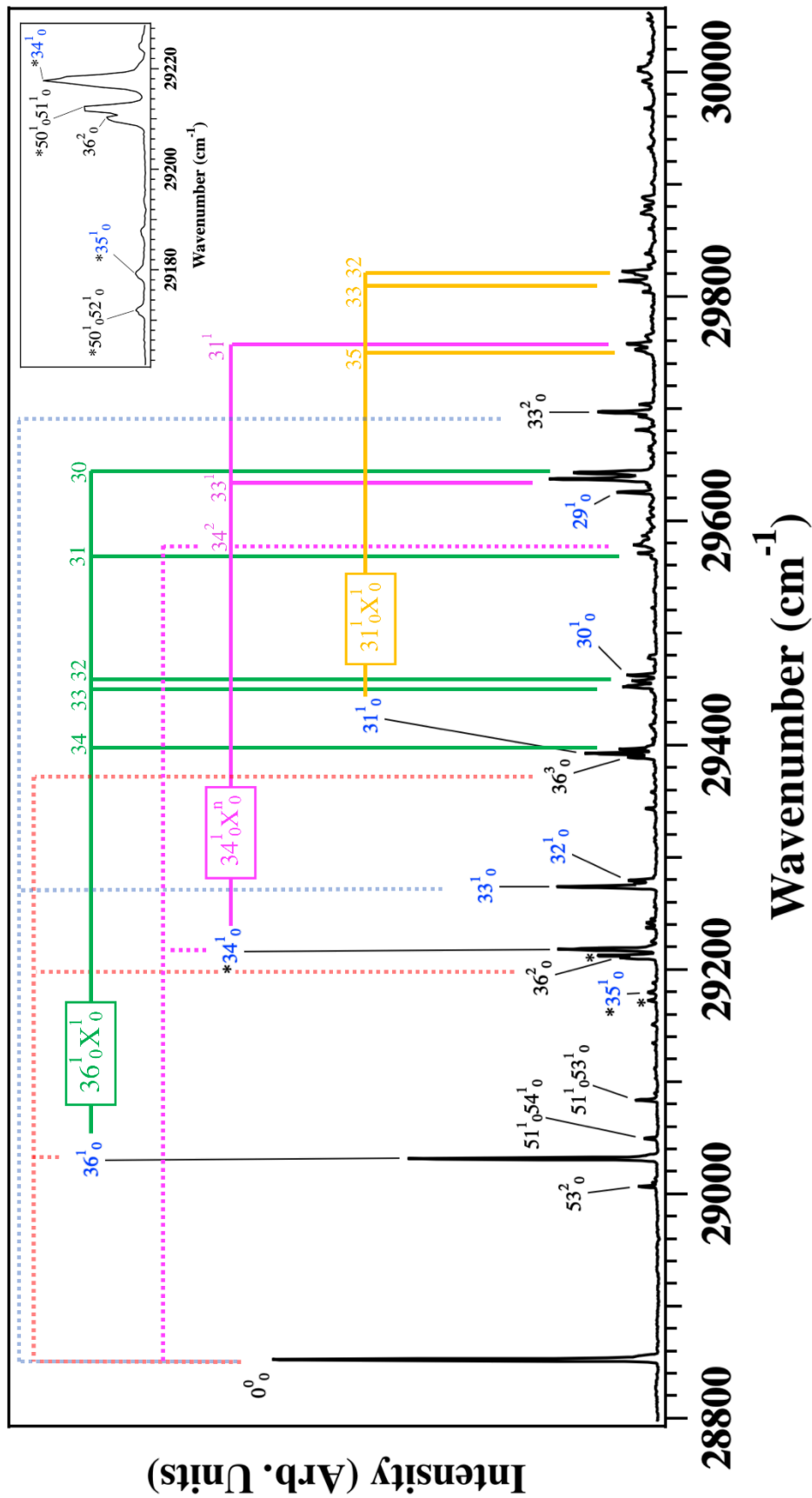


Figure 6.8. Assigned $S_0 - S_1$ LIF excitation spectrum of MA. Progressions in the in-plane modes ν_{36} (179 cm^{-1}), ν_{34} (366 cm^{-1}), and ν_{33} (421 cm^{-1}) are displayed via red, pink, and blue dotted tie-lines, respectively, while in-plane combination bands built off 36_0^1 , 34_0^1 , and 31_0^1 are shown with solid tie lines. The identity of mode X is listed above each respective tie line. The inset provides a close-up view of the two pairs of peaks identified as Fermi-resonance pairs.

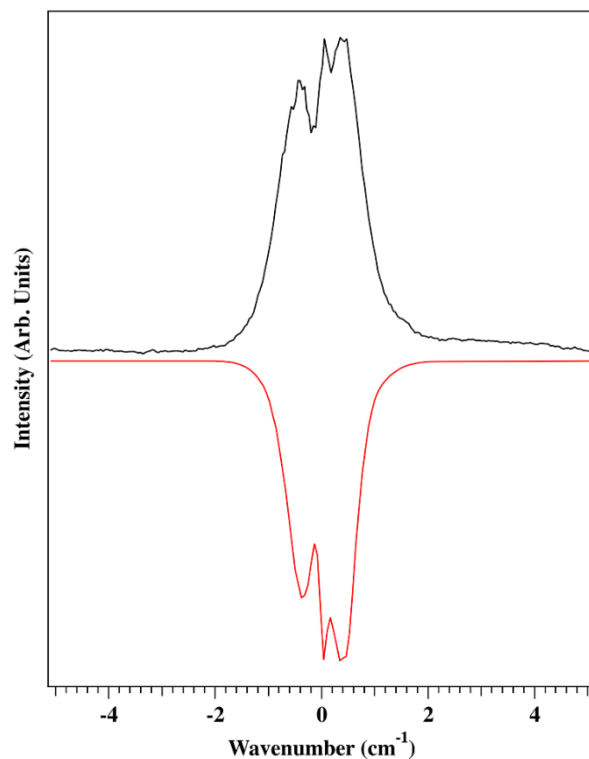


Figure 6.9. Rotational band contour (RBC) scan of the electronic origin transition (top trace), taken at a UV laser resolution of 0.15 cm^{-1} . The bottom trace is the computed fit using the calculated transition dipole moment ($a:b:c = 77:23:0$) components and rotational constants from calculated ground and excited states. This fit was computed using the JB95 spectral fitting program (ref. 26).

Table 6.1 lists the experimental and calculated S_0 and S_1 vibrational frequencies. The excitation spectrum of MA is composed of progressions in in-plane vibrations, even combination bands and overtone transitions of out-of-plane vibrations, and (1+1):1 Fermi resonance pairs between out-of-plane combination bands and in-plane fundamentals. Progressions in the in-plane modes ν_{36} (179 cm^{-1}), ν_{34} (366 cm^{-1}), and ν_{33} (421 cm^{-1}) are displayed via red, pink, and blue dotted tie-lines, respectively, while in-plane combination bands built off 36^1_0 , 34^1_0 , and 31^1_0 are shown with solid tie lines. All other assigned peaks, belonging either to in-plane fundamentals or out-of-plane combination bands, are labelled with tags.

It is noteworthy that, while the 0^0_0 transition is the largest peak in the spectrum, all eight of the lowest frequency in-plane fundamentals (ν_{36-29}) have measurable intensity in their X^1_0 fundamentals, indicating a geometry change along these normal coordinates between the ground and excited electronic states. The two pairs of peaks designated with asterisks (and shown in the

figure inset) are identified as Fermi-resonance pairs. The five lowest frequency out-of-plane modes, ν_{54-50} , appear as combination and, in the case of ν_{53} , overtone bands.

Table 6.1. Experimental and Calculated S_0 and S_1 Frequencies of MA, Best Fit Normal Coordinate Displacement Values, and Excited to Ground State Normal Mode Projections

S_0			S_1			
Mode	Exp Freq (cm^{-1})	Calc Freq ^a (cm^{-1})	<i>a' In-Plane Modes</i>			
			Exp Freq (cm^{-1})	Calc Freq ^a (cm^{-1})	Best-Fit Displacement ^b	$S_1 \rightarrow S_0$ mode projections ^c
36	179	183	179	183	0.97	33,31,29
35	333	340	327	333	0.10	
34	361	359	366	364	0.85	36,33,31,29
33	412	420	421	423	1.27	36,34,31,29
32	494	506	427	502	0.50	36, 33, 31,
31	567	574	540	559	0.60	33, 30
30	672	684	610	641	0.10	29
29	808	818	773	786	0.50	33
18	1355	1353	-	1381	-	-
<i>a'' Out of Plane Modes</i>						
Mode	Exp Freq (cm^{-1})	Calc Freq (cm^{-1})	Exp Freq (cm^{-1})	Calc Freq (cm^{-1})	Best-Fit D	$S_1 \rightarrow S_0$ mode projections
54	57	65	44	49	0	51,52,53
53	96	97	77	82	0	51,53,54
52	143	145	114	117	0	50,51
51	161	163	153	156	0	50,52,53,54
50	229	254	207	220	0	51,52

^a Frequencies calculated at the DFT B3LYP-D3BJ/def2TZVP level of theory.

^b Value calculated using the Franck-Condon fitting procedure discussed in text.

^c Determined from DFL data

DFL of the 0^0_0 Band and In-Plane Fundamentals

The assigned DFL spectrum of the electronic origin transition is shown in Figure 6.10. The peak positions and intensity pattern displayed in the first 1,200 cm^{-1} of the DFL spectrum largely mirror those of the excitation spectrum, as would be the case if Franck-Condon factors between the ground and excited state play a dominant role in the observed vibronic structure. This DFL spectrum shows progressions in three in-plane modes; ν_{36} , ν_{34} , ν_{33} , all of which also showed clear progressions in the excitation spectrum. Additionally, each in-plane fundamental that we observe in the excitation spectrum appears with an analogous $\Delta v=1$ transition in the origin DFL spectrum, with one additional higher frequency band appearing at +1355 cm^{-1} (ν_{18}). As was the case with the excitation spectrum, we also observe in-plane and out-of-plane combination bands and out-of-plane overtones in the DFL spectrum. The DFL spectrum also has a large number of in-plane combination bands, with a smaller number of out-of-plane combination bands.

Figure 6.11 presents the DFL spectra of the eight Franck-Condon active in-plane fundamentals present in the excitation spectrum. In the +327 cm^{-1} DFL spectrum (Figure 6.11b) there is a large peak at 333 cm^{-1} with no further progressions at that frequency. The majority of the remainder of the peaks built off of this transition, labelled with red dotted tie lines, are identical in relative frequency and intensity pattern to the entire set of peaks in the 0^0_0 DFL spectrum, indicating that the 333 cm^{-1} peak serves as a false origin (labelled with a red 0^0_0 in Figure 6.11). The strong intensity of the peak at 333 cm^{-1} , combined with the excellent agreement between calculated and experimental frequency, leads us to assign the +327 cm^{-1} transition to the 35^1_0 in-plane fundamental, and the 333 cm^{-1} peak as a $\Delta v=0$ transition (35^1_1). The intensity pattern this mode displays in the vibronic spectra, together with the 35^1_1 transition serving as a false origin, indicate a very small displacement of its respective potential wells between S_0 and S_1 states. The $\Delta v=0$ transition of several other excited state modes, ν_{31} , ν_{30} , ν_{29} (Figure 6.11f-h), also serve as false origins involving each of these vibrations.

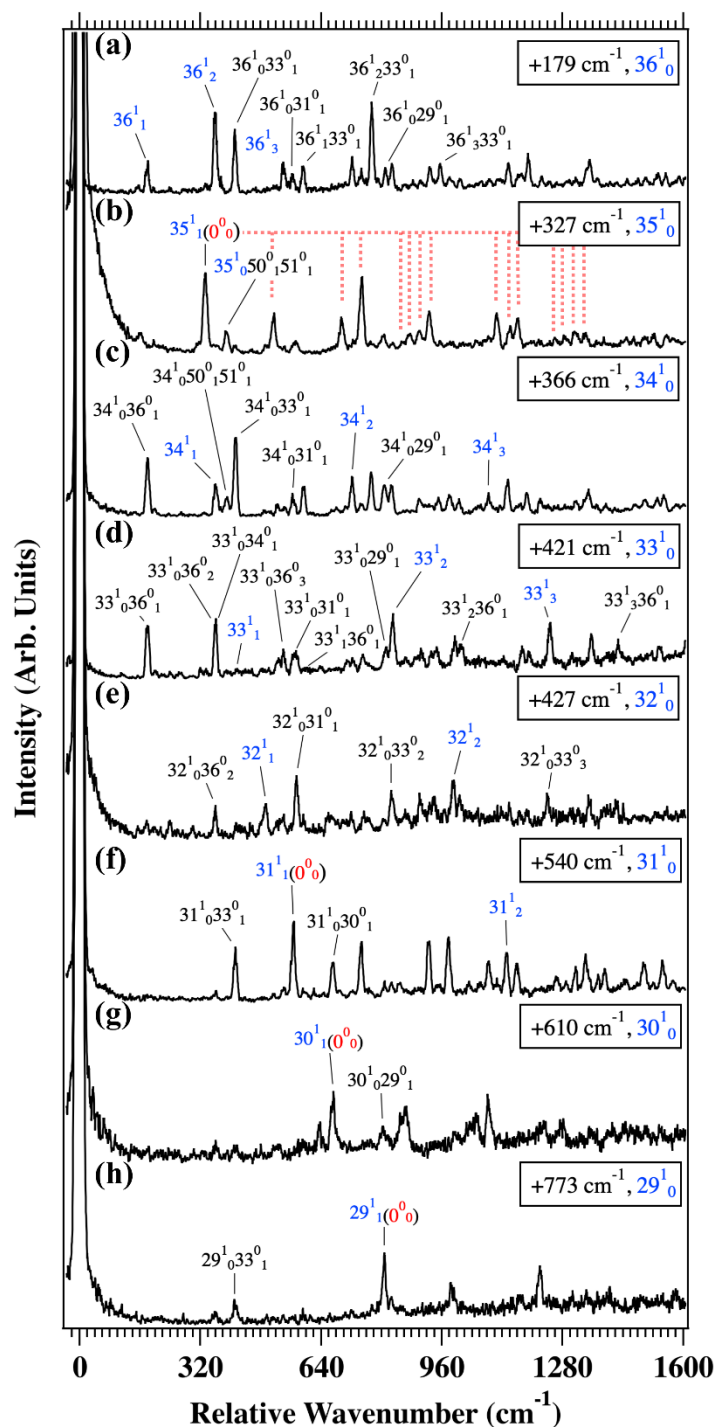


Figure 6.11. DFL spectra of the Franck-Condon active, in-plane fundamentals in MA: (a) 36^1_0 , (b) 35^1_0 , (c) 34^1_0 , (d) 33^1_0 , (e) 32^1_0 , (f) 31^1_0 , (g) 30^1_0 , and (h) 29^1_0 . Ground state progressions in analogous modes are labelled in blue text, and transitions which serve as false origins are marked with a red (0^0_0)

Many of these DFL spectra contain, among other transitions, progressions in their analogous ground state normal mode (labelled in blue in Figure 6.11). The DFL spectrum of the transition at $+179\text{ cm}^{-1}$, for example, displays a Franck-Condon progression in a 179 cm^{-1} mode in S_0 . Based on the extent of the Franck-Condon activity in the excitation and 0^0_0 DFL spectra in 179 cm^{-1} , one should expect concomitant progressions in the ground state when projecting from $v=1$ in S_1 . This evidence, in addition to the agreement between calculated and experimental frequencies, leads us to assign the $+179\text{ cm}^{-1}$ transition in the excitation spectrum to the 36^1_0 in-plane fundamental. The long progressions in the vibronic spectra of ν_{36} (with 36^1_n members up through $n=3$) implies an appreciable displacement of the respective normal mode coordinates upon electronic excitation.

This one-dimensional normal coordinate displacement, however, does not account for all of the peaks in the 36^1_0 DFL spectrum. There are also several cross-sequence bands present, most notably $36^1_n33^0_1$, $36^1_031^0_1$ and $36^1_029^0_1$. Such cross-sequence bands are signatures of Duschinsky mixing, in which the normal coordinates in the S_1 state are linear combinations of the ground state normal coordinates.²⁷ This may be thought of as a rotation of the normal coordinates on the S_1 potential energy surface (PES) relative to the S_0 PES, where the one-to-one correspondence between ground and excited state normal modes is lost to some degree.²⁸ The situation is further complicated for in-plane modes, where, in addition to mixing, displacements along the normal coordinate(s) may occur. We may deduce, then, via its Franck-Condon activity and cross-sequence bands, that the ν_{36} coordinate in S_1 is both rotated and its origin displaced relative to its corresponding coordinate in S_0 .

The prevalence of cross-sequence bands in the in-plane fundamental DFL spectra presented in Figure 6.11 implies a significant degree of Duschinsky mixing upon electronic excitation. Using similar logic as that outlined above, we have assigned nearly all of the transitions in the excitation and DFL spectra. Confidence in these assignments is bolstered by the strong agreement between calculated and experimentally assigned vibrational frequencies (Table 6.1). Figure 6.12 shows the ground state form of the Franck-Condon active in-plane normal modes. Based on the Franck-Condon activity, the largest displacements are in modes 36 (179 cm^{-1}) and 33 (421 cm^{-1}), similar to what is observed in anthranilic acid.¹⁵

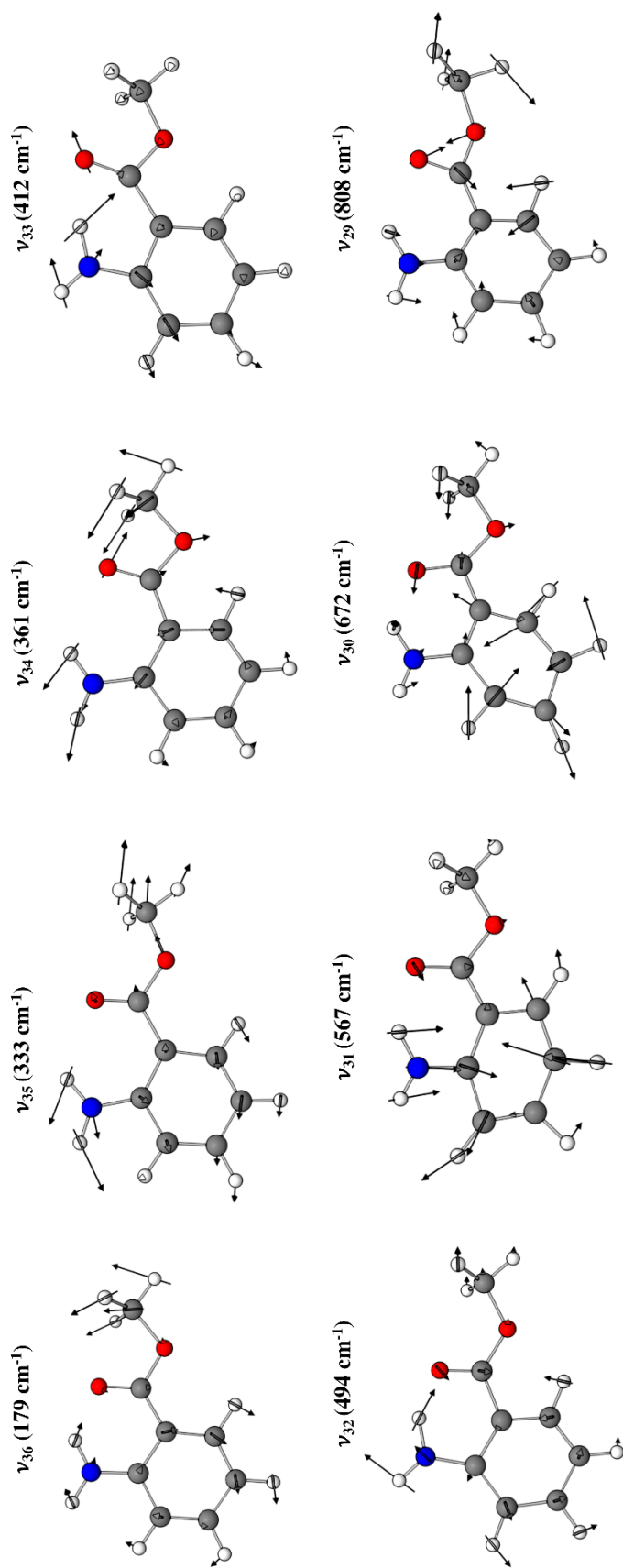


Figure 6.12. Ground state in-plane normal modes ν_{36} – ν_{29} of MA. Normal modes were calculated at the DFT B3LYP-D3BJ/def2TZVP level of theory.

Through the DFL spectra, we were also able to identify the onset of intramolecular vibrational energy redistribution (IVR) in the S_1 state. IVR results when the laser-prepared state carrying the oscillator strength in excitation anharmonically couples with a bath of background states at that energy. This bright state/background state mixing of the upper state wave function has the effect of taking what would be sharp vibronic transitions and broadening/shifting transitions due to the state's background character. Figure 6.13 presents a sequence of DFL spectra taken at increasing energies relative to the origin. At pump energies greater than 600 cm^{-1} we note the appearance of a broad, increasing baseline, most likely associated with the onset of IVR. The spectral signature of IVR is less clear in the context of MA than it is in many phenyl derivatives^{29, 30}, due to the much larger geometry change between S_0 and S_1 in MA.

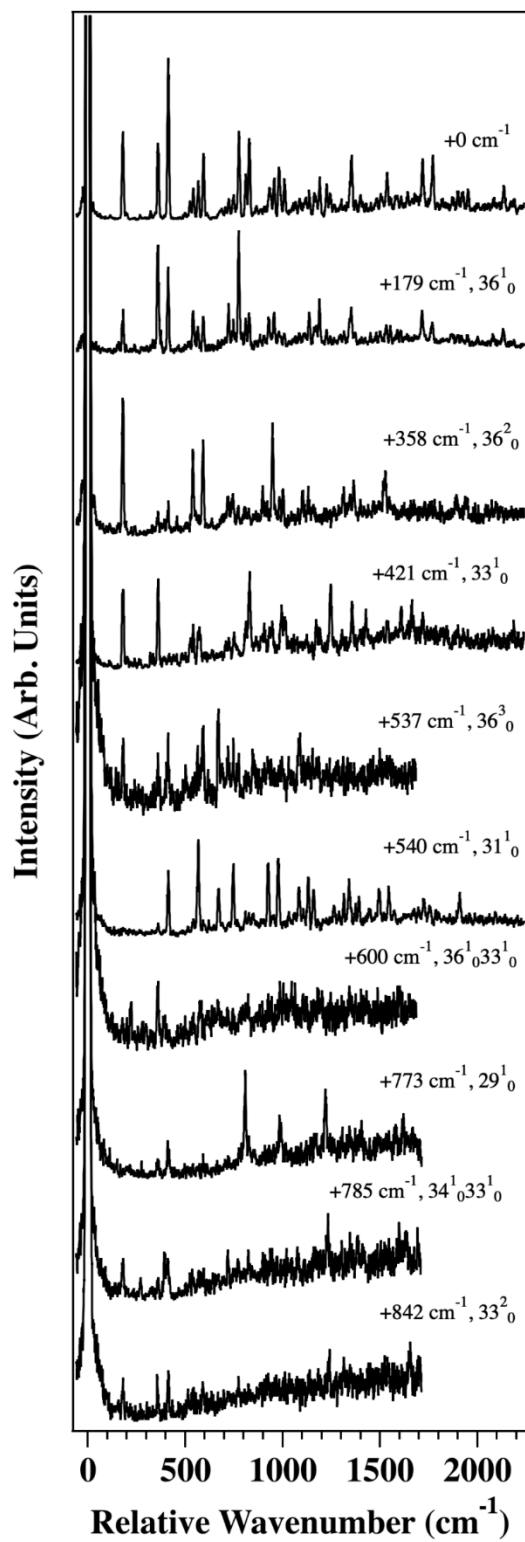


Figure 6.13. DFL spectra taken at increasing energies from the origin transition in MA.

DFL of the Out-Of-Plane Combination Bands and Fermi Resonance Pairs

The assigned DFL spectra of the transitions assigned to out-of-plane modes are shown in Figure 6.14. It is noteworthy that all assigned transitions involve even overtone and combination bands in the out-of-plane modes, providing convincing experimental evidence that the molecule retains C_s symmetry in both ground and excited states. Whereas in-plane modes may undergo both mixing and displacement upon electronic excitation in systems where C_s symmetry is preserved in both states, out-of-plane modes have zero displacement of normal coordinates upon excitation. This zero displacement results in transitions involving out-of-plane modes having weak intensity in the excitation or 0^0 DFL spectra.

In all of the DFL spectra in Figure 6.14 there are strong bands in the low frequency region that serve as false origins for transitions built off of them; that is, one can readily assign Franck-Condon activity built off these transitions that mirror the Franck-Condon activity present in the 0^0 DFL spectrum (Figure 6.10). It is noteworthy that, in all the spectra in Figure 6.14, the most intense false origin is not the $\Delta v=0$ transition (e.g., $X^1_1Y^1_1$ following excitation of $X^1_0Y^1_0$) but instead, one or more cross-sequence band(s).

The abundant cross-sequence transitions assigned in Figure 6.14 indicate extensive Duschinsky mixing among the out-of-plane modes. Figure 6.15 shows the form of these normal modes in the ground state, along with the reduced Duschinsky rotation matrix calculated at the B3LYP-D3BJ/def2TZVP level of theory. The matrix elements across a row (non-negligible off-diagonal components highlighted in blue) give the expansion coefficients of the indicated S_1 normal coordinate in terms of the S_0 coordinates. Without direct data on cross-sequence hot bands of the type $X^1_0Y^0_1$, it is difficult to carry out quantitative tests of the Duschinsky mixing^{28, 31}. Nevertheless, we can use this matrix to see whether it is qualitatively consistent with the experimental data; that is, by looking at which modes show clear evidence of mixing with one another. For example, the largest peak in the 53^2_0 DFL spectrum is the cross-sequence band $53^2_054^0_2$, consistent with the large off-diagonal mixing (-0.230) between these two modes. Indeed, DFL spectra from levels with excitation in modes 52, 53, and 54 show significant mixing between all three, as the Duschinsky matrix predicts.

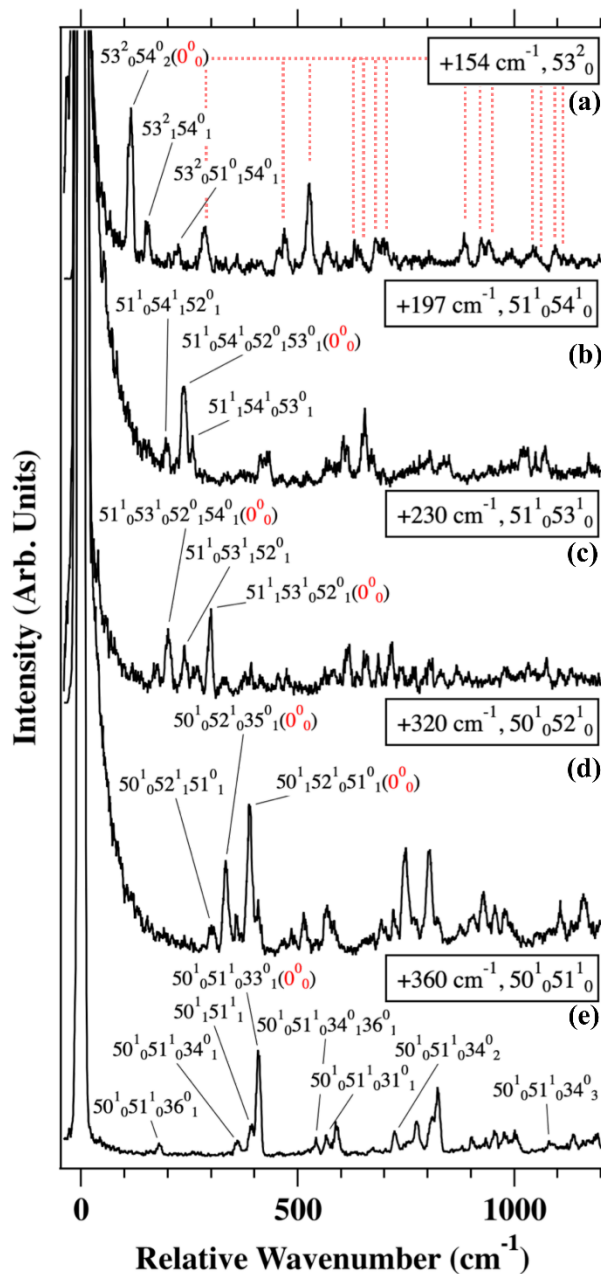


Figure 6.14. DFL spectra of transitions involving out-of-plane modes in MA: (a) $53^2_{054^0_2}$, (b) $51^1_{054^1_0}$, (c) $51^1_{053^1_0}$, (d) $50^1_{052^1_0}$, and (e) $50^1_{051^1_0}$. Transitions which serve as false origins are marked with a red (0^0_0)

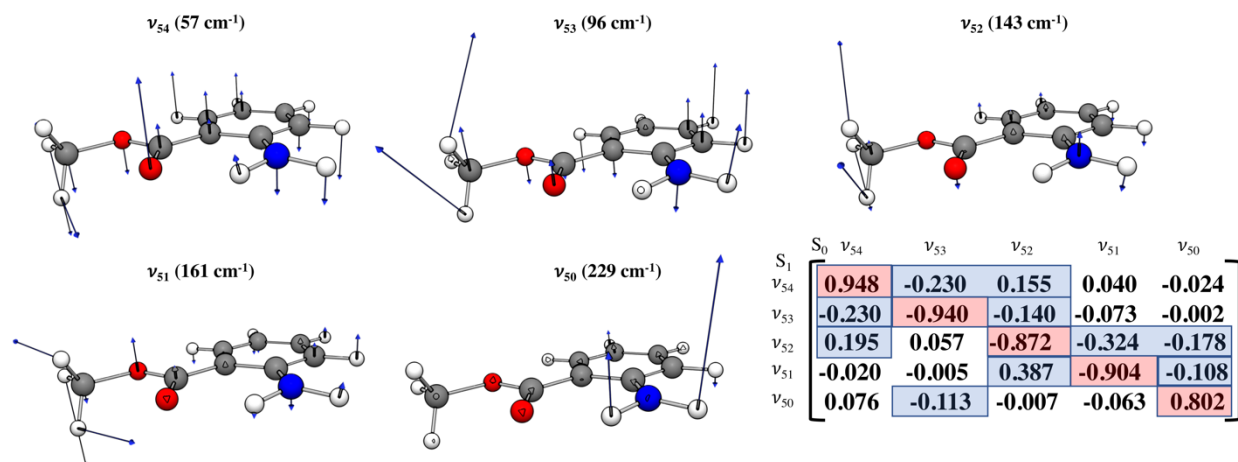


Figure 6.15. Ground state out-of-plane normal modes ν_{54} – ν_{50} of MA, along with the reduced Duschinsky matrix of these modes. The matrix row elements give the expansion coefficients of the indicated S_1 normal coordinate in terms of the S_0 coordinates. The normal modes and Duschinsky matrix were calculated at the DFT B3LYP-D3BJ/def2TZVP level of theory.

The spectra in Figure 6.14d,e show strong false origins in bands that cannot be understood purely in terms of Duschinsky mixing. Indeed, as the inset in Figure 6.8 shows, in the excitation spectrum, the $50^1_0 52^1_0$ and $50^1_0 51^1_0$ transitions appear in close proximity with the in-plane fundamentals 35^1_0 and 34^1_0 , respectively, marked with asterisks. The first set of peaks are assigned to the $50^1_0 52^1_0$ combination and Franck-Condon allowed 35^1_0 fundamental transitions. The DFL spectra coming out of this pair (shown in Figure 6.16a,b) provide evidence that they are in Fermi-resonance with one another. These spectra share almost all of the same transitions to the ground state, thus revealing their mixed character in the excited state. To substantiate this claim, consider the $50^1_0 52^1_0 35^0_1$ transition in the $50^1_0 52^1_0$ DFL spectrum. The excitation spectrum (Figure 6.8), origin and 35^1_0 DFL spectra (Figure 6.10 and Figure 6.11b) all show that ν_{35} has essentially no oscillator strength in its $\Delta v=1$ transitions. The substantial intensity of this transition in the $50^1_0 52^1_0$ DFL spectrum, then, implies that the upper state contains some 35^1 character. Furthermore, the lack of a $\Delta v=0$ $50^1_1 52^1_1$ transition in either DFL spectrum, but the corresponding presence of a $50^1_1 51^1_1$ transition in both, implies strong Duschinsky mixing between modes 51 and 52, as predicted by the Duschinsky matrix in Figure 6.15.

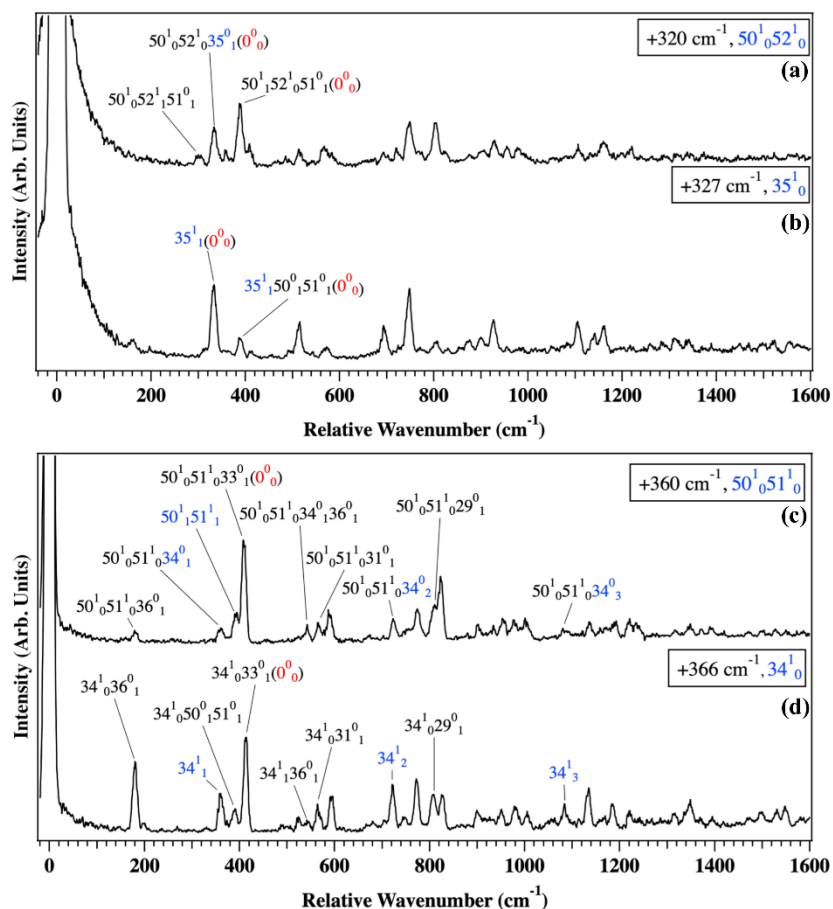


Figure 6.16. DFL of Fermi resonance modes (a) $50^1_052^1_0$ and (b) 35^1_0 , and (c) $50^1_051^1_0$ and (d) 34^1_0 of MA. Ground state transitions to Fermi-mixed components are labelled in blue text, and transitions which serve as false origins are marked with a red (0^0_0).

The second set of peaks is assigned to an excited state Fermi resonance between the $50^1_051^1_0$ combination level and the Franck-Condon allowed 34^1_0 in-plane fundamental. The DFL spectra coming out of these levels is shown in Figure 6.16c and Figure 6.16d, respectively. The presence of Fermi resonant mixing between the pair of excited state levels is manifested by the $\Delta v=0$ emission to both the $50^1_051^1_0$ and 34^1_0 ground state levels appearing in both DFL spectra. Oddly enough, the $50^1_051^1_0$ transition is the only observed case in which a fully $\Delta v=0$ transition is even observed in the DFL spectra of these out-of-plane combination levels. Nonetheless, the presence of this $\Delta v=0$ transition has enabled a quantitative analysis of the Fermi resonance mixing coefficients, α and β , to which we now turn.

In the S_1 electronic state, the Fermi-mixed wavefunctions may be expressed, using bra-ket notation, as a linear combination of the unmixed wavefunctions,

$$|\psi_{366}\rangle = \alpha|a'\rangle + \beta|2a''\rangle \quad (1)$$

and

$$|\psi_{360}\rangle = \beta|a'\rangle - \alpha|2a''\rangle \quad (2)$$

where $|a'\rangle$ is the S_1 34^1 wavefunction, $|2a''\rangle$ is the S_1 50^151^1 wavefunction, α and β are the mixing coefficients. Solving for the Franck-Condon factor (FCF) from the S_0 zero-point level, $\langle 0|$, to each of these S_1 vibrational levels, and assuming that the wavefunction overlap $\langle 0|2a''\rangle$ is negligible, we obtain

$$\text{FCF}_{0,366} = |\langle 0|\psi_{366}\rangle|^2 = \alpha^2|\langle 0|a'\rangle|^2 \quad (3)$$

and

$$\text{FCF}_{0,360} = |\langle 0|\psi_{360}\rangle|^2 = \beta^2|\langle 0|a'\rangle|^2 \quad (4)$$

Taking the ratio

$$\text{FCF}_{0,366} / \text{FCF}_{0,360} = \alpha^2 / \beta^2 \quad (5)$$

gives the relative intensities of the vibronic bands in the LIF spectrum. Integrating these experimental bands, we obtain

$$\alpha^2 / \beta^2 = 1.80 \quad (6)$$

Solving the FCF integrals for the projection of each Fermi-mixed S_1 level onto the individual S_0 components, $\langle a'|$ (34_1) and $\langle a''|$ (50_151_1), we obtain

$$|\langle a'|\psi_{366}\rangle|^2 / |\langle 2a''|\psi_{366}\rangle|^2 = (\alpha^2|\langle a'|a'\rangle|^2) / (\beta^2|\langle 2a''|2a''\rangle|^2) = \alpha^2 / \beta^2 = 1.80 \quad (7)$$

and

$$|\langle a' | \psi_{360} \rangle|^2 / |\langle 2a'' | \psi_{360} \rangle|^2 = (\beta^2 |\langle a' | a' \rangle|^2) / (\alpha^2 |\langle 2a'' | 2a'' \rangle|^2) = \beta^2 / \alpha^2 = 0.55 \quad (8)$$

where we have assumed a 1:1 correspondence between analogous S_0 and S_1 normal modes (i.e., no Duschinsky mixing). From the experimental DFL spectra, we measure the relative integrated intensities to be

$$|\langle a' | \psi_{366} \rangle|^2 / |\langle 2a'' | \psi_{366} \rangle|^2 = 1.70 \quad (9)$$

and

$$|\langle a' | \psi_{360} \rangle|^2 / |\langle 2a'' | \psi_{360} \rangle|^2 = 0.52 \quad (10)$$

The good agreement between calculated and measured peak intensities allows us to express the normalized S_1 Fermi-mixed wavefunctions as

$$|\psi_{366}\rangle = 0.802|a'\rangle + 0.597|2a''\rangle \quad (11)$$

and

$$|\psi_{360}\rangle = 0.597|a'\rangle - 0.802|2a''\rangle \quad (12)$$

As anticipated, the excited state level $+366 \text{ cm}^{-1}$ above the S_1 ZPL is about 64% 34^1 and 36% $50^1 51^1$, while the one at 360 cm^{-1} is the reverse; that is, 36% 34^1 and 64% $50^1 51^1$. Figure 6.17 reproduces the Fermi-mixed transitions in the LIF spectrum, where one can see the good agreement between experimental and calculated integrated intensities.

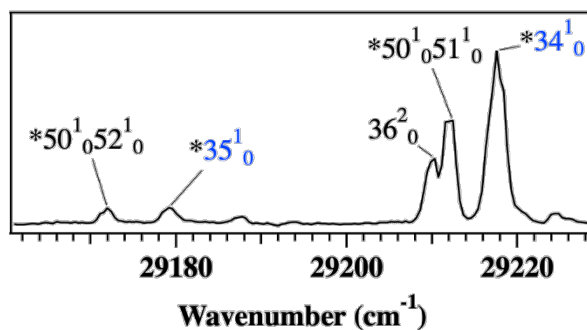


Figure 6.17. The portion of the LIF spectrum containing the two pairs of Fermi-mixed vibronic levels, marked with asterisks.

6.3.2 Methyl Anthranilate-Water Complex

Computational Predictions

Complexation of a single water molecule to MA (MA-H₂O) can occur at several binding sites, supporting numerous conformers. At the DFT B3LYP-D3BJ/def2TZVP level of theory we have calculated seven minima lying within 10 kJ/mol of the global energy minimum. These conformers are presented in Figure 6.18, and their relative energies and S₀ - S₁ excitation energies (vertical and adiabatic), are listed in Table 6.2. In each of these structures, the monomer portion adopts the same rotamer form that we have just assigned, i.e., with the amine group hydrogen bonded with the carbonyl group. None of the conformers have symmetry in their calculated S₀ or S₁ states. This is not due, as was the case in the MA S₀ geometry, to a symmetric double well potential along the NH₂ inversion coordinate, but rather the H₂O molecule asymmetrically binding to the MA monomer unit with an out-of-plane position for its center-of-mass. The calculated equilibrium structure of the assigned MA-H₂O complex in its S₀ and S₁ geometry is shown in Figure 6.19. This conformer was calculated to be the zero-point corrected energy minimum both with and without basis set superposition error (BSSE) correction.

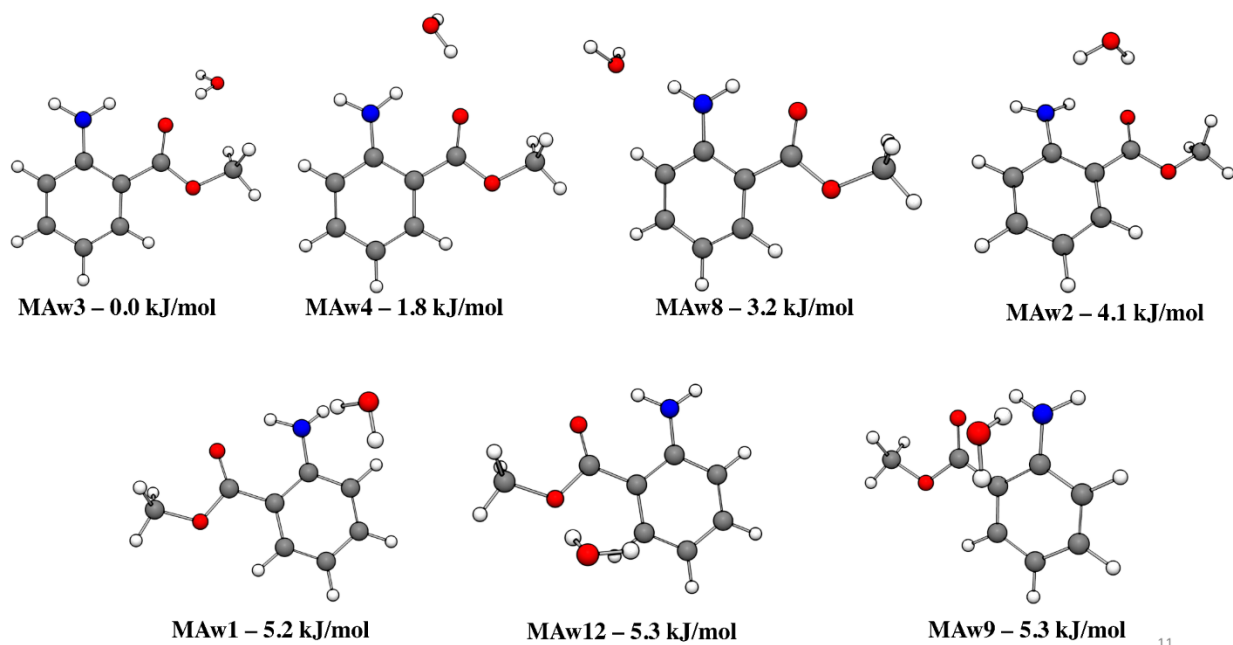


Figure 6.18. All MA-H₂O conformers, with their BSSE/ZPE-corrected energies, calculated to lie within 10 kJ/mol of the global minimum

Table 6.2. Relative zero-point corrected potential energies, BSSE and zero-point corrected potential energies, adiabatic and vertical excitation energies of the water complex conformers calculated to lie within 10 kJ/mol of the global minimum. Calculations performed at the DFT B3LYP-D3BJ/def2TZVP level of theory.

Complex	ZPE corr. Electronic energy (kJ/mol)	BSSE and ZPE corr. Electronic energy (kJ/mol)	TD-DFT Adiabatic S ₀ -S ₁ Excitation Energy (cm ⁻¹)	TD-DFT Vertical S ₀ -S ₁ Excitation Energy (cm ⁻¹)
MAw3 (assigned)	0	0	27,095	31,020
MAw4	0.299307	1.79729889	27,004	30,973
MAw8	3.7518395	3.243491765	27,171	30,928
MAw2	3.0482055	4.109389542	26,606	32,247
MAw1	4.6865175	5.209882307	27,534	32,923
MAw12	5.30351	5.344971633	27,345	31,299
MAw9	4.6812665	5.352848133	27,220	32,995

The loss of symmetry upon water complexation means that the in-plane/out-of-plane selection rules present in MA monomer are no longer present in the complex. As we shall see, however, the relative intensities of certain bands in the excitation spectrum suggest a weakening of these selection rules rather than a binary switch between on and off. The 63 normal modes of vibration of the complex are designated with the Mulliken scheme, from high to low frequency. Nevertheless, many of the MA vibrations retain much of their character upon water complexation, and we refer to this connection in what follows. Formally speaking, six new intermolecular vibrations are associated with hindered translation (3) and rotation (3) of the H₂O molecule relative to MA.

Vertical TD-DFT B3LYP-D3BJ/def2TZVP calculations predict that the S₁ electronic state of MA-H₂O is very similar to its character in MA monomer, with a nearly identical form for the molecular orbitals and their coefficients in the S₀-S₁ transition. The S₂ and S₃ states are now nearly isoenergetic with one another at the ground state geometry, lying 1.31 eV and 1.34 eV above S₁. Interestingly, the S₀-S₂ and S₀-S₃ electronic transitions now involve both nπ* and ππ* single electron transitions. Despite these differences, the large energy separation of S₁ from S₂/S₃ and smaller oscillator strength makes it unlikely that vibronic coupling will be manifested in the S₀-S₁ vibronic spectrum of the complex.

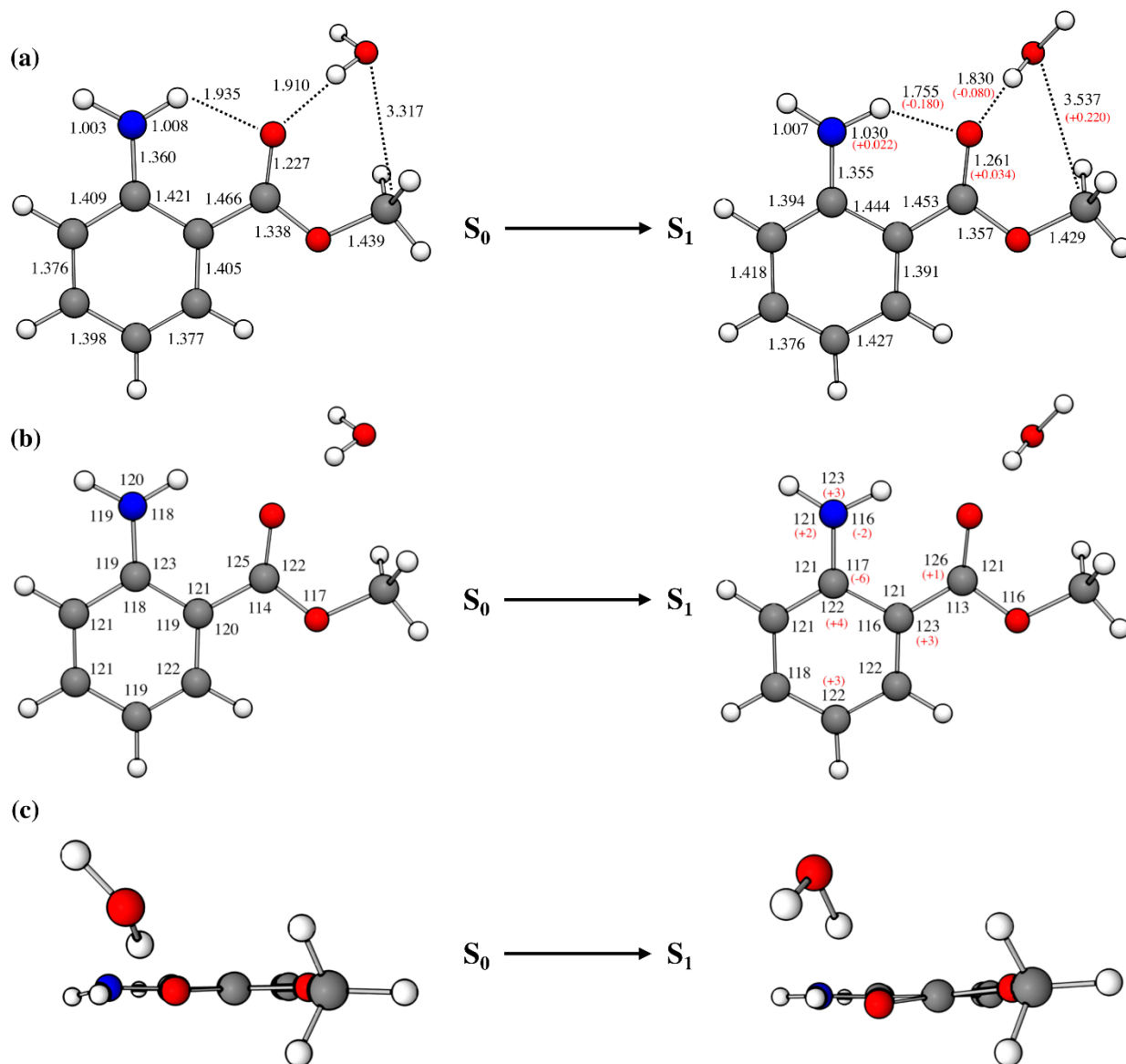


Figure 6.19. Optimized ground and S_1 excited state geometries of MA-H₂O with (a) bond distances and (b) bond angles labelled, and (c) a side view showing the change in water position upon electronic excitation. Bond lengths are in angstroms (Å) and angles are in degrees. The difference between select ground and excited state parameters are shown in red parentheses. Values were calculated at the DFT B3LYP-D3BJ/def2TZVP level of theory.

UV Excitation Spectroscopy

The labelled IR-UV HB spectrum of MA-H₂O is shown in Figure 6.20. The spectrum spans from 28,500 - 30,000 cm⁻¹, with the S₀ - S₁ electronic origin transition appearing at 28,574 cm⁻¹, shifted 278 cm⁻¹ to the red of the MA monomer origin due to the relative water binding energies in the S₀ and S₁ states. The lifetime of the S₁ state is measured to be 23 ns, very close to that of the monomer (see Figure 6.5 for the fluorescence decay trace). The MA-H₂O assignments included in Figure 6.20 were reached based on corroborating evidence from S₀ and S₁ vibrational frequency calculations, zero-point energy calculations, excitation and DFL spectra (discussed below). Progressions in modes ν_{56} (187 cm⁻¹) and ν_{49} (427 cm⁻¹) are displayed via dotted tie-lines, while combination bands built off of 49^1_0 are shown with solid tie-lines. All other assigned peaks are labelled with tags.

The Franck-Condon activity present in Figure 6.20 bears some resemblance to that in MA monomer, most notably in the progressions of ν_{56} and ν_{49} , which have their corresponding modes at similar frequencies in MA monomer (ν_{36} , 179 cm⁻¹ and ν_{33} , 421 cm⁻¹, respectively). Table 6.3 lists the experimental and calculated MA-H₂O S₀ and S₁ vibrational frequencies, along with their corresponding MA values. We note the presence of several analogous MA Franck-Condon active modes in the vibronic spectra of MA-H₂O. In many cases the frequencies increase in the presence of H₂O, indicating some stiffening of these in-plane vibrations (shown in Figure 6.21) when H₂O is present.

The triad of peaks immediately after the origin transition show an interesting intensity pattern, with each member of the triad more intense as frequency increases. If in both electronic states the geometry of MA-H₂O is non-planar, then one might expect to see large Franck-Condon activity in modes with mostly out-of-plane character. Instead, what we observe is the overtone of ν_{63} (63^2_0) being three times as intense as its fundamental transition (63^1_0), and the $62^1_063^1_0$ combination band twice again as intense as the 63^2_0 overtone. Both mode 62 and 63 are primarily intermolecular vibrations of the H₂O molecule, with ν_{63} mostly an out-of-plane motion (see Figure 6.21). These relative intensities suggest that the MA-H₂O complex retains a weakened form of its C_s selection rules in the complex; not surprisingly so, given that the electronic transition is localized on the planar MA monomer. As a result, the even overtone and 1+1 combination band are favored over the 63^1_0 out-of-plane intermolecular fundamental.

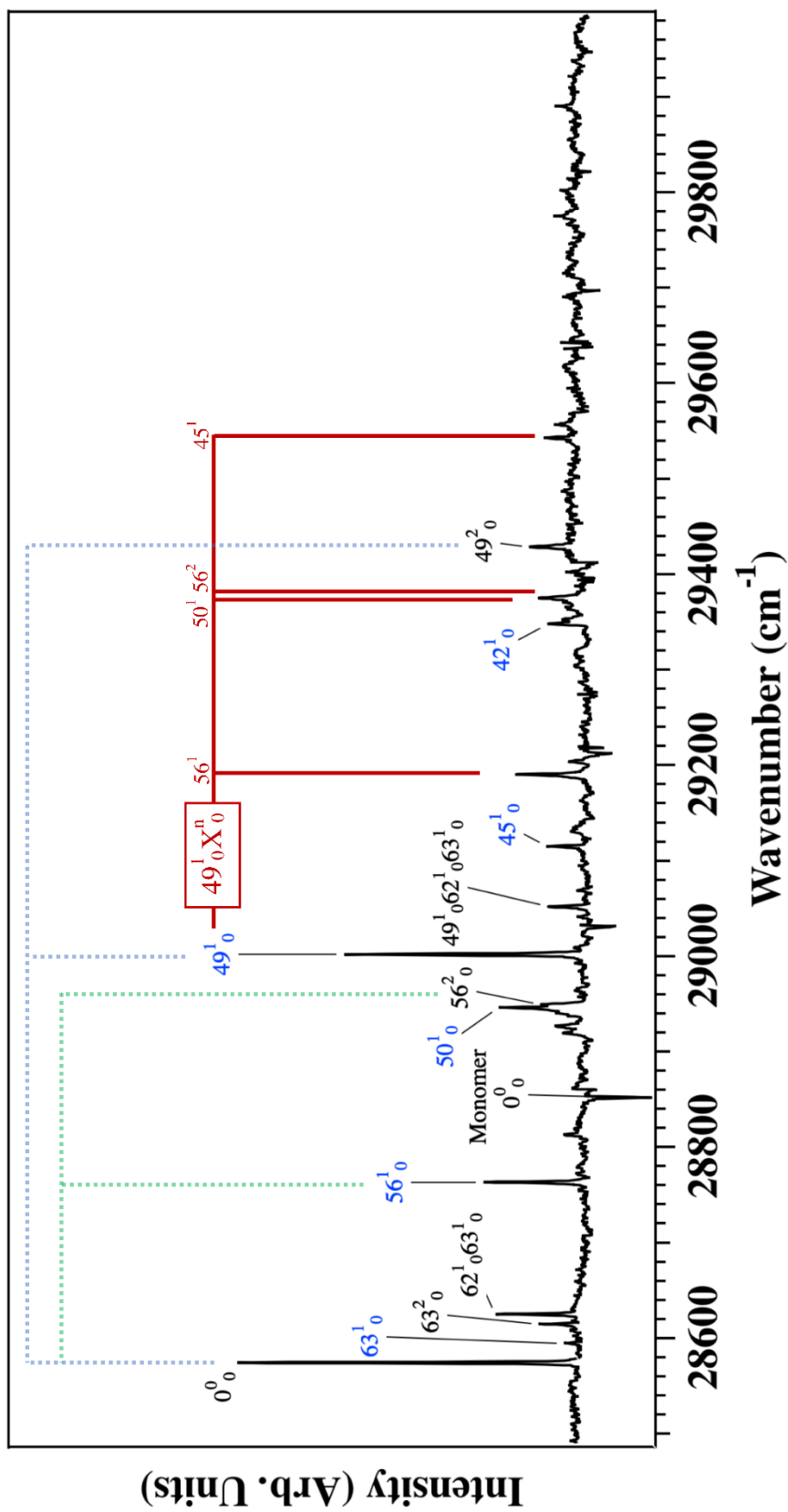


Figure 6.20. Assigned $S_0 - S_1$ LIF excitation spectrum of MA-H₂O. Progressions in the in-plane modes ν_{56} (189 cm⁻¹), and ν_{49} (427 cm⁻¹) are displayed via green and blue dotted tie-lines, respectively, while in-plane combination bands built off 49₀¹ are shown with solid tie lines. The identity of mode X is listed above each respective tie line.

Table 6.3. Experimental and Calculated S₀ and S₁ Frequencies of MA-H₂O

Mode	S ₀		S ₁	
	Exp Freq (cm ⁻¹)	Calc Freq ^b (cm ⁻¹)	Exp Freq (cm ⁻¹)	Calc Freq ^b (cm ⁻¹)
63	9	10	20	22
62	49	50	31	33
56 (36)	187 (179)	185	189 (179)	189
50 (34)	345 (361)	360	372 (366)	362
49 (33)	418 (412)	428	427 (421)	426
45 (31)	568 (567)	573	541 (540)	560
42 (30)	667 (672)	684	773 (610)	789
38 (29)	817 (808)	821	- (773)	789
23 (18)	1363 (1355)	1355	-	1382

^a values in parentheses are analogous values of MA.

^b Frequencies calculated at the DFT B3LYP-D3BJ/def2TZVP level of theory.

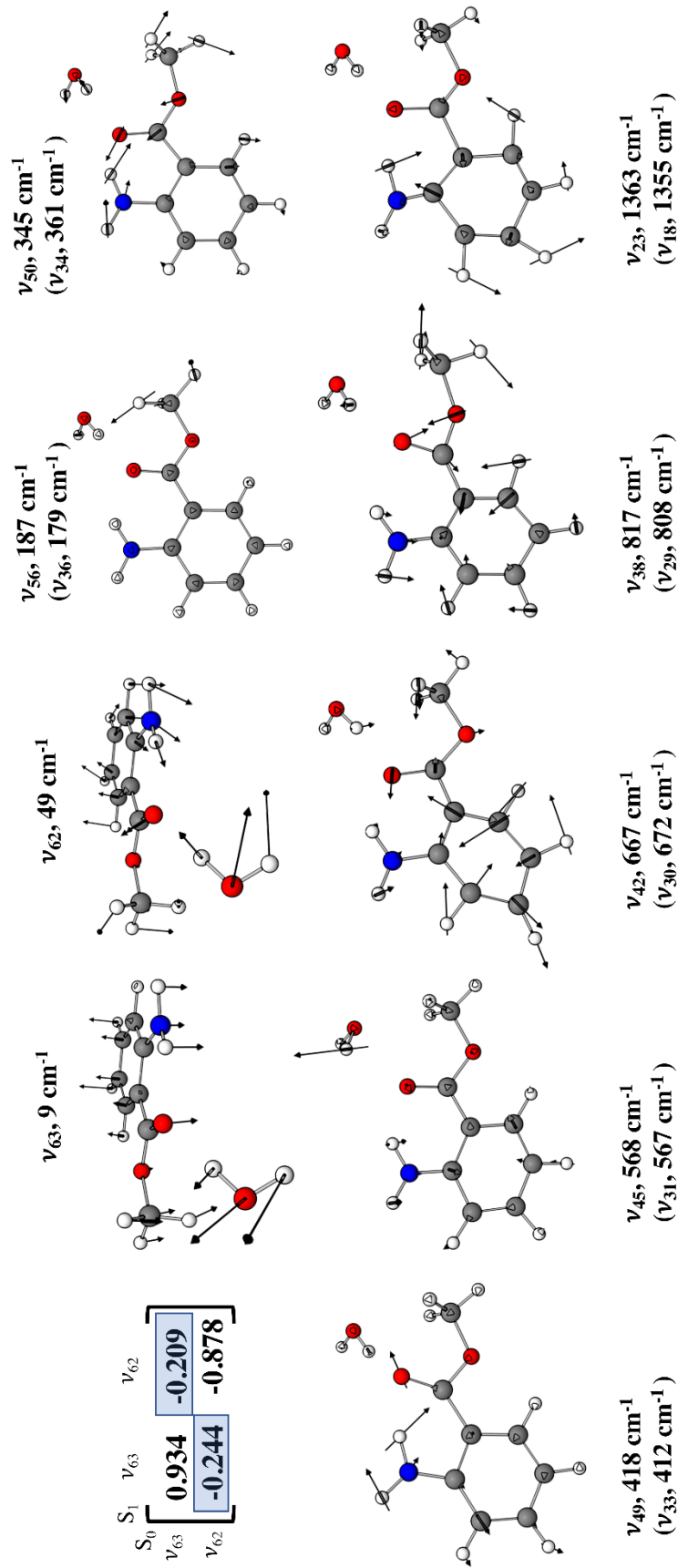


Figure 6.21. Reduced Duschinsky rotation matrix, and vector displacement representation of the Franck-Condon active normal modes of MA-H₂O. Values in parentheses are those corresponding values in the MA monomer. Calculations performed at the DFT B3LYP-D3BJ/defTZVP level of theory.

Origin DFL Spectrum

The assigned DFL spectrum of the 0^0_0 transition of MA-H₂O is shown in Figure 6.22. As with MA, this spectrum generally mirrors that of the MA-H₂O excitation spectrum, reflecting that Franck-Condon factors between the S₀ and S₁ electronic states of MA largely dictate the vibronic structure in both excitation and emission. The same two modes that were Franck-Condon active in the excitation spectrum, ν_{56} and ν_{49} , also appear as progressions in the DFL spectrum. Mode 49 is also an active member in combination band transitions.

The low frequency $62^0_1 63^0_1$ combination band at 58 cm⁻¹ in the 0^0 DFL spectrum is the analogous combination band transition that we observed in the excitation spectrum ($62^1_0 63^1_0$). Due to the presence of intense laser scatter, we are not able to see whether this DFL spectrum contains the analogous 63^0_1 and 63^0_2 transitions that appeared in the excitation spectrum. It is worth noting that the ground state modes 62 and 63 are substantially mixed with one another in S₁, as revealed by large off-diagonal components in the Duschinsky matrix (see Figure 6.21). Several of the modes present in the excitation spectrum appears in the DFL spectrum with analogous $\Delta v=1$ transitions. Similarly, one higher frequency band is present in the DFL spectrum, ν_{23} , appearing at 1363 cm⁻¹. This mode is analogous to ν_{18} in MA (see Table 6.3).

6.4 Discussion

6.4.1 Structural Changes Associated with Hydrogen Atom Dislocation

The Franck-Condon activity in several in-plane modes in the excitation and DFL spectra of MA indicate that the molecular geometries in the S_0 and S_1 states differ substantially from one another along these coordinates. We have carried out a near-complete assignment of the vibrationally-resolved LIF excitation scan and an array of DFL spectra out of single vibronic levels in the excited state. In all cases, the unscaled harmonic vibrational frequencies predicted by the DFT and TDDFT calculations at the B3LYP-D3BJ/def2TZVP level of theory closely reproduce the experimental values, with an average error of $\pm 10.5 \text{ cm}^{-1}$. Furthermore, the rotational constants and transition dipole moment direction from calculation faithfully reproduce the rotational band contour of the electronic origin without adjustment. This leads to the conclusion that the calculations faithfully reproduce the ground state and excited state potential energy surfaces around the S_0 and S_1 minima, and therefore are anticipated to be trustworthy in the more detailed structural changes accompanying electronic excitation.

From an experimental viewpoint, while all the low-frequency in-plane vibrations have some Franck-Condon activity, longer progressions extending to $v'=3$ in modes 36 and 33, and $v'=2$ in mode 34 are evident in the 0^0 DFL spectrum (Figure 6.10), reflecting largest geometry changes along these vibrational coordinates. Indeed, the majority of the vibronic structure in the excitation and DFL spectra can be accounted for as progressions and combination bands involving these three modes. These three modes all involve substantial in-plane motion of the NH_2 and CO_2Me groups relative to one another. These heavy atom motions modulate the average distance between the H-bonded NH donor and the carbonyl oxygen acceptor groups along what might be termed the 'reaction coordinate' for a hydrogen atom transfer or dislocation. In the next chapter, we will view these effects on the interactions between the NH and C=O groups more directly by presenting infrared spectra of MA and MA- H_2O in the NH stretch, NH bend, and C=O stretch regions in both S_0 and S_1 states.³²

The low-frequency Franck-Condon activity that is the subject of the present work gives insight principally on the heavy atom motions that accompany electronic excitation. MA affords the opportunity to view this structural change by projecting a range of excited state vibrational levels back onto the ground state via their dispersed emission. As a result, armed with a comprehensive assignment of the electronic spectra, we now turn to a more detailed discussion of

the structural change associated with the $\pi\pi^*$ electronic excitation, based on the optimized geometries shown in Figure 6.3.

In MA, the optimized ground state geometry has as its most characteristic feature the intramolecular H-bond between the NH_2 and $\text{C}=\text{O}$ groups, with a H-bond distance of 1.926 Å associated with a short, but bent H-bond. This places the NH_2 group in an unusual situation in that amines are known most for their role as good H-bond acceptors due to the lone pair on the N atom, not as H-bond donors. Nevertheless, in the ground state, the structural effects of the $\text{NH}\cdots\text{O}=\text{C}$ H-bond are modest, with neither the NH nor $\text{C}=\text{O}$ bond lengths being changed significantly from their ground state bond values in the singly-substituted analogs aniline (NH_2 only, $\Delta R = +0.001$ Å) or methyl benzoate (methyl ester only, $\Delta R = +0.012$ Å), both of which lack the intramolecular H-bond.

The structural changes associated with electronic excitation are more dramatic. The primary changes involve structural distortions and positional changes in the NH_2 group relative to the methyl ester. First, the $\text{N-H}_{\text{donor}}$ and $\text{O}=\text{C}$ bonds each increase in length by ~ 0.03 Å, characteristic changes associated with strengthening a H-bond between them. Second, the NH bond rotates towards the carbonyl oxygen, closing the CNH bond angle by 2° . Third, the CCN bond angle decreases from 122° to 116° . Taken together, these structural changes tilt and stretch the NH_2 group toward the methyl ester, contracting the 6-membered (C6) ring that is closed by the $\text{NH}\cdots\text{O}=\text{C}$ hydrogen bond. This results in a substantial decrease of the $\text{H}\cdots\text{O}$ hydrogen bonding distance by 0.203 Å, taking what is already a short H-bond ($R_{\text{H}\cdots\text{O}} = 1.926$ Å) and making it extraordinarily short ($R_{\text{H}\cdots\text{O}} = 1.723$ Å). Nearly identical structural changes occur in MA- H_2O upon electronic excitation. One interesting difference, however, is that the $\text{H}\cdots\text{O}$ distance decreases by 0.02 Å less in MA- H_2O than in MA. This is likely a result of the electronegative $\text{C}=\text{O}$ oxygen acting as H-bond acceptor to both the NH and water OH, thereby decreasing its affinity for the dislocated NH. Table 6.4 lists the S_0 , S_1 , and difference in structural parameters for MA and MA- H_2O .

Table 6.4. Structural Parameters of MA and MA-H₂O^a

	<u>Methyl Anthranilate</u>			<u>Methyl Anthranilate:H₂O</u>		
	S ₀	S ₁	Δ	S ₀	S ₁	Δ
R _{C-N} ^b	1.359	1.356	-0.003	1.360	1.355	-0.005
R _{N-Hdonor}	1.008	1.035	0.027	1.008	1.030	0.022
R _{N-Hfree}	1.003	1.007	0.004	1.003	1.007	0.004
θ _{H-N-H} ^c	120°	124°	4°	120°	123°	3°
D _{CNHH}	0°	0°	0°	11°	3°	-8°
R _{C=O}	1.220	1.252	0.032	1.227	1.261	0.034
R _{C-O}	1.349	1.364	0.015	1.338	1.357	0.019
θ _{O=C-O}	121	121°	0°	122°	121°	-1°
R _{H...O}	1.926	1.723	-0.203	1.935	1.755	-0.180
θ _{N-Hdonor-O}	130°	141°	11°	129°	139°	10°
R _{OH-O}	--	--	--	1.910	1.830	-0.080
R _{HO-C}	--	--	--	3.317	3.537	0.220
θ _{O-H...O}	--	--	--	171°	178°	7°

^aStructures calculated at the DFT B3LYP-D3BJ/def2TZVP level of theory.

^bDistances in Å.

^cAngles in degrees.

In previous work on anthranilic acid, the excited state structural change was labeled as a ‘hydrogen-atom dislocation’ to indicate its partial nature, as distinct from ‘hydrogen-atom transfer’, in which a hydrogen atom is completely transferred from one nucleus to another.¹⁵ The results presented herein allow us to compare similar systems to one another. We begin with MA and MA-H₂O. As we saw in section III, the LIF excitation and 0⁰₀ DFL spectra of MA and MA-H₂O are quite similar to one another, with analogous modes dominating the spectra of both. Aside from breaking the C_s symmetry of the monomer unit, the effect of water binding on molecular structure, and therefore, vibrational frequencies, seems to have little effect. This is evident by the small shift in analogous Franck-Condon active frequencies between hydrated and non-hydrated MA, shown in Table 6.2 of the main text. The MA-H₂O 0⁰₀ transition is 278 cm⁻¹ lower energy than that of MA. In a simple estimation, this shift may be explained by the polarization of molecular orbitals involved in the electronic transition by the water interaction.

The structural changes that occur in MA upon UV excitation also occur in MA-H₂O, to a degree that is modulated by the water interaction. Upon excitation in MA-H₂O the aromatic ring

flattens, the amine group tilts toward the methoxycarbonyl group, closing the C6 ring formed by the $\text{NH}\cdots\text{O}=\text{C}$ hydrogen bond. The $\text{N}-\text{H}_{\text{donor}}$ bond increases in length by 0.022 Å, the $\text{O}=\text{C}$ bond increases in length by 0.034 Å, resulting in a decrease of the $\text{H}\cdots\text{O}$ hydrogen bonding distance by 0.180 Å (going from 1.935 to 1.755 Å). Table 6.4 lists the S_0 , S_1 , and difference in structural parameters for MA and MA- H_2O . The water molecule rotates and moves out of plane. This has the effect of decreasing the $\text{OH}\cdots\text{O}=\text{C}$ hydrogen bonding distance by 0.080 Å and increasing the $\text{H}_2\text{O}\cdots\text{CH}_3$ distance by 0.220 Å. We see, then, that the structural change of MA- H_2O upon electronic excitation proceeds along the same hydrogen dislocation coordinate as that of MA, to a degree determined by the H_2O interaction.

Time dependent density functional theory results indicate that the electronic S_0 - S_1 transition in both MA and MA- H_2O may be described by two single-electron transitions from one molecular orbital to another. The molecular orbitals responsible for these transitions in MA and MA- H_2O are discussed in the next section. The orbitals, and coefficients, involved in the electronic transition in each case are nearly identical to one another and may be described as a textbook example of conjugated π bonding orbitals moving electron density onto conjugated π^* anti-bonding orbitals.

The nature of the structural change upon electronic excitation between MA and AA are very similar to one another. Hydrogen atom dislocation occurs in each case.¹⁵ The LIF excitation spectrum of each species also has progressions in the same normal modes, designated as modes ν_{36} and ν_{33} in MA. The single water complexes of MA and AA are also quite similar to one another.¹⁴ In each case, a water hydrogen bonds with the monomer $\text{C}=\text{O}$. In AA- H_2O , an additional hydrogen bond is formed between the water oxygen and monomer acid $\text{H}-\text{O}$ group, which MA lacks. The absence of water hydrogen bonding with the NH_2 in each case is perhaps not surprising, given the extremely strong hydrogen bond in which the amine group is already participating.

As we will discuss in more detail in the following section, in salicylic acid and similar molecules, the transfer involves $\text{O}-\text{H}$ bond lengthening, with relaxation along several heavy-atoms on the S_1 potential energy surface and subsequent red-shifted emission and/or non-radiative decay via an S_1/S_0 conical intersection (CI).^{2-4, 12} In MA, we have investigated the S_0 - S_1 Franck-Condon active region, and see no evidence of hydrogen atom transfer near the S_1 origin. This is demonstrated by the absence of non-radiative processes in the UV-D spectrum, and the lack of strongly red-shifted emission in the DFL spectra.

What the present study has achieved is a deeper understanding of what ‘hydrogen atom dislocation’ means in methyl anthranilate. As just summarized, the optimized excited state structure has an H \cdots O distance 0.203 Å shorter than in the ground state, with $R_{\text{H}\cdots\text{O}}=1.723$ Å. If full transfer were to shorten this distance to 1.0 Å, then the dislocation in MA is about 25% of full transfer. However, only 0.03 Å of this dislocation involves lengthening the NH bond, while the remaining 0.173 Å is due to the heavy atom motion just described that reorients the entire NH₂ group relative to the C=O acceptor.

To further quantify the difference between excited and ground electronic states of MA, we carried out one-dimensional Franck-Condon analyses of nearly all vibronically active normal modes. Harmonic Franck-Condon overlap integrals were calculated as a function of the parameters D and δ , which represent normal coordinate displacement upon excitation and square root of the ratio between ground and excited state vibrational frequencies, respectively³³. D is varied to find the best fit between calculated and experimental excitation and DFL spectra of the members of the progression under consideration. Figure 6.23 and Figure 6.24 show the calculated fits to the members of the 421 and 179 cm⁻¹ progressions, respectively. The best fit displacement value for these modes is 1.27 and 0.97, respectively. We find that, while the over-all fits are reasonably good, the spectral fits do not quantitatively emulate the DFL and LIF excitation spectra simultaneously, in that the best fits to the series of DFL spectra require larger Franck-Condon activity in excitation than is observed experimentally. Since the UV-D spectra shows no non-radiative turn on over the wavelength region we are probing, this is an indication that a one-dimensional analysis is not sufficient for the vibronic spectra of MA, which is further evidence of Duschinsky mixing in MA between the ground and excited state normal coordinates.

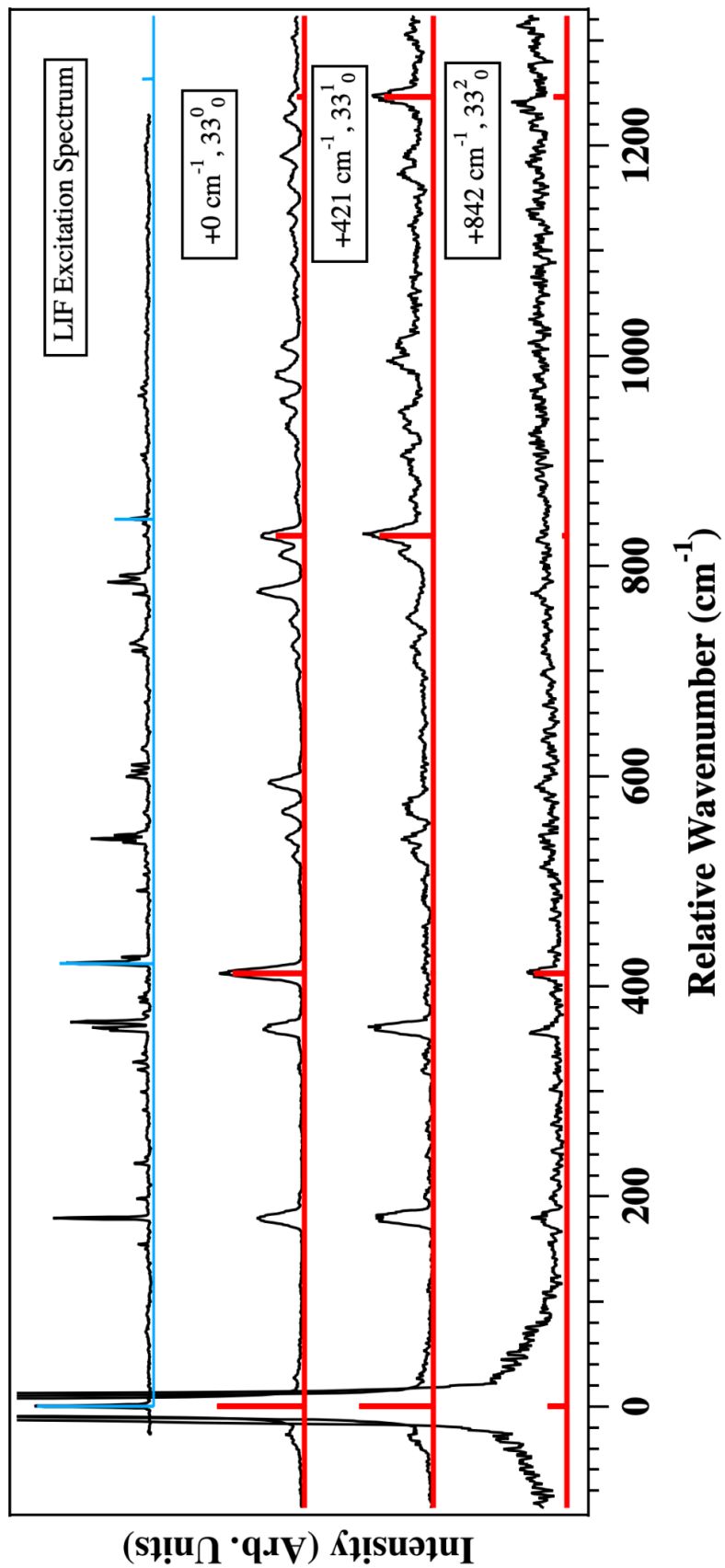


Figure 6.23. Franck-Condon factor fits of the members of the mode 33 progression. The best fit displacement for this mode is 1.27.

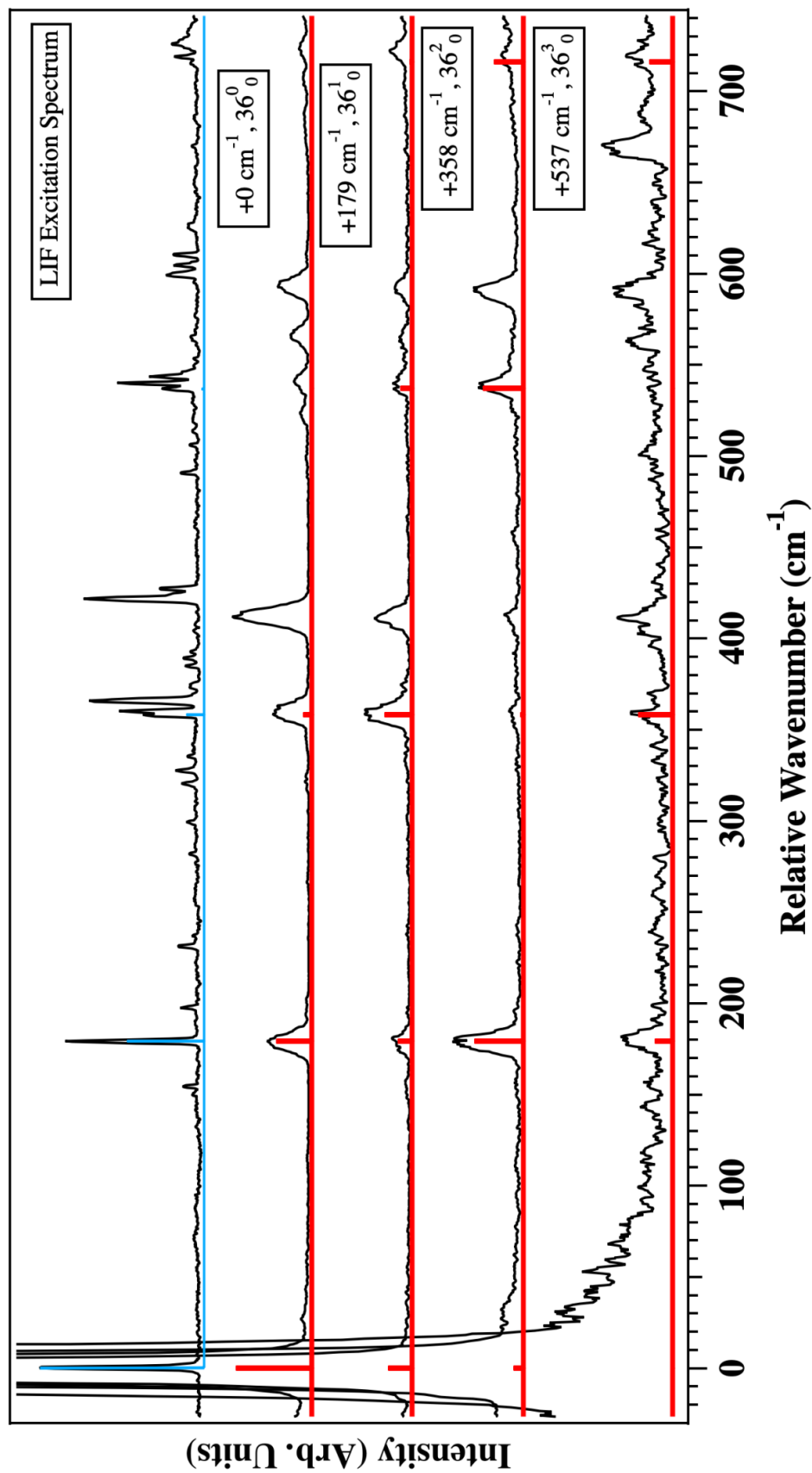


Figure 6.24. Franck-Condon factor fits of the members of the mode 36 progression. The best fit displacement for this mode is 0.97.

6.4.2 Photophysical Properties of MA and Implications as a Sunscreen Precursor

MA is the precursor to menthyl anthranilate (MenA), an FDA approved sunscreen agent. Rodrigues *et al.* have recently shown, in both condensed- and gas-phase, that MA and MenA exhibit nearly identical photochemical/photophysical properties.¹³ In order to put the absorption and photophysical properties of MA in proper context, we compare MA first to its simpler analogs, aniline (NH₂ substitution only) and methyl benzoate (CO₂Me substitution only).

Aniline is a prototypical aromatic amine that has been studied extensively. Its S₀-S₁ origin appears at 34,025 cm⁻¹, and is readily detected by both fluorescence and R2PI schemes.³⁴⁻³⁸ Using the same level of theory as in MA, we calculated S₀ and S₁ state optimized geometries for aniline. These structures, along with the molecular orbitals involved in the S₀-S₁ transition are shown in Figure 6.25. The S₀-S₁ transition of aniline is a prototypical $\pi\pi^*$ transition for a phenyl derivative, leading to expansion in the size of the aromatic ring, modest shortening of the CN bond ($\Delta R_{CN} = -0.026 \text{ \AA}$), and planarization of the NH₂ group in the S₁ state.

Methyl benzoate (MB), by contrast, has its S₀-S₂ transition (the first optically accessible singlet $\pi\pi^*$ state) at 36,105 cm⁻¹, but cannot be detected either in LIF or R2PI due to fast intersystem crossing (ISC) to the $n\pi^*$ triplet state that shortens the excited state lifetime and reduces the fluorescence quantum yield. Its spectroscopy has been studied using sensitized phosphorescence detection.³⁹ Table 6.5 shows the energetic ordering of electronic states of aniline, MB, MA, and MA-H₂O. The calculated structural changes associated with electronic excitation (shown in Figure 6.26) include expansion in the size of the aromatic ring, substantial lengthening of the C=O bond ($\Delta R_{C=O} = +0.110 \text{ \AA}$) and a closing of the O=C-O angle ($\Delta\theta_{O=C-O} = -10^\circ$). The molecular orbitals associated with this transition are shown in Figure 6.27, and those associated with the S₀ - T₃($n\pi^*$) transition are shown in Figure 6.28.

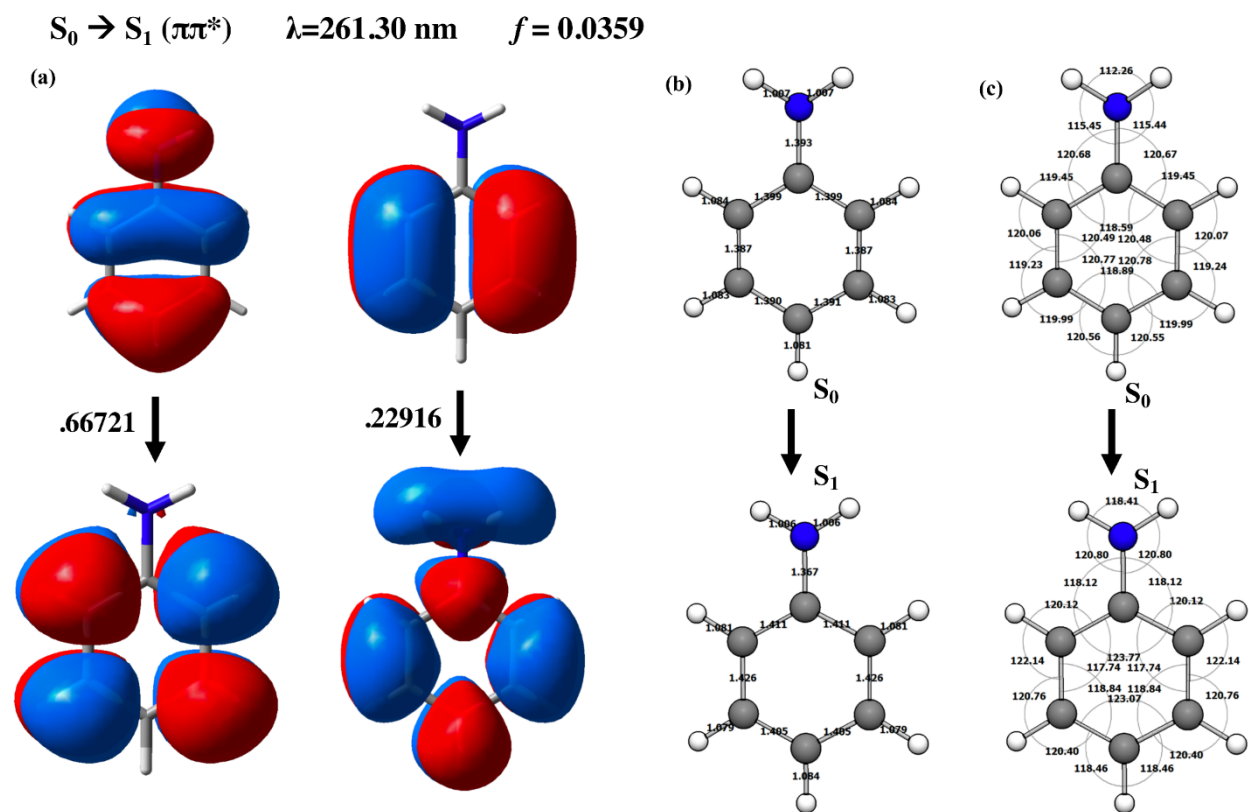


Figure 6.25. The (a) molecular orbitals, transition coefficients, oscillator strength, (b) bond distance, and (c) bond angle parameters associated with the $S_0 - S_1$ transition of aniline. Calculations performed at the DFT B3LYP-D3BJ/def2TZVP level of theory.

Table 6.5. Electronic States in Aniline, Methyl Benzoate, Methyl Anthranilate, and Methyl Anthranilate-H₂O^a

<u>Aniline</u>			<u>Methyl Benzoate</u>			<u>Methyl Anthranilate</u>			<u>Methyl Anthranilate-H₂O</u>		
State	Energy	f_{0n}	State	Energy	f_{0n}	State	Energy	f_{0n}	State	Energy	f_{0n}
	(eV)			(eV)			(eV)			(eV)	
$^3\pi\pi^*$	3.65	0.0000	$^3\pi\pi^*$	3.57	0.0000	$^3\pi\pi^*$	3.03	0.0000	$^3\pi\pi^*$	2.95	0.0000
$^3\pi\pi^*$	3.86	0.0000	$^3\pi\pi^*$	4.18	0.0000	$^3\pi\pi^*$	3.56	0.0000	$^3\pi\pi^*$	3.50	0.0000
$^3\pi\pi^*$	4.49	0.0000	$^3n\pi^*$	4.47	0.0000	$^1\pi\pi^*$	3.92	0.1036	$^1\pi\pi^*$	3.84	0.1077
$^1\pi\pi^*$	4.75	0.0359	$^3\pi\pi^*$	4.53	0.0000	$^3\pi\pi^*$	4.17	0.0000	$^3\pi\pi^*$	4.12	0.0000
$^3\pi\pi^*$	5.32	0.0000	$^1n\pi^*$	4.88	0.0001	$^3n\pi^*$	4.69	0.0000	$^3n\pi^*$	4.81	0.0000
$^3\pi\pi^*$	5.40	0.0000	$^1\pi\pi^*$	4.97	0.0153	$^1n\pi^*$	5.08	0.0002	$^1n\pi^*/\pi\pi^*$	5.15	0.0530
$^1\pi\pi^*$	5.42	0.0644	$^3\pi\pi^*$	5.07	0.0000	$^1\pi\pi^*$	5.23	0.0481	$^1n\pi^*/\pi\pi^*$	5.18	0.0117

^a Values calculated at the DFT B3LYP-D3BJ/def2TZVP level of theory

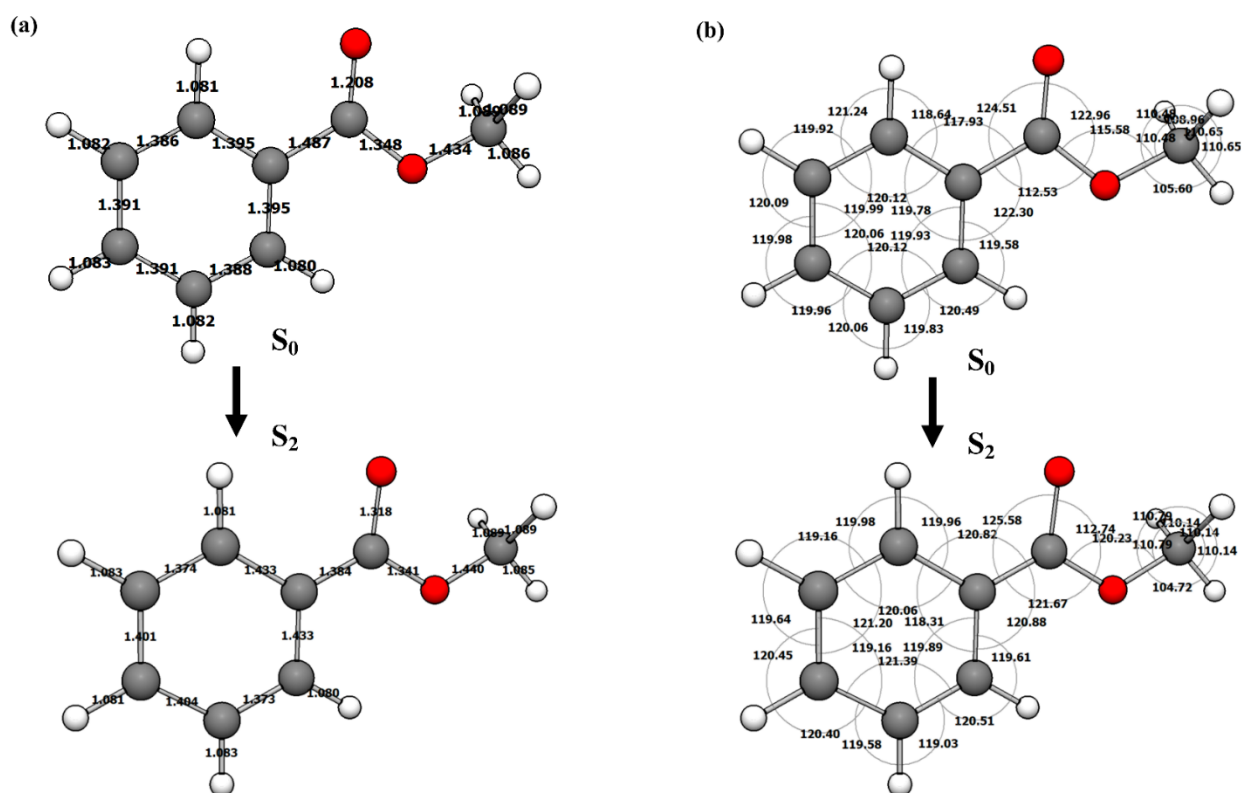


Figure 6.26. The (a) bond distance, and (b) bond angle parameters associated with the S₀ - S₂ transition of methyl benzoate. Calculations performed at the DFT B3LYP-D3BJ/def2TZVP level of theory.

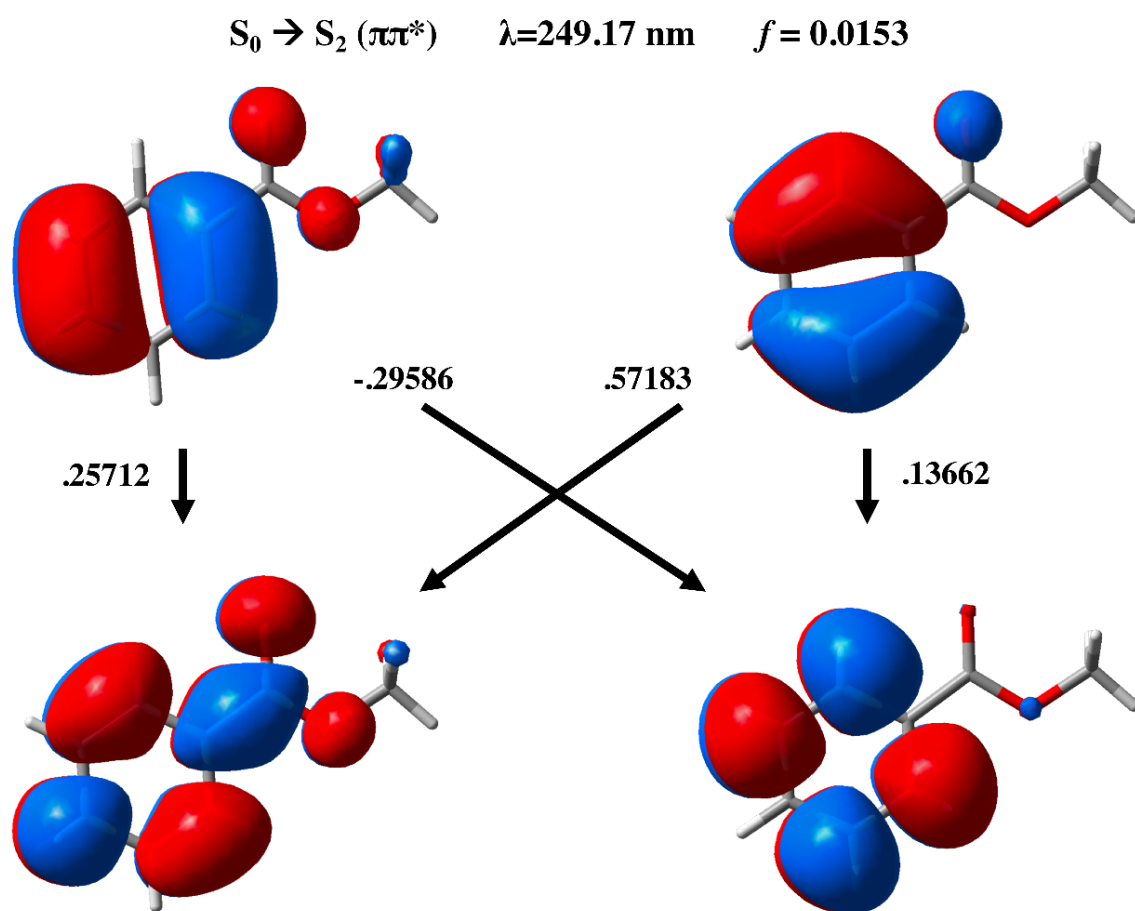


Figure 6.27. Molecular orbitals involved in the $S_0 - S_2$ electronic transition of methyl benzoate, along with the coefficients, calculated vertical excitation wavelength, and oscillator strength. Calculations performed at the DFT B3LYP-D3BJ/def2TZVP level of theory.

$S_0 \rightarrow T_3 (n\pi^*)$ $\lambda=276.88$ nm $f = 0.0000$

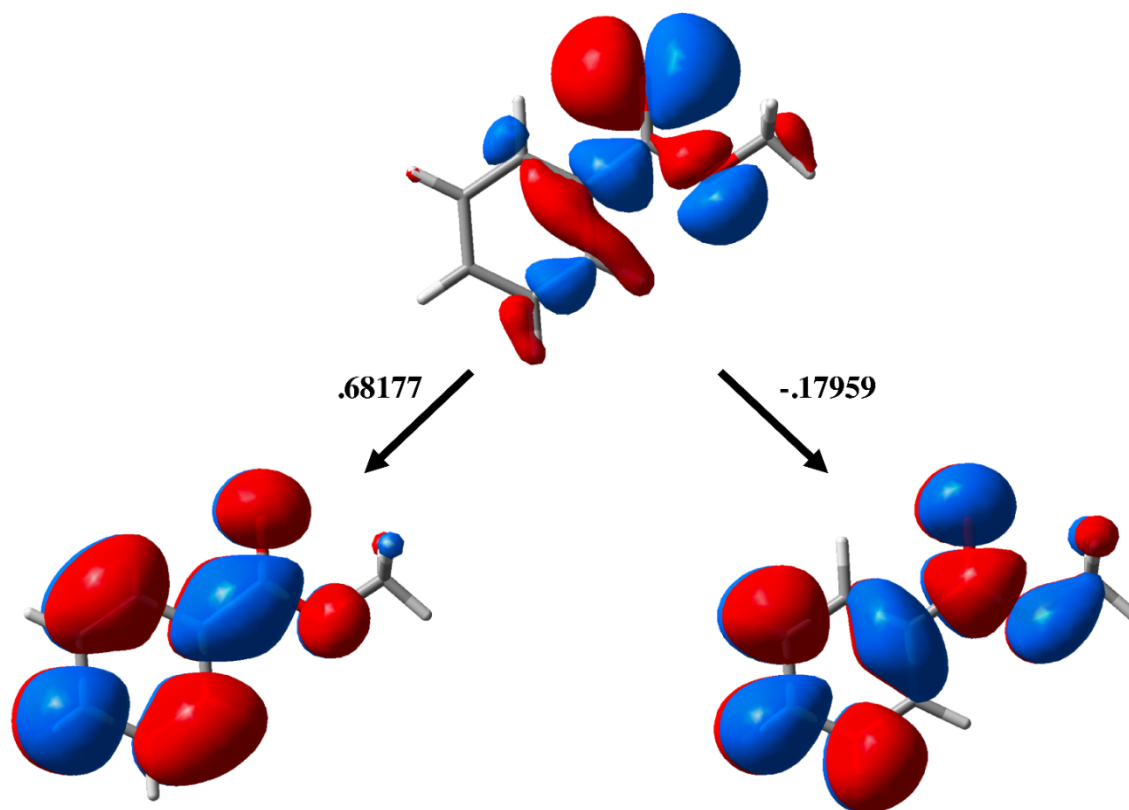


Figure 6.28. Molecular orbitals involved in the $S_0 - T_3$ electronic transition of methyl benzoate, along with the coefficients, calculated vertical excitation wavelength, and oscillator strength. Calculations performed at the DFT B3LYP-D3BJ/def2TZVP level of theory.

Inclusion of both methoxycarbonyl and amine groups as *ortho*-ring substituents in MA modifies the properties of the singly-substituted molecules in several ways. The absorbing states are redshifted from the UV-B (280 - 315 nm) region (276.9 nm in MB and 293.9 nm in aniline) into the UV-A region (315 - 400 nm), with S_0 - S_1 origin at 346.9 nm and low-frequency Franck-Condon activity stretching to 333.3 nm in the gas phase. Figures 6.29-32 and Figures 6.33-36 present the molecular orbitals involved in select electronic transitions of MA. The TDM vectors of the bright transitions of MB and Aniline essentially add to form the TDM vector in MA, with the oscillator strength of the MA nearly tripling that of aniline and increasing by nearly an order of magnitude in MB, respectively (see Figure 6.37).

Relative to MB, MA's inclusion of the amine group reorders the electronic states substantially. In MB, the ester C=O group gives rise to a triplet $n\pi^*$ state that, according to calculations, lies $4,033\text{ cm}^{-1}$ (0.5 eV) below the absorbing singlet $\pi\pi^*$ state (see Table 6.4). In accordance with El-Sayed's rule, $^1\pi\pi^* \leftrightarrow ^3n\pi^*$ ISC is efficient when energetically allowed, producing an experimentally observed long-lived non-fluorescent state.³⁹ The strong intramolecular hydrogen bond in MA, which includes bonding of the C=O lone electron pair, results in an increase in energy of the $n\pi^*$ state relative to the $\pi\pi^*$ state. According to calculations, this raises the energy of the triplet $n\pi^*$ state to $6,210\text{ cm}^{-1}$ (0.77 eV) above that of the absorbing singlet $\pi\pi^*$ state. The destabilization of the triplet $n\pi^*$ state in MA removes the possibility of ISC involving that state.

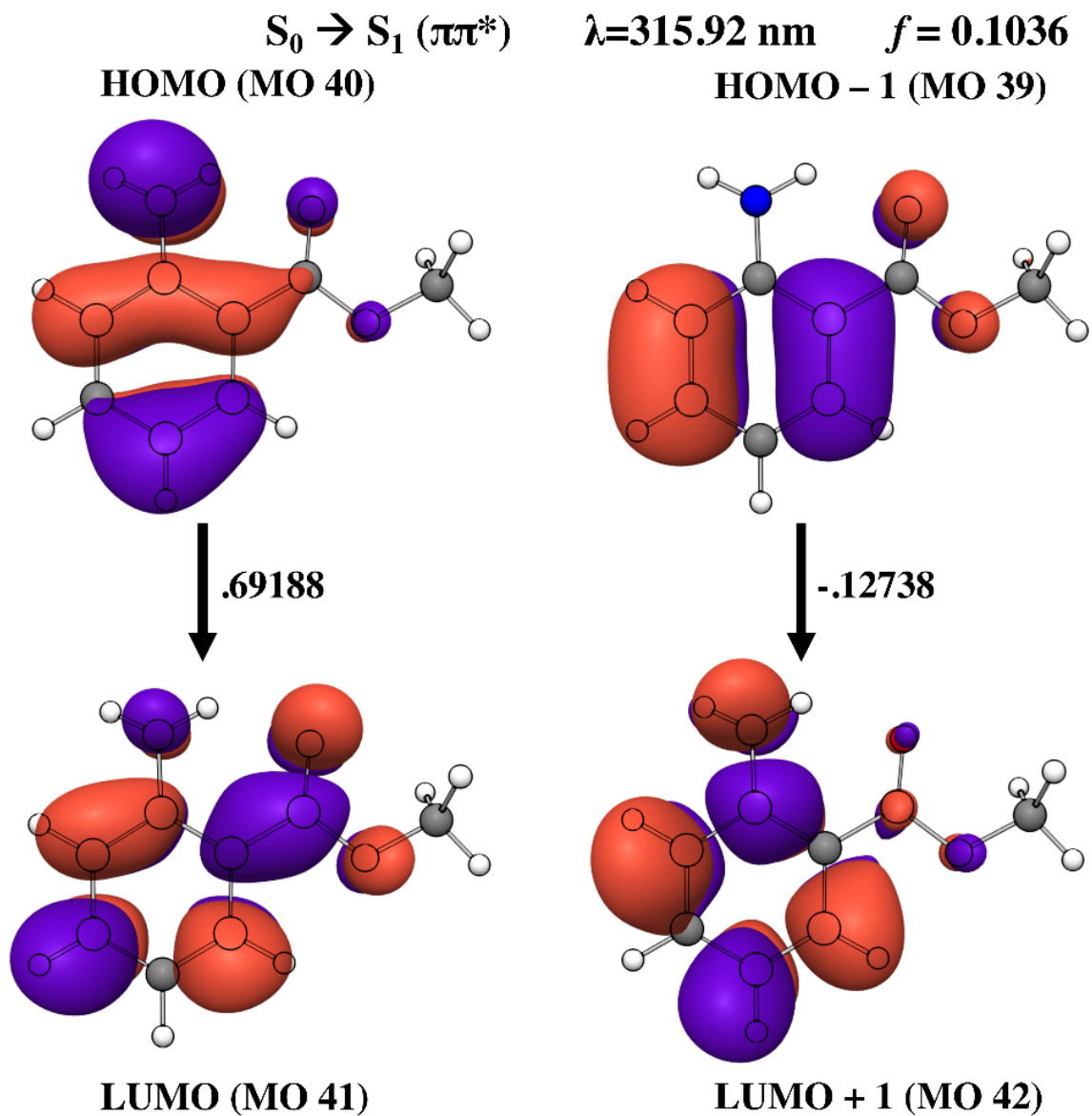


Figure 6.29. Molecular orbitals involved in the $S_0 - S_1$ electronic transition of MA, along with the coefficients, calculated vertical excitation wavelength, and oscillator strength. Calculations performed at the DFT B3LYP-D3BJ/def2TZVP level of theory.

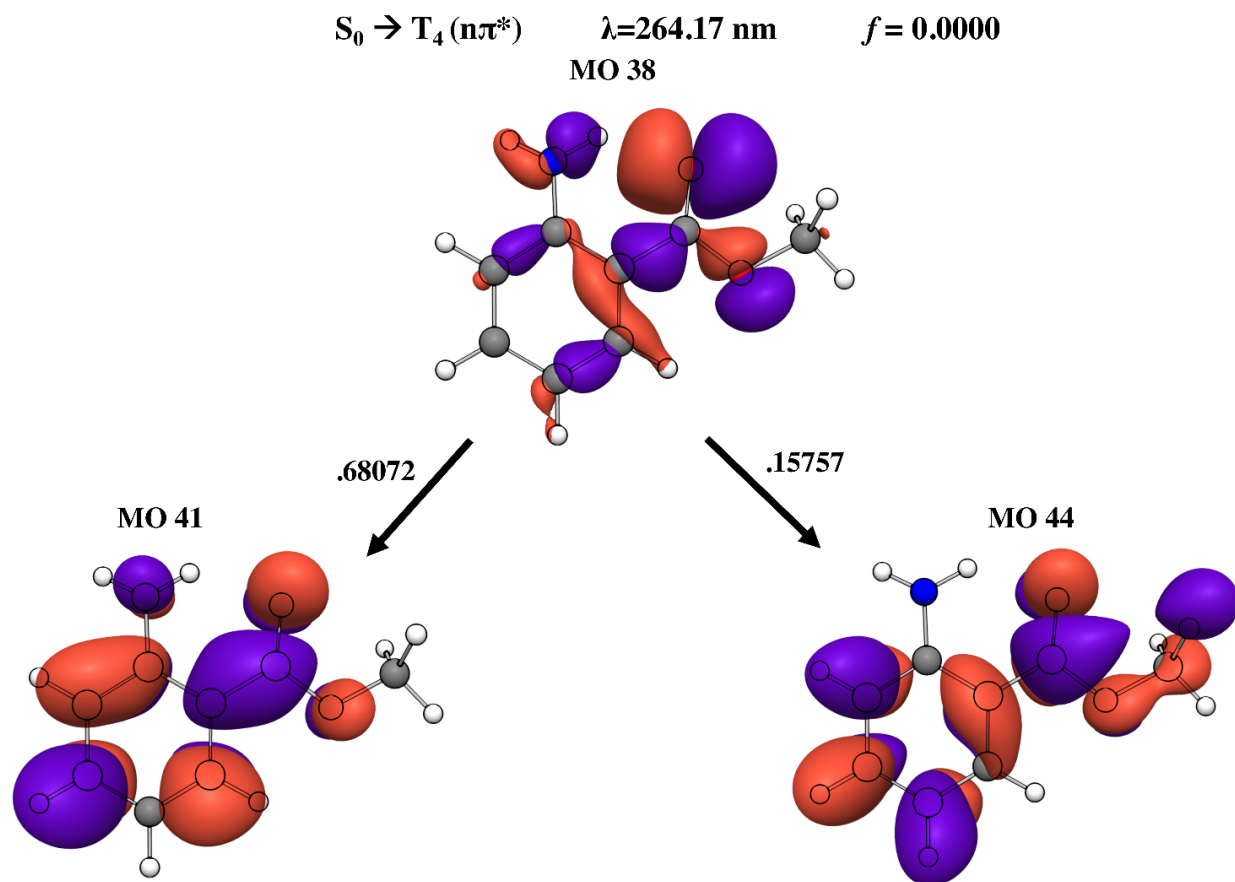


Figure 6.30. Molecular orbitals involved in the $S_0 - T_4$ electronic transition of MA, along with the coefficients, calculated vertical excitation wavelength, and oscillator strength. Calculations performed at the DFT B3LYP-D3BJ/def2TZVP level of theory.

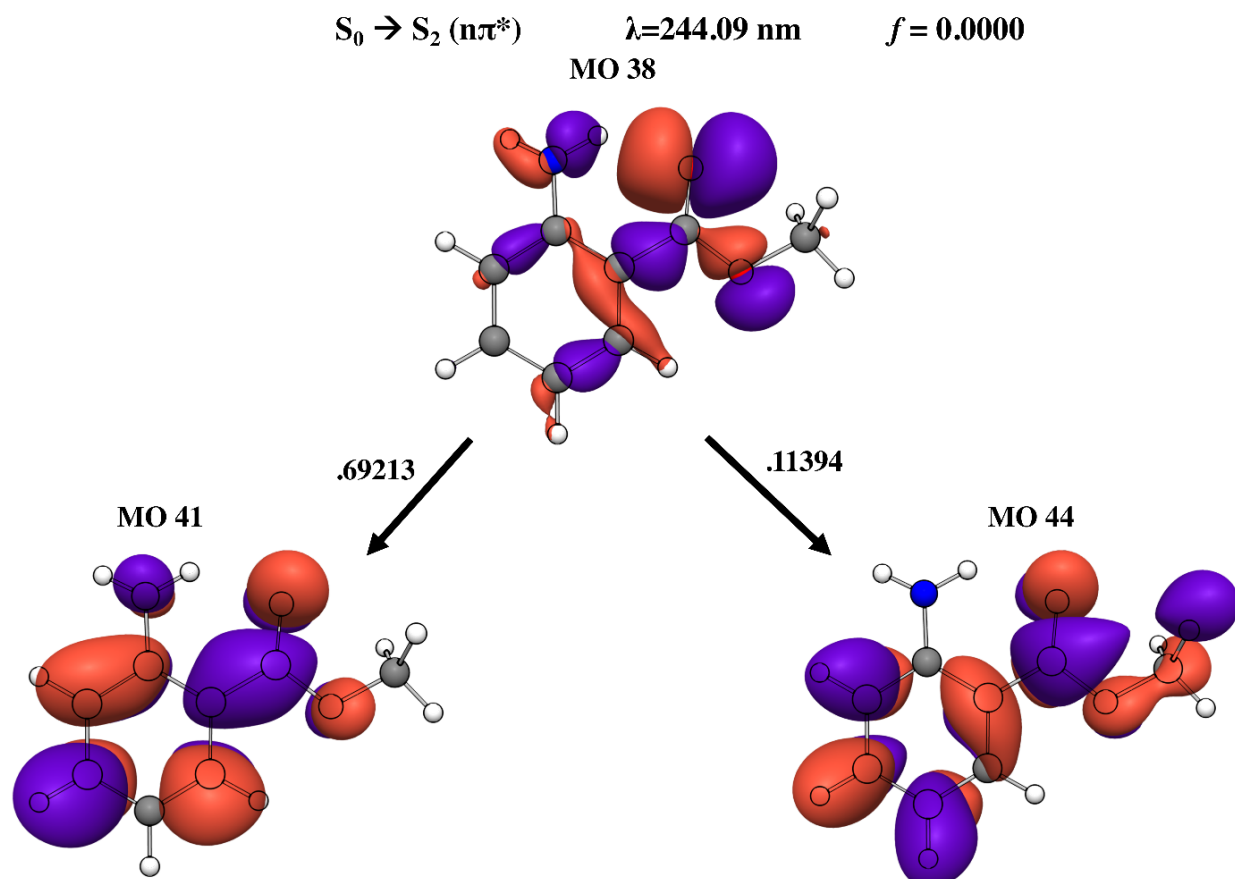


Figure 6.31. Molecular orbitals involved in the $S_0 - S_2$ electronic transition of MA, along with the coefficients, calculated vertical excitation wavelength, and oscillator strength. Calculations performed at the DFT B3LYP-D3BJ/def2TZVP level of theory.

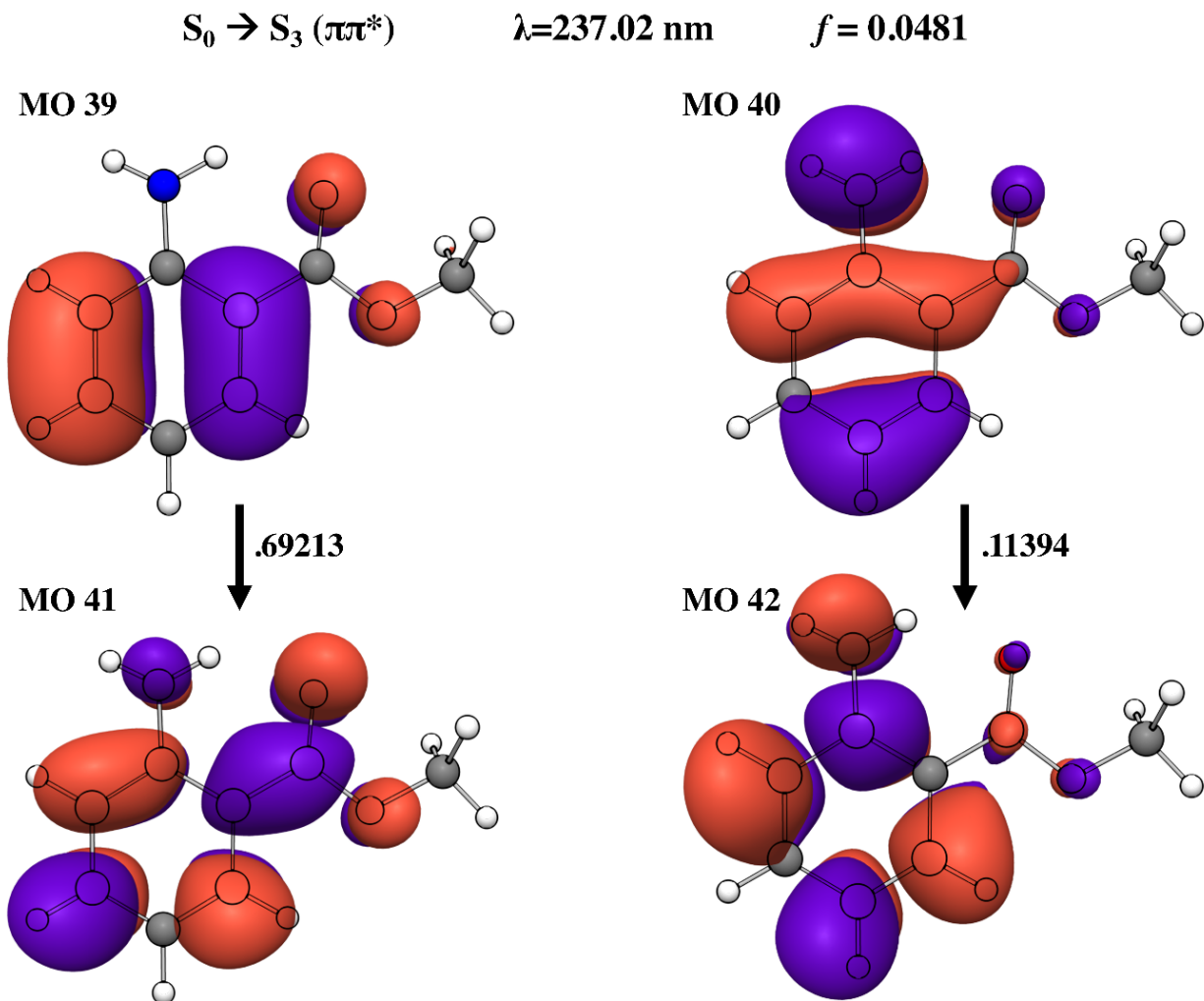


Figure 6.32. Molecular orbitals involved in the $S_0 - S_3$ electronic transition of MA, along with the coefficients, calculated vertical excitation wavelength, and oscillator strength. Calculations performed at the DFT B3LYP-D3BJ/def2TZVP level of theory.

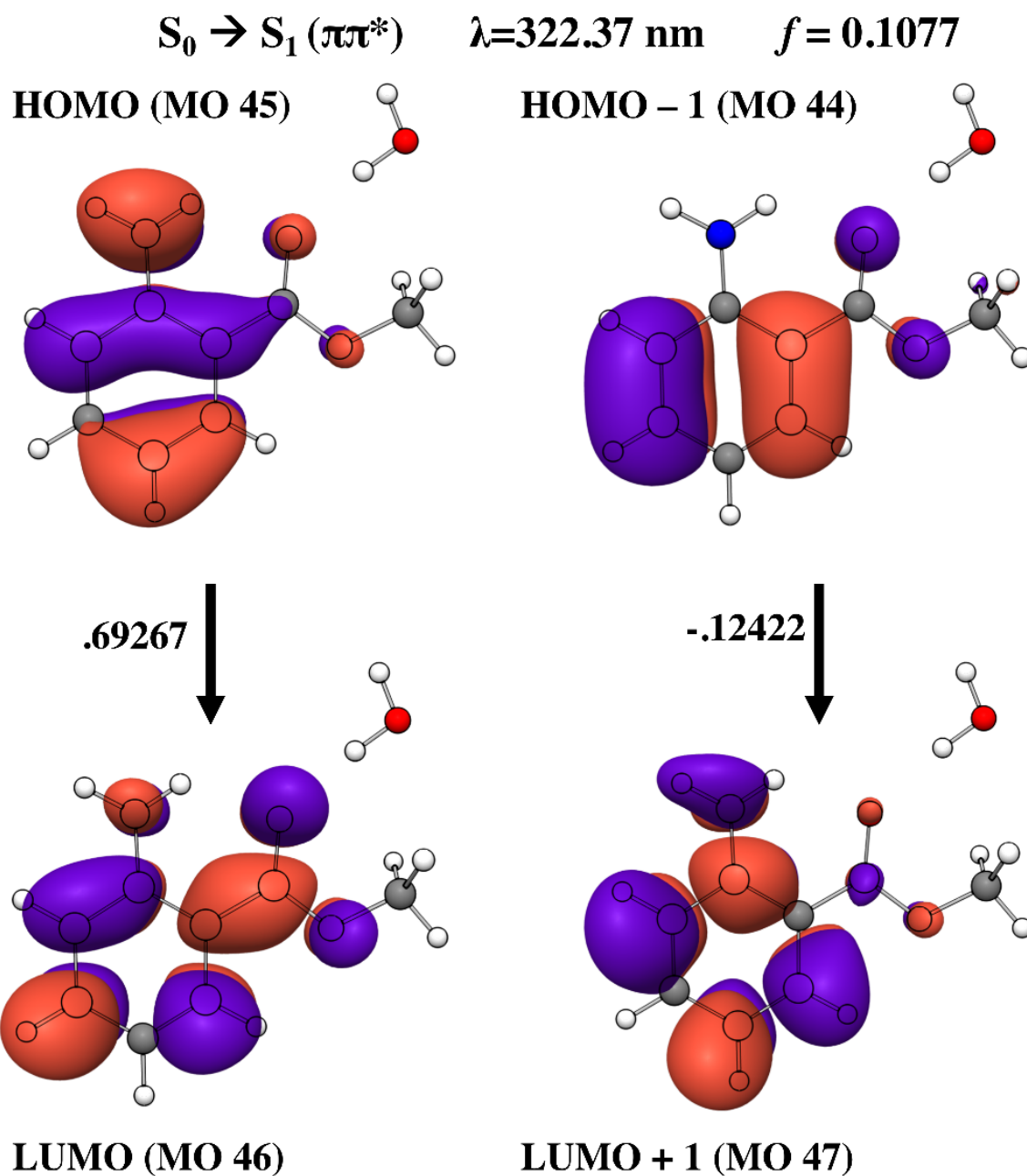


Figure 6.33. Molecular orbitals involved in the $S_0 - S_1$ electronic transition of MA-H₂O, along with the coefficients, calculated vertical excitation wavelength, and oscillator strength. Calculations performed at the DFT B3LYP-D3BJ/def2TZVP level of theory.

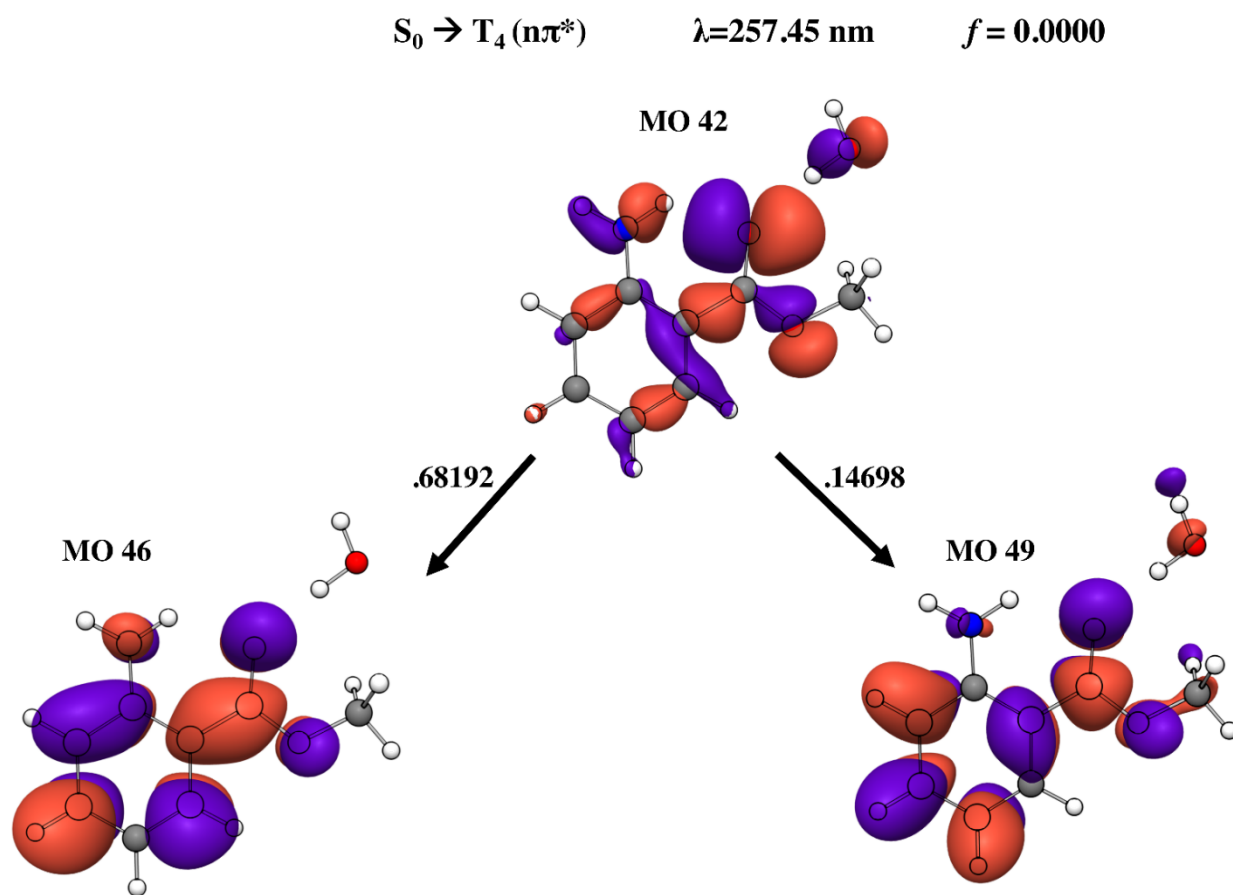


Figure 6.34. Molecular orbitals involved in the $S_0 - T_4$ electronic transition of MA-H₂O, along with the coefficients, calculated vertical excitation wavelength, and oscillator strength. Calculations performed at the DFT B3LYP-D3BJ/def2TZVP level of theory.

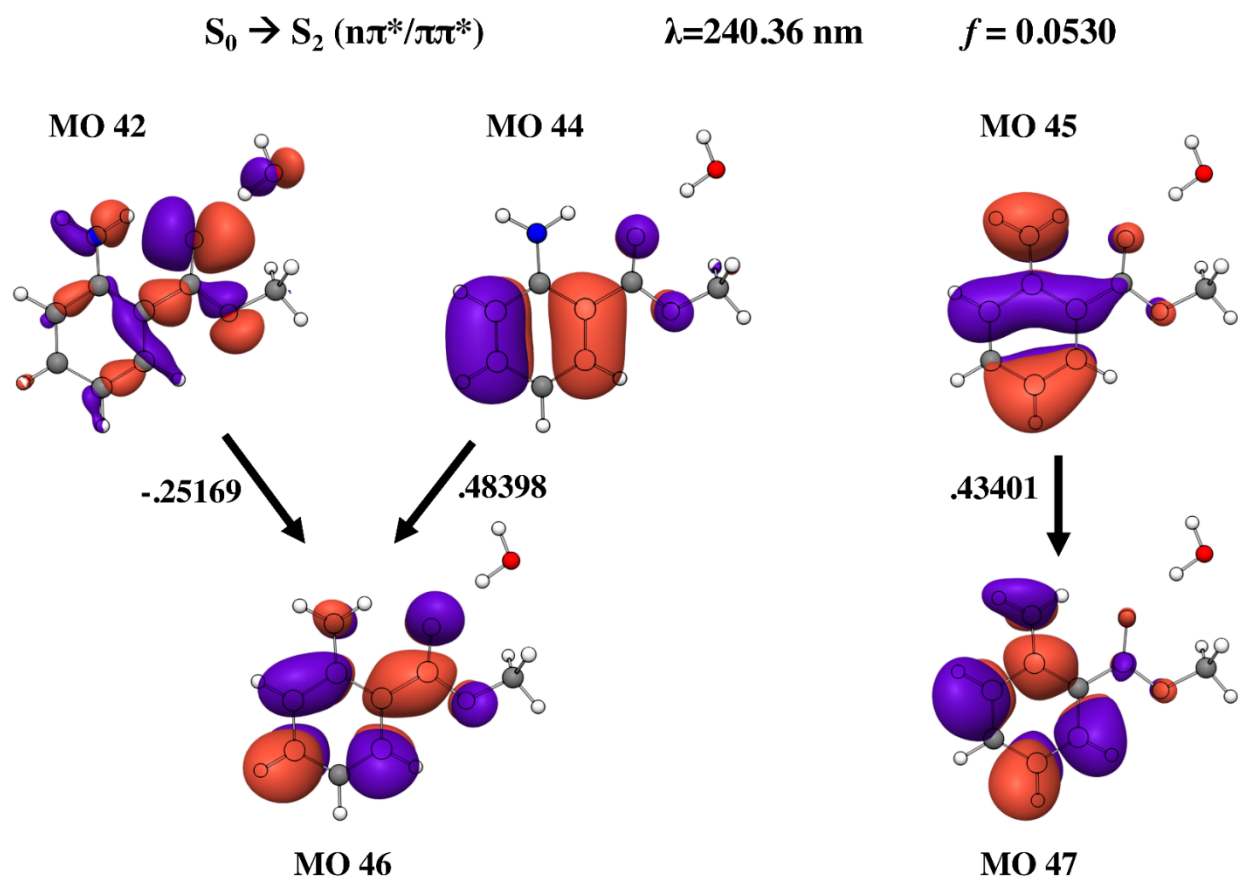


Figure 6.35. Molecular orbitals involved in the $S_0 - S_2$ electronic transition of MA- H_2O , along with the coefficients, calculated vertical excitation wavelength, and oscillator strength. Calculations performed at the DFT B3LYP-D3BJ/def2TZVP level of theory.

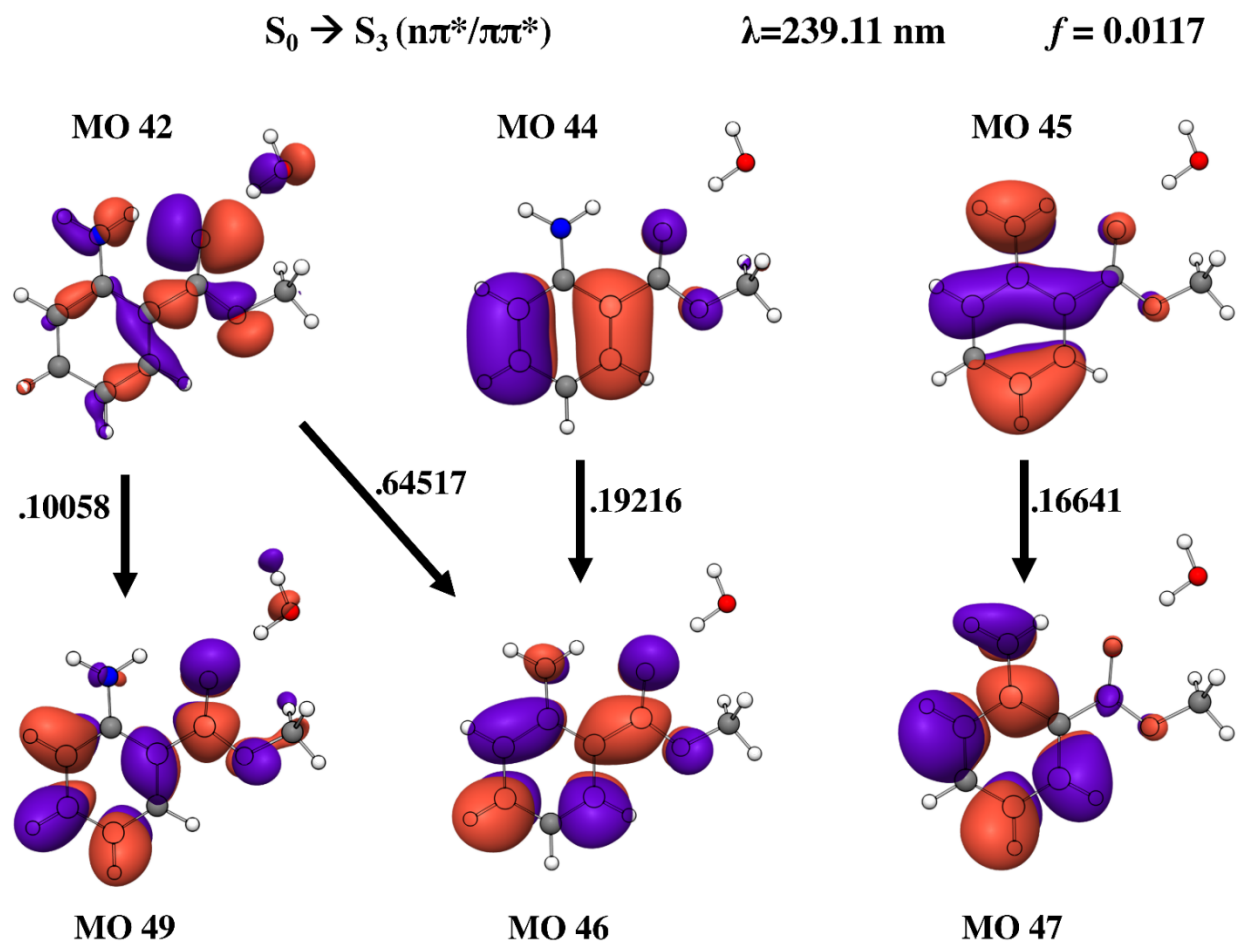


Figure 6.36. Molecular orbitals involved in the $S_0 - S_3$ electronic transition of MA-H₂O, along with the coefficients, calculated vertical excitation wavelength, and oscillator strength. Calculations performed at the DFT B3LYP-D3BJ/def2TZVP level of theory.

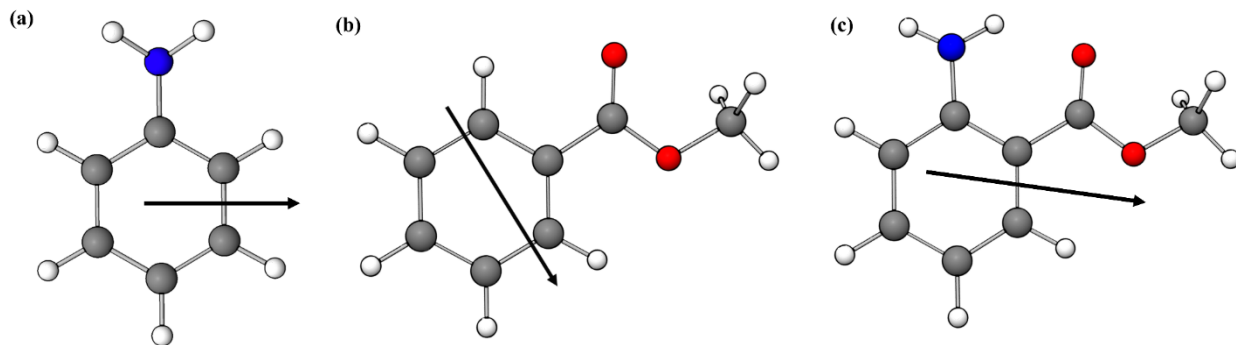


Figure 6.37. Transition dipole moment vectors for the lowest energy “bright” $S_0 - S_n$ electronic transition of (a) aniline ($S_0 - S_1$), (b) methyl benzoate ($S_0 - S_2$), and (c) methyl anthranilate ($S_0 - S_1$).

The lack of formation of long-lived, reactive, triplet state species upon photoexcitation of MA is in accordance with its having the same electronic chromophore as active sunscreen agents. On the other hand, effective sunscreens typically undergo efficient non-radiative decay from the excited state back to the ground state, thereby recycling their UV-absorption capacity. In several of these molecules, excited-state deactivation is thought to be facilitated by H-atom transfer on the S_1 surface^{3, 4, 40}, in some cases followed by transient C=C bond rotation, at which geometries the S_1 and S_0 surfaces meet at a conical intersection.^{5-7, 40-42} Internal conversion, accompanied by hydrogen atom back-transfer, restores the molecule to the ground electronic state configuration. Alternatively, as is thought to be the case with salicylic acid and methyl salicylate, the H-atom transferred excited state may become trapped in a local minimum on the S_1 surface, resulting in Stokes-shifted emission.^{3, 4, 9, 10}

Our characterization of the excited state of MA agrees with results from a recent time-domain study of MA by Rodriguez *et al.* where they presented experimental and computational evidence indicating that a complete hydrogen atom transfer from a region near the S_1 origin is endothermic.¹³ These authors computed a two-step, endothermic (no bound intermediates) pathway toward a conical intersection, involving motion along a 1700 cm^{-1} barrier to an unbound hydrogen atom transfer geometry followed by a 3200 cm^{-1} barrier to ester group (C=C) rotation, at which geometry S_1 and S_0 curves meet at a CI. In a follow up study, they observed damping of time-dependent quantum beat signals upon irradiation centered at 315 nm, at photoexcitation energies $\sim 1,200\text{ cm}^{-1}$ above the H-atom transfer barrier ($2,000\text{ cm}^{-1}$ below the CI barrier), which they attributed to the rapid redistribution of energy via IVR.⁴³ This is in good agreement with our observation of broadened DFL scans occurring in the excited state of MA with only $\sim 800\text{ cm}^{-1}$

excess energy, at which the density of S_1 vibrational states is calculated to be 14 states/cm⁻¹.⁴³ Their time- and our frequency-resolved data indicate that, in the S_0 - S_1 Franck-Condon active region, while the structural changes associated with electronic excitation would seem to facilitate H-atom transfer, there exists no bound intermediate on the excited state surface on which the tautomer product can exist. All of this data is in good agreement with the rarity in which Menthyl Anthranilate is included in modern sunscreens and bolsters the case for rational sunscreen design.

6.5 Conclusion

We have presented the LIF excitation and dispersed fluorescence spectra of methyl anthranilate, leading to assignment of nearly every vibronic transition in the first ~1,000 cm⁻¹ of the excitation and DFL spectra. The observed transitions prove that MA retains C_s symmetry in both its S_0 and S_1 states. The presence of cross-sequence bands in the DFL spectra of MA indicate a high degree of Duschinsky mixing between S_0 and S_1 states involving both out-of-plane and in-plane normal modes. The presence of so many in-plane normal modes in the vibronic spectra indicate a displacement of their respective normal mode coordinates upon electronic excitation, and reflect a significant change in geometry upon electronic excitation. More importantly, the spectrum is dominated by Franck-Condon progressions involving three low-frequency in-plane modes (ν_{33} , ν_{34} , and ν_{36}) that modulate the distance between the NH_2 and CO_2Me groups during their vibrational motion.

A combination of experimental and corroborating computational evidence provides a more detailed picture of this structural change, identifying it as a rocking and re-orientation of the NH_2 and CO_2Me groups that brings them closer to one another, thereby strengthening the six-membered hydrogen bonded ring between the two groups. In particular, upon electronic excitation, the $H\cdots O$ hydrogen bonding distance decreases by 0.203 Å to a value of just 1.723 Å. Since a full H-atom transfer would result in an O-H bond of about 1.0 Å, the 0.20 Å shortening is aptly labeled as a hydrogen-atom dislocation, although it is largely the heavy atoms that rearrange to close the transfer distance, since the $N-H_{\text{donor}}$ bond distance increases by only 0.027 Å. At the same time, the process is far short of a complete hydrogen atom transfer. Indeed, as the UV-D and DFL spectra indicate, in the Franck-Condon active region, the changes in MA associated with electronic excitation are primarily structural and not non-radiative.

We have also presented LIF excitation and 0^0_0 DFL spectra for the MA-H₂O complex. In the assigned structure, the water molecule hydrogen bonds to the ‘back side’ of the C=O group weakening but not disrupting the intramolecular NH \cdots O=C H-bond. As a result, much of the Franck-Condon activity associated with the electronic transition is retained in the complex.

While this chapter has focused attention on the electronic spectroscopy of MA and MA-H₂O, infrared spectroscopy can provide a complementary probe of the pre-reactive structural changes. In fact, the NH, OH, and C=O oscillators serve as sensitive reporters of their local environments. In the next chapter, we build upon our results here by reporting on the hydride stretch and mid-infrared spectra of MA and MA-H₂O in both ground and excited states.

6.6 References

1. A. Beeby and A. E. Jones, *Photochem. Photobiol.*, 2000, **72**, 10-15.
2. T. N. V. Karsili, B. Marchetti, M. N. R. Ashfold and W. Domcke, *J. Phys. Chem. A*, 2014, **118**, 11999-12010.
3. A. L. Sobolewski and W. Domcke, *PCCP*, 2006, **8**, 3410-3417.
4. P. B. Bisht, H. Petek, K. Yoshihara and U. Nagashima, *J. Chem. Phys.*, 1995, **103**, 5290-5307.
5. Y. Peperstraete, M. Staniforth, L. A. Baker, N. D. N. Rodrigues, N. C. Cole-Filipiak, W.-D. Quan and V. G. Stavros, *PCCP*, 2016, **18**, 28140-28149.
6. L. A. Baker, M. D. Horbury, S. E. Greenough, P. M. Coulter, T. N. Karsili, G. M. Roberts, A. J. Orr-Ewing, M. N. Ashfold and V. G. Stavros, *J. Phys. Chem. L.*, 2015, **6**, 1363-1368.
7. N. D. Rodrigues, M. Staniforth and V. G. Stavros, *Proceedings of the Royal Society A: Mathematical, Physical and Engineering Sciences*, 2016, **472**, 20160677.
8. L. A. Baker, B. Marchetti, T. N. Karsili, V. G. Stavros and M. N. Ashfold, *Chem. Soc. Rev.*, 2017, **46**, 3770-3791.
9. L. Heimbroom, J. E. Kenny, B. E. Kohler and G. W. Scott, *The Journal of Physical Chemistry*, 1983, **87**, 280-289.
10. L. A. Heimbroom, J. E. Kenny, B. E. Kohler and G. W. Scott, *J. Chem. Phys.*, 1981, **75**, 5201-5203.
11. J. Zhao, S. Ji, Y. Chen, H. Guo and P. Yang, *PCCP*, 2012, **14**, 8803-8817.
12. T. Raeker and B. Hartke, *J. Phys. Chem. A*, 2017, **121**, 5967-5977.

13. N. D. N. Rodrigues, N. C. Cole-Filipiak, M. D. Horbury, M. Staniforth, T. N. V. Karsili, Y. Peperstraete and V. G. Stavros, *J. Photochem. Photobiol. A: Chem.*, 2018, **353**, 376-384.
14. J. A. Stearns, A. Das and T. S. Zwier, *PCCP*, 2004, **6**, 2605-2610.
15. C. A. Southern, D. H. Levy, G. M. Florio, A. Longarte and T. S. Zwier, *J. Phys. Chem. A*, 2003, **107**, 4032-4040.
16. A. L. Sobolewski and W. Domcke, *J. Phys. Chem. A*, 2004, **108**, 10917-10922.
17. E. A. E.-H. Abou El-Nasr, A. Fujii, T. Yahagi, T. Ebata and N. Mikami, *J. Phys. Chem. A*, 2005, **109**, 2498-2504.
18. S. Leśniewski, P. Kolek, K. Pirowska, A. L. Sobolewski and J. Najbar, *J. Chem. Phys.*, 2009, **130**, 054307.
19. P. Kolek, M. Andrzejak, R. Hakalla and W. Szajna, *J. Phys. Chem. A*, 2018, **122**, 6243-6255.
20. S. Grimme, *J. Comput. Chem.*, 2004, **25**, 1463-1473.
21. S. Grimme, *J. Chem. Phys.*, 2006, **124**, 034108.
22. M. Frisch, G. Trucks, H. Schlegel, G. Scuseria, M. Robb, J. Cheeseman, G. Scalmani, V. Barone, G. Petersson and H. Nakatsuji, *Revision A*, 2016, **3**.
23. G. Zhurko and D. Zhurko, URL: <http://www.chemcraftprog.com>, 2009.
24. P. Butler, D. B. Moss, H. Yin, T. W. Schmidt and S. H. Kable, *J. Chem. Phys.*, 2007, **127**, 094303.
25. R. S. Mulliken, *J. Chem. Phys.*, 1955, **23**, 1997-2011.
26. D. F. Plusquellic, R. Suenram, B. Mate, J. Jensen and A. Samuels, *J. Chem. Phys.*, 2001, **115**, 3057-3067.
27. F. Duschinsky, *Acta Physicochim. URSS*, 1937, **7**, 551-566.
28. C. W. Muller, J. J. Newby, C.-P. Liu, C. P. Rodrigo and T. S. Zwier, *PCCP*, 2010, **12**, 2331-2343.
29. J. B. Hopkins, D. E. Powers and R. E. Smalley, *J. Chem. Phys.*, 1980, **72**, 5039-5048.
30. J. B. Hopkins, D. E. Powers, S. Mukamel and R. E. Smalley, *J. Chem. Phys.*, 1980, **72**, 5049-5061.
31. C.-P. Liu, J. J. Newby, C. W. Müller, H. D. Lee and T. S. Zwier, *J. Phys. Chem. A*, 2008, **112**, 9454-9466.

32. K. N. Blodgett, J. L. Fischer, D. Sun, E. L. Sibert III and T. S. Zwier, *Manuscript In Preparation*, 2019.
33. J. R. Henderson, M. Muramoto and R. A. Willett, *J. Chem. Phys.*, 1964, **41**, 580-581.
34. N. Mikami, A. Hiraya, I. Fujiwara and M. Ito, *Chem. Phys. Lett.*, 1980, **74**, 531-535.
35. M. Quack and M. Stockburger, *J. Mol. Spectrosc.*, 1972, **43**, 87-116.
36. E. R. T. Kerstel, M. Becucci, G. Pietraperzia, D. Consalvo and E. Castellucci, *J. Mol. Spectrosc.*, 1996, **177**, 74-78.
37. J. H. Brophy and C. T. Rettner, *Chem. Phys. Lett.*, 1979, **67**, 351-355.
38. J. T. Meek, E. Sekreta, W. Wilson, K. Viswanathan and J. P. Reilly, *J. Chem. Phys.*, 1985, **82**, 1741-1749.
39. S. Kamei, H. Abe, N. Mikami and M. Ito, *The Journal of Physical Chemistry*, 1985, **89**, 3636-3641.
40. T. N. Karsili, B. Marchetti, M. N. Ashfold and W. Domcke, *J. Phys. Chem. A*, 2014, **118**, 11999-12010.
41. K. Yamazaki, Y. Miyazaki, Y. Harabuchi, T. Taketsugu, S. Maeda, Y. Inokuchi, S.-n. Kinoshita, M. Sumida, Y. Onitsuka and H. Kohguchi, *J. Phys. Chem. L.*, 2016, **7**, 4001-4007.
42. S.-n. Kinoshita, Y. Miyazaki, M. Sumida, Y. Onitsuka, H. Kohguchi, Y. Inokuchi, N. Akai, T. Shiraogawa, M. Ehara and K. Yamazaki, *PCCP*, 2018, **20**, 17583-17598.
43. N. d. N. Rodrigues, N. C. Cole-Filipiak, K. N. Blodgett, C. Abeysekera, T. S. Zwier and V. G. Stavros, *Nature Communications*, 2018, **9**, 5188.

CHAPTER 7. THE MISSING NH STRETCH FUNDAMENTAL IN S₁ METHYL ANTHRANILATE: IR-UV DOUBLE RESONANCE EXPERIMENTS AND LOCAL MODE THEORY

7.1 Introduction

Excited state intramolecular hydrogen atom (or proton) transfer followed by internal conversion and subsequent hydrogen atom back-transfer is the regenerative mechanism by which many UV-absorbing sunscreen agents are understood to act.¹⁻⁷ Alternatively, as is the case for salicylic acid and its derivatives, excited state H-atom transferred products can undergo radiative decay to the ground state, which is detectable by its characteristic Stokes-shifted emission.^{2, 3, 8, 9}

Rather than full H-atom transfer, anthranilic acid (AA) has been described as undergoing hydrogen atom dislocation in the S₁ electronic state. This process is characterized by the strengthening of the 6-membered intramolecular HNH \cdots O=C hydrogen bond and was initially diagnosed in 2004 by Southern *et al.* via AA's infrared (IR) spectrum in the hydride stretch region.¹⁰ The authors reported that the coupled NH₂ group vibrations in S₀ appeared to uncouple from one another in S₁ and present as a 'free' NH stretch (3460 cm⁻¹) and a weak, broadened, redshifted 'dislocated' NH stretch centered at 2900 cm⁻¹. Shortly after, Sobolewski *et al.* published time-dependent density functional theory (TD-DFT) harmonic vibrational frequencies in the S₀ and S₁ electronic states of AA.¹¹ The S₁ frequencies agreed well with the experimental values, but the dislocated NH stretch intensity was calculated to be orders of magnitude larger than its experimentally assigned value. This intensity mismatch persists, with a recent computational study by Egidi *et al.* using second-order vibrational perturbation theory (VPT2) to calculate the excited state IR spectrum of AA, yielding qualitatively similar results.¹²

In Chapter 6 we presented results on the vibronic spectroscopy of jet-cooled methyl anthranilate (MA), the methyl ester of AA, and its water complex (MA-H₂O).¹³ Long Franck-Condon progressions of in-plane modes indicate significant heavy-atom rearrangement between the S₀ and S₁ electronic states. Accompanying these large geometry changes are extensive Duschinsky mixing involving both the in-plane and out-of-plane vibrations. Corroborating computational evidence (TD-DFT B3LYP-D3BJ/def2TZVP) indicates that the 6-membered HNH \cdots O=C hydrogen bond distance decreases by 0.203 Å (from 1.926 Å to 1.723 Å). Figure 7.1 presents the assigned, calculated S₁ geometries of MA and MA-H₂O, labelled with important

structural parameters and their changes from S_0 (shown in parentheses). The strengthening of the H-bond is facilitated by extensive reorientation of the NH_2 and CO_2Me groups. These structural parameters are similar to those calculated for AA.^{11, 12, 14}

In this chapter we expand upon the results presented in the previous chapter by presenting the ground and excited state IR spectrum of MA and MA-H₂O in the hydride stretch (2400-3800 cm^{-1}) and mid-IR (1400-1800 cm^{-1}) regions. With firm structural assignments in hand, we further characterize the H-atom dislocation from both the donor and acceptor's perspective. Using a local mode Hamiltonian in conjunction with DFT frequency calculations, we firmly assign all IR transitions the hydride stretch region in the S_0 and S_1 states of MA and MA-H₂O. With all transitions accounted for, we propose a novel explanation for the discrepancy between experimental and calculated intensity of the dislocated NH stretch transition, based on the adiabatic separation of the NH stretch and other internal coordinates.

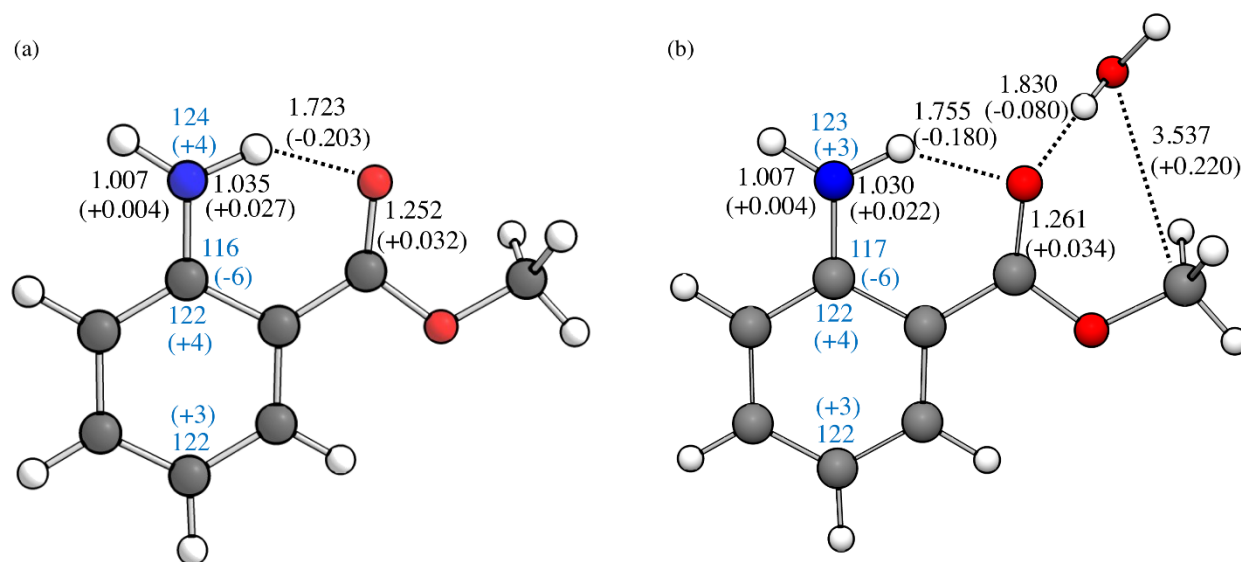


Figure 7.1. S_1 excited state optimized geometries of (a) methyl anthranilate and (b) its water complex. Bond distances are labelled in black text and angles in blue text. Changes in these parameters from their ground state values are shown in parentheses. Adapted from *Phys. Chem. Chem. Phys.*, 2019, 21, 21355 by permission of the PCCP Owner Societies.

7.2 Experimental Methods

Methyl anthranilate (MA) was purchased from Sigma-Aldrich ($\geq 99\%$ purity) and used without further purification. MA was seeded in Helium and pulsed (Parker General Valve Series 9) into a vacuum chamber, resulting in a free jet expansion. Trace water in the sample was sufficient for producing water complex population for fluorescence measurements while $\sim 5\%$ water was flowed over the $\sim 65^\circ\text{C}$ heated MA reservoir to create sufficient MA-H₂O complexes for ionization measurements. Both the laser-induced fluorescence and laser ionization/time-of-flight mass spectrometer chambers used to collect data have been described previously.^{15, 16} UV light was generated with nanosecond Nd:YAG pumped dye lasers (Radiant Dyes NarrowScan and Lambda Physik ScanMate Pro), while a Nd:YAG pumped KTA based optical parametric converter (LaserVision) was used as the tunable IR source.

Species-specific infrared spectra in the hydride stretch region ($2400\text{--}3800\text{ cm}^{-1}$) were recorded using fluorescence dip infrared (FDIR) spectroscopy.¹⁷ Collection of a ground state FDIR spectrum requires a scanning IR holeburn laser (10 Hz) and a UV probe laser (20 Hz) which is fixed on some intense vibronic transition. The IR laser temporally precedes ($\sim 100\text{ ns}$) the UV laser so that when the IR laser is resonant with the same species as the UV laser, population is removed from the ground state vibrational zero-point level, producing a depletion in the fluorescence intensity. Plotting the fluorescence depletion as a function of IR wavelength yields the ground state FDIR spectrum. Collection of excited-state FDIR spectra requires different laser timings. In this scheme, the fixed UV laser precedes the scanning IR laser by $\sim 10\text{ ns}$. When the IR laser is resonant with a vibrational transition of the electronically excited molecule, the rate of non-radiative decay is increased relative to that of the initially excited level, resulting in a dip in fluorescence signal. The excited-state FDIR spectrum results from plotting the fluorescence depletion against the IR wavelength.

Species-specific infrared spectra in the mid-IR region ($1400\text{--}1800\text{ cm}^{-1}$) were recorded using resonant ion-dip infrared (RIDIR) spectroscopy.¹⁷ The scheme for collecting ground state RIDIR spectra is nearly identical to that for collecting the corresponding FDIR spectra, except ion signal instead of fluorescence is measured. The ionization potential of MA and MA-H₂O are such that a second shorter wavelength laser is needed to ionize out of the prepared electronically excited states. Maximum ion signal is obtained with temporally overlapped UV lasers. Collection of excited state RIDIR spectra requires the temporal separation of the excitation and ionization laser

by ~ 16 ns so that the scanning IR laser can arrive between them. When the IR laser is resonant with an excited state vibrational transition the molecule access levels that decrease the ionization efficiency, *e.g.* through internal conversion or dissociation. When this occurs, fewer ions are generated, resulting in a dip in ion signal.

7.3 Computational Methods

Standard harmonic and anharmonic vibrational frequency calculations were performed with Gaussian16¹⁸ via (TD-)DFT using the B3LYP hybrid functional in conjunction with Grimme's dispersion correction (version D3)¹⁹, Becke-Johnson damping²⁰, and the def2TZVP basis set. Frequencies in the amide I and II regions (1400-1800 cm^{-1}) were scaled by a factor of 0.984 and compared directly with experiment.

The theoretical results include both ground and excited state calculations of the XH stretch vibrations (X=N, C, and O). We group the calculations into two areas. In the first, we apply a local model Hamiltonian with extensions for the descriptions of the NH and OH stretches in order to describe the vibrational band positions and make comparisons with experiment. In the second we develop models for the missing NH stretching vibration predicted to occur around 2900 cm^{-1} in normal mode and VPT2 calculations.

7.3.1 Description of the Local Mode Hamiltonians

We model the CH stretch region of the IR spectra following the method of Tabor *et al.*²¹ In this approach localized CH stretch vibrations are coupled via a 2:1 Fermi resonances to scissor vibrations. The localization of these modes follows from taking suitable linear combinations of the normal modes. The frequencies of these modes are then scaled, where the scale factor depends on the level of theory used in the electronic structure normal mode calculation. Select anharmonic terms, calculated for a model system, are added to the Hamiltonian. These terms lead to shifts and couplings between stretch states with one quantum of excitation and scissor states with two quanta of excitation. The dipole moment is taken as the linear dipole moment calculated *ab initio*. We expand on these steps in the paragraphs below.

We refer to the localized coordinates as localized normal coordinates as these coordinates are obtained directly from the normal coordinates \mathbf{Q} via an orthogonal transformation, $\mathbf{R} = \mathbf{A}\mathbf{Q}$.

The matrix \mathbf{A} is constructed in several steps. Using the stretches as an example, if there are N CH stretches, there will also be N normal modes that are predominantly admixtures of these CH stretches. Typically, these modes have frequencies that span a narrow enough frequency range that no other molecular motions contribute to these normal modes. We find a localized mode, associated with each CH, stretch by carrying out a normal mode calculation in which all the H atom masses are increased by a factor c , except for the H mass of the CH being localized. This mass retains its original value. In this calculation there will be a single normal mode that corresponds to a localized a CH stretch. The process is repeated for each of the N stretches in order to find N CH localized normal modes, \mathbf{Q}' . These modes are expressed as linear combinations of the original normal coordinates $\mathbf{Q}' = \mathbf{L}\mathbf{Q}$ with minor contributions from lower frequency modes.

Since the rows of \mathbf{L} are calculated from distinct normal mode calculations, this matrix is not orthogonal. It can be well approximated as an orthogonal matrix as follows. Calculating the overlap $\mathbf{S} = \mathbf{L}^T\mathbf{L}$ and solving for $\mathbf{S}^{-1/2}$ we find the desired localized coordinates $\mathbf{R} = \mathbf{L}\mathbf{S}^{-1/2}\mathbf{Q} \equiv \mathbf{A}\mathbf{Q}$ that describe the CH stretch vibrations. The resulting Hamiltonian is given by

$$H = \frac{1}{2}\sum_{i=1}^N P_i^2 + \frac{1}{2}\sum_{i=1}^N F_{ij}R_iR_j \quad (1)$$

where the F_{ij} elements are obtained by transforming the Hessian obtained from electronic structure calculations. If the normal mode force constants are given as f_{ii} , then $\mathbf{F} = \mathbf{A}\mathbf{f}\mathbf{A}^T$.

To account for diagonal anharmonicity and the modest level of theory, the frequencies of the uncoupled normal modes are then scaled, where the scale factor depends on the level of theory used in the electronic structure normal mode calculation. Select anharmonic terms, calculated for a model system, are added to the Hamiltonian. These terms lead to shifts and couplings between stretch states with one quantum of excitation and scissor states with two quanta of excitation. The dipole moment is taken as the linear dipole moment calculated *ab initio*.

The scaling factors of the OH stretches in the MA-H₂O complex were obtained by scaling the localized normal mode frequencies to best match the local mode OH stretch fundamentals obtained from the Paesani water potential for the book conformer of (H₂O)₆. To obtain these latter energies, which are based on a potential of CCSD(T)/pVTZ quality, we calculated sixth-order three-dimension stretch-bend localized normal coordinate force fields for each water molecule of the book conformer, constraining the remaining degrees of freedom to the equilibrium geometries.

We then carried out 4th order CVPT calculations to obtain effective Hamiltonians describing the anharmonic OH stretches, the scissor overtones, and the coupling between them. We denote the 12 transition energies of the OH stretches as $\tilde{\nu}^P$. We then calculated the 12 localized normal coordinate transition energies $\tilde{\nu}_{\text{local,calc}}$ for the book conformer at the harmonic level using the b3lyp/def basis set whose results we wish to scale. The scale factors are obtained via a least squares fit, $\tilde{\nu}_{\text{local,f}} = A\tilde{\nu}_{\text{local,calc}} + B$, to obtain the best fit to the $\tilde{\nu}^P$ values. The fit parameters are $A=.8464$ and $B=457.4 \text{ cm}^{-1}$.

The NH stretch fundamentals were scaled by a multiplicative factor of .957 to match the NH stretch fundamentals ($3390/3540 \text{ cm}^{-1}$) of the S_0 state of the monomer. These frequencies were used as input to the local mode model described above.

7.3.2 Theoretical Modeling of the NH Stretch Fundamentals

As we shall see, the differences between the theoretical and experimental results for the hydrogen bonded NH stretch are profound at the harmonic level. These differences persist even when anharmonicities are taken into account. Studies of anthranilic acid (AA) provide a good point of comparison. AA has a carboxylic acid group (COOH) that becomes a methyl ester in methyl anthranilate (COOMe). Second order perturbation studies of the vibrations on the S_1 electronic state have been carried out by Egidi et al.¹² These calculations, based on TDDFT with a B3LYP/SSND basis, predict a very intense H-bonded NH stretch peak around 2800 cm^{-1} . The authors note the discrepancy between theory and experiment, and point to the need for further studies. In this work we consider two theoretical approaches that extend beyond the perturbative approach in order to examine the role of anharmonic effects. These studies include an adiabatic treatment of the NH stretch and a reduced two-dimension grid-based study of the NH stretch-bend coupling.

NH Stretch Vibrationally Adiabatic Surface Determination

To find the adiabatic surfaces for the NH stretch vibrational levels, we use optimization approaches similar to those used in electronic structure theory. In such calculations, one inputs an initial geometry and then searches for a minimum using gradients and, if needed, second derivatives. The only difference here is that the NH stretch is also treated quantum mechanically.

In order to calculate the forces and the Hessian, for a given geometry, we use an electronic structure program to provide

$$F_i = -\frac{\partial V}{\partial x_i}; \quad H_{ij} = \frac{\partial^2 V}{\partial x_i \partial x_j}. \quad (2)$$

The forces and Hessian are transformed to a set of internal coordinates $\mathbf{x}=\mathbf{B}^{-1}\mathbf{S}$ that are comprised of stretches, angles, and dihedral angles. The elements of the B-inverse matrix $B_{ki}^{-1} = \frac{\partial x_k}{\partial S_i}$ and its higher order derivatives follow from the geometrical transformation between the internal coordinates in a given body-fixed frame and the Cartesian coordinates. Calculating these elements using finite difference methods, we determine the internal forces

$$f_i = -\frac{\partial V}{\partial S_i} = -\sum_k \frac{\partial x_k}{\partial S_i} \frac{\partial V}{\partial x_k} \quad (3)$$

and Hessian

$$h_{ij} = \frac{\partial^2 V}{\partial S_i \partial S_j} = -\sum_k \frac{\partial^2 x_k}{\partial S_i \partial S_j} F_k + \sum_{kl} \frac{\partial x_k}{\partial S_i} \frac{\partial x_l}{\partial S_j} H_{kl}. \quad (4)$$

We assume that $R=S_l$ corresponds to the NH stretch of interest and use Eqs. (3) and (4) to expand the potential to second-order in the remaining internal extension coordinates

$$V(R, S) = V(R) - \sum_i f_i(R)S_i + \frac{1}{2} \sum_{ij} h_{ij}(R)S_i S_j. \quad (5)$$

Here the summations are from $i=2$ to $3N-6$ where N is the number of atoms. In order to obtain the variables of Eq. (5) as a function of R , we carry out electronic structure calculations of the energy, force and Hessian keeping all the internal coordinates fixed except for R . This internal coordinate is evaluated at a set of equally space grid points that form the basis of a subsequent discrete variable representation (DVR) calculation. We solve for the NH stretch eigenfunctions by carrying out this DVR calculation using the stretch Hamiltonian

$$[\hat{T}_R + V(R, S = 0)]\Psi_n(R) = E_n(S)\Psi_n(R). \quad (6)$$

Here the kinetic contribution uses the reduced mass of the NH oscillator.

In order to minimize the energy $E_n(\mathbf{S})$ with respect to the remaining degrees of freedom for a given value of n , we calculate the Hellman-Feynman forces

$$\frac{\partial E_n}{\partial S_j} = \int dR \Psi_n \frac{\partial \hat{H}}{\partial S_j} \Psi_n = f_{nn}^j \quad (7)$$

where

$$f_{nm}^j = \int dR \Psi_n f_j(R) \Psi_m. \quad (8)$$

These matrix elements are easily evaluated in the DVR representation by summing over the contributions at the DVR points. The components of this calculation are shown in Figure 7.2 for the force along the CNH angle and the first excited state of the NH stretch.

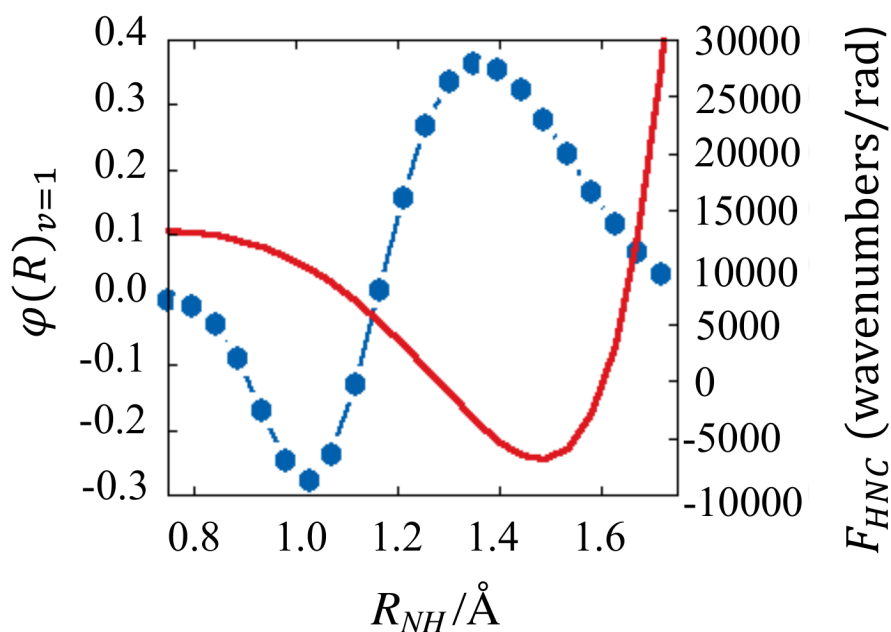


Figure 7.2. The $\Psi_1(R)$ wavefunction of Eq. (6) plotted as a function of NH stretch bond length R (in angstroms). Remaining coordinates are chosen to minimize the energy corresponding to this state. The points correspond to the centers of the DVR sinc functions used in the minimization. The solid red line is the force along the HNC angle in $\text{cm}^{-1}/\text{rad}$ as a function of R .

Combining these first derivatives with similarly calculated second derivatives allows us to estimate the changes in the values of the internal coordinates that minimize the NH stretch energy. In practice we had to repeat this process 11 times in order to find the minimum, due to the presence of higher order terms not included in Eq. (5). Figure 7.2 shows the components of Eq. (8) that are needed to carry out the integration in the DVR. The figure shows results for the second-to-last step in the minimization process. For this step, the expectation value of the force along the HNC angle with respect to $\Psi_1(R)$ has been reduced to $60 \text{ cm}^{-1}/\text{rad}$. This small residual force led to predicted shift in the HNC angle of only $.0008 \text{ rad}$. In the subsequent step of the minimization these two values reduce to an average force of $1.4 \text{ cm}^{-1}/\text{rad}$ and a predicted step size of $.00001 \text{ rad}$ so the calculation was assumed to be converged. All other average forces at the minimum were smaller in magnitude. The noteworthy feature of the figure is that the force is highly nonlinear over the large expanse of the NH stretch coordinate for which the wave function has appreciable amplitude.

Description of the Reduced-Dimension Stretch-Bend Hamiltonian

The mode most strongly coupled to the NH stretch is the contiguous CNH bend. We solved the Schrodinger equation for these two degrees of freedom assuming that the remaining coordinates are constrained to the geometry that minimizes the $v_{\text{NH}} = 0$ state following the procedure described above. The eigenfunctions and eigenvalues are obtained using a two-dimensional DVR calculation following the procedure outlined by Luckhaus.²² When focusing on the S_1 state NH stretch transitions, the input data for the calculation are the potential points for the S_1 surface calculated on a 20×20 grid of points obtained at the B3LYP/6-311++(d,p) level of theory with Grimme's empirical dispersion.¹⁹ The g-matrix elements are evaluated numerically at each of these points. The advantage of the Luckhaus approach is that it allows us to incorporate the coordinate dependence of the g-matrix in a straightforward way as well as include the stretch-bend couplings in the kinetic energy contribution to the Hamiltonian.

7.4 Results

7.4.1 Methyl Anthranilate Monomer

The assigned FDIR spectra in the hydride stretch region of MA in the ground electronic states is shown in Figure 7.3a. Three distinct sets of fundamental vibrational transitions appear, due to the NH₂, aromatic CH, and methyl CH stretches, the last of which is replete with 2:1 Fermi resonance contributions with the CH scissor overtones. The stick diagram below the experimental spectrum displays the results of the local mode anharmonic modeling. The match between experiment and theory is excellent, with an average error of 4 cm⁻¹. Assigned experimental and calculated frequencies for methyl anthranilate can be found in Table 7.1.

Table 7.1. Select experimental and theoretical frequencies of methyl anthranilate

<i>S</i> ₀			<i>S</i> ₁		
<i>exp/cm</i> ⁻¹	<i>calc/cm</i> ⁻¹	<i>assignment</i>	<i>exp/cm</i> ⁻¹	<i>calc/cm</i> ⁻¹	<i>assignment</i>
3540	3543 [†] (3540 [*])	NH ₂ AS stretch	3457	3482 [†] (3483 [*])	'free' NH stretch
3390	3388 [†] (3387 [*])	NH ₂ SS stretch	2600-2800	2991 [†] (2991 [*]) (2761 ^{**})	'dislocated' NH stretch
3029	3031 [†] (3021 [*])	CH ₃ FR	3016	3018 [†] (3007 [*])	CH ₃ FR
3002/2995	3000 [†] (2989 [*])	CH ₃ FR	2983	2981 [†] (2970 [*])	CH ₃ FR
2962	2958 [†] (2924 [*])	CH ₃ FR	2956	2950 [†] (2912 [*])	CH ₃ FR
2919	2917 [†]	CH ₃ FR	2914	2916 [†]	CH ₃ FR
2913	2913 [†]	CH ₃ FR	-	2909 [†]	CH ₃ FR
2904	2900 [†]	CH ₃ FR	2896	2899 [†]	CH ₃ FR
2896	2894 [†]	CH ₃ FR	-	2886 [†]	CH ₃ FR
2889	2884 [†]	CH ₃ FR	2880	2878 [†]	CH ₃ FR
2856	2849 [†]	CH ₃ FR	2845	2844 [†]	CH ₃ FR
1720	1697 [*]	C=O stretch	1637	1636 [*]	C=O stretch
1632	1632 [*]	NH ₂ bend	1557	1535 [*]	NH ₂ bend

* scaled harmonic frequency

** anharmonic frequency

[†] frequency from local mode model

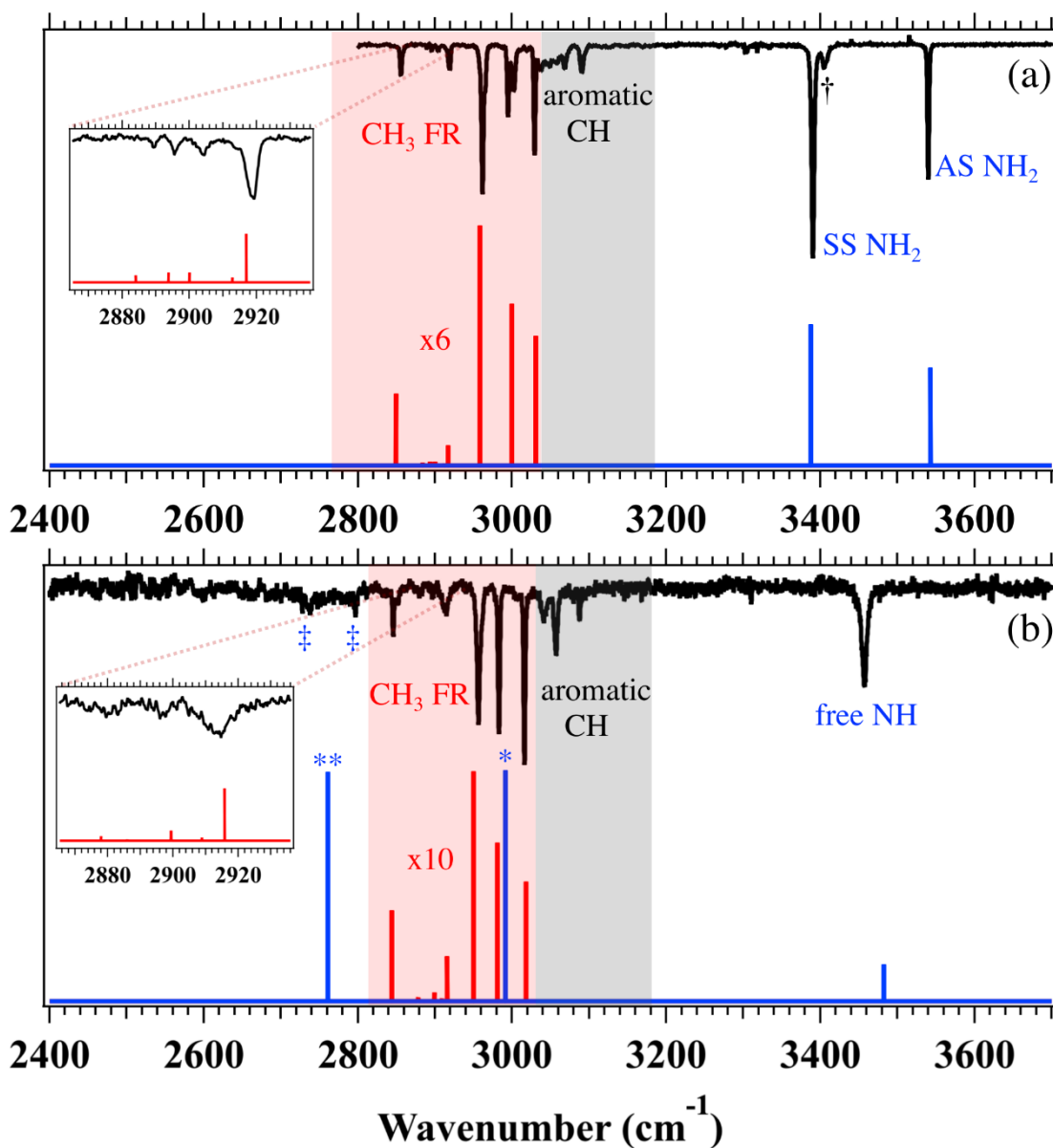


Figure 7.3. (a) Ground and (b) S_1 excited state FDIR spectra from 2400 - 3700 cm^{-1} of methyl anthranilate. The spectra are divided into four regions: NH stretch, aromatic CH stretch (shaded in grey), CH₃ stretch (shaded in red), and low frequency. The experimental spectrum (black trace) is compared with the predictions of local mode modeling (unmarked stick spectra) in both electronic states. In both states the red stick spectra corresponding to the CH₃ Fermi-mixed transitions have been multiplied by a scale factor for a more ready comparison with experiment. The blue stick in (b) with a single asterisk at 2991 cm^{-1} is the calculated harmonic dislocated NH stretch while the blue stick marked with a double asterisk at 2761 cm^{-1} is the calculated standard anharmonic dislocated NH stretch transition. See text for further discussion.

The bands at 3540 and 3390 cm^{-1} are assigned to the coupled NH stretch modes of the NH_2 group. In the ground state, these two fundamentals are best described as asymmetric and symmetric stretch fundamentals, respectively, despite the presence of the H-bond involving one of the NH bonds. In aniline, the unperturbed SS and AS fundamentals appear at 3508 and 3422 cm^{-1} , respectively.²³

The weak transition just on the high frequency side of the symmetric stretch NH_2 fundamental (marked with a dagger) is likely the result of a 2:1 Fermi resonance between the NH_2 SS fundamental and the C=O stretch overtone. The transitions from $\sim 3030 - 3100 \text{ cm}^{-1}$ belong to aromatic CH stretch transitions, which are coupled via resonances with ring CH bend modes. We have made no attempt to fit this region of the spectrum.

The remaining peaks (shaded in red) in the spectrum are due to Fermi resonance mixed methyl CH stretch transitions. Note the excellent fit between experiment and the local mode theory (Sec. III.A). That the intensity of this region of the spectrum is comparable to the NH stretch region is due to saturation effects at the IR laser powers used to record the spectra.

Figure 7.3b shows the S_1 state FDIR spectrum over the 2400-3700 cm^{-1} region. The high frequency region differs substantially from that of the ground state. We observe a single band at 3457 cm^{-1} with a FWHM of 8 cm^{-1} , nearly double the width of the ground state NH stretch transitions. S_1 normal mode calculations at the B3LYP-D3BJ/def2TZVP level indicate that this vibration is localized almost entirely on the free NH bond, indicating that the NH_2 group vibrations have almost completely decoupled from one another due to the $\text{NH}\cdots\text{O}=\text{C}$ H-bond. The intense transition just below 3000 cm^{-1} in blue in Figure 7.3b (single asterisk) is that predicted for the H-bonded, ‘dislocated’ NH stretch fundamental in S_1 by harmonic calculations at the same level of theory (with the same scale factor as for the free NH stretch). When standard corrections due to anharmonicity are included, the frequency of this transition is lowered to 2761 cm^{-1} (double asterisk), with no scale factor applied. In both cases, this transition is calculated to be more than ten times more intense than all other transitions in the region.

Notably, all the peaks in the methyl CH stretch region (2800-3000 cm^{-1} , red sticks) are firmly assigned to the methyl group by the CH stretch local mode Fermi resonance model. The ability of the model to account quantitatively for all observed transitions in this region makes the absence of a high intensity experimental NH stretch transition all the more conspicuous. While the region from 2400 - 2800 cm^{-1} does contain some broad, weak bands (marked with blue double

daggers), we note the absence of a well-resolved intense transition. We return to this point later in the discussion.

The S_0 and S_1 -state IR spectra of MA in the 1400 - 1800 cm^{-1} regions are shown in Figure 7.4a and 4b, respectively. We anticipate the presence of strong IR transitions in this region due to the C=O stretch and NH_2 scissor fundamentals. In the ground electronic state, the carbonyl stretch fundamental appears as the intense peak at 1721 cm^{-1} , while the NH_2 bend is observed at 1632 cm^{-1} .¹ Already in the ground state, these transitions appear at frequencies that reflect a substantial $\text{NH}\cdots\text{O}=\text{C}$ H-bond, lowering the frequency of the ester C=O stretch fundamental and raising the frequency of the NH_2 bend relative to their counterparts in the absence of a hydrogen bond between them. For instance, the corresponding C=O stretch and NH_2 bend transitions in benzoic acid (free C=O group) and aniline (free NH_2 group) are at 1752 and 1623 cm^{-1} , respectively.²⁴⁻²⁷

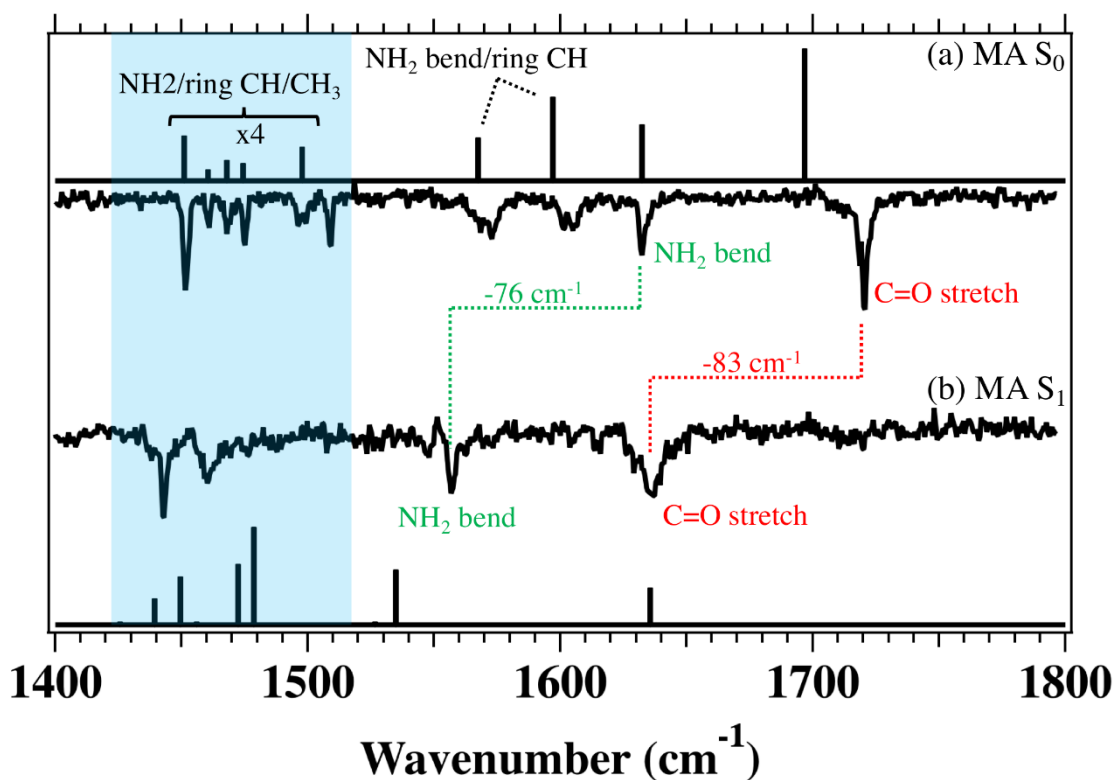


Figure 7.4. (a) Ground and (b) S_1 excited state RIDIR spectra from 1400 - 1800 cm^{-1} of methyl anthranilate. The calculated scaled harmonic normal mode frequencies (black stick spectra) are compared with experiment. See text for further discussion.

The excited state spectrum shows a broadened C=O stretch transition at 1637 cm^{-1} , shifted 83 cm^{-1} lower in frequency than its ground state counterpart. The NH₂ bend shows a similar redshift of 76 cm^{-1} to 1557 cm^{-1} in S₁. While captured by the calculations, the shift of the NH₂ bend to lower frequency upon $\pi\pi^*$ excitation is surprising, because the NH₂ group is engaged in a stronger H-bond to C=O in the S₁ state, which typically would raise the frequency of the NH₂ bend. These substantial frequency shifts upon electronic excitation reflect both the extensive heavy-atom rearrangement and subsequent change in hydrogen bonding strength from both the acceptor and donor's point of view, both of which are facilitated by the shifting electronic charge upon excitation. Figure 7.5 presents the calculated change in electrostatic potential mapped onto the surface of increasing electron density in going from S₀ to S₁. The carbonyl oxygen picks up substantial negative charge and electron density while the nitrogen picks up positive charge. These combined effects result in a substantial increase in hydrogen bond strength on the S₁ surface.

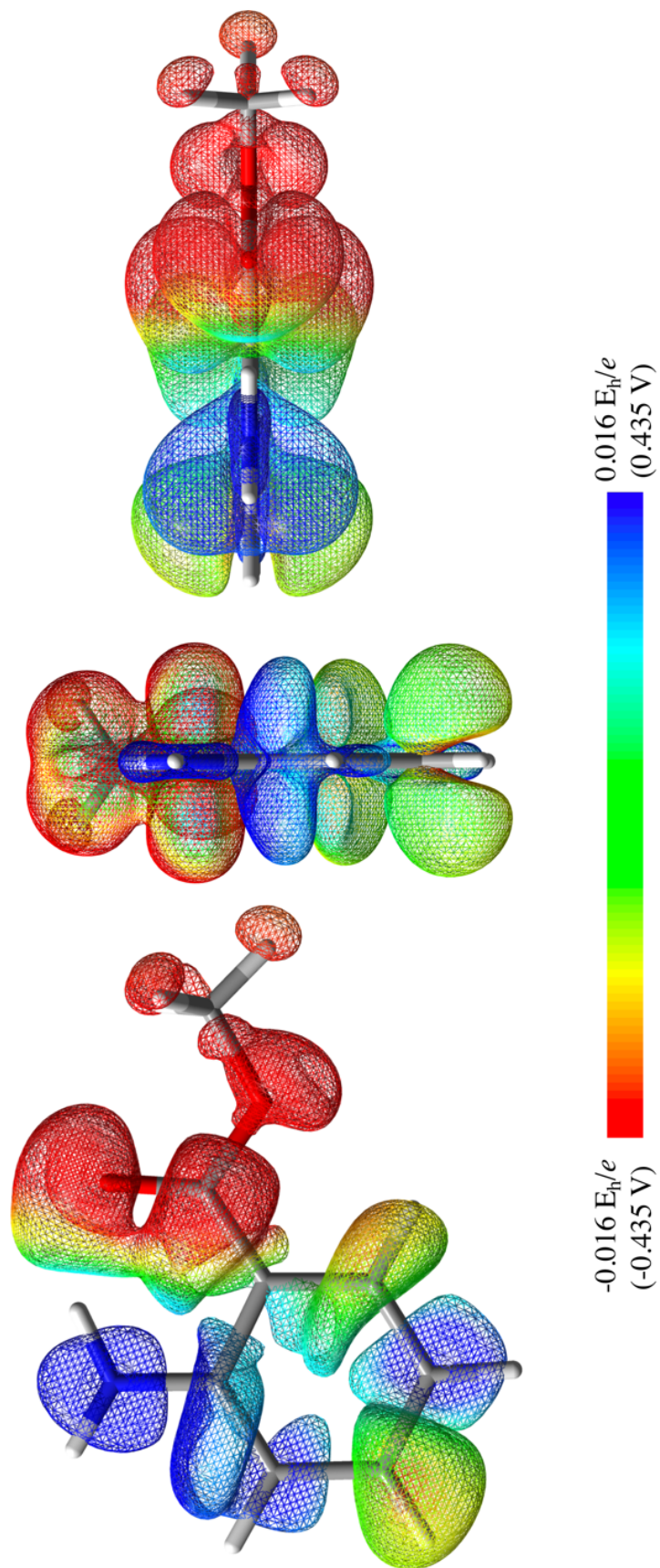


Figure 7.5. The change in electrostatic potential mapped onto the surface of increasing electron density in going from $S_0 - S_1$ in methyl anthranilate. Calculated at the TD-DFT B3LYP-D3BJ/def2TZVP level of theory.

7.4.2 Methyl Anthranilate-H₂O Complex

The corresponding S₀ and S₁-state FDIR spectra of the MA-H₂O complex in the hydride stretch region are shown in Figure 7.6a and 6b. The stick diagram below the experimental spectrum displays the results of the local mode anharmonic modeling. The match between experiment and theory is excellent, with an average error of 8.5 cm⁻¹. The S₀ asymmetric and symmetric NH₂ stretches appear at 3543 and 3405 cm⁻¹, respectively. The smaller splitting of these coupled stretches relative to that in the monomer reflects the weaker NH...O=C hydrogen bonding strength in the water complex as a result of the carbonyl acting as a dual H-bond acceptor. The two higher frequency transitions at 3725 and 3569 cm⁻¹ belong to the asymmetric and symmetric H₂O vibrations, respectively. The aromatic CH and fit Fermi coupled CH₃ regions show similar structure to that found in the monomer spectrum. Assigned experimental and calculated frequencies for MA-H₂O can be found in Table 7.2.

Table 7.2. Select experimental and theoretical frequencies in methyl anthranilate-H₂O

S ₀			S ₁		
<i>exp/cm⁻¹</i>	<i>calc/cm⁻¹</i>	<i>assignment</i>	<i>exp/cm⁻¹</i>	<i>calc/cm⁻¹</i>	<i>assignment</i>
3725	3731 [†] (3725*)	H ₂ O AS stretch	3721	3723 [†] (3717*)	H ₂ O AS stretch
3569	3563 [†] (3534*)	H ₂ O SS stretch	3516	3483 [†] (3441*)	H ₂ O SS stretch
3543	3541 [†] (3539*)	NH ₂ AS stretch	3460	3487 [†] (3484*)	'free' NH stretch
3405	3396 [†] (3398*)	NH ₂ SS stretch	-	3072 [†] (3072*)	'dislocated' NH stretch
-	3188 [†]	H ₂ O bend overtone	3196	3196 [†]	H ₂ O bend overtone
3036	3040 [†] (3026*)	CH ₃ FR	3022	3022 [†] (3008*)	CH ₃ FR
3012	3016 [†] (3002*)	CH ₃ FR	2995	2988 [†] (2973*)	CH ₃ FR
2966	2964 [†] (2929*)	CH ₃ FR	2958	2955 [†] (2909*)	CH ₃ FR
2922	2927 [†]	CH ₃ FR	2914	2929 [†]	CH ₃ FR
-	2921 [†]	CH ₃ FR	2910	2921 [†]	CH ₃ FR
2908	2904 [†]	CH ₃ FR	-	2904 [†]	CH ₃ FR
-	2901 [†]	CH ₃ FR	-	2898 [†]	CH ₃ FR
-	2888 [†]	CH ₃ FR	-	2883 [†]	CH ₃ FR
2865	2847 [†]	CH ₃ FR	2853	2841 [†]	CH ₃ FR
1702	1690*	C=O stretch	1611	1615*	C=O stretch
1634	1634*	NH ₂ bend	1548	1548*	NH ₂ bend
1620	1616*	H ₂ O bend	1636	1632*	H ₂ O bend

* scaled harmonic frequency

** anharmonic frequency

† frequency from local mode model

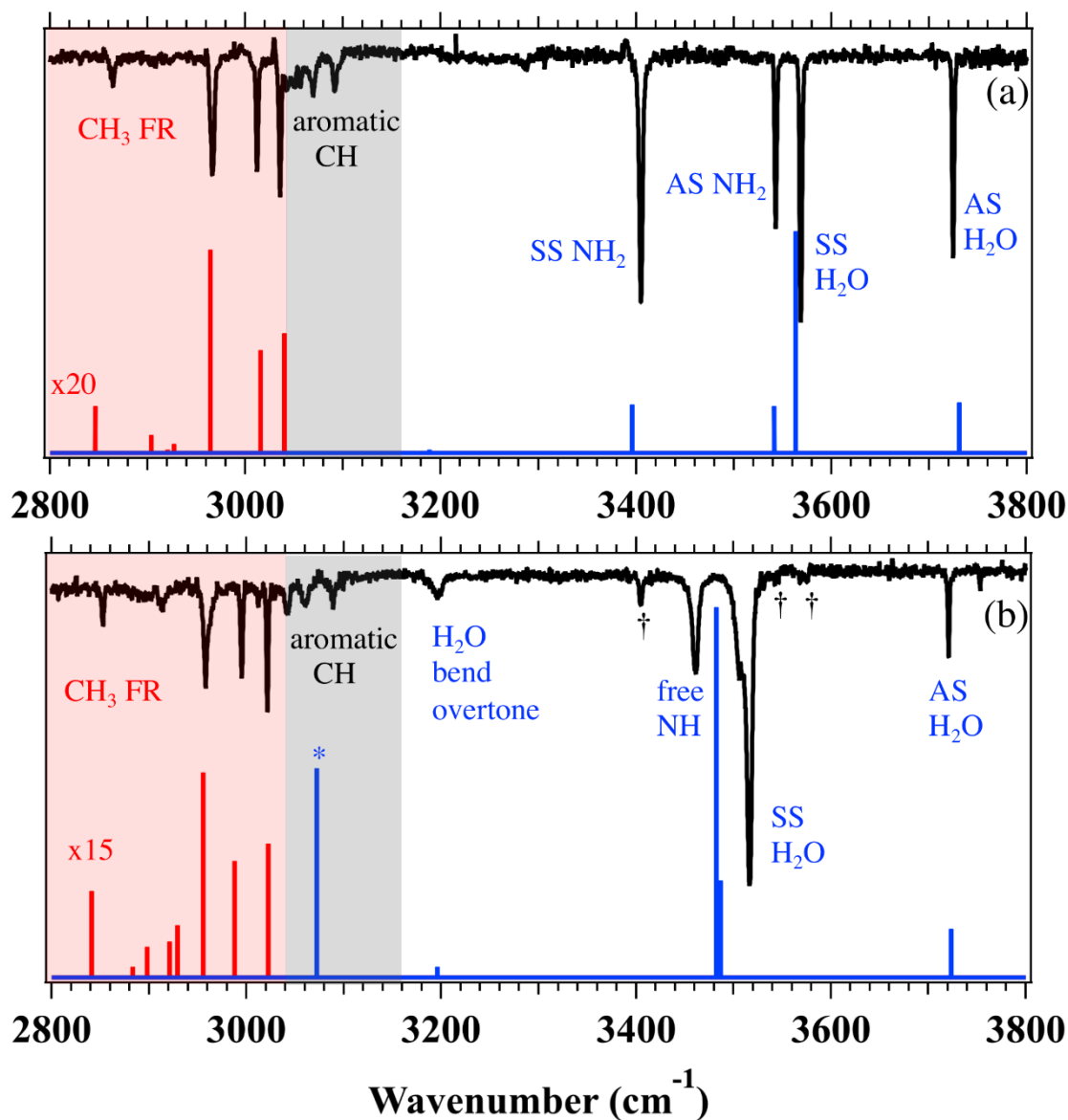


Figure 7.6. (a) Ground and (b) S₁ excited state FDIR spectra from 2800 - 3800 cm⁻¹ of methyl anthranilate-H₂O. The spectra are divided into three regions: NH stretch, aromatic CH stretch (shaded in grey), and CH₃ stretch (shaded in red). The experimental spectrum (black trace) is compared with the predictions of local mode modeling (unmarked stick spectra) in both electronic states. The transitions marked with daggers in (b) are small contributions from the S₀ MA-H₂O spectrum, which appear as a result of the slight overlap of the UV and IR lasers necessitated by a short excited state lifetime (23 ns) and less than ideal fluorescence signal. In both states the red stick spectra corresponding to the CH₃ Fermi-mixed transitions have been multiplied by a scale factor for a more ready comparison with experiment. The blue stick in (b) with a single asterisk at 3072 cm⁻¹ is the calculated harmonic dislocated NH stretch transition. See text for further discussion.

The high frequency region of the S_1 MA-H₂O spectrum (Figure 7.6b) is markedly different from the ground state spectrum above it. The tiny peaks marked with daggers are small contributions from the S_0 MA-H₂O spectrum, which appear as a result of the slight overlap of the UV and IR lasers necessitated by a small excited state lifetime (23 ns) and less than ideal fluorescence signal. In the S_1 state spectrum, the asymmetric and symmetric water stretch transitions are at 3721 and 3516 cm⁻¹, respectively, the latter of which is shifted 53 cm⁻¹ lower in frequency than in the ground state. This shift is indicative of an increasing OH \cdots O=C hydrogen bond strength, as supported by the assigned geometry (Figure 7.1) and the calculated shortening of the OH \cdots O=C H-bond length (by 0.080 Å) upon electronic excitation (Figure 7.1b). Much as in the monomer ground state spectrum, a band with FWHM of 7 cm⁻¹ at 3461 cm⁻¹ is assigned to the free NH stretch of the uncoupled NH₂ group. The calculated, intense transition (blue stick) marked with an asterisk at 3072 cm⁻¹ is due to the H-bonded ‘dislocated’ NH stretch transition, which is absent from the experimental spectrum in both frequency position and intensity. Indeed, the local mode modelling of the CH₃ stretches firmly assigns all experimental bands to Fermi coupled states in this region, as it did in the MA monomer. This leaves all observed bands accounted for except for the 14 cm⁻¹ FWHM peak at 3196 cm⁻¹, which according to our local mode modelling is the H₂O bend overtone.

The S_0 -state mid-IR spectrum of MA-H₂O is presented in Figure 7.7a. The C=O stretch fundamental of the water complex appears at 1702 cm⁻¹, shifted 18 cm⁻¹ to lower frequency than in the monomer. This frequency shift reflects that the C=O group is accepting an additional H-bond from the water OH group. The NH₂ bend appears at 1634 cm⁻¹, nearly the same frequency as its monomer counterpart. This unperturbed band position provides evidence that the H₂O molecule is not interacting directly with the amine group, conforming our assigned structure (Figure 7.1b).

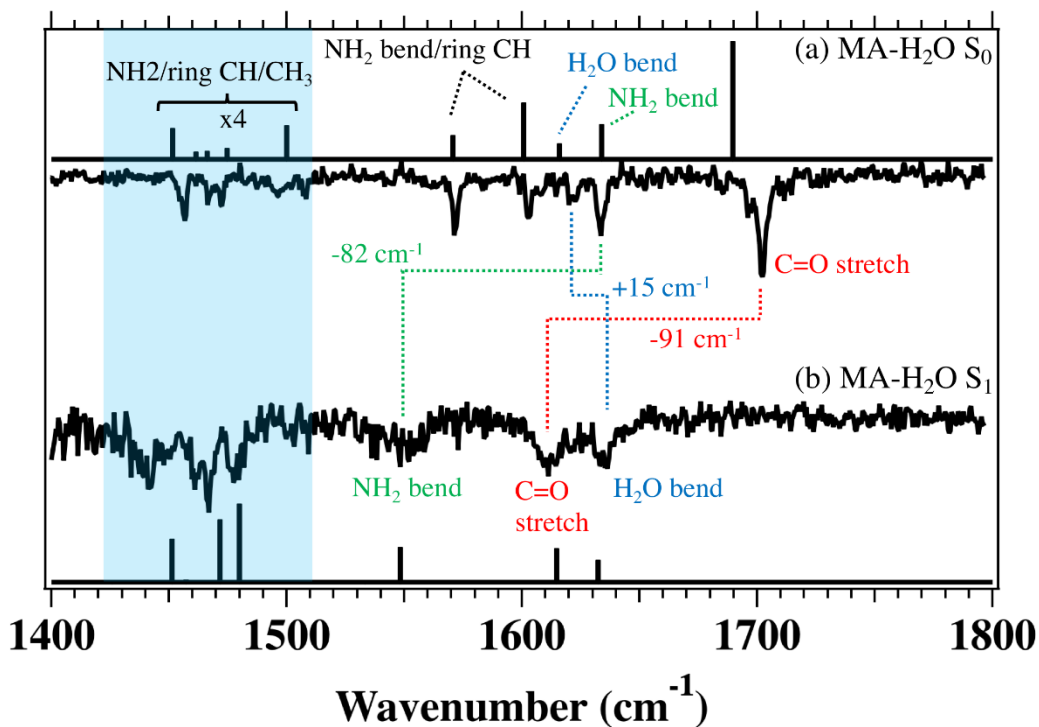


Figure 7.7. (a) Ground and (b) S_1 excited state RIDIR spectra from 1400 - 1800 cm^{-1} of methyl anthranilate- H_2O . The calculated scaled harmonic normal mode frequencies (black stick spectra) are compared with experiment. See text for further discussion.

The mid-IR spectrum in the S_1 state reflects the general structural change present in the monomer, modified by the H_2O molecule forming a second H-bond to the $\text{C}=\text{O}$ group. For instance, the $\text{C}=\text{O}$ stretch transition in S_1 MA- H_2O is shifted down in frequency relative to S_0 by 91 cm^{-1} to 1611 cm^{-1} . This low frequency, 26 cm^{-1} lower than in the monomer, is consistent with the double acceptor nature of the carbonyl group, with calculated H-bond distances between the $\text{C}=\text{O}$, and NH/OH groups of 1.755/1.830 Å, respectively. Upon electronic excitation the NH_2 bend frequency follows that of the monomer, shifting down 82 cm^{-1} to 1552 cm^{-1} , nearly identical to that in MA monomer. This is further evidence that in both S_0 and S_1 electronic states the amine group is largely unperturbed by the water molecule, consistent with the assigned structure in which the H_2O molecule binds to $\text{C}=\text{O}$ from the ester pocket (Figure 7.1b).

Finally, in the ground state, the H_2O bend fundamental appears at 1620 cm^{-1} , a value close to that in free H_2O (1595 cm^{-1}). However, in the S_1 state spectrum (Figure 7.7b), we tentatively assign the transition at 1635 cm^{-1} to the bend fundamental based on comparison with calculations. A value this high in frequency reflects a substantial strengthening of the H-bond between H_2O and

MA in the S_1 state. This blue shift in frequency upon strengthening of the intermolecular hydrogen bond is consistent with the analogous hydrogen bond donor H_2O bend frequency in the water dimer of 1629 cm^{-1} .²⁸ This change in vibrational frequency is a response to the shifting electron density of the MA monomer, where vertical TD-DFT calculations indicate increasing electron density and negative charge on the carbonyl oxygen upon electronic excitation, thereby making it a better hydrogen bond acceptor. The change in electrostatic potential mapped onto the surface of increasing electron density in going from S_0 to S_1 is presented in Figure 7.8, and shows nearly identical features to that of the monomer (Figure 7.5), i.e., increasing electron density and negative charge on the carbonyl oxygen and increasing electron density and positive charge on the nitrogen atom.

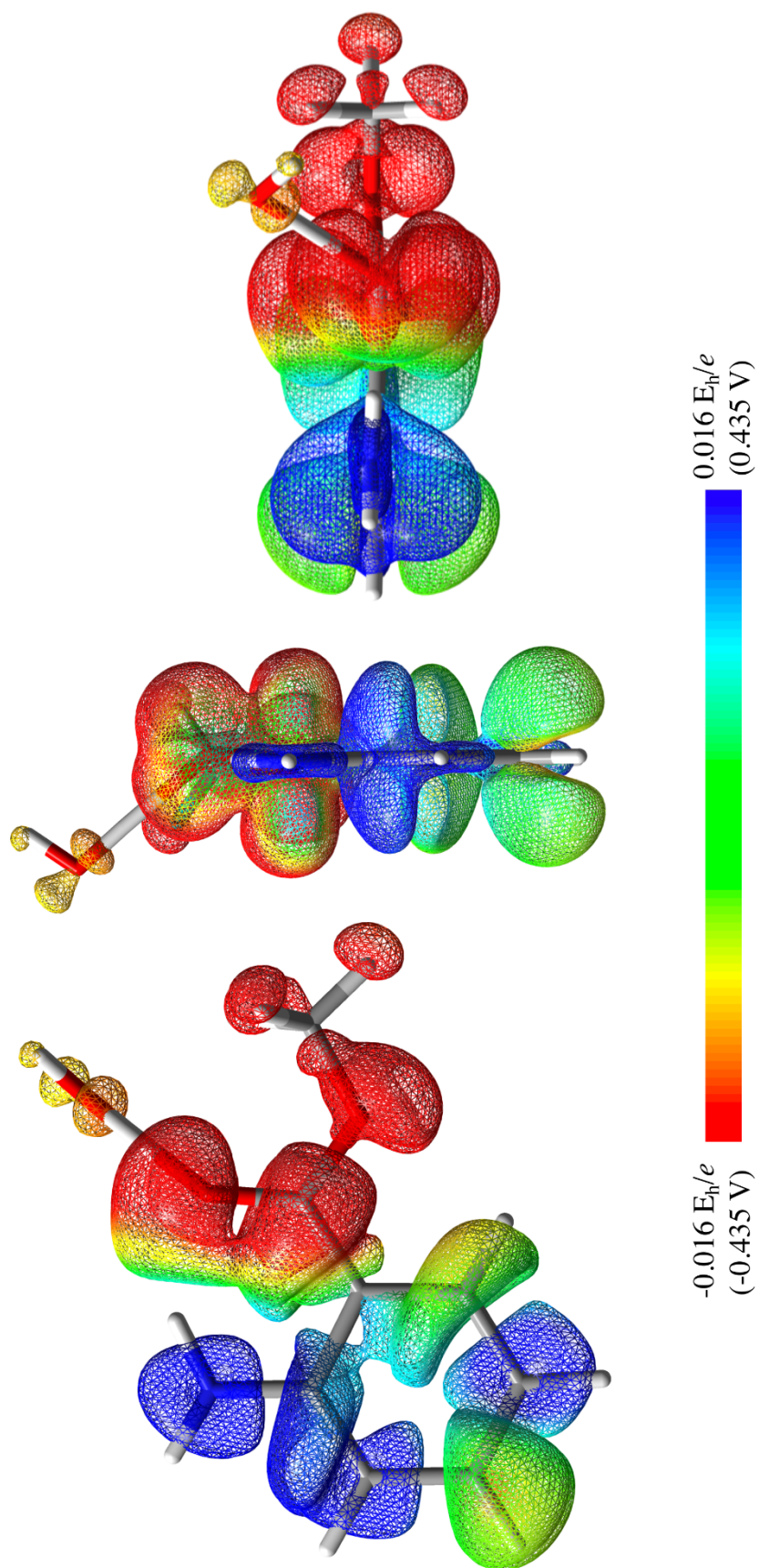


Figure 7.8. The change in electrostatic potential mapped onto the surface of increasing electron density in going from S₀ - S₁ in methyl anthranilate-H₂O. Calculated at the TD-DFT B3LYP-D3BJ/def2TZVP level of theory.

7.5 Discussion

With the aid of a combination of anharmonic models based on a local mode Hamiltonian and DFT calculations, we have assigned all experimental bands in the high-frequency IR spectrum of MA and MA-H₂O in both the S₀ and S₁ electronic states. In the excited state, normal mode calculations predict the uncoupling of the NH₂ group vibrations into localized NH stretches of the free and H-bonded NH groups. In both the monomer and water complex, the transition associated with the ‘free’ NH stretch is firmly assigned to the band at 3457 and 3461 cm⁻¹, respectively. The vibrational transition associated with the hydrogen bonded ‘dislocated’ NH stretch is calculated to lie ~500 cm⁻¹ lower in frequency and have an intensity more than 10 times that of any other band in the region.

The striking absence of this transition in the spectra of both MA and MA-H₂O requires an explanation. We note that missing IR transitions have been observed previously in excited state IR spectra (e.g., in indole derivatives) due to the presence of a dissociative excited state (e.g., πσ*) not far above the excited state origin.²⁹ However, the S₁ state of MA is well isolated from other excited states, and there is no evidence for such a mechanism being at play (see Table 6.5). As a result, the missing NH stretch fundamental in MA stimulated development of the theoretical models outlined in Sec. III.B. In what follows, we describe the results of the adiabatic modelling of the NH stretch vibration of the MA monomer in the $\nu_{\text{NH}} = 0$ and 1 states of the H-bonded, ‘dislocated’ NH stretch transition with an eye toward explaining this striking anomaly.

We focus attention in this section on the NH stretch adiabatic calculations. To that end, we minimized the NH(D) stretch $\nu_{\text{NH}}=0$ and $\nu_{\text{NH}}=1$ energies on the S₀ and S₁ surfaces as a function of select coordinates. Of the 54 internal coordinates, 32 were constrained to their equilibrium values. The 6 carbon atoms and 4 hydrogen atoms of the substituted phenyl ring were held rigid. In addition, the internal coordinates of the methyl group, with the exception of its torsional motion, were constrained. The NH(D) stretch is treated quantum mechanically, while the remaining internal coordinates were allowed to vary.

Figure 7.9 compares results for the $\nu=0$ and $\nu=1$ NH stretch levels on the S₁ (upper) and S₀ surfaces. These results are obtained with 27 DVR points along the NH stretch, but results obtained for 17 points were similar. The red potential curves correspond to *ab initio* energies obtained by varying the NH internal coordinate keeping all remaining coordinates fixed. Shown in Figure 7.9a, the minimum in the $\nu_{\text{NH}} = 0$ S₁ potential curve is 99 cm⁻¹ with respect to the global potential

minimum. The zero-point energy of the NH stretch with respect to the latter minimum is $E_0=1618$ cm^{-1} , and the energy of the $\nu_{\text{NH}} = 1$ state is 4542 cm^{-1} . In contrast, in Figure 7.9b the minimum energy of the S_1 NH stretch potential is 1202 cm^{-1} and the energy of the $\nu_{\text{NH}} = 1$ state with respect to the global minimum is $E_1 = 3900$ cm^{-1} . By varying the remaining internal coordinates in a minimization procedure, we have reduced the total energy of this state by $\Delta E_s = 642$ cm^{-1} . The driving force for the structural change is due to the fact that at the geometry of Figure 7.9b, the energy of the NH stretch fundamental transition is only 1604 cm^{-1} .

The analogous curves for the S_0 state are shown in Figure 7.9c and 9d, from which it is apparent that the change in structure upon NH stretch excitation is much reduced. For $\nu_{\text{NH}} = 1$ we find that $\Delta E_s = 34$ cm^{-1} . This contrast between S_0 and S_1 states makes clear the unusual effects present in the S_1 state, which are largely absent in the S_0 state, despite the presence of a significant $\text{NH}\cdots\text{O}=\text{C}$ H-bond there as well.

The biggest changes in the internal coordinates correspond to out-of-plane displacements of both the O and H involved in the enhanced H-bonding. Both atoms move in the same out-of-plane direction with changes in dihedral angles of 9° and 8° , respectively, from the planar equilibrium structure. As such there are two equivalent minima structures. The H-bonded NCH angle decreases from 116.2° to 108.5° . In the language of electronic transitions, the vertical transition energy is 642 cm^{-1} greater than the energy difference corresponding to the minima. This result suggests that spectral congestion via vibrational Franck-Condon factors should be significant. The center of the transition frequency would correspond to the energy of the vertical transition which is 2924 cm^{-1} , but the lowest possible transition energy would be 642 cm^{-1} less.

While the current experimental study does not address isotopic effects, it is worthwhile to consider how these results might change in ND_2 compared to NH_2 . As shown in Figure 7.10c and 10d, the analogous structural rearrangement calculated to occur upon ND stretch excitation is substantially less dramatic. The difference between the vertical and minimum energies for the $\nu_{\text{ND}} = 1$ state is $\Delta E_s = 151$ cm^{-1} compared to the analogous 642 cm^{-1} value found for the NH stretch.

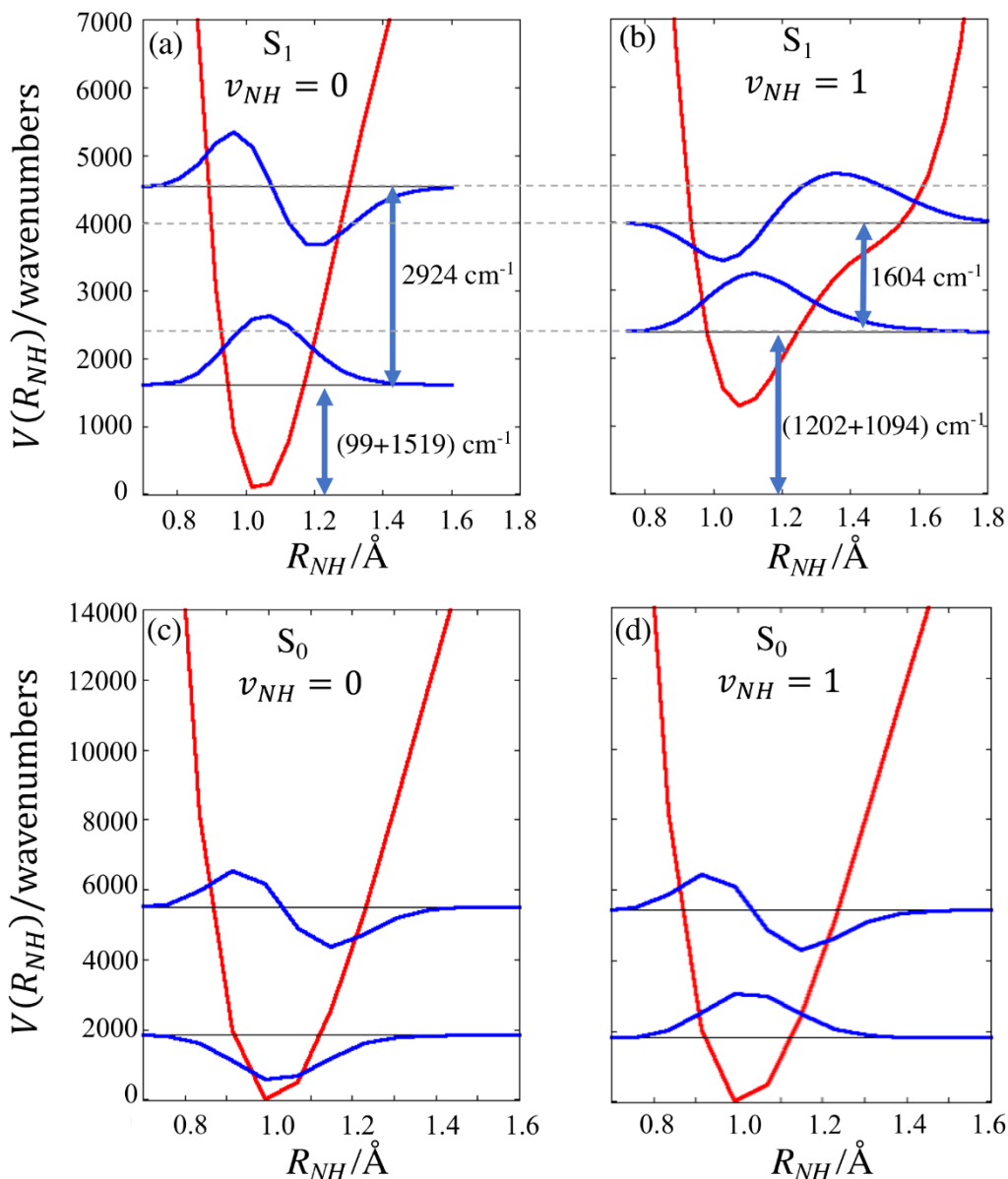


Figure 7.9. (a) and (b) show the two lowest energy NH stretch eigenfunctions and corresponding potentials in S_1 plotted as a function of bond length. The zero of energy is the true calculated potential minimum of the excited state. Remaining coordinates values were chosen to minimize $E(v=0)$ in (a) and $E(v=1)$ in (b). In (a) there is 99 cm^{-1} of energy at the bottom of the well; in (b) there is 1202 cm^{-1} of energy. In (a) $E(v=0)$ is 1618 cm^{-1} and $E(v=1)$ is 4542 cm^{-1} . In (b) $E(v=0)$ is 2296 cm^{-1} and $E(v=1)$ is 3900 cm^{-1} . The energy difference between 4542 and 3900 cm^{-1} will get deposited into the remaining degrees of freedom. Results are for excited states using TD/B3LYP/6-311++(d,p) level of theory with dispersion. (c) and (d) show analogous results for the S_0 electronic state. In both plots all coordinates but the NH stretch internal coordinate are held fixed. The NH stretch coordinate is varied to obtain the potential (red) and the associated wave functions. In (c) the remaining internal coordinates are held at the equilibrium geometry, and in (d) the remaining internal coordinates are held at values that minimize the energy of the state with one quantum of excitation in the NH stretch.

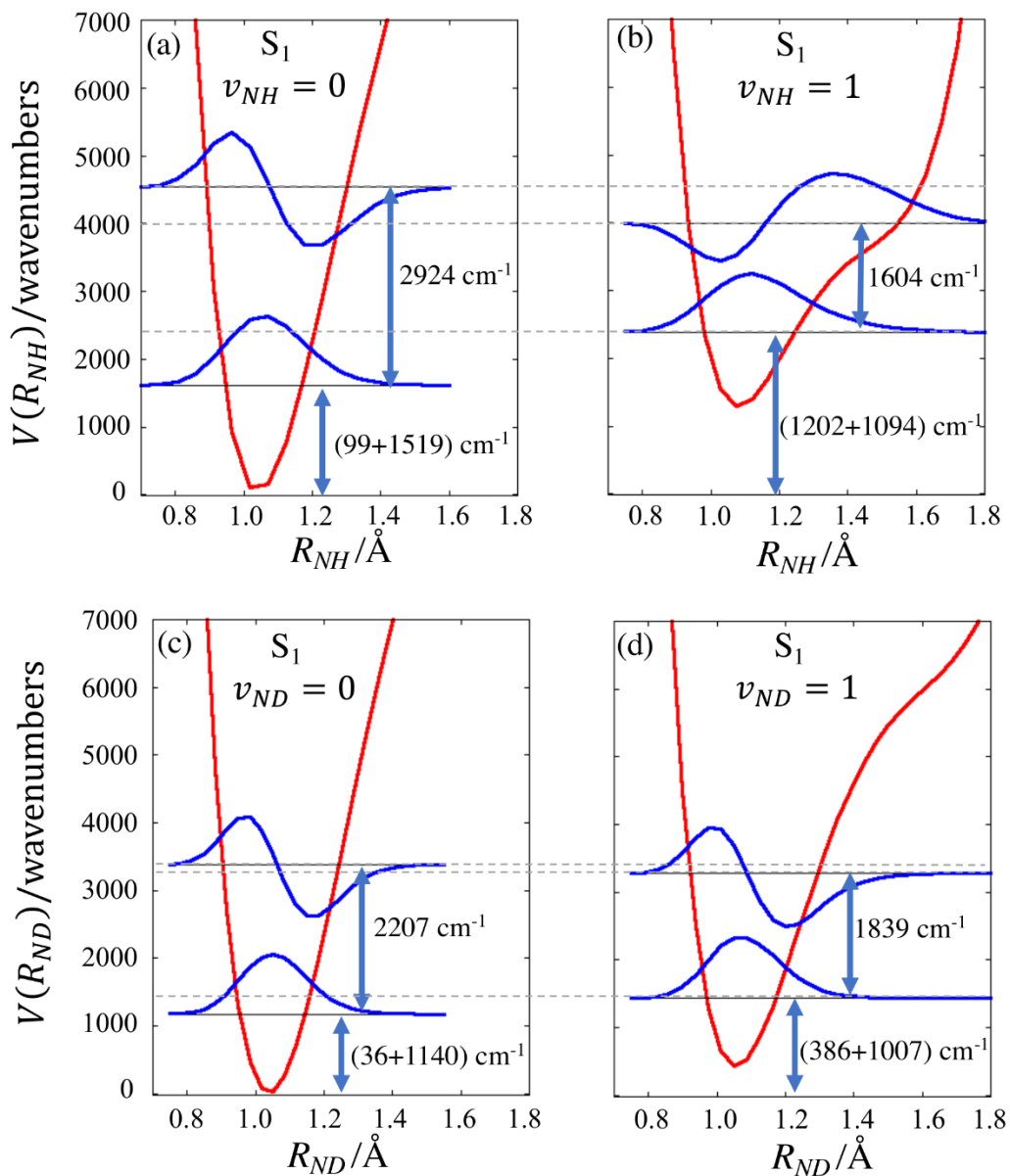


Figure 7.10. (a) and (b) show the two lowest energy NH stretch eigenfunctions and corresponding potentials in S_1 plotted as a function of bond length. The zero of energy is the true calculated potential minimum of the excited state. Remaining coordinates values were chosen to minimize $E(v=0)$ in (a) and $E(v=1)$ in (b). In (a) there is 99 cm⁻¹ of energy at the bottom of the well; in (b) there is 1202 cm⁻¹ of energy. In (a) $E(v=0)$ is 1618 cm⁻¹ and $E(v=1)$ is 4542 cm⁻¹. In (b) $E(v=0)$ is 2296 cm⁻¹ and $E(v=1)$ is 3900 cm⁻¹. The energy difference between 4542 and 3900 cm⁻¹ will get deposited into the remaining degrees of freedom. Results are for excited states using TD/B3LYP/6-311++(d,p) level of theory with dispersion. (c) and (d) displays analogous results for the S_1 state of the ND stretch. The difference between vertical and minimum energies for the $v_{ND} = 1$ state is $\Delta E_s = 151$ cm⁻¹ compared to the analogous 642 cm⁻¹ value found for the NH stretch.

In order to examine the combined effects of the stretch and the bend we show the potential surface as a function of these two modes in Figure 7.11a. The remaining coordinates are constrained to the geometry that minimizes the $\nu_{\text{NH}} = 0$ state following the procedure described above. The equipotential energy contours (every 1000 cm^{-1}), indicate that the NH stretch is strongly coupled to the bend, with the stretch potential being qualitatively different for the two slices at $\theta_{\text{HNC}} = 1.8$ and 2.2 radians. The four lowest energy eigenfunctions, along with their associated eigenvalues are displayed in Figure 7.11b-e. The excitation energy of the NH stretch fundamental is calculated to be 2634.7 cm^{-1} .

In order to gauge the role of the potential anharmonicity, we repeat the calculation with the same kinetic energy operator but assume a quadratic potential obtained from a Taylor series for these two degrees of freedom at the $\nu_{\text{NH}} = 0$ geometry. These analogous plots are displayed in Figure 7.11f-j. We obtain an NH stretch fundamental transition energy of 3128.6 cm^{-1} . That value is similar to the 3190.7 cm^{-1} value obtained from a normal mode calculation obtained at the global minimum, indicating that the very large shifts are due to the unusually large anharmonicity of the potential shown in Figure 7.11a.

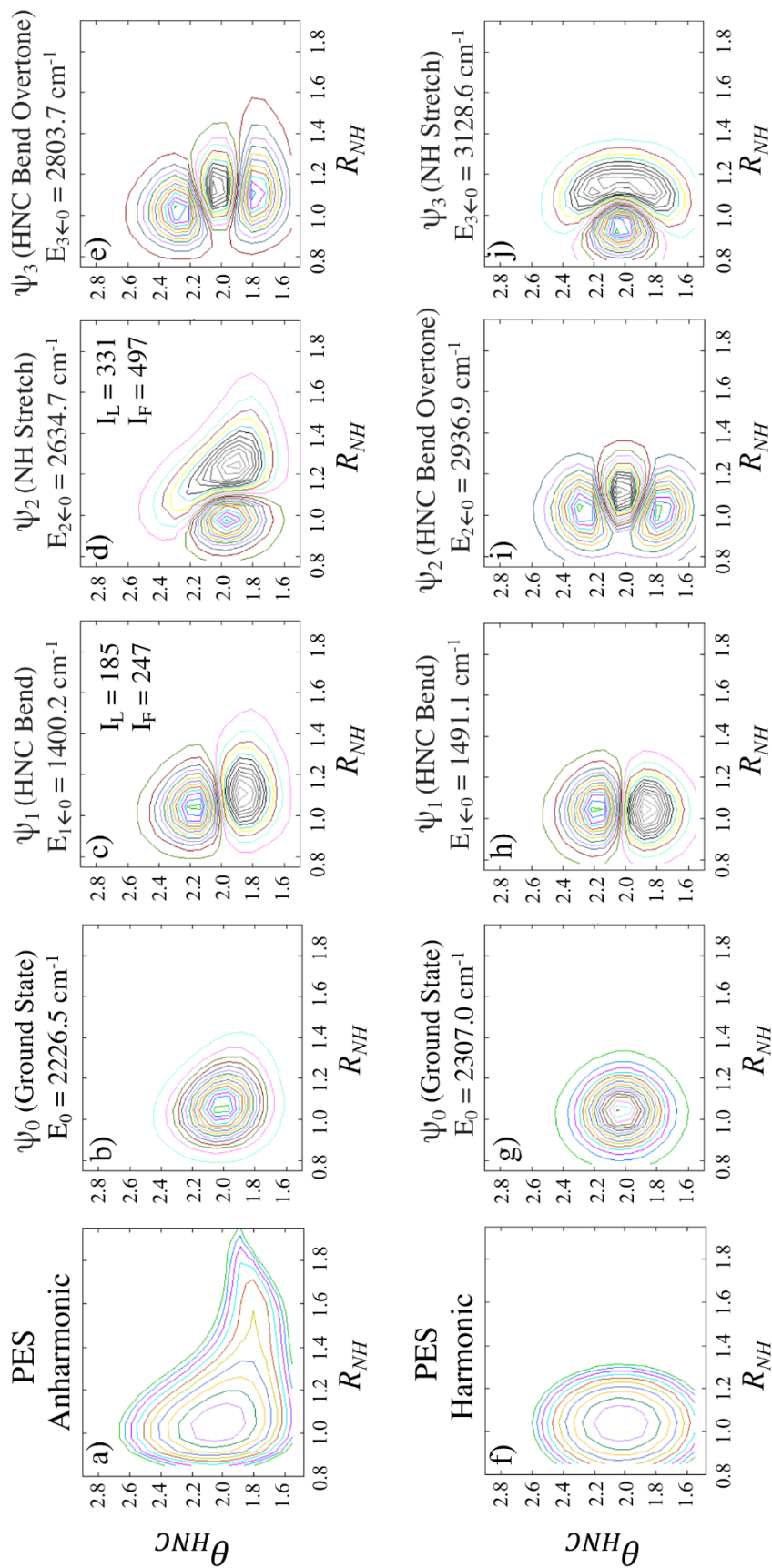


Figure 7.11. Equipotential curves plotted every 1000 cm^{-1} as a function of NH stretch and HNC bend coordinates. The remaining coordinates are constrained to the geometry that minimizes the $\nu_{NH} = 0$ state following the adiabatic procedure described in the text. (a) displays the anharmonic calculated potential energy surface and (b) - (e) show the four corresponding lowest energy eigenfunctions along with their associated eigenvalues. Intensities (km/mol) are given for select transitions using a linear dipole (I_L) and full dipole (I_F), the latter of which is evaluated at the DVR grid of points. (f) and (g) - (j) show analogous plots obtained with a quadratic potential from a Taylor series for the two degrees of freedom at the $\nu_{NH} = 0$ geometry. See text for further discussion.

Figure 7.11 also includes the results of intensity calculations. The results (given in km/mol) shown indicate that for the NH fundamental the linear dipole leads to an intensity of $I_L = 331$ km/mol versus 497 km/mol for the dipole evaluated at the DVR grid of points. The purpose of the stretch-bend model is to show that the bending motion is strongly coupled to the NH stretch. These results should not be compared to experiment, since the bend itself is strongly coupled to other modes. Indeed, at least 12 calculated normal modes display significant HNC bend character, with many other vibrations at similar frequencies to that of the bend. There are also other modes directly coupled to the NH stretch.

The above two calculations suggest that the NH stretch fundamental should be strongly coupled to other degrees of freedom and that the intensity of the mode should be broadly distributed amongst several transitions spread over several hundred wavenumbers. Perhaps the low-intensity, diffuse bands seen near 2800 cm^{-1} (Figure 7.3b) and in AA at 2900 cm^{-1} can be ascribed to some of these features. As noted above, this effect would not be accounted for in VPT2 calculations. This suggests that a restricted, rectilinear, quartic potential is unlikely to capture the key features of the potential shown in Figure 7.11a. This is not too surprising given its shape; a low order Taylor series expansion cannot be expected to capture the valley that appears as the HNC angle is reduced from its equilibrium configuration. The shape of this valley indicates that orientation plays a critical role in the H-atom dislocation; only when the bend angle decreases to about 1.8 rad is there a low energy pathway for this dislocation.

7.6 Conclusion

We have postulated that the apparent absence of a transition ascribable to the NH stretch of the H-bonded, ‘dislocated’ NH group in the S_1 state of MA and MA-H₂O is the result of an extreme instance of anharmonic mixing involving the NH stretch and the CNH bend. Using an adiabatic vibrational model involving the NH stretch, we have demonstrated that this absorption will have its oscillator strength spread over transitions spanning hundreds of wavenumbers. If these transitions are in turn broadened by strong coupling with other background states, it would lead to a broad background that is hard to observe, consistent with experiment. Since observation of a structured background could add further insight to the pre-reactive H-atom transfer process, future studies that can detect it with good sensitivity are still needed. Alternatively, analogous

studies of the ND₂ MA isotopomer would also confirm the model, as we predict a significant reduction in the effects there.

It is interesting to compare the current NH stretch results on the S₁ surface with the observed OH stretch spectrum of benzoic acid dimer.³⁰ In the latter system there is especially strong hydrogen bonding that profoundly affects the IR spectrum leading to an intense absorption centered around 2900 cm⁻¹ with features spanning 600 cm⁻¹. Despite its breadth, this feature completely dominates this region of the IR spectrum, a situation that starkly contrasts with the disappearance of the NH stretch band. Comparing the intensities of the associated normal NH and OH stretches we find $I_{NH}=420$ km/mol for the former and $I_{OH}=6692$ km/mol for the latter using the B3LYP hybrid functional in conjunction with Grimme's dispersion correction (version D3)¹⁹, Becke-Johnson damping²⁰, and the def2TZVP basis set. We believe that this large intensity difference combined with the NH stretch spectral features being predicted to spread over twice the spectral range, are key factors that lead to dramatically different spectra.

Finally, it seems likely that a similar strong stretch-bend coupling is present in other molecules that engage in excited-state keto-enol tautomerisation, including salicylic acid. Indeed, the H-bonded OH stretch has not been identified in the S₁ state of SA and its derivatives, suggesting that a similar mechanism may be in operation.^{11, 31, 32} The time-dependent development of the infrared spectra in the anthranilate and salicylate derivatives is worth future effort.

7.7 References

1. T. N. Karsili, B. Marchetti, M. N. Ashfold and W. Domcke, *J. Phys. Chem. A*, 2014, **118**, 11999-12010.
2. A. L. Sobolewski and W. Domcke, *PCCP*, 2006, **8**, 3410-3417.
3. P. B. Bisht, H. Petek, K. Yoshihara and U. Nagashima, *J. Chem. Phys.*, 1995, **103**, 5290-5307.
4. Y. Peperstraete, M. Staniforth, L. A. Baker, N. D. N. Rodrigues, N. C. Cole-Filipiak, W.-D. Quan and V. G. Stavros, *PCCP*, 2016, **18**, 28140-28149.
5. L. A. Baker, M. D. Horbury, S. E. Greenough, P. M. Coulter, T. N. Karsili, G. M. Roberts, A. J. Orr-Ewing, M. N. Ashfold and V. G. Stavros, *J. Phys. Chem. L.*, 2015, **6**, 1363-1368.
6. N. D. Rodrigues, M. Staniforth and V. G. Stavros, *Proceedings of the Royal Society A: Mathematical, Physical and Engineering Sciences*, 2016, **472**, 20160677.

7. L. A. Baker, B. Marchetti, T. N. Karsili, V. G. Stavros and M. N. Ashfold, *Chem. Soc. Rev.*, 2017, **46**, 3770-3791.
8. L. Heimbrook, J. E. Kenny, B. E. Kohler and G. W. Scott, *The Journal of Physical Chemistry*, 1983, **87**, 280-289.
9. L. A. Heimbrook, J. E. Kenny, B. E. Kohler and G. W. Scott, *J. Chem. Phys.*, 1981, **75**, 5201-5203.
10. C. A. Southern, D. H. Levy, G. M. Florio, A. Longarte and T. S. Zwier, *J. Phys. Chem. A*, 2003, **107**, 4032-4040.
11. A. L. Sobolewski and W. Domcke, *J. Phys. Chem. A*, 2004, **108**, 10917-10922.
12. F. Egidi, D. B. Williams-Young, A. Baiardi, J. Bloino, G. Scalmani, M. J. Frisch, X. Li and V. Barone, *J. Chem. Theor. Comp.*, 2017, **13**, 2789-2803.
13. K. N. Blodgett, D. Sun, J. L. Fischer, E. L. Sibert and T. Zwier, *PCCP*, 2019.
14. P. Kolek, M. Andrzejak, R. Hakalla and W. Szajna, *J. Phys. Chem. A*, 2018, **122**, 6243-6255.
15. C. A. Arrington, C. Ramos, A. D. Robinson and T. S. Zwier, *J. Phys. Chem. A*, 1998, **102**, 3315-3322.
16. F. A. Ensminger, J. Plassard, T. S. Zwier and S. Hardinger, *J. Chem. Phys.*, 1995, **102**, 5246-5259.
17. T. S. Zwier, *J. Phys. Chem. A*, 2001, **105**, 8827-8839.
18. M. Frisch, G. Trucks, H. Schlegel, G. Scuseria, M. Robb, J. Cheeseman, G. Scalmani, V. Barone, G. Petersson and H. Nakatsuji, *Revision A*, 2016, **3**.
19. S. Grimme, *J. Comput. Chem.*, 2004, **25**, 1463-1473.
20. S. Grimme, *J. Chem. Phys.*, 2006, **124**, 034108.
21. E. L. Sibert, D. P. Tabor, N. M. Kidwell, J. C. Dean and T. S. Zwier, *J. Phys. Chem. A*, 2014, **118**, 11272-11281.
22. D. Luckhaus, *J. Chem. Phys.*, 2000, **113**, 1329-1347.
23. T. Nakanaga, F. Ito, J. Miyawaki, K. Sugawara and H. Takeo, *Chem. Phys. Lett.*, 1996, **261**, 414-420.
24. J. M. Bakker, L. Mac Aleese, G. von Helden and G. Meijer, *J. Chem. Phys.*, 2003, **119**, 11180-11185.
25. S. Stepanian, I. Reva, E. Radchenko and G. Sheina, *Vib. Spectrosc.*, 1996, **11**, 123-133.

26. H. Piest, G. von Helden and G. Meijer, *J. Chem. Phys.*, 1999, **110**, 2010-2015.
27. M. Mukherjee, B. Bandyopadhyay, P. Biswas and T. Chakraborty, *Indian Journal of Physics*, 2012, **86**, 201-208.
28. J. Paul, R. Provencal, C. Chapo, K. Roth, R. Casaes and R. Saykally, *J. Phys. Chem. A*, 1999, **103**, 2972-2974.
29. B. C. Dian, A. Longarte and T. S. Zwier, *J. Chem. Phys.*, 2003, **118**, 2696-2706.
30. G. Florio and T. Zwier, *J. Chem. Phys.*, 2003, **118**, 1735.
31. T. Yahagi, A. Fujii, T. Ebata and N. Mikami, *J. Phys. Chem. A*, 2001, **105**, 10673-10680.
32. E. A. E.-H. A. El, A. Fujii, T. Ebata and N. Mikami, *Chem. Phys. Lett.*, 2003, **376**, 788-793.

Conformer-Specific and Diastereomer-Specific Spectroscopy of $\alpha\beta$ Synthetic Foldamers: Ac–Ala– β_{ACHC} –Ala–NHBn

Karl N. Blodgett,[†] Xiao Zhu,[‡] Patrick S. Walsh,^{†,||} Dewei Sun,[†] Jaeyeon Lee,[§] Soo Hyuk Choi,[§] and Timothy S. Zwier^{*,†,||}

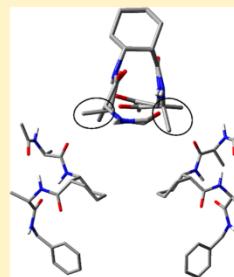
[†]Department of Chemistry, Purdue University, 560 Oval Drive, West Lafayette, Indiana 47907-2084, United States

[‡]Research Computing, Information Technology at Purdue (ITA/P), West Lafayette, Indiana 47907-2114, United States

[§]Department of Chemistry, Yonsei University, Seoul 03722, Korea

S Supporting Information

ABSTRACT: The folding propensities of a capped, cyclically constrained, mixed α/β diastereomer pair, (SRSS) Ac–Ala– β_{ACHC} –Ala–NHBn (hereafter RS) and (SSRS) Ac–Ala– β_{ACHC} –Ala–NHBn (SR), have been studied in a molecular beam using single-conformation spectroscopic techniques. These α/β -tripeptides contain a cyclohexane ring across each C_{α} – C_{β} bond, at which positions their stereochemistries differ. This cyclic constraint requires any stable species to adopt one of two ACHC configurations: equatorial C=O/axial NH or equatorial NH/axial C=O. Resonant two-photon ionization (R2PI) and infrared–ultraviolet hole-burning (IR–UV HB) spectroscopy were used in the S_0 – S_1 region of the UV chromophore, revealing the presence of three unique conformational isomers of RS and two of SR. Resonant ion-dip infrared spectra were recorded in both the NH stretch (3200–3500 cm^{-1}) and the amide I (1600–1800 cm^{-1}) regions. These experimental vibrational frequencies were compared with the scaled calculated normal-mode frequencies from density functional theory at the M05-2X/6-31+G(d) level of theory, leading to structural assignments of the observed conformations. The RS diastereomer is known in crystalline form to preferentially form a C11/C9 mixed helix, in which alternating hydrogen bonds are arranged in near antiparallel orientation. This structure is preserved in one of the main conformers observed in the gas phase but is in competition with both a tightly folded $C7_{\text{eq}}/C12/C8/C7_{\text{eq}}$ structure, in which all four amide NH groups and four C=O groups are engaged in hydrogen bonding, as well as a cap influenced $C7_{\text{eq}}/\text{NH}\cdots\pi/C11$ structure. The SR diastereomer is destabilized by inducing backbone dihedral angles that lie outside the typical Ramachandran angles. This diastereomer also forms a C11/C9 mixed helix as well as a cap influenced bifurcated $C7_{\text{ax}}-C11/\text{NH}\cdots\pi/C7_{\text{eq}}$ structure as the global energy minimum. Assigned structures are compared with the reported crystal structure of analogous α/β -tripeptides, and disconnectivity graphs are presented to give an overview of the complicated potential energy surface of this tripeptide diastereomer pair.



■ INTRODUCTION

Synthetic foldamers are oligomers that are composed of any mixture of natural and/or non-natural monomeric building blocks, usually designed to mimic the natural machinery of nature or expand upon it.^{1–3} These compounds have been shown to be resistant to natural protein degradation mechanisms and have been designed to have applications as potent antimicrobial agents and cholesteryl ester uptake inhibitors.^{4–7} Among α -peptides, helices are the most common secondary structure, and among helices, the α -helix (3.6₁₃-helix) and the 3₁₀-helix are the most prominent.^{8–10} Studies on homogeneous backbone peptides using purely β -amino acid building blocks, which extend the backbone chain length by one carbon, revealed new helical structures not accessible to α -peptides, including the 12/10-, 14-, 8-, and 10-helices, where the numbers indicate the number of atoms in each hydrogen-bonded cycle that comprises the helix.^{11–14}

Building off of our group's study of the inherent conformational preferences of synthetic foldamers,^{8,14–22} we consider here a diastereomeric mixed α/β pair, (SRSS) Ac–Ala– β_{ACHC} –

Ala–NHBn (referred to as RS) and (SSRS) Ac–Ala– β_{ACHC} –Ala–NHBn (SR), molecules which differ from one another by their exchange of chirality along the ACHC (*cis*-2-aminocyclohexanecarboxylic acid) residue. These structures are presented in Figures 1a,b, respectively. The ACHC residue has two stable minimum structures, a chair conformation, in which the NH is in the equatorial (eq) position, and the C=O is in the axial position, and vice versa (Figure 1e).

Lee et al. showed that a structure analogous to the RS diastereomer, differing only in the capping units (N-terminal *tert*-butyloxycarbonyl and C-terminal methyl ester caps) is known in crystalline form to prefer 11/9 mixed helical folding, which arises from (*i,i*+3) and (*i,i*-1) C=O \cdots H–N hydrogen bonding.²³ A similarly analogous structure to the SR diastereomer crystallizes with no intramolecular hydrogen bonding (see Figure S1 for crystal structures), while room

Received: February 5, 2018

Revised: March 20, 2018

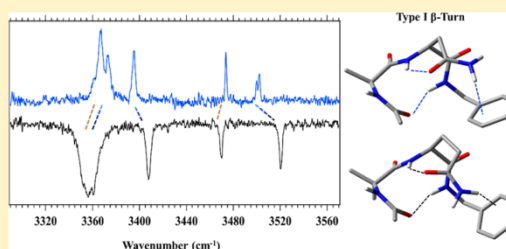
Published: March 20, 2018

Conformation-Specific Spectroscopy of Asparagine-Containing Peptides: Influence of Single and Adjacent Asn Residues on Inherent Conformational Preferences

Karl N. Blodgett,[†] Joshua L. Fischer,[†] Jaeyeon Lee,[‡] Soo Hyuk Choi,[‡] and Timothy S. Zwier^{*,†}[†]Department of Chemistry, Purdue University, West Lafayette, Indiana 47907-2084, United States[‡]Department of Chemistry, Yonsei University, Seoul 03722, Korea

Supporting Information

ABSTRACT: The infrared and ultraviolet spectra of a series of capped asparagine-containing peptides, Ac-Asn-NHBn, Ac-Ala-Asn-NHBn, and Ac-Asn-Asn-NHBn, have been recorded under jet-cooled conditions in the gas phase in order to probe the influence of the Asn residue, with its $-\text{CH}_2-\text{C}(=\text{O})-\text{NH}_2$ side chain, on the local conformational preferences of a peptide backbone. The double-resonance methods of resonant ion-dip infrared (RIDIR) spectroscopy and infrared–ultraviolet hole-burning (IR–UV HB) spectroscopy were used to record single-conformation spectra in the infrared and ultraviolet, respectively, free from interference from other conformations present in the molecular beam. Ac-Asn-NHBn spreads its population over two conformations, both of which are stabilized by a pair of H-bonds that form a bridge between the Asn carboxamide group and the NH and C=O groups on the peptide backbone. In one the peptide backbone engages in a 7-membered H-bonded ring (labeled C7_{eq}), thereby forming an inverse γ -turn, stabilized by a C6/C7 Asn bridge. In the other the Asn carboxamide group forms a C8/C7 H-bonded bridge with the carboxamide group facing in the opposite direction across an extended peptide backbone involving a C5 interaction. Both Ac-Ala-Asn-NHBn and Ac-Asn-Asn-NHBn are found exclusively in a single conformation in which the peptide backbone engages in a type I β -turn with its C10 H-bond. The Asn residue(s) stabilize this β -turn via C6 H-bond(s) between the carboxamide C=O group and the same residue's amide NH. These structures are closely analogous to the corresponding structures in Gln-containing peptides studied previously [Walsh, P. S. et al. *PCCP* 2016, 18, 11306–11322; Walsh, P. S. et al. *Angew. Chem. Int. Ed.* 2016, 55, 14618–14622], indicating that the Asn and Gln side chains can each configure so as to stabilize the same backbone conformations. Spectroscopic and computational evidence suggest that glutamine is more predisposed than asparagine to β -turn formation via unusually strong side-chain–backbone hydrogen-bond formation. Further spectral and structural similarities and differences due to the side-chain length difference of these similar amino acids are presented and discussed.



1. INTRODUCTION

The polar amino acids asparagine and glutamine, differing by one methylene group, are the only two naturally occurring amino acids that contain carboxamide groups in their flexible side chains. Both amino acids are heavily involved in neurodegenerative disease pathogenesis.^{1–5} At the genetic level, CAG codon repeat disorders result in long tracts of glutamine residue repeats within proteins, which subsequently fold into β -sheet oligomers that aggregate to form insoluble amyloid fibrils, the hallmark of neurodegenerative disease.^{6,7} Nine late-onset neurodegenerative diseases, including Huntington's disease, are attributed to polyglutamine expansions.^{8,9}

Prion diseases, on the other hand, are characterized by the misfolding of native proteins into self-aggregating β -sheet units which ultimately form insoluble amyloid fibrils that wreak havoc on the central nervous system.^{10,11} The so-called prion-forming domains of the proteins, which are responsible for protein misfolding, are rich in both asparagine (Asn, N) and

glutamine (Gln, Q).^{12–14} In humans, prion diseases are caused by the misfolding of the PrP^C protein into its prion form, PrP^{Sc}.¹⁵ These diseases include Creutzfeldt–Jakob disease, fatal familial disease, and Gerstmann–Straussler–Scheinker syndrome.^{15,16} Rather than being propagated through the genome, prion forms of misfolded proteins induce other normally folded proteins to isomerize to the prion state, thereby causing a chain reaction of protein misfolding and disease propagation.

These amyloid fibrils all appear to contain a common structural motif: the steric zipper. In this structure at least two β -sheets are interdigitated with one another, oftentimes sterically locking in asparagine and glutamine residues.^{2,17,18} Studies using solid-state NMR spectroscopy, X-ray crystallog-

Received: August 29, 2018

Revised: October 16, 2018

Published: October 21, 2018



Cite this: DOI: 10.1039/c9cp04556b

Vibronic spectroscopy of methyl anthranilate and its water complex: hydrogen atom dislocation in the excited state†

 Karl N. Blodgett,^a Dewei Sun,^a Joshua L. Fischer,^a Edwin L. Sibert III^b and Timothy S. Zwier^{*,a}

Laser-induced fluorescence (LIF) excitation, dispersed fluorescence (DFL), UV–UV-hole burning, and UV-depletion spectra have been collected on methyl anthranilate (MA, methyl 2-aminobenzoate) and its water-containing complex (MA–H₂O), under jet-cooled conditions in the gas phase. As a close structural analog of a sunscreen agent, MA has a strong absorption due to the S₀–S₁ transition that begins in the UV-A region, with the electronic origin at 28 852 cm⁻¹ (346.6 nm). Unlike most sunscreens that have fast non-radiative pathways back to the ground state, MA fluoresces efficiently, with an excited state lifetime of 27 ns. Relative to methyl benzoate, inter-system crossing to the triplet manifold is shut off in MA by the strong intramolecular NH···O=C H-bond, which shifts the ³nπ* state well above the ¹ππ* S₁ state. Single vibronic level DFL spectra are used to obtain a near-complete assignment of the vibronic structure in the excited state. Much of the vibrational structure in the excitation spectrum is Franck–Condon activity due to three in-plane vibrations that modulate the distance between the NH₂ and CO₂Me groups, ν₃₃ (421 cm⁻¹), ν₃₄ (366 cm⁻¹), and ν₃₆ (179 cm⁻¹). Based on the close correspondence between experiment and theory at the TD-DFT B3LYP-D3BJ/def2TZVP level of theory, the major structural changes associated with electronic excitation are evaluated, leading to the conclusion that the major motion is a reorientation and constriction of the 6-membered H-bonded ring closed by the intramolecular NH···O=C H-bond. This leads to a shortening of the NH···O=C H-bond distance from 1.926 Å to 1.723 Å, equivalent to about a 25% reduction in the H···O distance compared to full H-atom transfer. As a result, the excited state process near the S₁ origin is a hydrogen atom dislocation that is brought about primarily by heavy atom motion, since the shortened H-bond distance results from extensive heavy-atom motion, with only a 0.03 Å increase in the NH bond length relative to its ground state value.

 Received 16th August 2019,
Accepted 11th September 2019

DOI: 10.1039/c9cp04556b

rsc.li/pccp

1. Introduction

Methyl anthranilate (MA) is the precursor to menthyl anthranilate (MenA), an FDA approved sunscreen agent.¹ Upon UV absorption, efficient sunscreen molecules are able to non-radiatively decay back to their ground electronic state, thereby regenerating their UV-absorbing capacities. In some cases, internal conversion is thought to be facilitated on the S₁ surface by H-atom transfer.^{2–8} As such, much theoretical and experimental work has been directed toward understanding excited state hydrogen atom, or proton, transfer processes in this family of molecules. There are circumstances, however, in which excited state intramolecular H-atom transfer does not

completely quench fluorescence, but instead leads to a Stokes-shifted fluorescence that signals its occurrence, as in the case of salicylic acid and methyl salicylate.^{3,4,9,10} This shifted emission provides a ready means of assessing the efficiency of the process as a function of vibrational level in the excited state.

For a hydrogen atom transfer process to occur, a donor hydrogen must be oriented toward an acceptor atom. Upon electronic excitation the donor X–H becomes more acidic while the acceptor Y becomes more basic, and the X–H bond is broken, resulting in the transfer of the hydrogen to the acceptor atom.^{11,12} In so doing, the excited state geometry rearranges as it moves on the potential energy surface, producing broad, red-shifted emission back to highly excited vibrational states in the ground state. This red-shifted emission is characteristic of these transient hydrogen transfer products. Alternatively, the excited state molecule may, through displacements along one or more internal coordinates, reach a conical intersection and non-radiatively decay back to the electronic ground state.^{3,11–13}

^a Department of Chemistry, Purdue University, West Lafayette, Indiana 47907-2084, USA. E-mail: zwier@purdue.edu

^b Department of Chemistry, University of Wisconsin–Madison, Madison, Wisconsin 53706, USA

† Electronic supplementary information (ESI) available. See DOI: 10.1039/c9cp04556b